Electron Transport in Integrated Quantum Systems

Chengyu Yan

Department of Electronic and Electrical Engineering
University College London

This dissertation is submitted for the degree of
Doctor of Philosophy

November 2016

Declaration

I, Chengyu Yan confirm that the work presented in this thesis is my own. Where information has been derived from other sources, I confirm that this has been indicated in the thesis

Chengyu Yan
November 2016

Acknowledgements

First and foremost, I should thank Prof. Sir Michael Pepper who leads me to the astonishing field, physics of mesoscopic system, and I am pretty sure that I will be excited by this still rapidly developing field in the foreseeable future. Both my academical career and daily life are deeply influenced by Mike. His enthusiasm, knowledge, and courage reshape my understanding on what a true physicist should be. Discussion with him always make me believe a new world is there to be explored, such feeling is the intrinsic motivation for someone who works in a well established field. In brief, Mike has forged me from a freshman without too much physics background into a physicist, hopefully a promising one, in the past few years.

I am graceful to Dr. Sanjeev Kumar whom I worked with everyday and witnessed both highs and lows in my PhD. I hold deep respect to Sanjeev. I used to hold a belief that OK is acceptable for everything, however, this is apparently not the right attitude of doing physics where precession and accuracy matter a lot, Sanjeev is the one who points out the problem and sets the strict standard. Discussion with Sanjeev on the optimization of device design and experiment setup makes the works present in this thesis possible.

Working with Dr. Kalarikad J. Thomas is an invaluable experience. His knowledge and experience on mesoscopic physics and low temperature measurement helps me make the realistic choice.

Thanks Ian Farrer and Dave Ritchie for growing the high quality wafers which leaves me flexibility in device design. Thanks Patrick See's help in fabricating nanoscale devices which is actually tricky and challenging, his experience makes the devices with particular dimension and shape doable thus I do not need make compromise between device performance and yield.

I would like to acknowledge my college Hume, Guang, Henry, Wei and Elias who helps me in varying ways. For Hume, Guang and Henry, I wish you every success in your future career; For Wei and Elias, good luck to your PhD. Also thanks to other post-docs in the group, for suggestion and discussion which make things go smoothly.

Last my greatest thanks to my parents who always support and help me, their love and understanding gives me the courage to take this course of PhD and go further.

Abstract

In this thesis, integrated quantum devices defined using a split gate technique are studied experimentally. These integrated devices provide a novel platform to investigate the property of quantum systems, such as spin polarization, via non-local measurement. Information extracted from these integrated devices leads to a comprehensive understanding of the puzzling phenomenon such as the 0.7 anomaly. Meanwhile, these devices are possibly suitable for studying quantum entanglement because perturbation due to measurement is minimized in the non-local setup. Devices demonstrated here are also promising to be used as a building block such as quantum injector/detector or quantum bus (which is a information channel where quantum information can be transported coherently) for more complicated quantum systems.

In the first experiment, a transverse electron focusing in n-type GaAs heterojunction is present where pronounced splitting of odd focusing peaks are observed. From the asymmetry of sub-peaks of the first focusing spin polarization is extracted directly, this provides direct evidence for intrinsic spin polarization in a quasi-one-dimensional system. Parameters which may affect transverse electron focusing are studied systemically. Changing the shape of the injector, thus tuning the adiabaticity of the injection process, can influence the presence of peak splitting or not, with the sharp (non-adiabatic) injector the peak splitting is absent while peak splitting is observed with the flat (adiabatic) injector. Adjusting the length of injector affects the spin polarization, the longer the channel the higher the spin polarization can be achieved. This highlights the role of exchange interaction which results in the spin polarization in the quasi-1D channel. Applying a dc source-drain bias leads to such a result, peak splitting is preserved with negative bias while it smears out with positive bias when the bias is above a particular value (0.5 mV in the experiment), this proves the existence of spin-gap.

In the second experiment, the coupling between different quantum devices are investigated by using an integrated quantum device consisting of an QPC and electronic cavity, where the cavity is defined with the arc-shaped gate and an inclined reflector. Unique features such as the double-peak structure occurs in the 1D-2D transition regime of the arc-QPC and

fine oscillations associated with conductance plateaus and 0.7 anomaly are observed when the reflector voltage is sufficiently negative and these features smear out when the reflector voltage is less negative. The double-peak structure and fine oscillations are proved to arise from the coupling between the discrete states in the QPC and continuum cavity state by the manifestation of Fano resonance via tuning reflector voltage or small transverse magnetic field.

In the third experiment, quantum interference in a double-cavity system is studied by magneoresistance measurement. An unique evolution of the line shape of the magnetoresistance are observed, the magnetoresistance has a Lorentzian shape, corresponding to ergodic and chaotic motion, when the injector conductance is sufficiently small and then alters into linear line shape arising from non-ergodic and regular motion when injector is opens a bit more and finally a Lorentzian shape when the injector opens even further. Apart from the line shape, the strength of the magnetoresistance is found to fluctuate with injector conductance, it is enhanced at conductance plateaus and weakens elsewhere. Such behaviours are likely to arise from both deformation of the arc-shaped potential barrier at the vicinity of injector and detector QPC as well as the non-uniform spatial distribution of the cavity state.

Table of contents

List of figures

List of tables

Chapter 1

Introduction

It has been known for decades that electron transport diffusively in macroscopic devices, i.e. electrons scatter multiple times along the propagation path, and the current density can be universally described by drift-diffusion equation

$$J = e(n\mu E + D \bigtriangledown n) \tag{1.1}$$

where e is electron charge, n is electron density, μ is electron mobility , E is electric field and D is diffusion constant ($\bigtriangledown$ is gradient operator). Conductivity, according to Drude model, can be expressed as,

$$\sigma = \frac{\partial J}{\partial E} = en\mu = \frac{e^2 n\tau}{m^*} \tag{1.2}$$

where τ, the mean free time, is the average time between scatterings and m^* is electron effective mass. Then it suggests a striking result that resistivity converges to 0 if the device size is much smaller than meam free path l_m (defined as $l_m = v\tau$, v is electron velocity) because in this case reflection due to scattering will not occur within the propagation length.

To verify the prediction above, the reduce device size can be reduced or the mean free path enlarged. The former is achieved with the improvement of fabrication techniques especially molecular-beam epitaxy (MBE) and electron-beam lithography (EBL), devices with size smaller than 0.1 μm are easily accessed nowadays. The latter can be realized by removing disorder in devices which act as scattering centres, lowering temperature and reducing dimensionality (e.g. from three-dimensional to two-dimensional).

Besides, unlike macroscopic devices where behaviour of electrons are semi-classical and quantum mechanics is only necessary in order to decide some intrinsic parameters of the material (e.g. energy band gap), quantum mechanics dominates with reducing physical size

and dimensionality. Therefore investigation of properties on systems with smaller size and lower dimensionality is of fundamental importance for both theoretical understanding and practical application.

1.1 Electron transport in low dimension

It is possible to restrict motion of electrons along particular directions by applying large confinement. A thin layer of two dimensional gas (2DEG) forms when electrons are confined in one direction (for the ease of description this direction is denoted as z-direction), this has been realized at the interface between different semiconductors, surface of clean metal film or monolayer material also known as 2D material. Notable results are observed in 2DEG, such as the discovery of integer quantum Hall effect[1] and fractional quantum Hall effect[2].

Applying confinement to a 2DEG in one or more directions leads to the formation of a 1D (quantum wire) or 0D structure (quantum dot). Quantization of conductance[3, 4] is one of most remarkable results in 1D while Coulomb blockade[5] is a good example of observations in 0D.

Properties of low dimensional systems play a key role in this work and hence various aspect of mesoscopic transport will be discussed in the following sections.

1.1.1 Density of states

Density of states g(E), electron distribution against energy E per unit volume for 3D or per unit area for 2D or per unit length for 1D, decides the transport properties of electron system. In general, g(E) can be expressed as below,

$$g(E) = \frac{\mathrm{d}n}{\mathrm{d}E} = \frac{\mathrm{d}n}{\mathrm{d}k} \cdot \frac{\mathrm{d}k}{\mathrm{d}E} \tag{1.3}$$

where n is the carrier density and k is momentum. $\frac{\mathrm{d}n}{\mathrm{d}k}$, number of available states in the range of k to $k+\Delta k$, can be derived from Bohr-Sommerfeld condition,

$$\left.\frac{\mathrm{d}n}{\mathrm{d}k}\right|_{2D,3D} = (\frac{k}{\pi})^{N-1} \tag{1.4}$$

where N is the dimensionality, the form is different for 1D,

$$\left.\frac{\mathrm{d}n}{\mathrm{d}k}\right|_{1D} = \frac{2}{\pi} \tag{1.5}$$

$\frac{dk}{dE}$ can be extracted from the dispersion relation,

$$\frac{dk}{dE} = \sqrt{\frac{2m}{E}} \cdot \frac{1}{2\hbar} \tag{1.6}$$

as a result the formula for the density of states can be obtained as below,

$$g_{3D}(E) = \frac{m}{\pi\hbar^2} \cdot \sqrt{\frac{2mE}{\pi\hbar}} \tag{1.7}$$

$$g_{2D}(E) = \frac{m}{\pi\hbar^2} \tag{1.8}$$

$$g_{1D}(E) = \frac{m}{\pi\hbar^2} \cdot \frac{2\hbar}{\sqrt{2mE}} \tag{1.9}$$

it is clear that g(E) is strongly dimensionality dependent. It is noteworthy that for 2D system the density of states has a constant form while for 1D it has a singularity at E = 0.

1.1.2 Conductance of a quasi-1D constriction

Equipped with the density of state obtained in the last section, the conductance of the idealized 1D constriction could be derived as below. Here, by referring to an ideal 1D conductor, it suggests that the electron are only allowed to move along one direction denoted as x-direction while motion along y and z directions are completely restricted (momentum along these two direction equal to 0). Electrons occupy discrete energy levels in a low dimensional system, for the ideal 1D constriction where the energy spacing between subbands is infinite, therefore electrons only occupy the lowest available energy level which is the ground state.

Starts with the definition of current,

$$I = en_{1D}v = eg_{1D}(E)v\Delta\mu = eg_{1D}(E)veV \tag{1.10}$$

substitute Eq.(1.9) into Eq.(1.10), it gives the expression for conductance G:

$$G = \frac{dI}{dV} = e \cdot \frac{1}{\pi\hbar} \cdot \sqrt{\frac{2m}{E}} \cdot \sqrt{\frac{E}{2m}} \cdot e = \frac{2e^2}{h} \tag{1.11}$$

the result indicates the conductance of an ideal 1D conductor is not affected by any external parameters but only depends on basic physical constant e (charge of electron) and h (Planck constant), this is of particular significance to quantum metrology[6].

In a more realistic case, electrons take non-zero momentum along the confined direction, hence the energy spacing is finite and there might be multiple subbands contributing to the transport of electrons. Each of these subbands give a quantized conductance $2e^2/h$, and the total conductance is then,

$$G_{tot} = N \cdot \frac{2e^2}{h} \tag{1.12}$$

where N is number of occupied subbands.

The discussion above assumes ideal transport between the environment (termed as the reservoir) and the 1D channel. In a real device, potential barriers form at the entrance and exit of the channel with respect to the surrounding 2DEG (denoted as source and drain reservoir) due to confinement which defines the 1D channel, and the potential barriers affect the conductance. To account for the influence of the potential barrier, Landauer ,Büttiker and Imry[7–9] introduced the transmission coefficient T to Eq. (1.11) and then the corrected conductance is as below,

$$G = \frac{2e^2}{h} \cdot T \tag{1.13}$$

and it is found experimentally that in the high mobility devices T $\approx$ 1, and the total conductance is then modified accordingly,

$$G_{tot} = \sum_{n=1}^{N} \frac{2e^2}{h} \cdot T(n) \tag{1.14}$$

and *T(n)* is the transmission probability for each 1D subband.

1.2 Realization of 1D system

Section 1.1 briefly mentions the idea of realising a low dimensional electron gas via confinement. This section focuses on the experiment realization of these low dimensional system.

1.2.1 Modulation doped heterostructure

$GaAs/Al_xGa_{1-x}As$ modulation doped hetero structures, where x is the fraction of aluminium, have been one of the most convenient system to realise 2DEG since its first experimental realization by Störmer et al.[11]. The method used to grow such heterostructures was readily

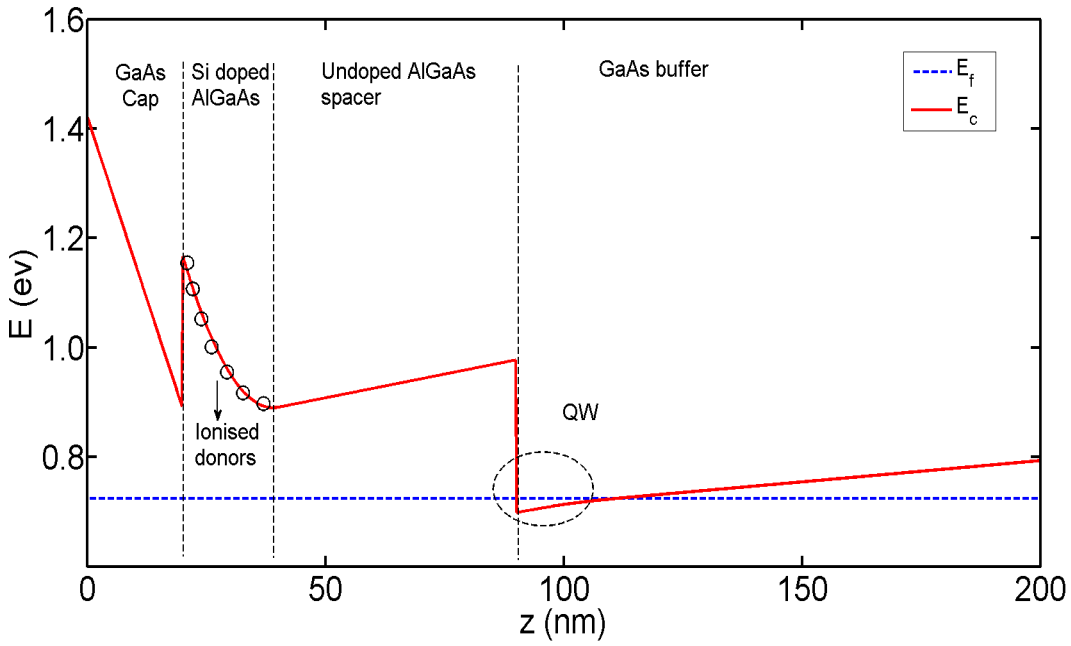

Fig. 1.1 Band structure for a typical GaAs/$Al_xGa_{1-x}As$ modulation doped heterostructure. The bold red line stands for edge of conduction band E_c while blue line is for Fermi level E_f. A triangular quantum well forms at the interface of AlGaAs spacer and GaAs buffer. Simulation is performed using nanoHUB 1D hetero tool (available online[10]).

extended and applied to other materials and paving the way to investigate the low dimensional systems.

The advantages of GaAs/$Al_xGa_{1-x}As$ modulation doped heterostructure are several fold: Firstly, GaAs and $Al_xGa_{1-x}As$ have similar lattice constants and therefore defects due to mismatch of lattice of different layers are minimized. This problem can be further optimised by inserting GaAs and $Al_xGa_{1-x}As$ superlattice (periodic layers of such assembling) to the stack structure. Secondly, mobile electrons in the 2DEG are relatively far away from the ionized donors and therefore chance of scattering due to background potential fluctuation arising from donors is considerably reduced, however, this can become the dominant scattering mechanism when carrier concentration is extremely low[12]. Thirdly, electron effective mass in III-V semiconductor is small, e.g. $m^* = 0.069m_0$ in GaAs where m_0 is electron rest mass. These advantages are crucial for achieving high electron mobility.

A better understanding can be obtained from the band structure of a typical GaAs/$Al_xGa_{1-x}As$ modulation doped heterostructure as shown in figure1.1. The wafer is grown with MBE technique. Under the GaAs cap layer, a Si-doped AlGaAs layer is deposited and used to supply electrons. An AlGaAs spacer which is not doped is necessary for preventing electrons

in 2DEG to back-tunnel to the doped region. The net electric field, which could be derived from Gauss's law, in the doped region leads to a pronounced deviation between the doped and undoped AlGaAs regime and gives the V-shape band edge shown in figure 1.1. At the interface of AlGaAs and GaAs a triangular quantum well forms due to difference in conduction band edge in these two layers (GaAs has a band gap of 1.42eV while $Al_xGa_{1-x}As$ has a larger gap), at low temperature electrons occupy the lowest energy level of the triangular quantum well. Because the electrons are highly concentrated within a small regime along the growth direction, the cluster of electrons can be treated as 2D system.

Apart from the modulation doped heterostructure, it is also possible to define a 2DEG without doping but by electrostatical method using side gates[13, 14]. This alternative technique allows one to tune electron concentration by almost one order within same wafer and thus gives more flexibility in device design.

1.2.2 Split-gate devices

Creating a 1D constriction from 2DEG requires further confinement to restrict electron motion along one of the in-plane directions. Split gates device, first fabricated by Thornton et al.[15], has proved to be one of the most successful way to define a quasi-1D channel. Schematic for a typical split gate device is illustrated in figure 1.2. A pair of split gates are patterned on the surface of the heterostructure. When a negative voltage is applied to the gate, electrons underneath are depleted and thus a quasi-1D channel is left. The width of the 1D channel is controllable by tuning the gate voltage. The channel is defined electrostatically, thereby the confinement edge is free from disorder and ballistic transport over long distances is easier to achieve.

Confinement due to split gates plays an important role in 1D transport and it can be well described by the saddle-point model[16] where the potential within the 1D channel is expressed as below:

$$V(x,y) = V_0 - \frac{1}{2}m\omega_x^2 x^2 + \frac{1}{2}m\omega_y^2 y^2 \tag{1.15}$$

It assumes that the confinement changes parabolically against coordinate. As a result, energy subbands formed in the channel have equal subband-spacing.

To check the validity of the saddle-point model, a simulation which only considers electrostatic contribution of split gate is performed following framework of Ref.[17] and the result is shown in figure1.3. The simulated split gate is with a lithography defined size of 300 nm $\times$ 300 nm. The top left and top right inset show the potential of a cut through the origin along X (direction of current flow) and Y direction respectively and the

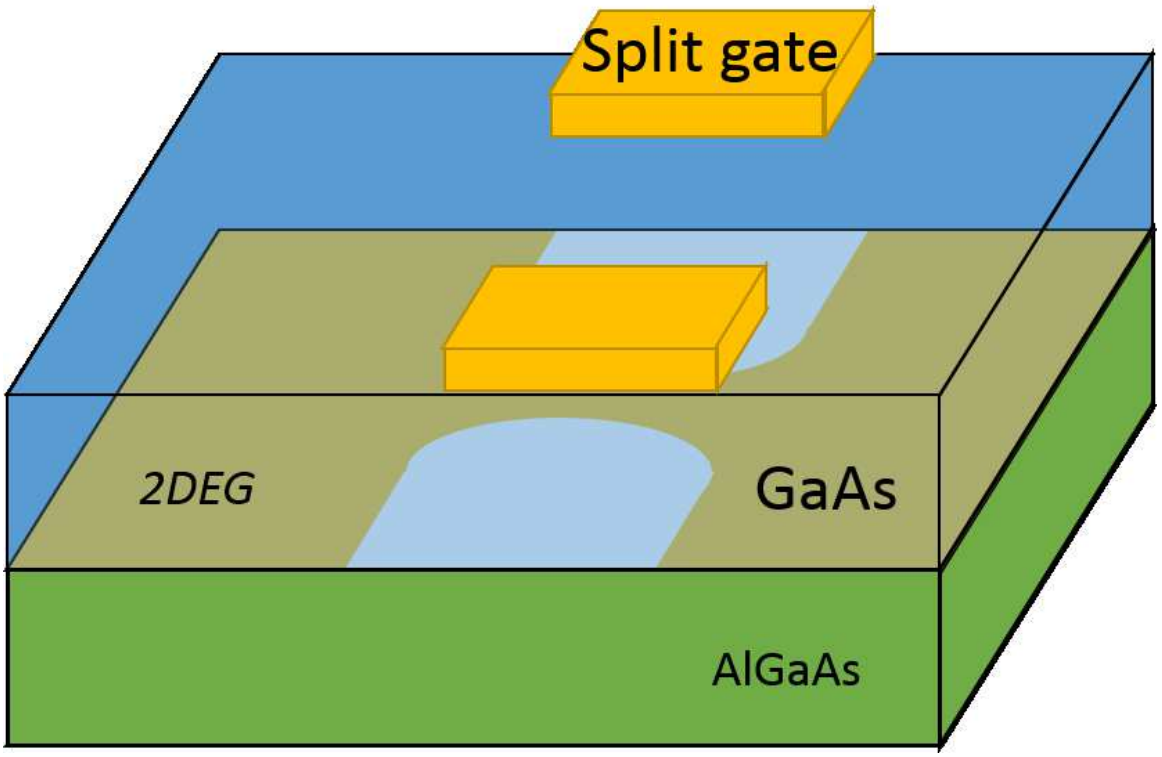

Fig. 1.2 Schematic of a typical split gate device where the quasi-1D channel forms by applying negative gate voltage to deplete 2DEG underneath.

corresponding parabolic fittings, it is seen that the simulated potential varies rapidly within the 1D constriction and then saturates outside.

Combining the saddle point model and conductance of an ideal 1D constriction discussed in section1.1.2, the simulated conductance of a real split gate device can be obtained. Figure 1.4 is the simulation result of split gate device defined in figure 1.3 based on a phenomenological model[18] which points out that the number of available 1D subbands is decided by the energy window between the Fermi level and top of the saddle point. It is seen that conductance appears as a series of plateaus quantized in unit of $2e^2/h$, in addition, the plateaus become shorter when the gate voltage becomes less negative due to the reduction of 1D subband spacing, this agrees with experimental result[19].

1.2.3 Alternative Realizations

Apart from split-gate technique, 1D constriction can be realised with alternative approaches including 1D nanowire[20], focussed ion beam implantation[21], wet etching techniques[22], cleaved edge overgrowth[23], and selective oxidation using an atomic-force microscope[24].

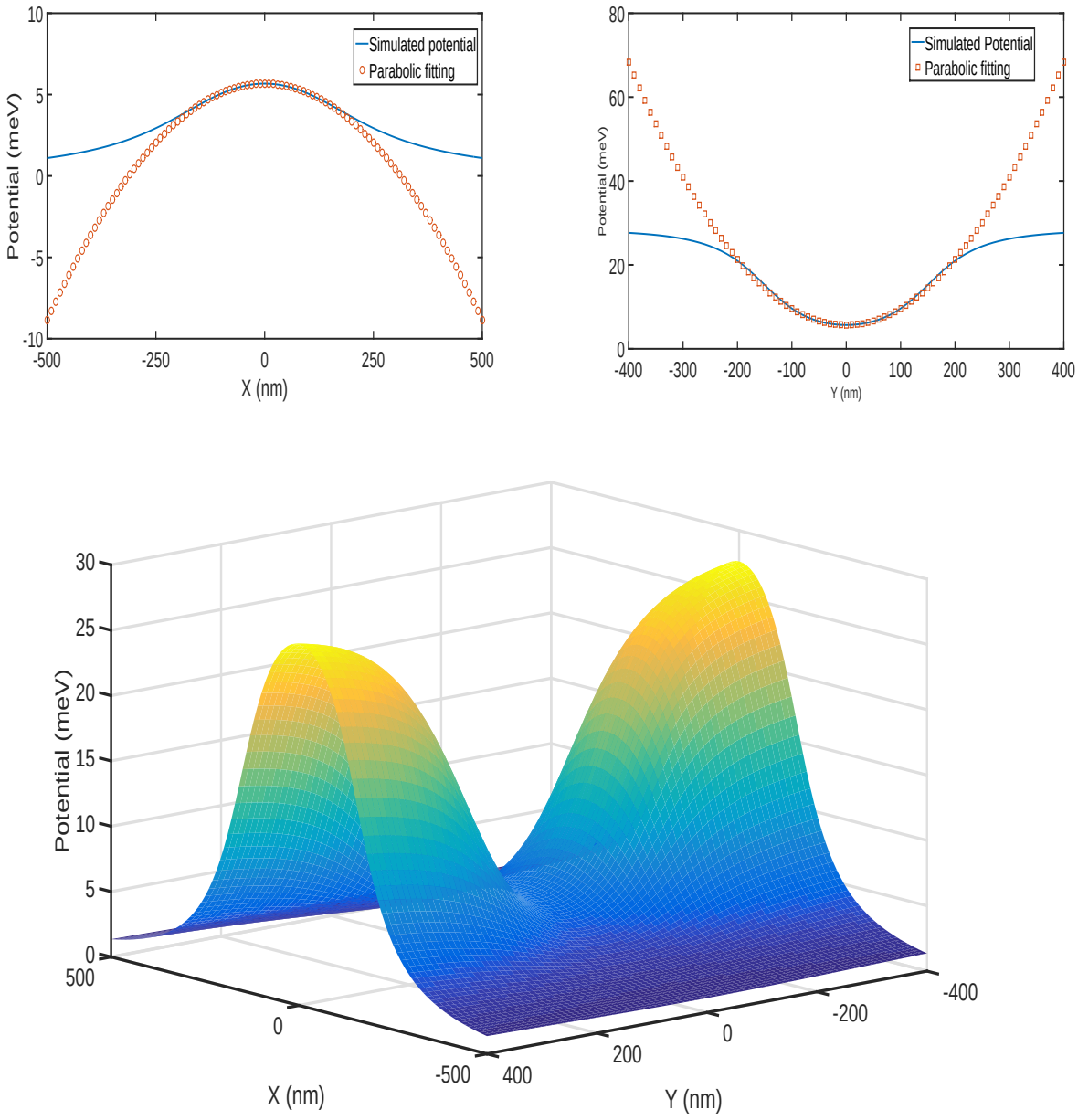

Fig. 1.3 Main plot: Simulated electrostatic potential of a 300 nm $\times$ 300 nm split gate device with an applied gate voltage of - 1 V. X is the direction of current flow while Y is the direction of confinement. Top left: Potential of a cut through the origin along X direction and its parabolic fitting. Top right: Potential of a cut through the origin along Y direction and the corresponding parabolic fitting.

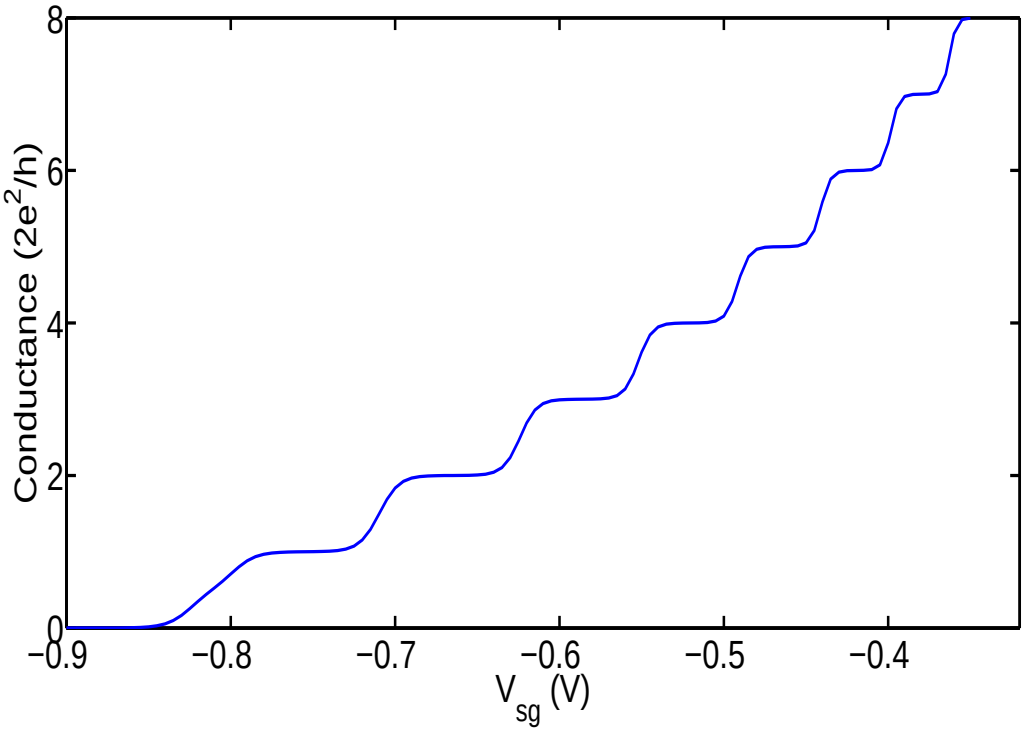

Fig. 1.4 Simulated conductance of split gate device defined in figure1.3. The conductance is quantized in unit of $2e^2/h$ and the length of the plateaus reduce when the gate voltage become less negative.

Conductance quantization is universally observed, however, roughness of the 1D channel obtained with these technique may lead to additional structures superpose on conductance plateaus. Although there exists some drawbacks, these techniques are found to be more suitable in getting long 1D channel compared to split gate (because electrons have to tunnel through series of saddle points formed in a long 1D channel defined bt split gate, this will affect the conductance significantly).

1.3 Spin polarization in a quasi-1D constriction

The quantized conductance plateau itself can be well understood within a single-particle framework where the role of spin is only manifested as the prefactor 2, due to spin degeneracy, in the quantized conductance $2e^2/h$. It is interesting to investigate whether or not it is possible to get intrinsic spin polarization when electrons pass through a 1D channel. E. Lieb and D. Mattis studied the problem theoretically and they pointed out that spin polarization is forbidden for the ground state of the ideal 1D chain[25]. However, the conclusion is

challenged by the 0.7 structure (an additional shoulder/plateau occurs near $0.7\times 2e^2/h$) which is observed in various 1D system[20, 26, 27].

Among all the properties of the 0.7 structure, the magnetic field dependence is most relevant to the subject here. It is found that 0.7 structure evolves towards to $0.5 \times 2e^2/h$[26] with increasing magnetic field. The electrons tend to align their spin orientation in parallel with magnetic field to reduce the total energy thus generating a spin polarized state. This suggests 0.7 structure is probably spin-related. Different explanations have been proposed for the 0.7 structure, however, a comprehensive understanding is still lacking and this motivates further study.

Apart from its importance in fundamental physics, the possible polarization produced by a 1D constriction may boost the development of spintronics. In spintronics spin rather than charge is used for information processing and storage. Spintronics studied up to date either utilizes magnetic field or puts special requirement on material, and this somehow complicates the design. Design of spintronic devices will be simplified significantly if the intrinsic spin polarization in 1D constriction is understood comprehensively

1.4 Outline of the thesis

The thesis focuses on the investigation of the properties of quantum devices such as spin polarization which are beyond the capacity of standard transport measurement. These devices are defined in a $GaAs/Al_xGa_{1-x}As$ 2DEG. Devices with different geometry and functionality are studied systemically.

Chapter 1 gives brief introduction on the background of the low dimensional system.

Chapter 2 will discuss properties of a quantum wire in detail. It starts with previous experiments on conductance measurement of the 0.7 structure and source-drain bias induced 0.25 structure. Then theoretical proposals including spontaneous spin polarization, Kondo screening and spin-gap are going to be reviewed as they are particularly relevant to the work here. The chapter will end up with transverse electron focusing and spin-related interference phenomenon.

Chapter 3 is mainly about the fabrication of devices used in this thesis, only shallow GaAs/AlGaAs HEMTs (high electron mobility transistor) are used in this work. Low temperature measurement technique will be another topic in this chapter, both two-terminal and four-terminal measurement will be introduced.

Chapter 4 presents results of the transverse electron focusing in a n-type GaAs hetero-junction where a pronounced focusing peak splitting is observed. Spin polarization of the

injected electrons can be extracted from the asymmetry of sub-peaks directly and the energy difference between different spin branches can be measured from the splitting. Different aspects of transverse focusing such as temperature and in-plane magnetic field dependence have been studied systemically. The possible origin of the splitting is discussed at the end of the chapter.

Chapter 5 studies the coupling between different quantum devices by using an integrated quantum device consisting of an QPC (quantum point contact) and an electronic cavity by monitoring the features such as double-peak structure and fine oscillations, arising from interference between states in different quantum devices, which occur in particular regimes of gate voltage.

Chapter 6 investigates quantum interference in a double-cavity system via magneoresistance. A unique evolution of the line shape of the magneoresistance is observed, the magneoresistance is with a Lorentzian shape when the injector conductance is at sufficiently low conductance and then alters into linear line shape when the injector opens further and finally a Lorentzian shape when the injector opens widely. The device can be used as a quantum bus with multiple modes.

Chapter 7 draws together the experiments in the three chapters above to conclusion, and suggestion for further investigation which can be carried out in the future is also discussed.

Chapter 2

Overview of spin polarization in quasi-1D system

2.1 Introduction

It is noticed that the spin degree of freedom plays an important role for electron transmission through a 1D channel and this chapter presents both theoretical and experimental studies on spin polarization in quasi-1D systems up to date. First of all, transport in the presence of a magnetic field will be discussed because magnetic field dependence is widely used to verify whether or not an observation is spin-related in 1D transport. The next section is about the 0.7 anomaly, which is universally observed in quasi-1D constrictions and is believed to arise from spin. Both experimental and theoretical works will be reviewed. Following this section, transport in the presence of source-drain bias is considered because it yields the possibility of electronic generation of fully spin polarized states. In section 2.4 the transverse electron focusing technique (TEF) will be introduced in detail and result of TEF in different materials is also included. The TEF technique provides a direct way to measure the degree of spin freedom and thus provides comprehensive understanding of spin-related phenomenon. The last section of this chapter is about interference/interaction in devices with different geometry and functionality, it provides an elegant way to demonstrate the quantum nature of electron transport in low dimensional systems and can be used as a sensitive tool to monitor properties such as correlation and entanglement between electrons.

2.2 1D transport in the presence of magnetic field

To begin with, when magnetic field is introduced to the system, a magnetic vector potential $\vec{A}$ should be included,

$$\vec{B} = \bigtriangledown \times \vec{A} \tag{2.1}$$

and this would replace momentum $\vec{P}$ in Hamiltonian with $\vec{P} - \frac{e\vec{A}}{c}$ and thereby lead to result below,

$$H = \frac{(\vec{P} - \frac{e\vec{A}}{c})^2}{2m} + V \tag{2.2}$$

where V is the confinement potential, solving the Hamiltonian it is found that the trivial energy subband is modified by an additional Zeeman energy term $g\mu_B BS$, where g is the Landé-g factor, μ_B is Bohr mageneton and S is spin of electron which equals to $\pm 1/2$. For 1D transport, Zeeman energy leads to splitting of spin-degenerate 1D subands, considering the saddle-point model the expression of each spin-resolved subband can be written explicitly as below,

$$E_{n,\uparrow} = V_0 + \hbar\omega(n - \frac{1}{2}) + \frac{1}{2}g\mu_B B \tag{2.3}$$

$$E_{n,\downarrow} = V_0 + \hbar\omega(n - \frac{1}{2}) - \frac{1}{2}g\mu_B B \tag{2.4}$$

where n is subband index and V_0 is bottom of the lowest subband, here it assumes that the spin-up subbands have higher energy level while the spin-down subbands have lower energy. Each of the spin-resolved subband is populated by electrons with the given spin orientation. In terms of conductance measurements, the total conductance equals the sum of the contribution of the two spin-branches, only plateaux at integer multiples of $\frac{2e^2}{h}$ are observable when the magnetic field is small where the two branches are not resolved while additional conductance plateaux occur at odd integer of $\frac{e^2}{h}$ start to appear when the field is large where degeneracy of the two spin branches is lifted[3], and the appearance of half integer plateaux are taken as an indication of formation of fully spin-polarized state.

Figure 2.1 shows result of simulation of conductance of a quasi-1D constriction at different magnetic fields. It is noticed that at large magnetic field where Zeeman energy is sufficiently strong, plateaux at multiples of $\frac{2e^2}{h}$ vanish and only the half integer plateaux are observed, both half integer and integer plateaux are present at intermediate magnetic field and eventually only integer conductance plateaux are left when the field is small. The

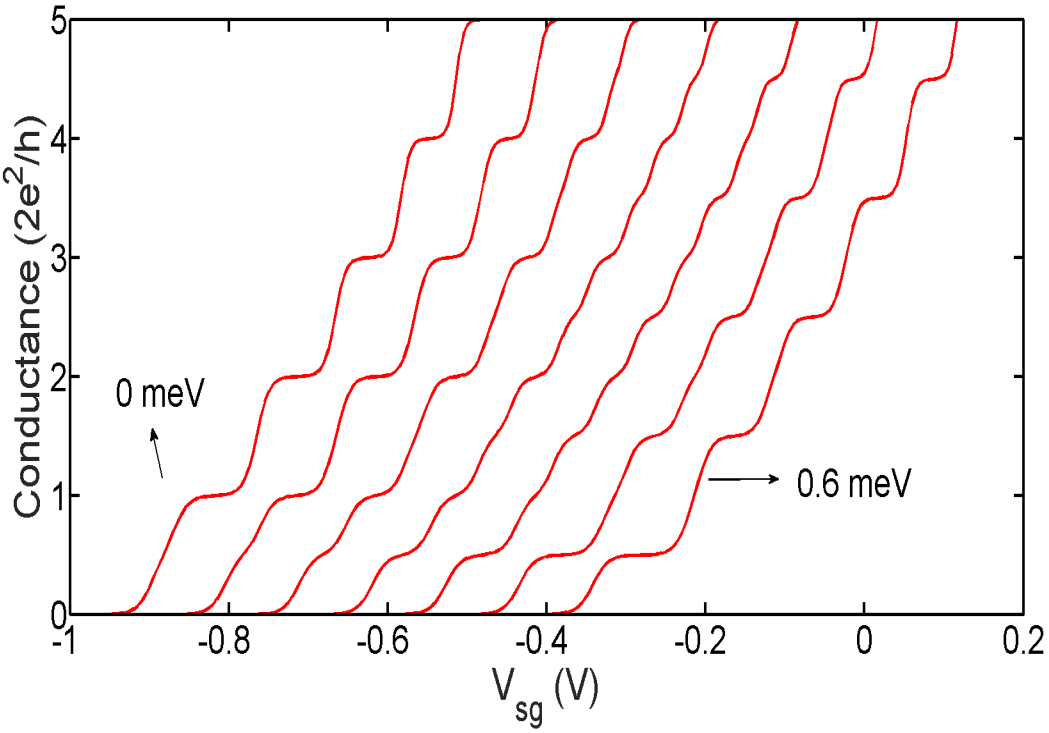

Fig. 2.1 Simulated conductance of a split gate device defined in figure1.3 in the presence of magnetic field. From left to right, Zeeman energy is increased from 0 to 0.6 meV with a step of 0.1 meV, half-integer plateaux form gradually with increasing magnetic field. Temperature is set to 100 mK. Data are offset horizontally for clarity.

transition occurs when Zeeman energy becomes comparable with thermal energy k_BT where k_B is Boltzmann constant and T is temperature.

In addition to Zeeman splitting, magnetic field can also modulate 1D transport via other mechanisms and these modulation are sensitive to the orientation of the field.

2.2.1 Magnetic field perpendicular to 2DEG

In presence of magnetic field which is perpendicular to 2DEG plane, denoted as B_z, electrons take cyclotron motion due to Lorentz force and occupy discrete energy levels, known as Landau levels, which are separated by $\hbar\omega_c$ where ω_c is cyclotron frequency and defined as $\omega_c = \frac{eB}{m}$. The Landau levels lead to Shubnikov de-Haas (SdH) oscillations and the quantum Hall effect[1].

However, the situation become different with the application of the lateral electrostatic confinement. The energy subband in presence of transverse magnetic field B_z can be written as[28],

$$E_{k,n} = V_0 + \frac{\hbar^2 k^2}{2m_B} + (n - \frac{1}{2})\hbar\sqrt{\omega^2 + \omega_c^2} \pm \frac{1}{2} g\mu_B B \tag{2.5}$$

where $m_B = m\frac{\omega^2+\omega_c^2}{\omega^2}$ is the magnetic modified effective mass. The transverse magnetic field enhances the confinement which in turn enlarges subband spacing, as the result, conductance plateau becomes longer.

A more intuitive understanding can be obtained by considering the competition between the cyclotron radius $r = \frac{mv_F}{eB}$ and electrostatic width of 1D channel w. When magnetic field is small so that $r \gg w$, motion of electrons is more similar to that without field and current flow is mainly through centre of the channel. Increasing magnetic field further to make $r \approx w$, the probability of scattering between electrons and potential wall increases dramatically, meanwhile some electrons may get localized in the channel and make no contribution to the conductance. In the large field regime where $r \ll w$, electrons are confined to the edge of potential wall and the density of state is significantly modified[28], the electron transport is dominated by the edge states (Landau levels).

2.2.2 Magnetic field in-plane and parallel to quantum wire

In-plane magnetic field is of particular interest in studying 1D transport property and widely used to achieve a spin polarized state. When the field is in the plane and parallel to the quantum wire, the subbands are then[29]

$$E(k, n_y, n_z) = \frac{\hbar^2 k_x^2}{2m} + (n_y + \frac{1}{2})\hbar\omega_1 + (n_z + \frac{1}{2})\hbar\omega_2 \tag{2.6}$$

where

$$\omega_{1,2}^2 = \frac{1}{2}(\omega_c^2 + \omega_y^2 + \omega_z^2 \pm \sqrt{(\omega_c^2 + \omega_y^2 + \omega_z^2)^2 - \omega_y^2\omega_z^2}) \tag{2.7}$$

It is seen that trivial 1D and 2D subbands represented by $\hbar\omega_y$ and $\hbar\omega_x$ are coupled into $\hbar\omega_1$ and $\hbar\omega_2$ respectively.

It is easy to see that ω_1 increases with field while ω_2, after binomial expansion the leading term is

$$\omega_2 \approx \frac{\omega_y\omega_z}{\sqrt{\omega_c^2 + \omega_y^2 + \omega_z^2}} \tag{2.8}$$

so it decreases with field. As a result, the modified 1D subbands experience a diamagnetic field shift which implies that the subband spacing may follow a non-monotonic change with increasing magnetic field.

Although it involves in the contribution of both 1D and 2D subbands, in most of the experiment considered here only the lowest 2D subband is occupied and thus the influence of 2D subband is less important.

2.2.3 Magnetic field in-plane and perpendicular to quantum wires

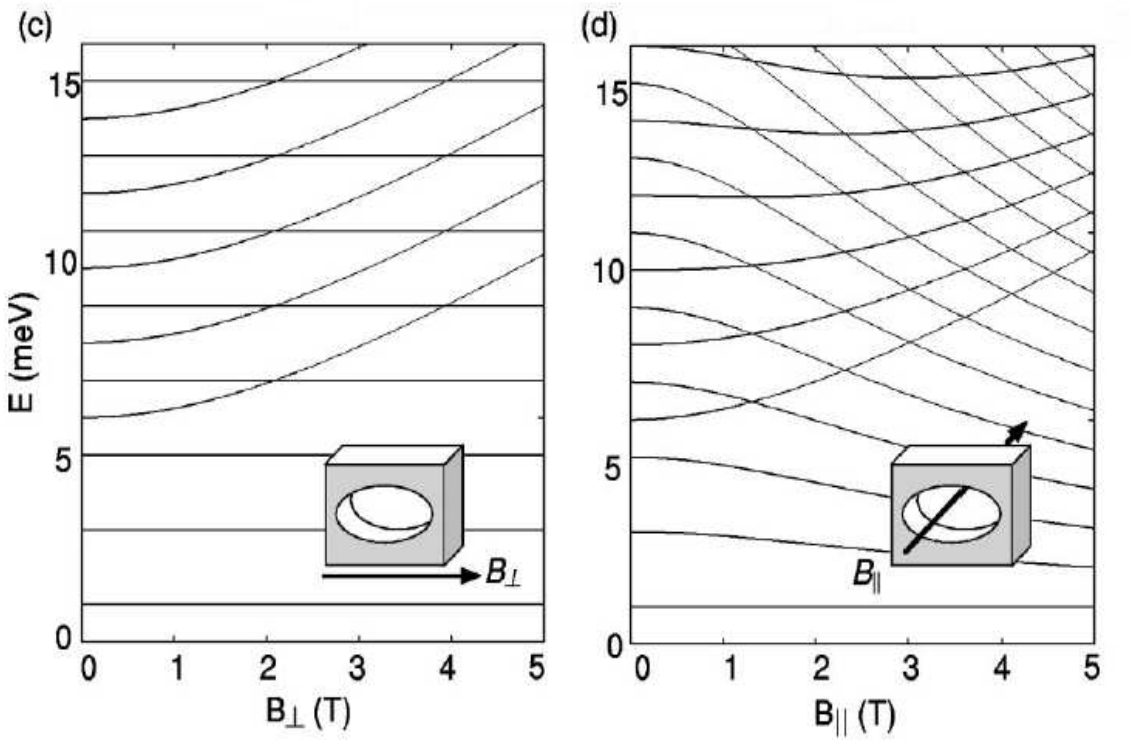

Fig. 2.2 Calculated 1D subbands of ballistic electron waveguide against in-plane perpendicular field (left) and in-plane parallel field (right), decreasing of 1D subband energy is only observable for parallel field. Figure adapted from Ref. [29].

When field is orientated in-plane and perpendicular to quantum wires the corresponding energy level reads[29]

$$E(k,n_y,n_z)=\frac{\hbar^2k_x^2}{2m_B}+(n_y+\frac{1}{2})\hbar\omega_y+(n_z+\frac{1}{2})\hbar\sqrt{\omega_z^2+\omega_c^2} \tag{2.9}$$

magnetic field does not affect the 1D part. On the other hand, 2D contribution shows a field dependence. Besides, the tuning of the dispersion relation by magnetic field is manifested by replacing m with m_B.

Calculated 1D subbands for both in-plane perpendicular field and in-plane parallel field are presented in figure 2.2, it is seen that although level crossing is observed in both cases decreasing of 1D subband energy is only present with in-plane parallel magnetic field, this property can be used to decide the magnetic field orientation for the possible sensor application.

2.3 0.7 anomaly in 1D constriction

2.3.1 Experimental investigation of the 0.7 anomaly

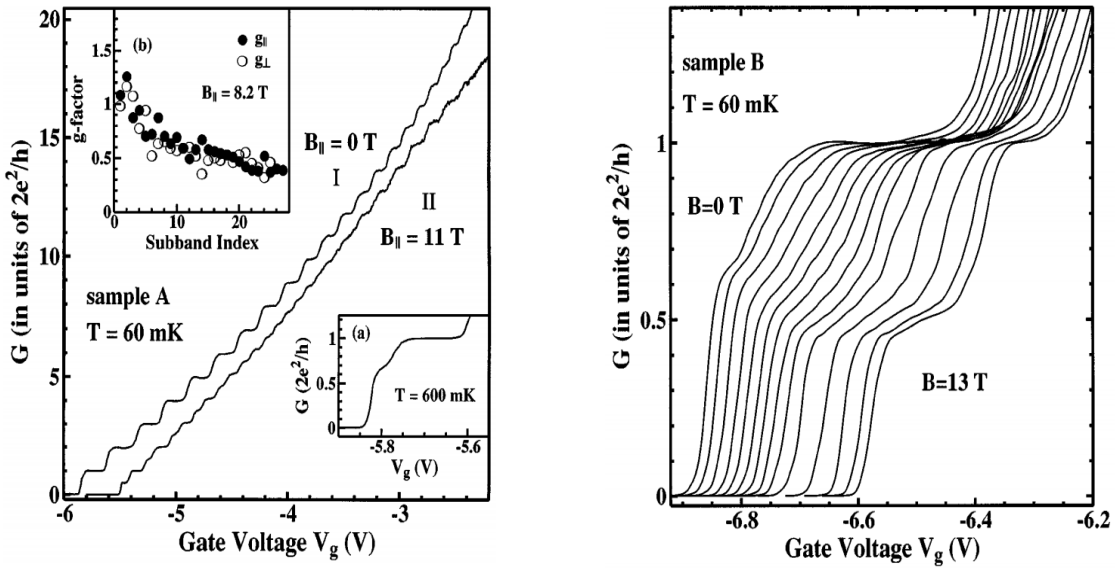

Fig. 2.3 Magnetic field dependence of 0.7 structure in different sample. Left: In sample A, at base temperature 60 mK. 0.7 structure observed at zero magnetic field becomes the 0.5 plateau with a in plane field of 11 T, upper inset shows g-factor for different subband while lower inset shows 0.7 structure at 600 mK. Right: Smooth evolution of 0.7 structure against magnetic field in sample B. Figure adapted from Ref. [26].

As mentioned in the introduction, it has been believed for a long time that spin polarization is not permitted in 1D system according to the theoretical work done by Lieb and Mattis[25] until the observation of 0.7 structure which refers to an additional structure occurs around $0.7\times\frac{2e^2}{h}$.

The 0.7 structure is widely observed in 1D channels with different dimensions fabricated in a wide range of materials. In addition, this structure is robust against thermal cycling and lateral shift of channel[26, 27], therefore it is clear that 0.7 is not a disorder induced structure. Among the early works on 0.7, the field dependence is probably the most interesting and informative. As shown in figure 2.3, with the application of an in plane magnetic field, the 0.7 structure evolves smoothly into the 0.5 plateau.

In plane magnetic field induces Zeeman splitting and aligns spin orientation. As it is known that the 0.5 plateau at high magnetic field corresponds to a fully polarized state, it is natural to think that the 0.7 structure is a partially polarized state[26]. Further evidence is the enhancement of Landé-g factor. It is proved that in a fully spin polarized state the g factor can be several times larger than the value for bulk material due to the large exchange energy[30], and similar enhancement is observed at 0.7 structure as well[26, 31, 32].

Boosted by the initial success of investigation of 0.7 structure, considerable experiments have been performed to give a clue about the origin of this anomaly. Experiments introduced below are most relevant to our work.

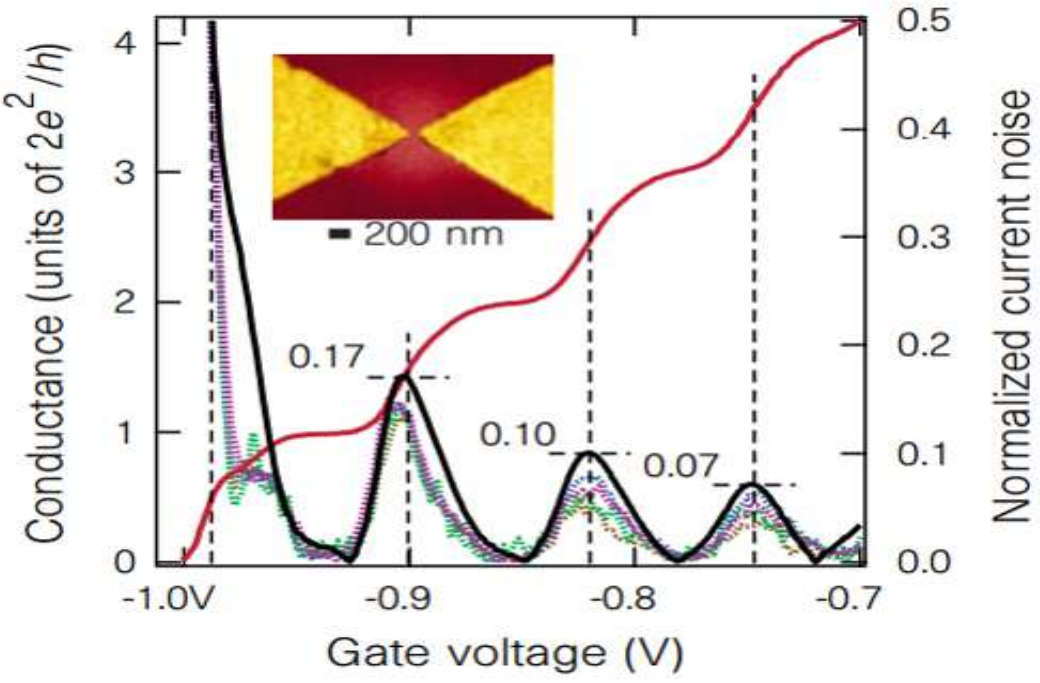

Fig. 2.4 Conductance (the bold red trace, left scale) and corresponding shot noise (the oscillating traces, right scale) of a QPC, noise suppress at conductance plateau significantly and increases rapidly at 0.7 structure. Figure adapted from Ref. [33].

As the 0.7 structure is likely to be a partially polarized state, it is suspected that such a state arises from transitions between different spin branches. Transition between different channels generate large shot noise which is directly proportional to the fluctuation in the population of electrons in each conducting channel. Shot noise measurement with quantum point contacts, as shown in figure 2.4, indicates that the noise signal vanishes at conductance plateau but shoots up at 0.7 structure[33–35] and this clearly proves that the 0.7 structure arises from two channels with different transmission coefficient[35]. A central problem is then what leads to the difference in transmission probability of the two spin-branches which should be degenerated according to Lieb-Mattis theory.

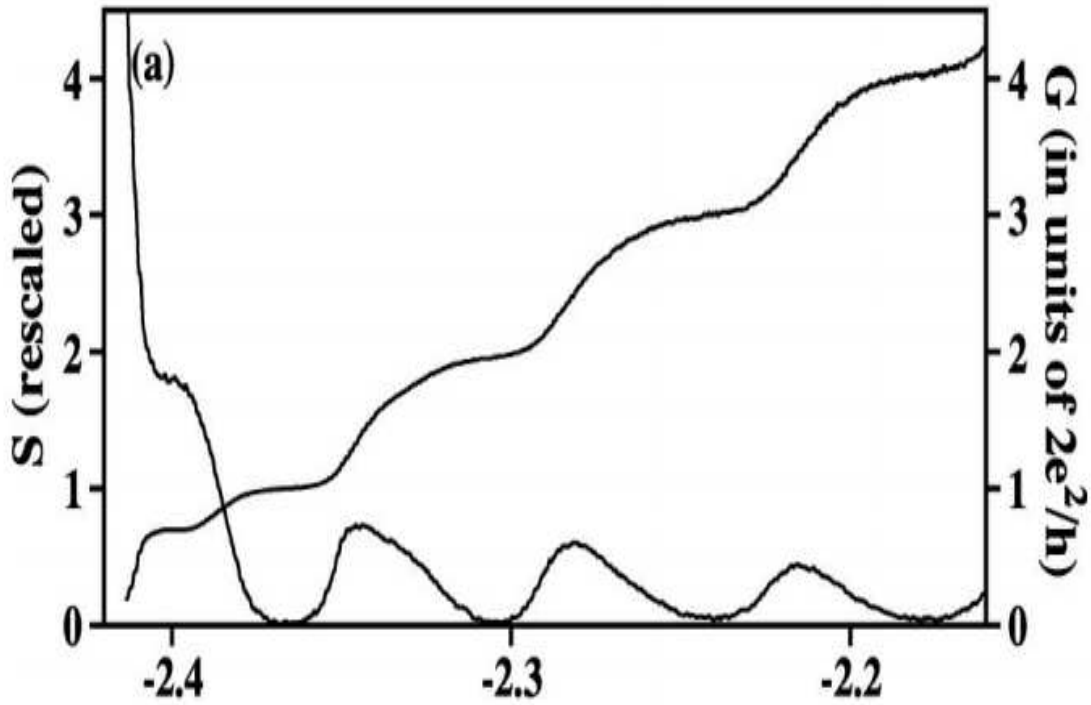

Fig. 2.5 Thermopower (left scale) drop to zero at conductance plateaus and remains finite at the transition between energy states, an additional thermopower plateau occurs at 0.7 structure. Figure adapted from Ref. [36].

Similar to shot noise measurement, thermopower measurement[38, 36] can also be used to verify that the 0.7 anomaly is related to transition between spin-resolved energy levels . Thermopower reduces to 0 at conductance plateaux and gives finite reading at transition between different energy level, these result can be reproduced with Mott's model[39], however, the finite thermopower plateau occurs at 0.7 structure shown in figure 2.5 violates

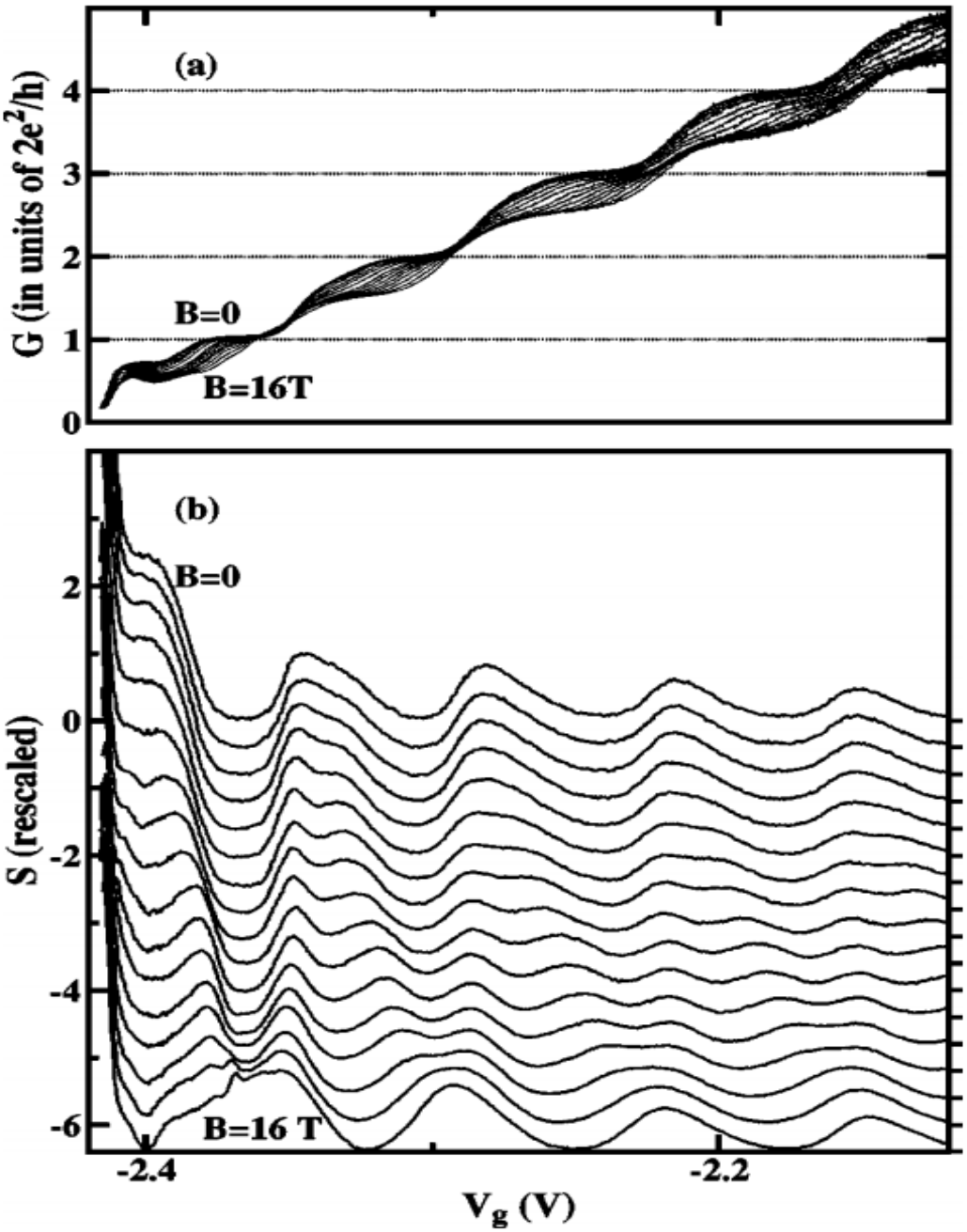

Fig. 2.6 Upper plot: Conductance measured at different magnetic field, 0.7 structure goes downward to 0.5 plateau. Lower plot: Magnetic field dependence of thermal power, the finite thermal power plateau at 0.7 structure disappears at high in plane field. Figure adapted from Ref. [36].

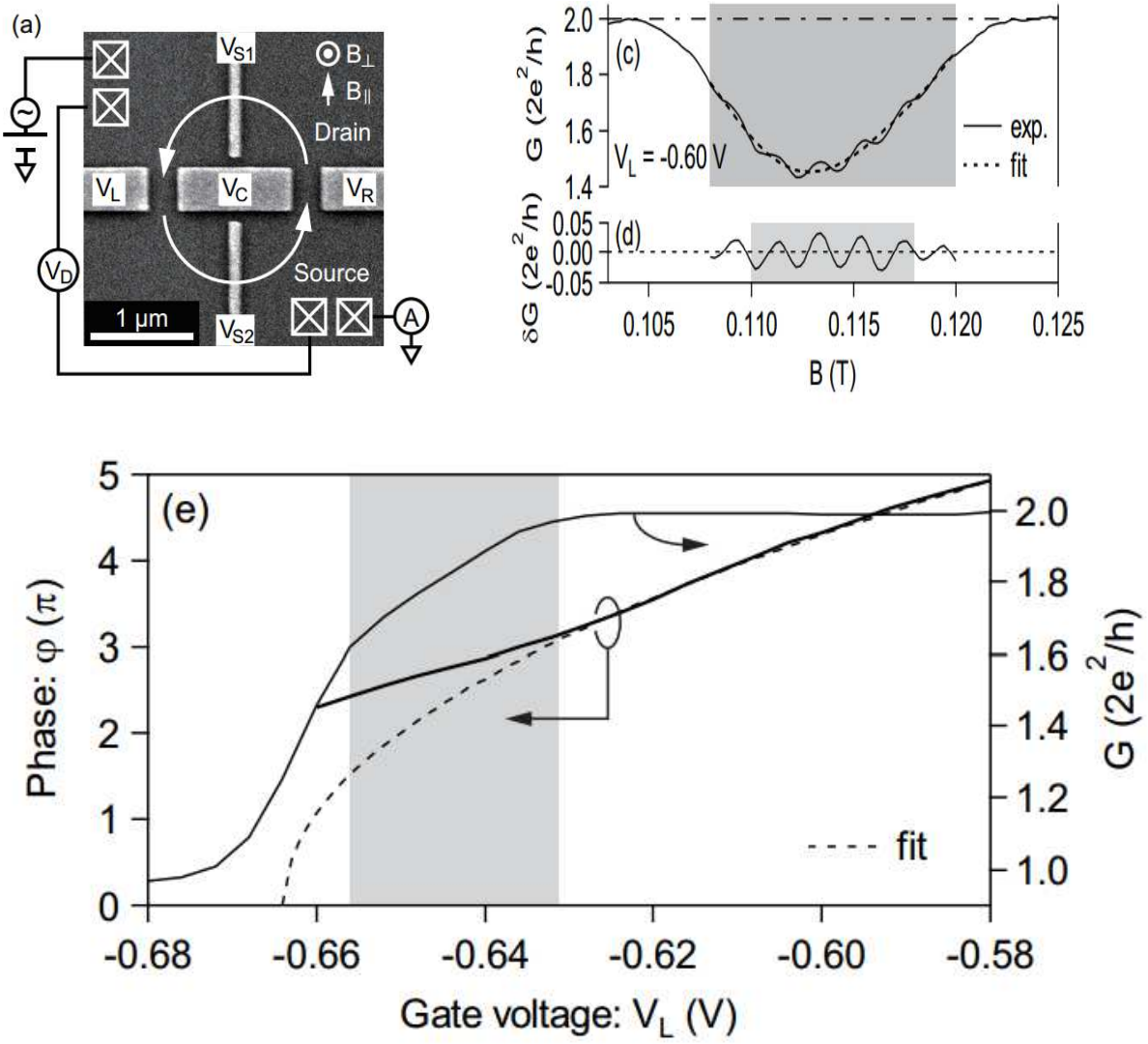

Fig. 2.7 Upper left: SEM image and experiment setup of transmission phase measurement. Upper right: Conductance oscillation against magnetic field. Main plot: Transmission phase extracted from the Fourier transform of the oscillation and the corresponding conductance as function of gate voltage. Figure adapted from Ref. [37].

the framework which predicts there should be an overshooting below the last conductance plateau.

In addition, with the application of in plane magnetic field the finite thermopower plateau at 0.7 structure goes down and finally disappears while the corresponding conductance follows the typical 0.7 structure to 0.5 plateau evolution as shown in figure 2.6. This indicates the apparent difference between 0.5 plateau (corresponds to a spin-resolved subband) and 0.7 anomaly (transition between two spin-resolved subbands). However, the thermopower plateau at 0.7 structure remains to be studied further.

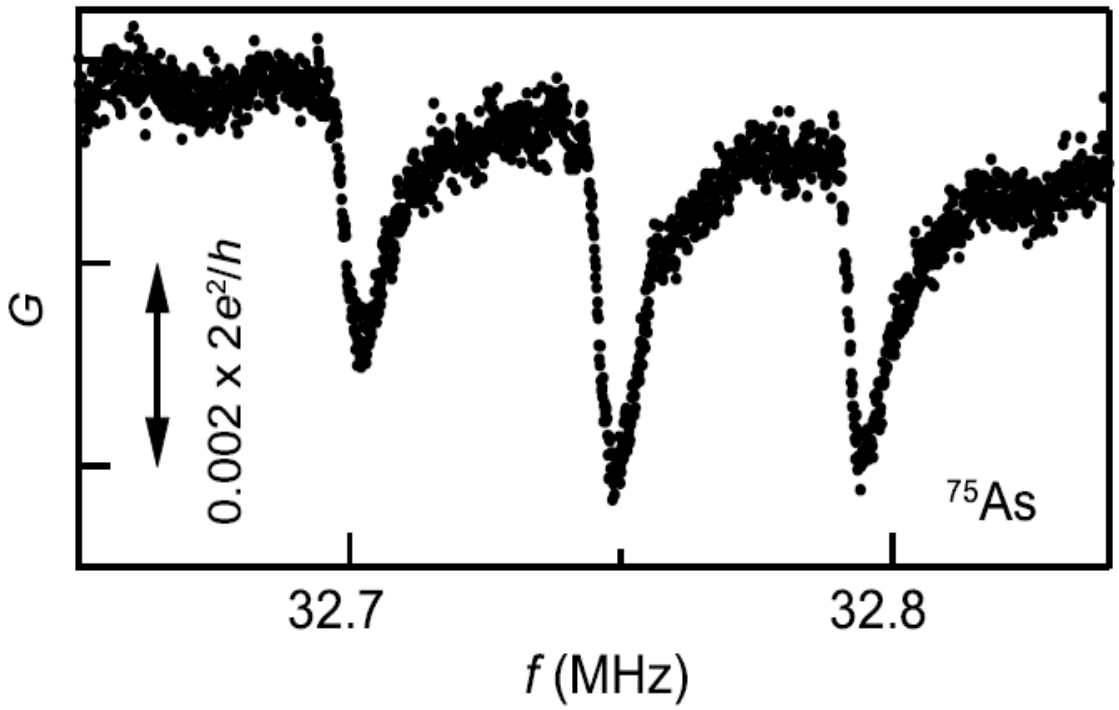

Fig. 2.8 Nuclear magnetic resonance of a QPC when gate voltage is set at the centre of 0.7 regime, several dips are clearly visible. Figure adapted from Ref. [40].

Encouraged by the result above which supports the 0.7 anomaly arising from spin it is then natural to give a direct measurement of the spin itself, however, this is challenging with a direct conductance measurement. To overcome this limitation of conductance measurement, several novel experiments have been proposed.

In conductance measurement the phase information which is spin sensitive cannot be revealed because the transmission coefficient $T \propto \psi\psi^*$ where ψ is the wavefucntion and ψ^* is the complex conjugate and the phase information cancels out. On the other hand,

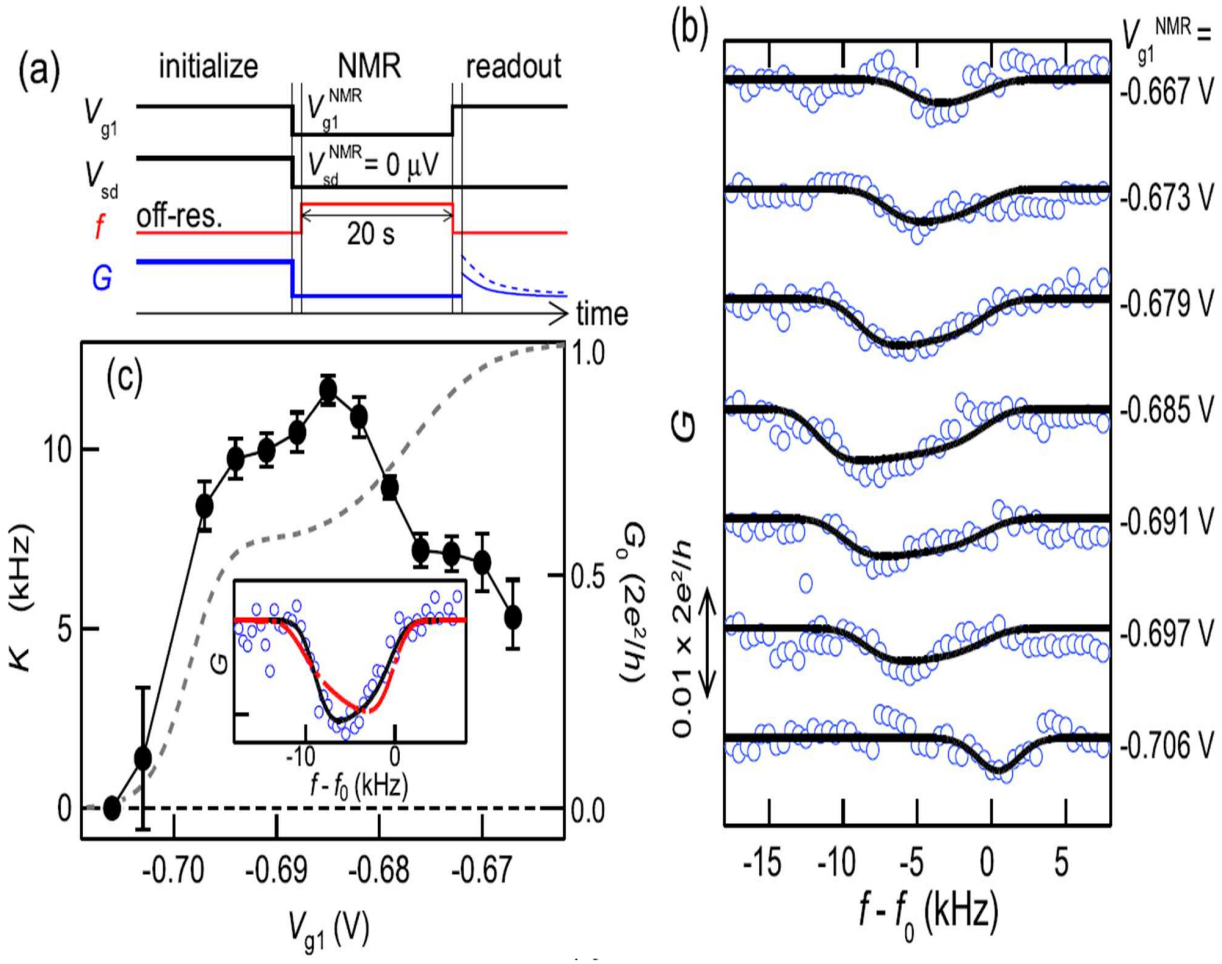

Fig. 2.9 (a) Procedure for initializing nuclei spins and measurement (b) Knight shift measured at different gate voltage (c) Frequency corresponding to maximum change of conductance in (b) plotted as gate voltage. Figure adapted from Ref. [40].

quantum interference is sensitive to phase information and thus with a specially designed interferometer it is possible to study the transmission phase of the 0.7 structure.

Figure 2.7 shows such an interferometer for measuring the transmission phase[37]. Topologically speaking this device is similar to an Aharonov-Bohm ring. In such a setup the measured conductance equals to the sum of conductance of both QPCs with corrections arising from quantum interference. It is clear that the conductance fluctuates against transverse magnetic field as shown in right upper panel of figure 2.7. Two types of oscillations, a slow one and fast one, can be differentiated. The slow and pronounced oscillations arise from transverse electron focusing signal while the fast oscillations are typical AB oscillations. The total phase possessed by electrons after each close loop is $\varphi(G)$=$\varphi_{AB} + \varphi_{QPC}(G)$, where φ_{AB} is the magnetic phase and $\varphi_{QPC}(G)$ is the transmission phase introduced by QPCs, and

this phase information can be extracted from Fourier transform of the fast oscillation. By repeating the this procedure at different gate voltage, i.e. different conductance, it then allows one to map $\varphi(G)$ to the corresponding conductance G. In addition, considering the fact the enclosed area of electron trajectory is not sensitive to the change of QPC conductance therefore φ_{AB} is assumed to be constant and the transmission phase $\varphi_{QPC}(G)$ can be resolved. The obtained transmission phase $\varphi_{QPC}(G)$ is shown in main plot of figure 2.7, it is seen that $\varphi_{QPC}(G)$ changes almost linearly against gate voltage when conductance is larger than 0.7 G_0, however, this linear dependence breaks down when it enters into the 0.7 regime.

The dramatic change in the transmission phase is an indication of a change in the dominant mechanism of the transport process. The authors attributed their observation to transition between Luttinger liquid (LL) and spin incoherent Luttinger liquid (SILL)[37]. However, considering the fact 0.7 structure is actually observed under the condition where Luttinger model or spin incoherent Luttinger model is not valid (e.g. high electron density or at high temperature), so LL to SILL transition mechanism somehow cannot explain the origin of 0.7 anomaly consistently with other experiments.

The last experiment considered here measured the spin polarization directly with nuclear magnetic resonance technique (NMR). The conductance of a QPC changes significantly when the frequency of the oscillating magnetic field B_{rf} matches the Larmor frequency of the nuclei[40] as shown in figure 2.8; the resonance frequency can be shifted by the hyperfine interaction between electron and nuclei and such shift is known as the Knight shift. The strength of hyperfine interaction, directly proportional to the electronic and nuclear spin polarization, and can be extracted from Knight shift[41].

In Ref.[40], an elegant method is used to initialise nuclear spin polarization as shown in figure 2.9(a) to guarantee nuclear spin polarization remains almost constant when other parameters are adjusted, thus Knight shift depends on electron magnetization only. It is seen that the Knight shift K reaches its maximum at 0.7 regime and drops down on both conductance plateau and near pinch-off regime. According to the relation,

$$K = \alpha_x (n_{\uparrow}^{1D} - n_{\downarrow}^{1D}) \frac{2}{\omega_y} \frac{2}{\omega_z} \tag{2.10}$$

where α_x nuclear-species dependent coupling coefficient, ω_y and ω_z describes electrostatic confinement. The magnetization $m^{1D} = n_{\uparrow}^{1D} - n_{\downarrow}^{1D}$ can be extracted, therefore it is straightforward to say magnetization is higher in 0.7 regime. Converting magnetization into spin polarization, the authors suggest that the 0.7 anomaly in their sample is associated with a spin polarization of 70% and in addition 0.7 anomaly does not arise from a bound state[40].

2.3.2 Theoretical proposals for 0.7 anomaly

Spontaneous spin polarisation

Wang and Berggren performed self-consistent density functional theory (DFT) calculation on both an infinite long quasi-1D channel[42] and a QPC with finite length [43] by taking Hartree and exchange interaction into account, so the Hamiltonian reads as below,

$$\begin{aligned}(\frac{p_x^2+p_y^2}{2m}+\frac{(p_z+eB_y)^2}{2m}+V_{conf}(y)+V_{conf}(z)\\ +V_H+V_{exch}^{\sigma}+g\mu_B B\sigma)\psi^{\sigma}=E^{\sigma}\psi^{\sigma}\end{aligned} \tag{2.11}$$

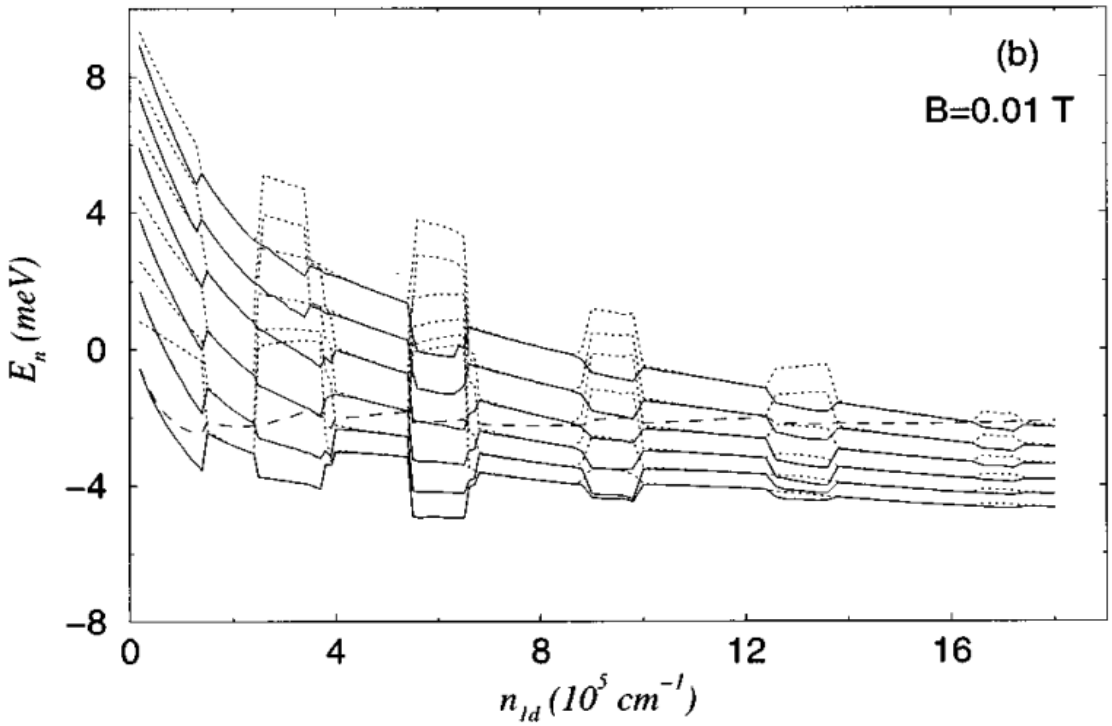

Fig. 2.10 Subband edge against 1D electron density, the solid line is spin-up subband (parallel with field) and the dotted line is spin down subband, Fermi level is represented by the dash line. Figure adapted from Ref. [42].

where V_H and V_{exch} denote Hartree and exchange interaction respectively and σ is for different spin orientation, the exchange interaction has the form below,

$$V_{exch}^{\sigma}=-\frac{e^2}{\varepsilon\varepsilon_0\pi^{\frac{3}{2}}}\sqrt{n^{\sigma}} \tag{2.11}$$

where n^{σ} is the population of a given spin-up and spin-down subbands. They predict an oscillatory spin splitting of 1D subbands when the subbands cross with the Fermi level as shown in figure 2.10 in a small magnetic field. However, it is necessary to emphasize that the magnetic field is only required to give an initial imbalance between population of electrons for spin-up and spin-down subband and then the imbalance will be further enhanced by exchange interaction.

It is seen in figure 2.10 that at lowest density regime, there is a large spin gap between spin-up and spin-down subbands and the spin gap gradually closes when Fermi level moves above the subbands. The large spin gap prefers an pronounced $0.5\times\frac{2e^2}{h}$ plateau rather than 0.7 anomaly at low temperature, this disagrees with the experiment result. To counter the discrepancy between experiment and theoretical calculation, a correlation energy term is introduced as a perturbation[44] to reduce the spin gap. The exchange and correlation energy leads to different transmission coefficient for different spin branch, thus the resultant conductance is between $0.5\times\frac{2e^2}{h}$ and $\frac{2e^2}{h}$.

The model can also explain why the 0.7 anomaly evolves into the 0.5 plateau in the presence of magnetic field, considering exchange interaction gets enhanced with increasing field. However, it fails to reproduce the temperature dependence of the 0.7 structure. The model suggests that the 0.7 anomaly is more pronounced at low temperature and weakens gradually when temperature increases, because the transition between the two spin branches, alternatively speaking spin-flip scattering, due to thermal excitation leads to reduction in exchange energy, this prediction apparently contradict the experimental observation that that 0.7 get stronger at higher temperature[26].

Spin gap model

As the spontaneous spin polarisation model is not able to capture the temperature dependence of the 0.7 anomaly, it suggests that the new models that can explain the observation are required. In contrast to the spin polarisation model where the energy gap between different spin subbands opens only when Fermi level crosses with the subband and then closes gradually, some models[45–47] assume that the spin gap remains all the way through once it is open. However, there are different views on the spin gap, Bruus et al. suggests the spin gap is fixed[45] while Reilly et al. propose that the spin gap is electron density dependent[46, 47].

In the density independent spin gap model[45] the authors suggests the exchange interaction is not necessary to produce the 0.7 anomaly, this is the major difference compared to spontaneous spin polarisation model.

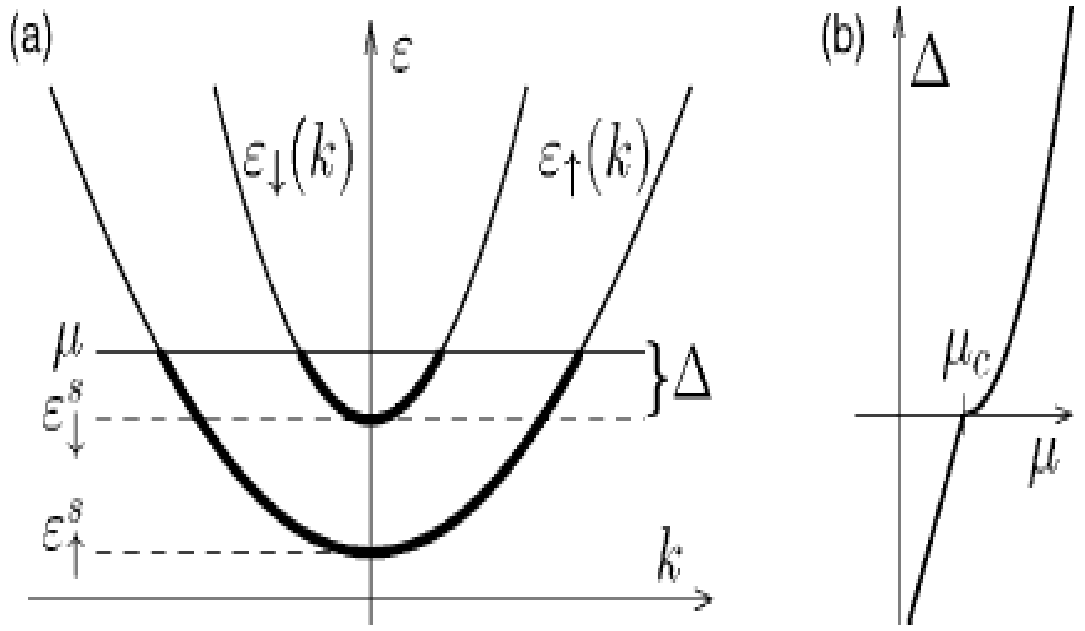

Fig. 2.11 (a) Band structure for the fixed spin gap model (b) Position of the bottom of spin down subband with respect to the chemical potential. Figure adapted from Ref. [45].

As illustrated in figure 2.11, because of the spin gap, only one spin subband is populated when the chemical potential μ is in the spin gap while both spin branches can be filled when the chemical potential moves above the spin gap. Solving the local spin density self-consistently leads to an important result[45] for the separation between bottom of higher spin subbands and chemical potential, $\Delta\mu = \mu - \varepsilon^s_\downarrow(\mu)$,

$$\Delta(\mu) = C(\mu - \mu_c)^2, \quad for \quad \mu > \mu_c \tag{2.12}$$

$$\Delta(\mu) = D(\mu - \mu_c), \quad for \quad \mu < \mu_c \tag{2.13}$$

where C and D are device dependent constant, μ_c is the associated with spin gap. The change in the gradient of $\Delta(\mu)$ in turn means a rapid change in populating rate around Fermi level, the dispersion relation for spin up and spin down can then be rewritten and gives total conductance,

$$G(T) = \frac{e^2}{h}(f[\varepsilon^s_\uparrow - \mu] + f[-\Delta(\mu)]) \tag{2.14}$$

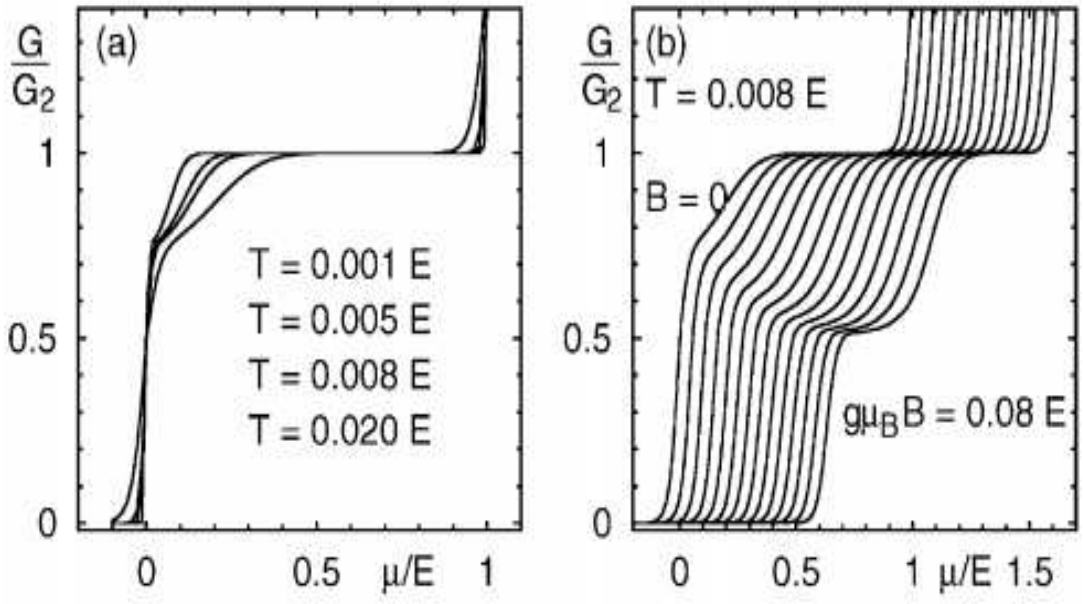

Fig. 2.12 (a) Calculated conductance at different temperature according to the fixed spin gap model (b) Calculated magnetic field dependence. Figure adapted from Ref. [45].

The typical temperature and magnetic field dependence predicted by this model is shown in figure 2.12. The enhancement of 0.7 anomaly with rising temperature is reproduced correctly. However, the origin of the spin-gap itself is still a puzzle.

On the other hand, Reilly et al. argued that the spin-gap should be density dependent[46, 47] as shown in figure 2.13, similar to the spontaneous spin polarization model the spin gap opens when the Fermi level aligns with 1D subbands, thus the appearance of the spin gap is more natural.

The density dependent spin gap model demonstrates that the behaviour of the 0.7 structure is sample dependent[46] although the detailed microscopic interpretation is still lacking. In devices where the spin gap opens quickly with increasing 1D density, a structure near 0.5 G_0 rather than 0.7 G_0 should occur at low temperature; On the contrary, in devices where spin gap opens slowly there is no 0.5 plateau while the 0.7 structure will be quite faint at low temperature. The most successful point of the density dependent spin-gap model is the ability to reproduce the top-gate dependence of 1D conductance[48].

Besides, the density dependent spin gap model also suggests the spin gap for lower subbands opens faster than that for higher subbands, thus it predicts the crossing between spin-up branches of ground states $N_1^{\uparrow}$ and spin-down branch of first excited state $N_2^{\downarrow}$ by changing electron density even in absence of magnetic field (similar for other states).

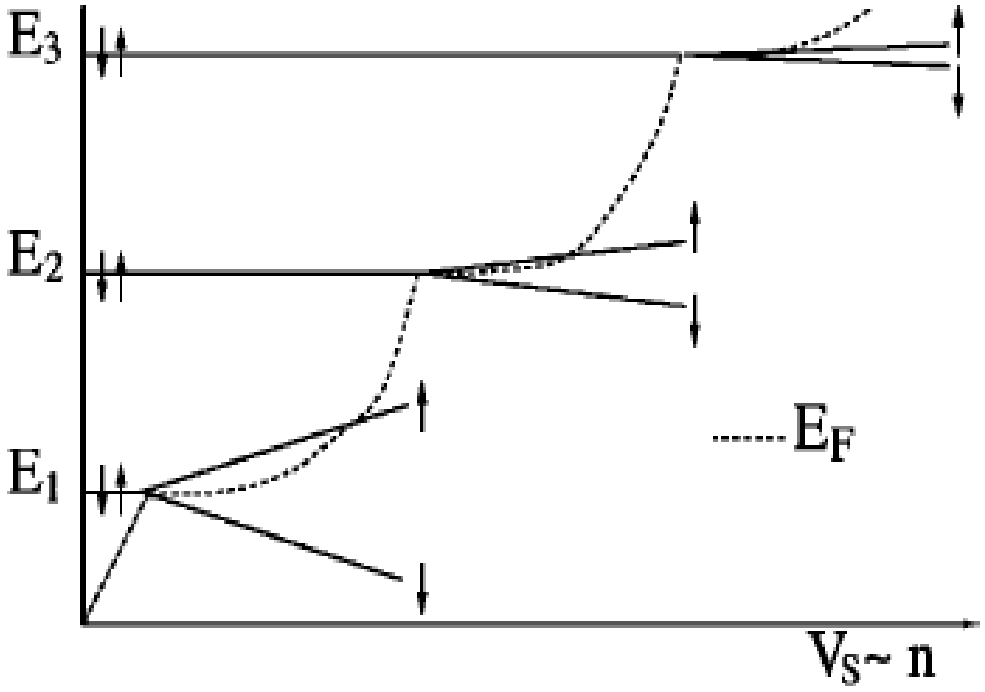

Fig. 2.13 Schematic for the density dependent spin gap model, the gap opens when the subband is populated and keeps increasing when density increases. Figure adapted from Ref. [46].

Kondo screening

Kondo effect occurs when mobile electrons with a given spin orientation screen a magnetic impurity with opposite spin and thus lead to an correction to the transport probability. Kondo effect is widely observed in quantum dots[49, 50] and manifests itself as an enhancement of the conductance through the quantum dot.

Considering the inverted parabolic shape of the electrostatic potential produced by a split gate along x-axis (see figure 1.3), electrons may get trapped in the middle of the QPC and acts as dynamic magnetic impurities[52]. Assuming the the magnetic impurities are spin-up, then transmission probability for spin-down electrons from the 2D reservoir is enhanced while that for spin-up electrons is reduced as a direct result of the Pauli exclusion principle. As a result, the Kondo effect lead to a correction of the QPC conductance by introducing different transmission probability to spin-up and spin-down spin-subbands, therefore it may be the origin of the 0.7 anomaly. One of the hallmarks of the Kondo effect in QPC is the zero bias anomaly (ZBA), which implies that the conductance of the QPC is enhanced at zero

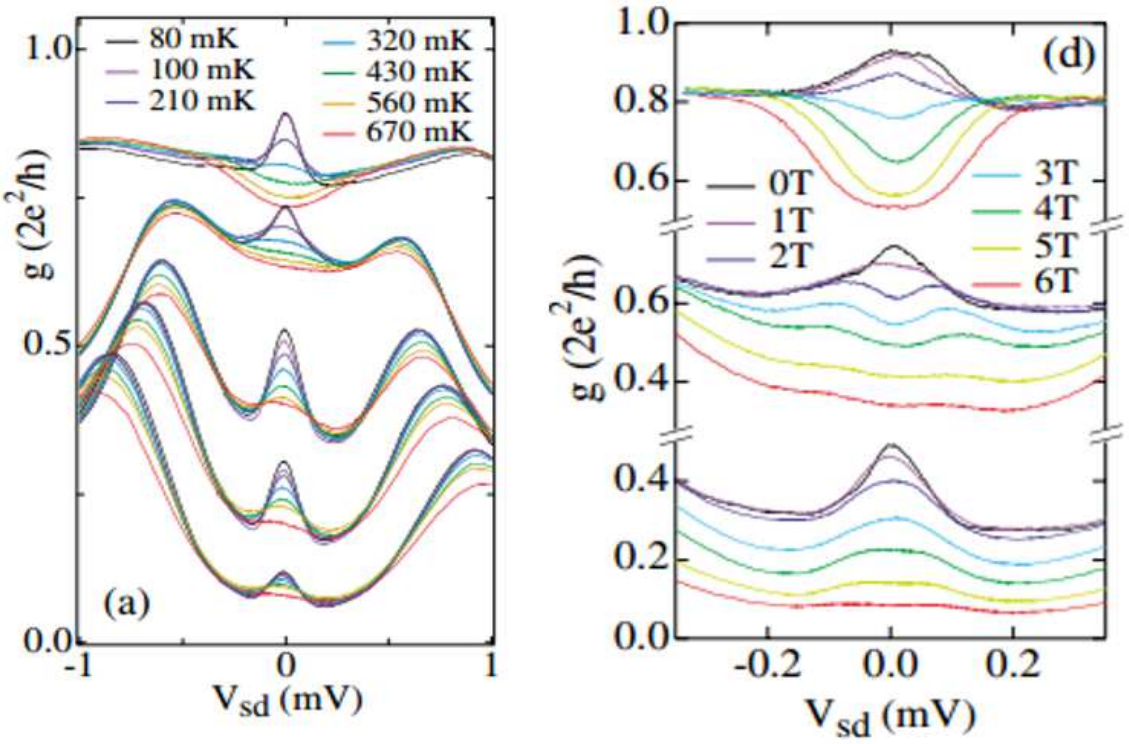

Fig. 2.14 Left: Temperature dependence of zero bias anomaly (ZBA). Right: Magnetic field dependence of ZBA. Figure adapted from Ref. [51].

source-drain bias compared to conductance at the same electrostatic confinement but with a small source-drain bias.

Figure 2.14 (a) and (b) show the temperature and magnetic field dependence of a ZBA[51], respectively. For temperature dependence, ZBA is more pronounced at lower temperature and weaker at higher temperature, this can be explained by the fact the spin of dynamic magnetic impurities relaxes at faster rate at high temperature due to larger thermal energy. For magnetic field dependence, it is clear that the ZBA peak splits into two at higher magnetic field which is the result of Zeeman splitting of the reservoir electrons.

The Kondo-effect based interpretation for the 0.7 anomaly is under debate because the 0.7 structure is widely observed in devices where there is ZBA signature.

2.4 Transport in the presence of source-drain bias

In order to avoid disturbing the system due to electron heating, the transport measurement is usually performed with small ac excitation applied between the source and drain reservoir. As a consequence, the measurement mainly manifests the property of electrons with energy

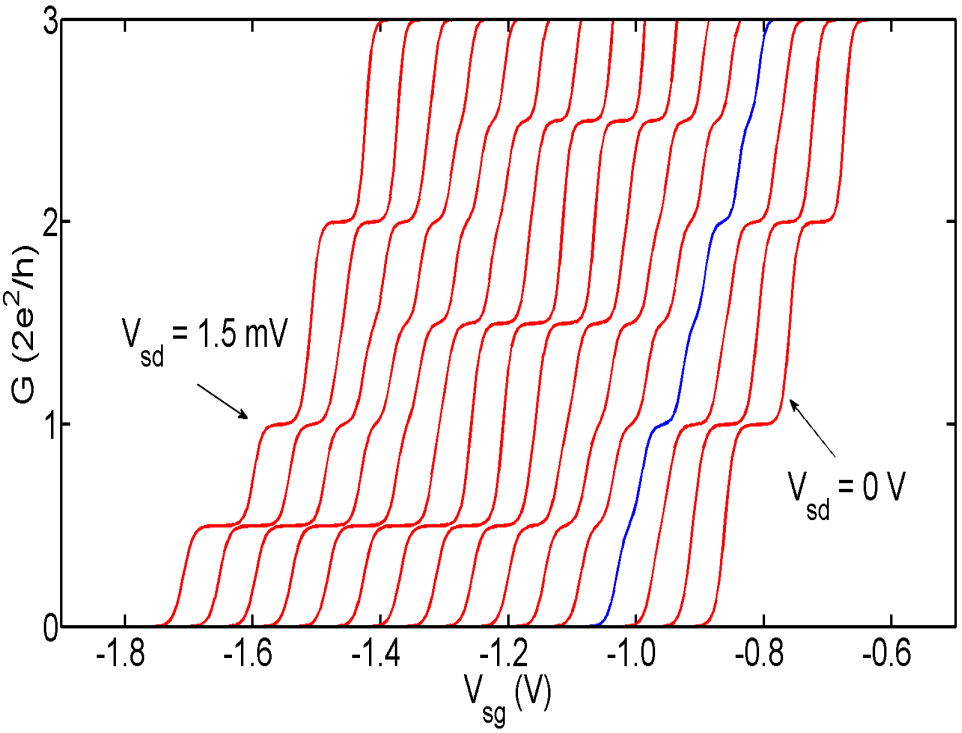

Fig. 2.15 Calculated conductance of device defined in figure 1.3 in the presence of source drain bias, the right most trace is with zero bias while the left trace is with a bias of 1.5 mV. Data have been offset horizontally for clarity.

in the vicinity of Fermi level. Under this condition, the system is in linear response regime, i.e. if the excitation changes by a factor K the response will change by the same factor so that the measured conductance/resistance remain the same regardless of the amplitude of excitation. With the application of finite source-drain bias the system can be driven from the linear response regime into the non-linear one, and in this case the transport properties of the system are affected by the electrons within a relatively large bias window instead of a small snapshot around the Fermi level, thereby, more information can be extracted.

Glazmann et al.[53] predicts that half conductance plateaus occur with large source drain bias. The idea is further developed by Martín-Moreno and applied to a constriction with saddle point potential[18]. In this model it assumes that the voltage drop only happens at the interface between the 1D constriction and the source/drain reservoir due to the non-dissipation nature of ballistic transport within the 1D channel, so that the chemical potential at source and drain reservoir can be expressed as,

$$\mu_s = E_f + \beta e V_s d \tag{2.15}$$

and

$$\mu_d = E_f - (1-\beta)eV_s d \tag{2.16}$$

in a symmetric system $\beta = \frac{1}{2}$ (for the ease of discussion β is assumed to be $\frac{1}{2}$ below), as a result, the number of occupied subbands below μ_s differs from that below μ_d, and the total current is given by,

$$I = \frac{2e}{h}[\sum_{l_s}(\mu_s - E_l)T_l(E) - \sum_{l_d}(\mu_d - E_l)T_l(E)] \tag{2.17}$$

with some simple algebra the conductance is,

$$G = \frac{2e^2}{h}[\frac{N_s}{2} + \frac{N_d}{2}] \tag{2.18}$$

μ_s and μ_d pass the 1D subband in succession, therefore half integer plateaus are expected.

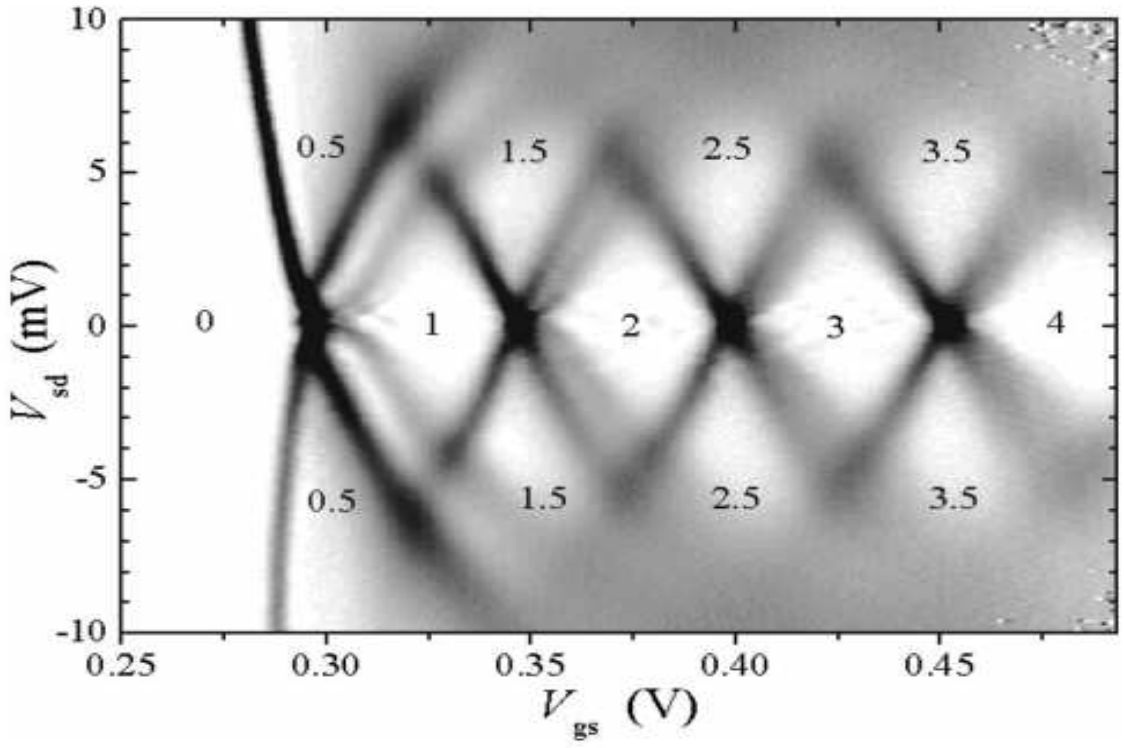

Fig. 2.16 $\frac{dG}{dV_{sg}}$ as a function of both gate voltage V_{sg} and source-drain bias V_{sd}, the dark strip stands for large transconductance regime while the bright region is for conductance plateau. Figure adapted from Ref. [54].

Figure 2.15 shows the calculated conductance of the QPC in the presence of source drain bias. In this calculation the Fermi energy is set to be 6 meV, and the subband spacing is 0.5 meV (derived from parabolic fitting in figure 1.3). The blue trace, V_{sd}=0.3 mV, indicates where the 0.5 plateau starts forming. It is interesting to notice that the simulation predicts the coexistence of half integer and integer conductance plateaus with large source-drain bias, this is somehow not observed in experiment such as that in Ref[54].

2.4.1 Additional conductance structure with source-drain bias

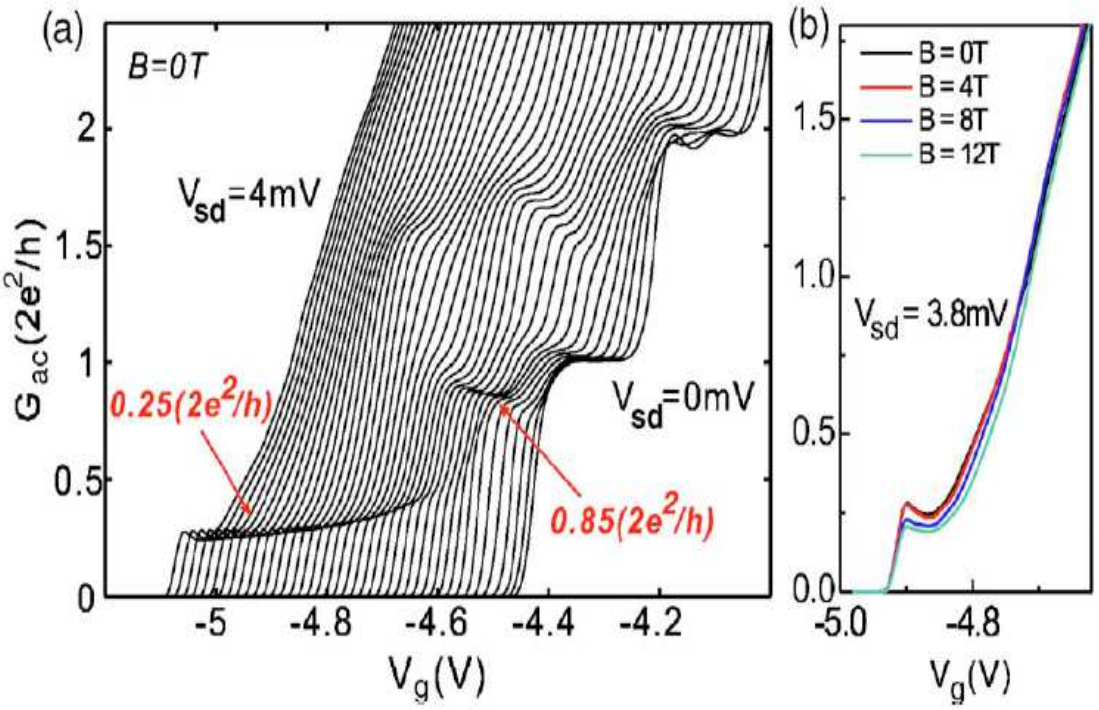

Fig. 2.17 Left: Conductance measured with source-drain bias, data have been offset horizontally for clarity. Right: Magnetic field dependence of 0.25 structure, it is clear that 0.25 structure is insensitive to the field. Figure adapted from Ref. [55].

Source-drain bias is widely used in studying subband spacing as shown in figure 2.16[54] which shows $\frac{dG}{dV_{sg}}$ against both gate voltage V_{sg} and source-drain bias V_{sd}. In the figure the dark strip stands for high transconductance regime while the bright regime is for conductance plateau. It should note that for a given source-drain bias, either only integer conductance plateaux are observed (in small bias regime) or the only half integer plateaux are present (in large bias regime), the coexistence of integer and half integer plateaux at the same

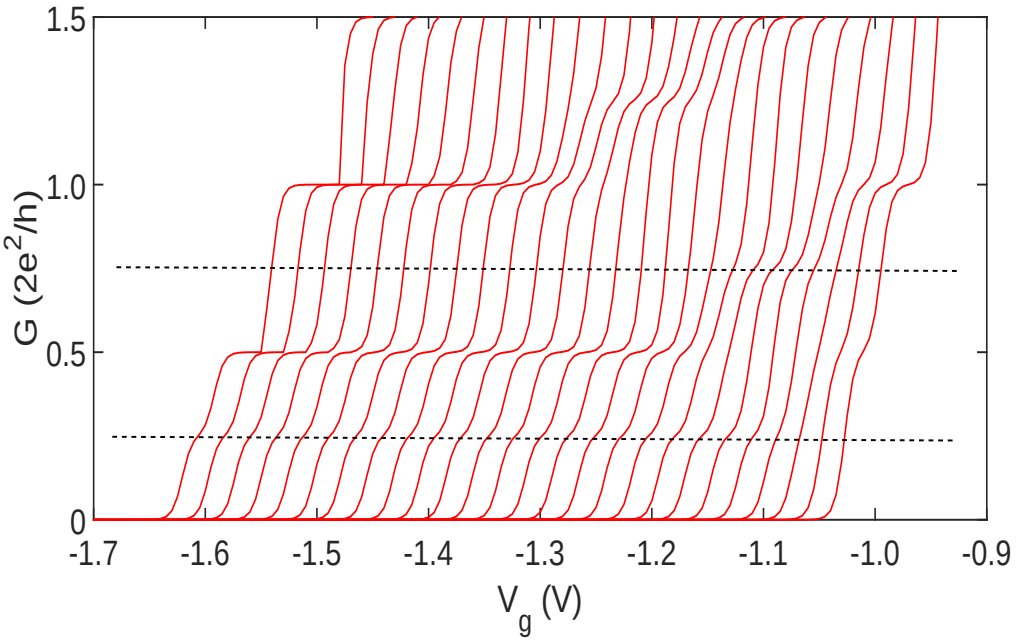

Fig. 2.18 Simulation of source-drain dependence assuming a fixed spin gap, the source-drain bias increases from 0 to 2.5 mV from right to left. The horizontal dash lines highlight 0.85 and 0.25 structure. Data have been offset horizontally for clarity.

source drain bias is not observed. The first intersection between dark strips occurs at $\pm$ 6.5 meV suggests subband spacing ε_1-ε_0 = 6.5 meV while the higher intersection points happen at lower bias voltage value and this is consistent with saddle point model. Besides, the symmetry of the gray scale plot against source-drain bias suggests $\beta = 0.5$ (β is the parameter in Eq.(2.16)).

Apart from measurement of subband spacing, source-drain bias is also found to be useful in studying the spin configuration in quasi-1D constriction. It is noticed that with increasing source-drain bias, additional structures form at $0.85 \times \frac{2e^2}{h}$ and $0.25 \times \frac{2e^2}{h}$ [55] as shown in figure 2.17 (a).

The observed 0.85 and 0.25 structure cannot be derived from Eq.(2.18) which only involves the momentum degeneracy. In order to confirm whether or not the 0.85 and 0.25 structures are spin related, a magnetic field dependence is performed, it found that the 0.85 and 0.25 structures can survive at relatively large magnetic field, especially the 0.25 structure is almost unaffected to a field up to 12 T as shown in figure 2.17 (b). The fact 0.25 structure is insensitive to magnetic field suggests it might be a spin polarized state.

Figure 2.18 shows the simulated conductance in the presence of source drain bias by assuming the existence of a fixed spin-gap. 0.85 (actually in the simulation it occurs at

$0.75 \times \frac{2e^2}{h}$) and 0.25 structures are reproduced. This indicates 0.85 and 0.25 structure are related to the lifting of spin degeneracy in the 1D constriction. However, the simple model suggests half integer plateaux and/or integer plateaux can coexist with the 0.85 and 0.25 structures in a wide range of source-drain bias, this contradicts the experimental observations.

To get more clues on the 0.85 and 0.25 structures, Chen et al. measured dc conductivity[55]. Differential conductance (also ac conductance) changes when the subband edge passes through μ_s or μ_d and thus cannot be used to monitor what happens when subband moves within the bias window, on the other contrary, the dc conductance,

$$G_{dc} = \frac{I}{V_{sd}} = \frac{2e^2}{h} \times \frac{\Delta E}{eV_{sd}} \tag{2.19}$$

is proportional to ΔE which is the energy difference between μ_s (assume $\mu_s > \mu_d$) and the bottom of the 1D subbands, therefore it reveals how the subbands are populated. In addition, the ac conductance and dc conductance follow the relation below,

$$G_{dc} = \frac{\int_0^{V_{sd}} G_{ac} dv}{V_{sd}} \tag{2.20}$$

Figure 2.19 (a) plots the dc conductance and the corresponding ac conductance at different source-drain bias. It is clear that when the ac conductance is at end of 0.25 structure, the dc conductance is around $0.5 \times \frac{2e^2}{h}$ and such correlation is observed at different dc bias. This proves that in the 0.25 regime only the lower spin-subband is populated, otherwise the corresponding dc conductance would be larger than 0.5 G_0 and meanwhile it will change once the source-drain bias changes.

Based on the observation, Chen et al. interpret the 0.85 and 0.25 anomalies as a result of level pining[55] as shown in figure 2.19 (b). When both spin-up and spin-down subband are not yet populated they are degenerate, as shown in phase (a), proceeding with phase (b) to (d) which says when the subbands approach μ_s spin-up subband would pin to μ_s so that this subband is not populated and thus makes no contribution to the conductance (here thermal excitation is ignored), meanwhile the spin-down subband is populated normally, finally in phase (e) when spin-down subband pass through μ_d spin-up subbands starts populating.

In another experiment[32] Chen et al. measured ac conductance in small source-drain regime in the presence of large magnetic field which lifts spin degeneracy. The main result is summarised in figure 2.20. It is seen that the transconductance peaks corresponding to spin-down subbands remain as a single peak while peaks for spin-up subbands gradually

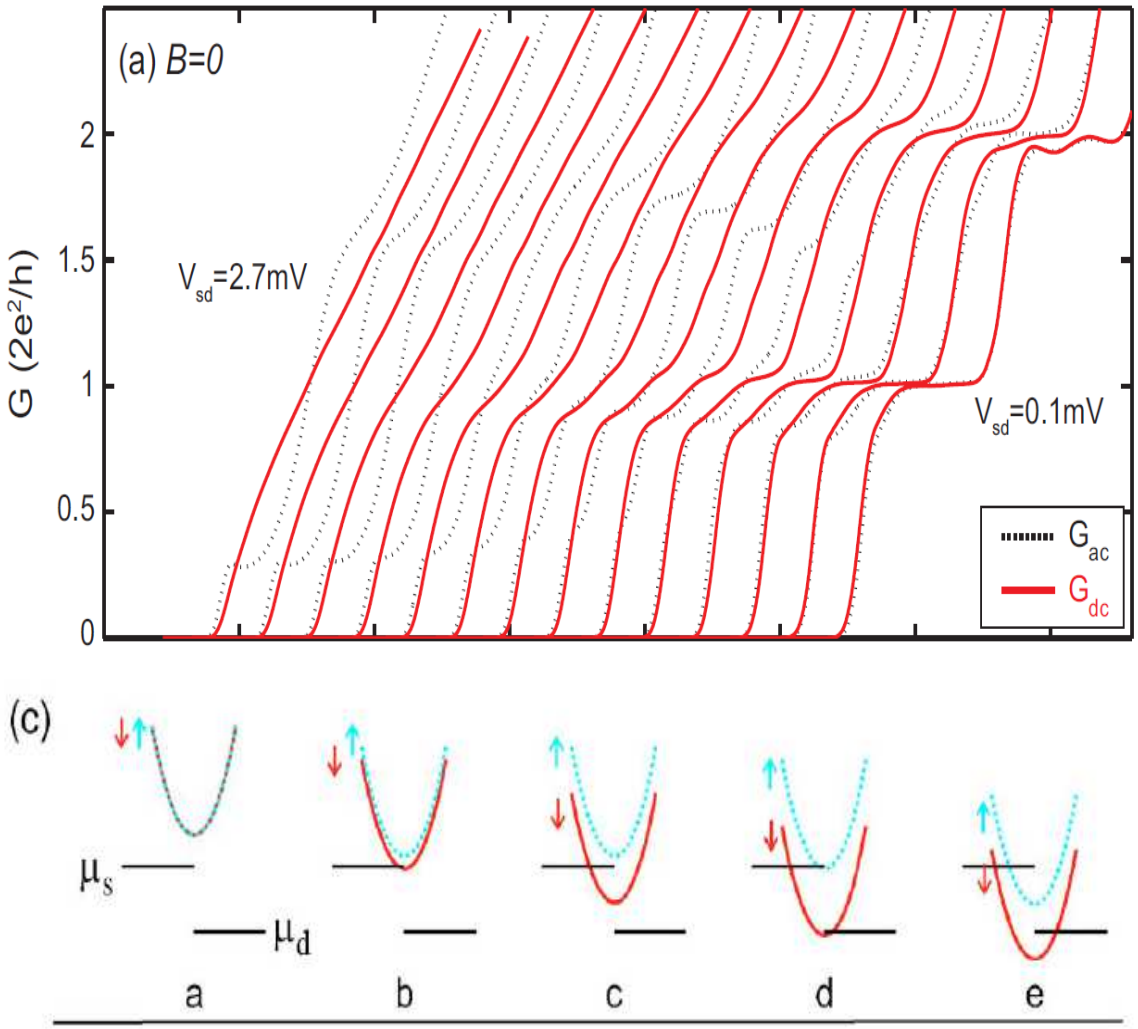

Fig. 2.19 Upper plot: dc conductance (red trace) and ac conductance (dash trace) against gate voltage. Data are offset for clarity. Lower plot: Schematic of moving of spin resolved subband. Figure adapted from Ref. [55].

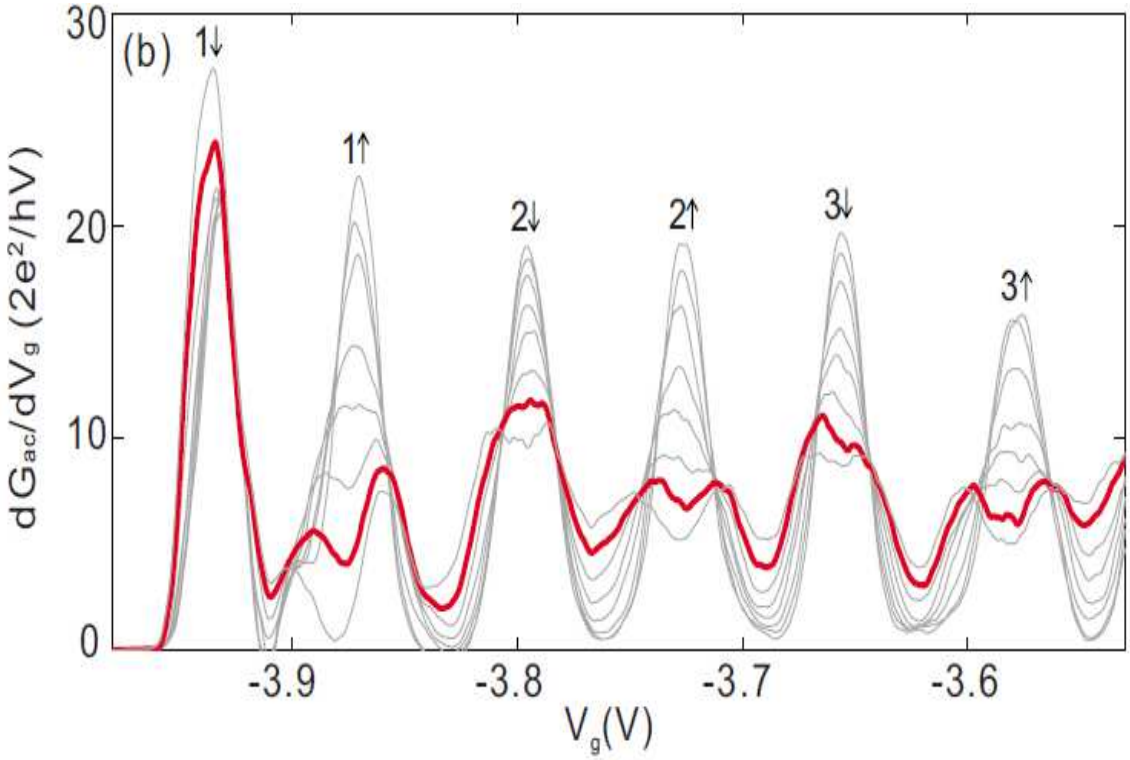

Fig. 2.20 $\frac{dG_{ac}}{dVg}$ at B=14 T in presence of source-drain bias V_{sd} from 0 to 0.42 mV (top to bottom). The red trace is the result with a source-drain bias of 0.36 mV. Figure adapted from Ref[32].

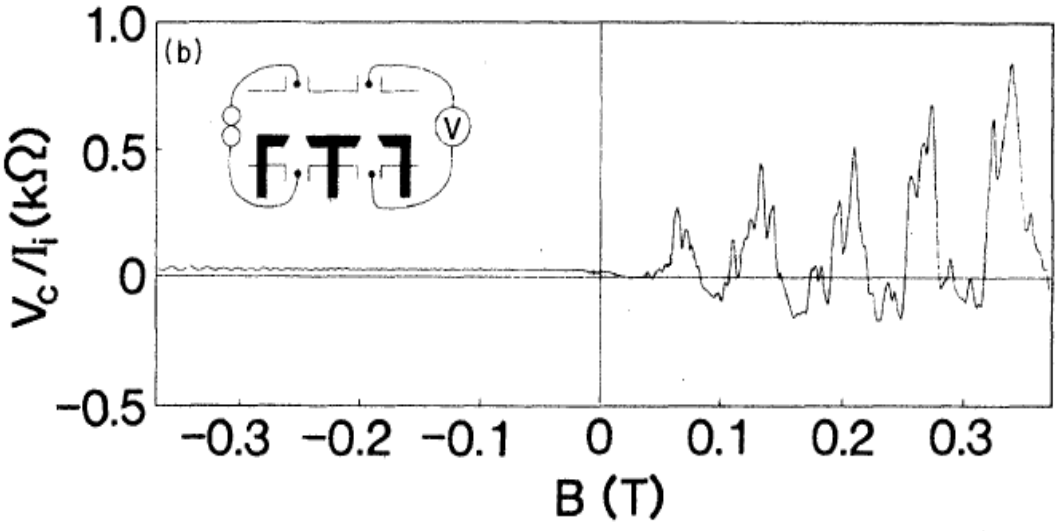

Fig. 2.21 Typical result of transverse electron focusing, periodic peaks are observed. Inset shows the experiment setup and device schematic. Figure adapted from Ref[56].

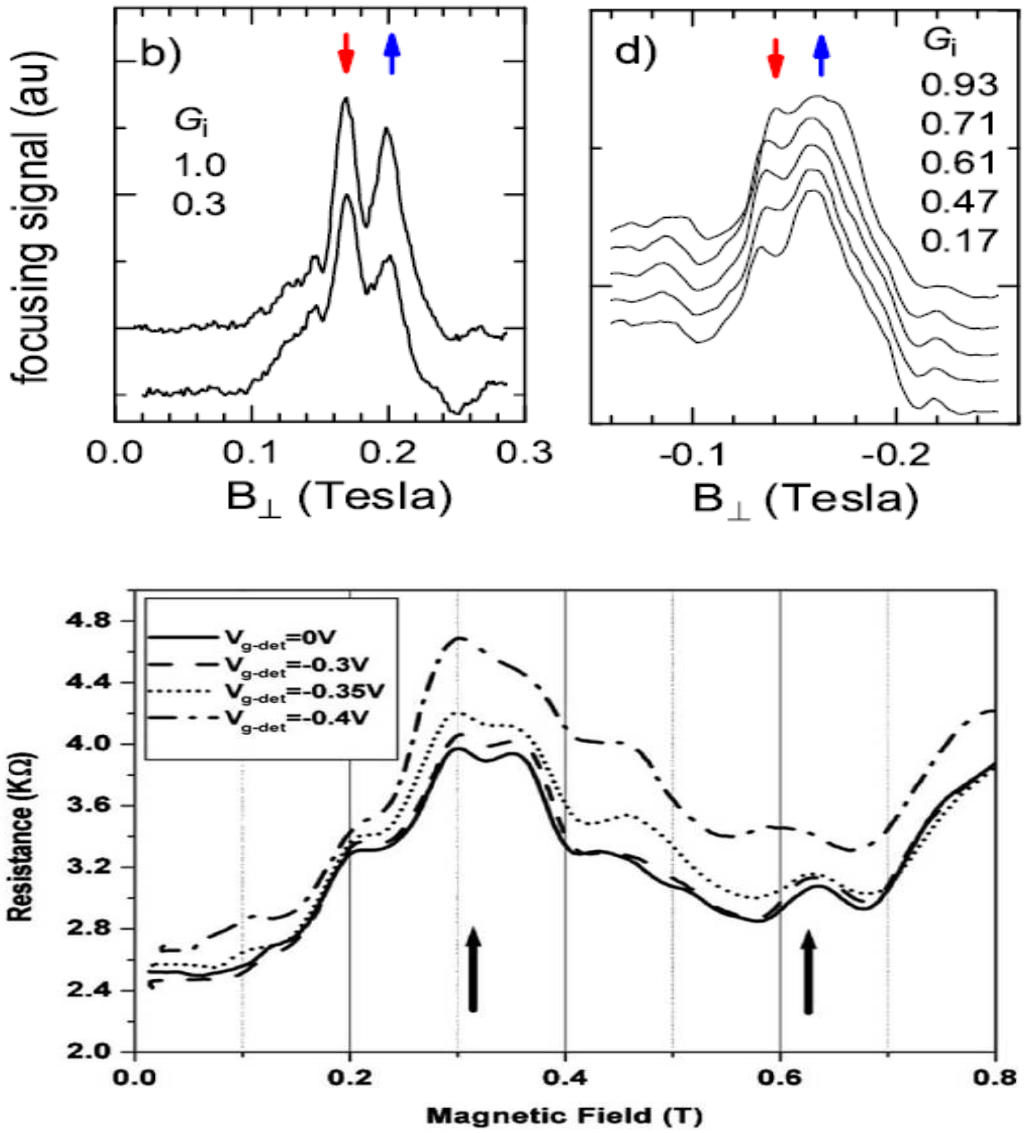

Fig. 2.22 Upper plot: (b) and (d) show the splitting of focusing peak in p-type GaAs grown along different direction. Figure adapted from Ref. [57]. Lower plot: The splitting of focusing peak in n-type InSb. Figure adapted from Ref. [58].

splits into two with increasing source-drain bias. Ideally speaking, a transconductance peak is generated when subband pass through either μ_s or μ_d in the presence of a finite source-drain bias, i.e. each subband should produce two transconductance peak, however, if the populating rate is large while the source-drain bias is small the two peaks may smear out. The spin-down subbands do not pin to the chemical potential and they have a relatively large populating rate and therefore only one transconductance peak is observed. On the contrary, the populating rate of the spin-up subbands is slowed down because of the pinning to the chemical potential, thus two peaks are well defined.

The level pinning proposal is successful in explaining the formation of the 0.25 plateau and the absence of half integer plateau in the ac measurement. However, the level pinning model somehow cannot explain all the observation self-consistently. For instance, there should be a pronounced 0.75 or 0.85 structure according to phase (e) of figure 2.19 in the presence of a large source-drain bias, however, 0.75 structure is not present in the experiment in large bias regime. More importantly, half integer plateaus observed in other experiments[54] are somehow absent in Chen's experiment. Thus it requires further study to figure out the origin of the 0.25 and 0.85 structures.

2.5 Direct measurement of spin polarization

Although conductance measurement is an useful tool, however, it is not able to address the degree of spin polarization directly. To overcome this problem, Usaj and Balserio proposed a measurement[60] based on the transverse electron focusing technique where the spin information is converted into charge information. In a typical transverse electron focusing experiment the trajectory of electrons will be bent by the Lorentz force in the presence of a transverse magnetic field from the injector to detector (usually defined with QPC), periodic peaks occur when the applied magnetic field fulfils the condition[56],

$$B_{focus} = \frac{2\hbar k_f}{eL} \tag{2.21}$$

where k_f is the Fermi wavevector and L is the separation between injector and detector, the height of the focusing peaks is directly proportional to the number of detected electrons.

In materials with spin-orbit interaction, electrons injected into 2DEG will possess different k_f according to their spin orientation and thus give two peaks in the spectrum. The splitting

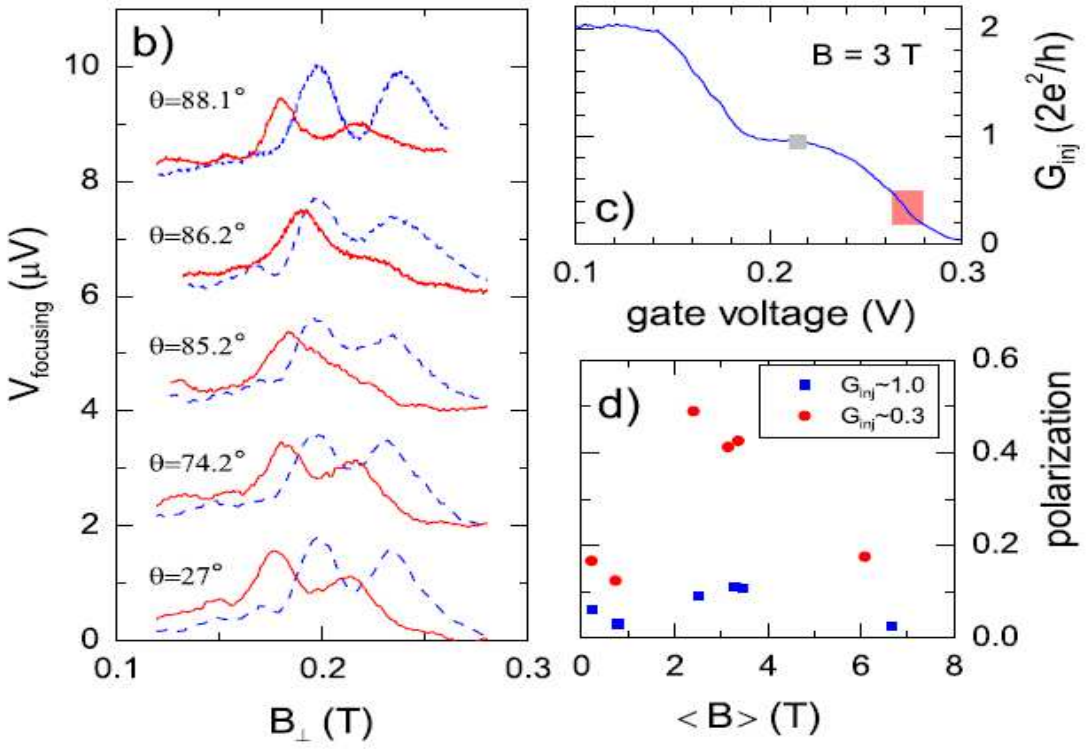

Fig. 2.23 In plane field dependence of focusing peak splitting in hole gas and the corresponding polarization. Figure adapted from Ref. [59].

between the two sub-peaks is given by[60],

$$\Delta B = \frac{4\alpha m^* c}{L\hbar e} \tag{2.22}$$

where α is spin-orbit constant while m^* is the effective mass. In addition, if there is a non-zero spin polarization of electrons in the 1D channel, the imbalance between electron population of the two spin resolved subbands, it would lead to a difference in the height of the sub-peaks.

The splitting has been demonstrated experimentally in a GaAs hole gas[57] and an InSb electron gas[58] where spin-orbit interaction is strong as shown in figure 2.22. When the conductance of the injector is set to conductance plateau, the sub-peaks are almost equal in height. On the other hand, the two peaks diverge from each other if the conductance of injector is different from integer of $\frac{2e^2}{h}$. By changing the growth direction which in turn means the orientation of effective magnetic field, it is seen that preferred spin orientation is changed correspondingly[57]. Conductance of a 1D constriction is sensitive to in-plane magnetic field, so is the peak height, as shown in figure 2.23

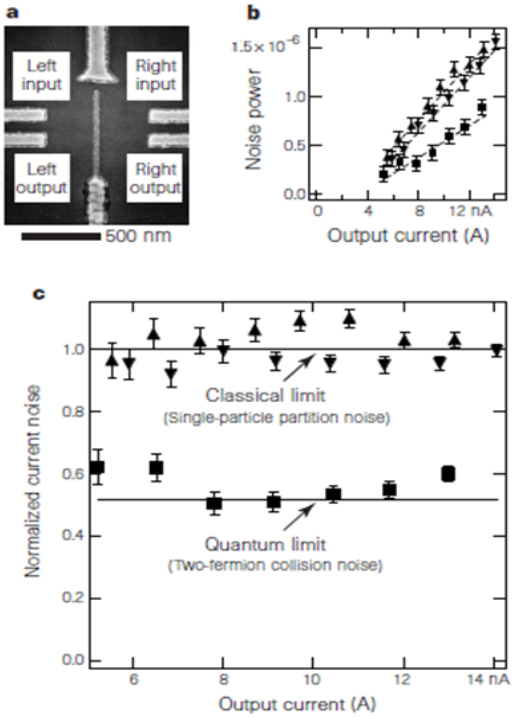

Fig. 2.24 **a**, the SEM image of the electronic Hong-Ou Mandel device. **b**, the measured shot noise when the two QPCs are biased separately (trangular marker) and biased simultaneously (square marker). **c**, same data as shown in plot **b** but after normalization. Figure adapted from Ref. [75].

2.6 Quantum interference in mesoscopic systems

Quantum interference, one of the most remarkable effects of quantum mechanics, arising from the wave nature of particles has led to some of the most celebrated results in mesoscopic systems, including weak localization in two dimensional (2D) systems[61–63], Aharonov-Bohm oscillations in ring structures[64–66], sharp peaks in magnetoresistance in a chaotic cavity[67, 68] etc. Among its various applications, quantum interference has been used successfully as a tool to investigate the properties of particles such as monitoring the correlation and entanglement as demonstrated in Mach-Zehnder interferometer[69, 70], Aharonov-Bohm interferometer[71, 72] and Hanbury Brown-Twiss interferometer[73, 74], and to highlight the difference between fermion and boson with an electronic analogue of the Hong-Ou-Mandel device[75, 76]. Among all the striking phenomenon, it is particularly interesting to note that quantum interference is extremely suitable for studying coupling between different quantum systems[77–79] which is crucial for the design of an integrated quantum circuit.

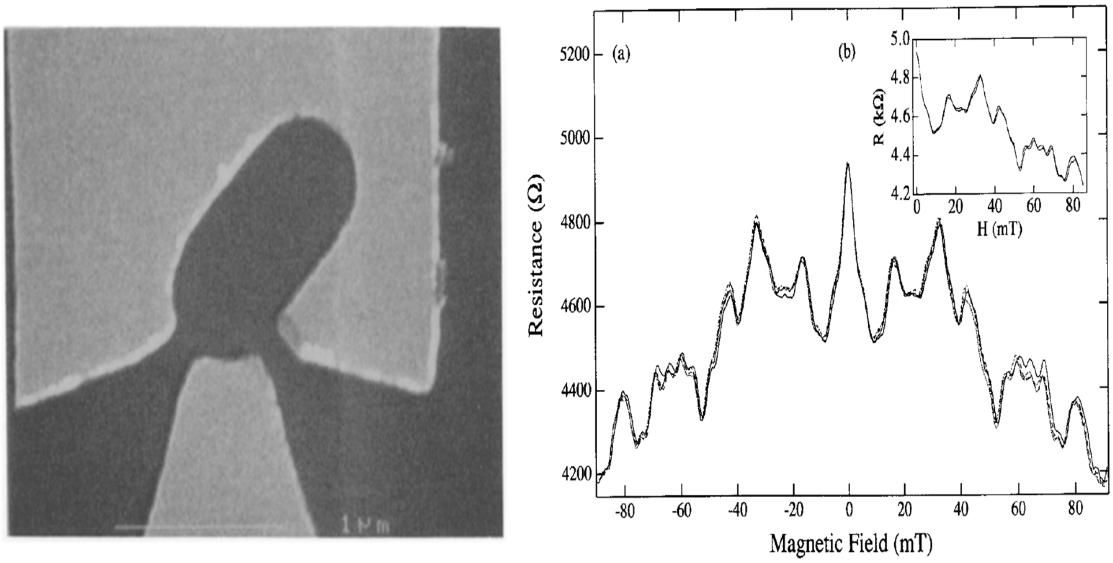

Fig. 2.25 Left panel: SEM image of a chaotic cavity fabricated from a n-type GaAs/AlGaAs heterojunction. Right panel: Magnetoresistance through the cavity at 1.5 K. Figure adapted from Ref. [80].

In this section several typical quantum interference experiments will be discussed.

The first experiment is the electronic analogy of Hong–Ou–Mandel experiment which beautifully demonstrated the fermion nature of electrons[75]. The experiment is summarised in figure 2.24. In this experiment, two streams of ballistic electrons are injected from the first mode of left and right QPCs and collide at the central splitter which is tuned to 50% transparency regime (i.e. both the reflection and transmission probability are 50%), the collision process then removes the path information. If the injected particles are bosons, the two particles will be detected at the same side; On the other hand, two fermions will be detected exactly one on each side. As a consequence, the power of shot noise measured when two streams of Boson injected simultaneously will be the same when they are injected separately (i.e. just have one stream), while for fermions the shot noise will be halved when they are injected simultaneously. The result of shot noise measurement as shown in figure 2.24 (b) and (c) beautifully reproduce the 50% reduction of shot noise power.

The other interesting interference experiment is deciding the nature of electron motion in a quantum cavity[80] which is challenging with the conductance measurement. In such an experiment electrons are injected into a cavity where the gradient of the confinement wall changes dramatically as shown in figure 2.25 (a). The magnetoresistance in such a device shows a series of sharp peaks which are symmetric with respect to magnetic field and the

central peak at 0 T has a Lorentzian line shape which is a direct manifestation of the chaotic motion of electrons in the cavity[81].

Chapter 3

Device fabrication and measurement techniques

3.1 Introduction

Although the devices studied in this thesis vary quite a lot in terms of characteristic and design, generally speaking they are fabricated following the standard procedure of a gated HEMT.

As introduced in chapter 1, a 2DEG confined at the interface of a GaAs/AlGaAs heterojunction is the fundamental of low dimensional physics, hence a modulation-doped MBE-grown HEMT wafer is the starting point of the fabrication. Wafers used in this study were grown by Ian Farrer of the Cavendish Laboratory. To isolate the 2DEG from the rest, a mesa is etched into the wafer, ohmic contacts are then formed at the ends of the mesa to make electrical contacts between the 2DEG and the environment. Following the first step, the optical gates (gates patterned using photolithography) are patterned on the surface of the wafer by photolithography and metallised in a thermal evaporator. The fine gates (also the EBL gate), used to form the desired structure, with a size of the order of 100 nm is defined with electron beam lithography (EBL). If a top gate, usually lying directly above the split gates, is required then an dielectric layer such as PMMA (poly methyl methacrylate) should be deposited between the split gate and the top gate to prevent shorting between the gates. The PMMA is patterned via EBL similar to the split gate.

Following the brief introduction, the fabrication will be discussed in detail in the next several sections.

3.2 High mobility epitaxially grown wafers

Heterostructures used in this study were grown by molecular beam epitaxy (MBE) on the surface of a semi-insulating GaAs substrate along the [001] direction and the 2DEG is 90 nm below the cap layer of the heterostructure. Although the detail of the wafers may vary, the structure is always pretty similar to that listed in table 3.1.

Layer	Thickness	Material
substrate	500 μm	bulk GaAs
buffer	500 nm	GaAs
supperlattice	200 $\times$ 5 nm	alternating GaAs/AlGaAs
host	1000 nm	GaAs
spacer	40 nm	AlGaAs
doping	40 nm	Si-doped AlGaAs
cap	10 nm	GaAs

Table 3.1 Typical structure of a shallow wafer. The wafer is grown from substrate to cap layer. Structure for a deep wafer is similar to this one but the thickness of each layer changes accordingly.

The growth starts from the substrate and then a buffer GaAs layer is deposited onto the substrate to provide a smooth surface. A superlattice is grown afterwards, the superlattice consists of multiple layers of alternating GaAs/AlGaAs (each layer is 5nm in thickness). The superlattice is crucial for a high quality wafer because it prevents crystal defects from propagating from the bulk substrate into the active region (where the 2DEG forms), traps impurities, and smooths the surface of the wafer. In the next step, a high quality GaAs buffer layer is grown and followed by a AlGaAs spacer, due to the difference in conduction band edge, the 2DEG forms at the interface of GaAs buffer and AlGaAs spacer (see figure 1.1). Above the spacer is the doped AlGaAs layer which is used to provide electrons. The spacer layer reduces disorder in 2DEG from the dopant atoms and thus enhances the mobility of the wafer. In the last step, a thin GaAs cap layer is deposited to prevent oxidization of AlGaAs.

In general, the doping concentration is of the order of $1 \times 10^{17} cm^{-3}$. The obtained carrier density and mobility is usually of the order $1 \times 10^{11} cm^{-2}$ and $1 \times 10^{6} cm^{2}/Vs$ at 1.5 K.

3.3 Hall bar

To make the device function properly, it is necessary to isolate the 2DEG which is usually realized by etching out most of the wafer to leave an island (it is only necessary to etch

through the dopant layer), the so called 'mesa', and then make ohmic contacts to this island. In this thesis, most of the mesas are with the shape of a Hall bar which is 1500 μm in length and 80 μm in width as shown in figure 3.1.

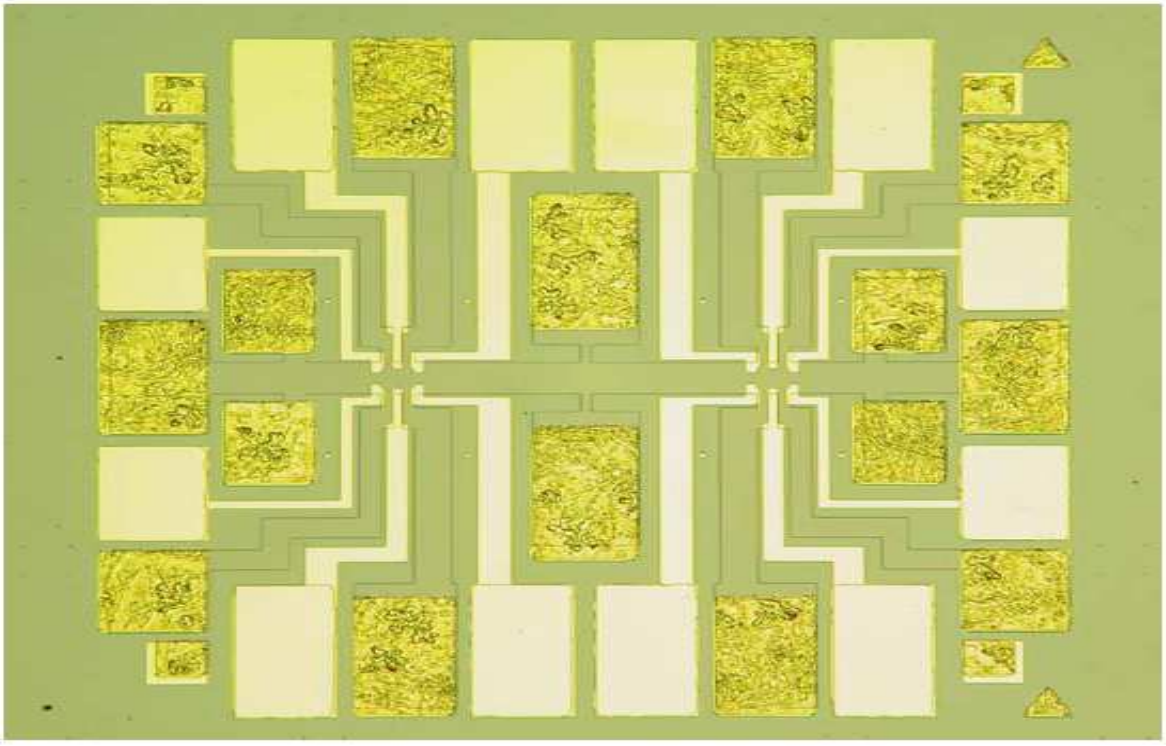

Fig. 3.1 An optical micrograph of a Hall bar. The black outline shows the edge of mesa, the spiky gold pads are ohmic contacts while the smooth ones are optical defined gates. Fine gates are not patterned yet.

Etching mesa

Before the real work, it is usual dip the cleaved wafer, the chip, first into acetone with ultrasonic excitation for around 5 min and then transfer into isopropanol (IPA). Particulates will be removed in this step. After drying with nitrogen gas, the chip is ready for processing.

To define the shape of the Hall bar, the chip is coated with a negative photoresist (Shipley 1813) and then exposed to UV light through a mask patterned as a Hall bar. After this the chip is developed into MF319 for roughly 30 s to remove the photoresist from the exposed area. Therefore only the hall bar itself is covered by photoresist after this step. Finally the chip is etched with a etch solution (1:8:120 $H_2SO_4 : H_2O_2 : H_2O$), the uncovered part is etched out to leave a raised mesa. In general, the etching is divided into two steps. In the

first step, the chip is etched for a short period (e.g. 2 s) and then the height difference before etching and after etching is measured with a DEKTAK surface profiler, the etching rate can be decided thereby. In the second step, a long etching is performed to ensure that it etches through the 2DEG (e.g. for a shallow HMET where the 2DEG is 90 nm below the surface, it is usual to etch down to 100 nm). After etching, the chip is dipped into acetone to remove remaining photoresist.

Ohmic contact

Ohmic contacts are required in order to contact the 2DEG to the environment. To begin with, the etched sample is coated with photoresist, exposed to ultraviolet (UV) light and then developed. Then an alloy of AuGeNi is deposited onto the surface of chip in a thermal evaporator. After this step the whole surface is coated with metal, however, only metal on ohmic contacts are required. To remove the residual metal, the chip is dipped in 1165 remover for 10 min and then the metal film can be blown off with a pipette. Remaining photoresist is again removed with acetone. The metal will contact the 2DEG (forms at low temperature) electrically from the side. The next important step is annealing the ohmic contact to optimize contact resistance. This is achieved by annealing the chip in forming gas (95% N_2 and 5% H_2, to avoid oxidation of the metal) first at 220 °C for 30 s and then 430 °C for 80 s and finally 220 °C for another 30 s. The contact resistance at room temperature is usually several 10 kΩ.

Optical defined gate

The optical defined gate provides a bonding pad to the fine gate. The first several steps are quite similar to ohmic contact, i.e. coating, exposing and developing). Then the gate is metallised with 20/60 nm Ti/Au (Ti is used to improve adhesion to the surface of the wafer) in a thermal evaporator. The chip is then lift-off in acetone for at least 1 hour and cleaned.

Electron beam lithography

The feature size of devices used in this thesis is typically of order of 100 nm, thus optical lithography cannot lead to reliable result and electron beam lithography (EBL) is applied. First of all, a PMMA layer (working as photoresist) is deposited on the chip and baked at 150 °C for 60 min. Then the PMMA layer is exposed by the electron beam. Then the chip is developed in IPA:MIBK (1:3). After this, a 10/60 nm Ti/Au film is metallized to the chip. The last step is lift-off in acetone. To get well defined EBL gates, is is suggested to lift-off

for a relatively long time (e.g. overnight). It is important to ensure that the EBL gate is continuous with the optical defined gate, thus it is usual to write the EBL gate pattern a bit further rather than just at the edge of the optical defined gate. Above is the procedure of fabrication of standard quantum point contact.

Generally speaking, the thickness of gate should not exceed the size of device to prevent leakage. However, sometimes it requires thick gates to define complicated structures, thus one needs to deposit another layer of PMMA onto the first layer. The procedure itself is quite similar to the first layer.

3.4 Low temperature measurement

Although quantum effects start dominating when device size decreases, however, the thermal energy may lead to an averaging out of the quantum effects, therefore, lowering the experiment temperature is required to observe them. Various cryogenic or cryogen free systems are used to provide a low temperature environment in the experiment.

Measurement at 2.4 K

Devices used in this thesis are usually first tested to ensure the ohmics and gates work in a cryomech PT403 cryorefrigerator which has a base temperature of 2.4 K. The 2.4K system is a dry system which means it does not use cryogenic liquid. The inner can of the system, where the cooling process occurs, is always at high vacuum to prevent contamination. The system is cooled down by ^{4}He gas circulated in a close loop. Initially the gas is compressed by pulse tube compressor and hence liquidized, then the liquid ^{4}He absorbs heat from the sample space where the device is mounted and become ^{4}He vapour, then vapour is pumped to the compressor and finishes a cycle. The liquid ^{4}He has a boiling point of 4.2 K at 1 atm (atmosphere pressure), and by reducing the pressure the temperature is lower further.

Thermal energy at 2.4K is around 0.2 meV while the subband spacing of a typical split gate device is in the order of 1 meV, hence weak conductance plateaus may be observable at this temperature. Of course, in a narrow split gate device where the subband spacing is large well defined conductance plateaus can be observed. As introduced in chapter 2 the 0.7-structure is enhanced by temperature, thus the 0.7-structure is usually the most pronounced feature at this temperature.

Measurement at 1.5 K

Devices tested at 2.4 K system are then shifted to an Oxford Instrument TeslatronPT system which can be cooled down to 1.5 K. The operation principle of the 1.5 K system is the same as the 2.4 K system but with a larger cooling power. Besides, a superconducting magnet which can reach up to 8 T is integrated in the 1.5 K system.

Wafer characteristics e.g. carrier concentration and mobility after gate patterning can be measured in the 1.5 K system via Shubnikov-de Haas (SdH) and quantum Hall effect (QHE) with the help of the magnet. On the other hand, in terms of 1D behaviour, conductance plateaus become better defined due to the reduction of thermal energy.

Measurement at cryogen free dilution fridge

Although in most cases, 1.5 K system is sufficient to get well defined conductance plateaux, however, phenomena related to spin or quantum interference which are the central issue of the thesis are still quite faint at this temperature. Thus, an even lower environment temperature is necessary and this is provided by an Oxford Instrument cryogen free dilution fridge (the Triton system). The base temperature of the Triton system is around 10 mK.

The Triton system is cooled stage by stage which means the top most stage is set at the highest temperature (around 100 K) and the bottom stage which is closest to the sample space is at the lowest temperature (around 10 mK). Cooling from 100 K to 1.3 K is achieved by ^{4}He only in the outer closed loop as in the previous sections. Cooling below 1.3 K is achieved with ^{3}He/^{4}He mixture in the inner closed loop. The inner loop is formed by a mixing chamber, a still and a 1K pot (to be strict, only the feedback tube goes through 1K pot) and then a ^{3}He pump. The mixing chamber touches to the sample space directly and contains a mixture of ^{3}He/^{4}He which is separated into two phases (this happens automatically when temperature is below 870 mK), a pure ^{3}He phase on the top and a ^{4}He rich mixture phase at the bottom, when heat is absorbed by the mixing chamber it leads to the evaporation of ^{3}He due to its smaller mass, besides, when the top ^{3}He evaporates out then the ^{3}He in the bottom mixture phase starts to release and this lowers temperature even further because it requires relatively large energy to break the mixture phase, the ^{4}He is left due to its higher boiling point. The resultant ^{3}He vapour is pumped upward and passes through the still which is at around 600 mK, the evaporated ^{4}He (if there is any) will be condensed in the still and only pure ^{3}He is allowed to pass. The ^{3}He is collected at the ^{3}He pump which is made of carbon block. In the next step, the ^{3}He vapour is fed back through a vortex tube where one end is wider and the other end is narrower, the ^{3}He vapour is cooled down and is liquefied due

to the sudden change in pressure, the liquid ^{3}He obtained thereby goes back to the mixing chamber and again forms ^{3}He/^{4}He mixture and hence finishes a cycle.

Due to the large cooling power, the Triton fridge is equipped with a superconducting magnet which is able to go to 12 T.

3.5 Measurement technique

Depending on what is to be measured, the measurement technique can vary quite a lot. In this section it focuses on the measurement of conductance or resistance which is also the most typical measurement. Generally a small excitation is fed to the device, current excitation is around 10 nA while voltage excitation is about 10 μV, to avoid electron heating and remain in the linear response regime. To reduce the influence of electrical noise, a lock-in technique, which utilizes (frequency-dependent) phase sensitive signal detection, is generally used.

Two-terminal measurement

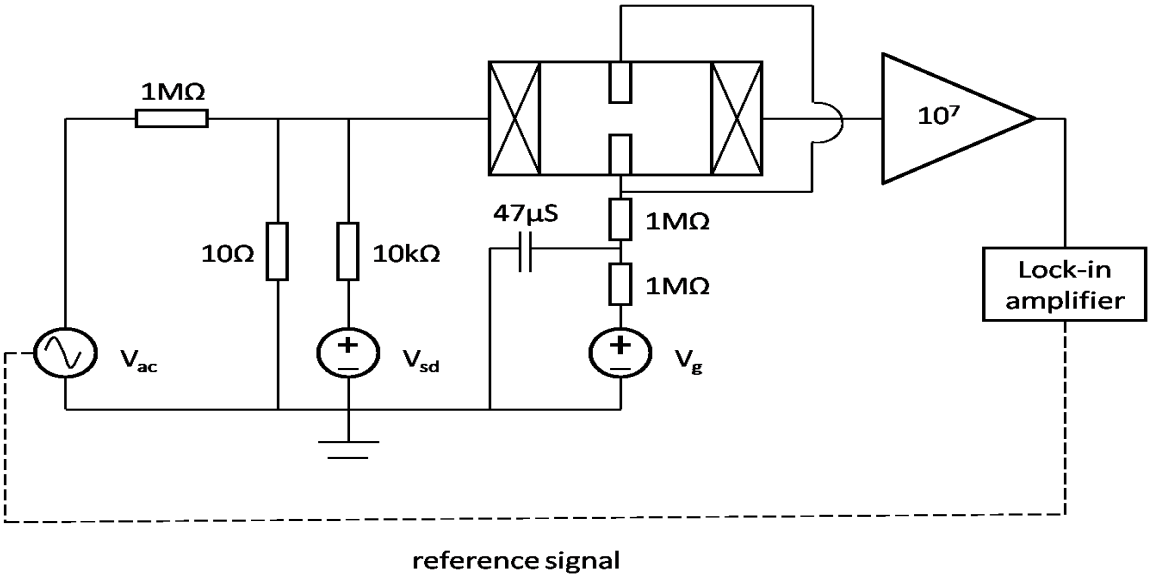

Fig. 3.2 Schematic of a circuit diagram of a typical two-terminal measurement. The dashed line is the reference signal fed from the excitation to the lock-in amplifier, if the inner oscillator of the lock-in amplifier is used then this loop should be removed.

The most straight forward measurement is the two-terminal measurement shown in figure 3.2, a 1 V sinusoidal excitation passes through a 10^5 : 1 potential divider, i.e. 10 μV after convert, and then feeds into the ohmic contact of the devices. The resulting current is

pre-amplified by an op-amp current to voltage converter and recovered as a voltage signal and then measured by a lock-in amplifier. For the ease of data acquisition the dividing ratio and gain of pre-amplifier is set in this way that a 10 kΩ resistor (working as sample) should lead to a reading of 1 V in the lock-in amplifier. Meanwhile, the magnitude of excitation is calibrated with a 10 kΩ resistor before real experiment.

Conductance obtained via two-terminal measurement is the conductance of the whole circuit, i.e. apart from the conductance of the 1D channel it also includes the conductance of the wires, 2DEG and ohmic contacts, as these components are in series with 1D channel and thus the residual resistance arising from them is denoted as series resistance. As a result of series resistance the measured result diverges from the ideal one, e.g. the first integer conductance plateau is lower than $\frac{2e^2}{h}$. The series resistance can be estimated from the variation between $\frac{2e^2}{h}$ and real value of conductance plateau. Alternatively, 2D resistance, more strictly speaking resistance when gate voltage is at 0, can be used to estimate series resistance, however, it is found out this value is smaller than the one that should be subtracted to move the conductance plateaux to the ideal value, because the resistance arising from electron reflection at the interface between the 2DEG and the 1D channel is not included in the 2D resistance.

Four-terminal measurement

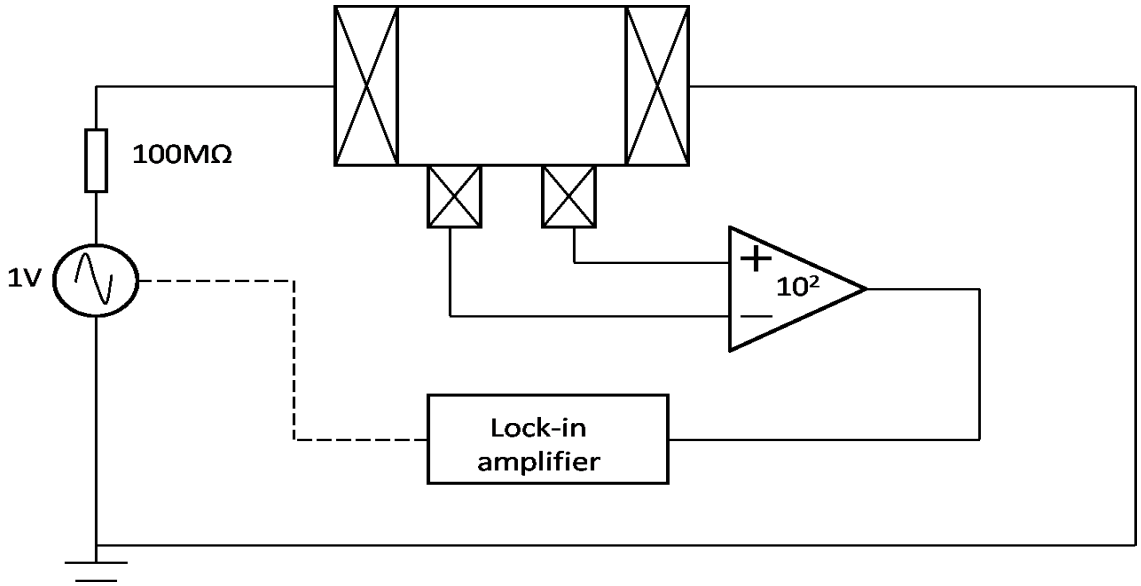

Fig. 3.3 Schematic of circuit diagram of a typical four-terminal measurement. Connection for gates are the same as that in two-terminal measurement and hence omitted.

To overcome the limitation of two-terminal measurement, i.e. series resistance, a four-terminal measurment which measures resistance can be used and the setup is demonstrated in figure 3.3. In the four-terminal measurement a constant current (usually 10 nA) is fed into the device and the flows into the ground, the voltage across a particular part of the sample is measured simultaneously. Because the voltage drop arises from the active area of the device, the resistance due to wires or ohmic contacts are then excluded.

Four-terminal measurement is not generally used for a 1D measurement, because it is known that the 1D conductance/resistance is sensitive to the Fermi level, and with a constant current excitation the Fermi level changes when the conductance changes (this change can be significant especially in the low conductance regime) and in turn leads to inaccuracy of the result. On the other hand, 2D resistance (e.g. SdH oscillation or QHE) is always monitored with four-terminal measurement.

Non-local measurement

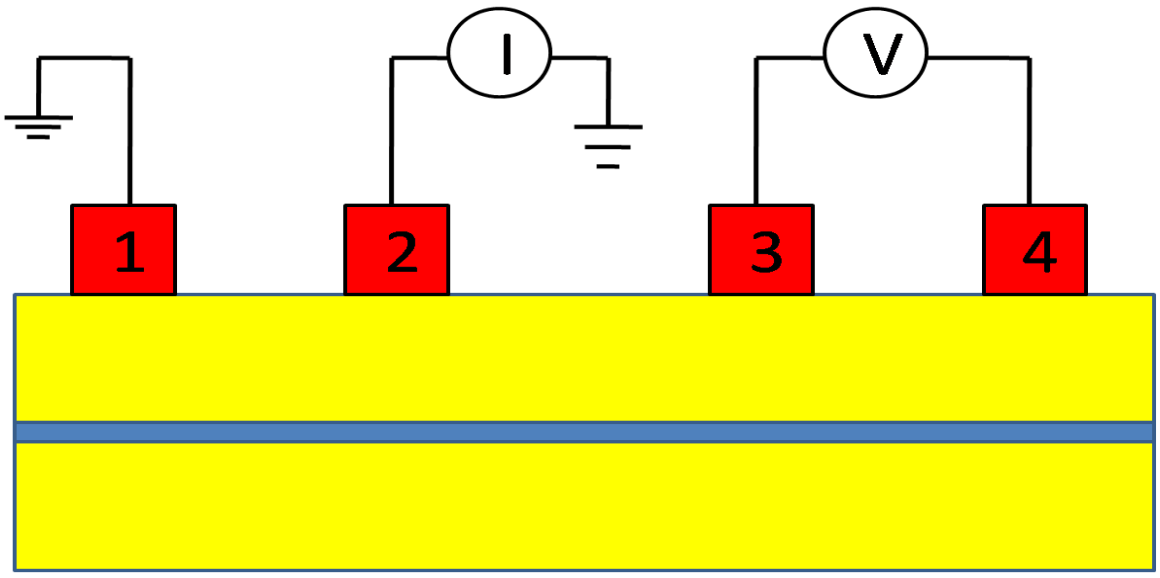

Fig. 3.4 Schematic of a non-local measurement, the yellow layers stand for semiconductor materials, the thin blue layer represents the 2DEG, the red blocks are ohmic contacts. The non-local resistance is defined as $R_{34,12} = \frac{V_{34}}{I_{12}}$.

A non-local measurement is an unique measurement setup where the excitation signal does not actually propagates through the measured area (e.g. the device), thus it ensures that properties of the device such as the local spin configuration are not perturbed by the

excitation, the non-local measurement has been applied most successfully in spin diffusion experiments[82, 83].

Noise reduction

Various noise sources are involved in the measurement, mainly including thermal noise and electrical noise. Thermal noise is minimized automatically at low temperature, thus the key issue is optimizing electrical noise.

As introduced in previous section, a lock-in technique is quite efficient in noise reduction, however, it is ought to emphasise the reference frequency of lock-in amplifier should be away from 50 Hz and its higher harmonics (50 Hz is the frequency of power supply in UK), in this thesis the reference frequency is set to 77 Hz. In terms of the measurement circuit, there should be only one common ground otherwise the current flow between the multiple ground will give rise to noise with a frequency of 50 Hz (this can be checked with spectrum function of lock-in amplifier).

Data acquisition

As shown in figure 3.2 and figure 3.3, a variety of equipments have been used to form the measurement setup. The 77 Hz sinusoidal excitation is generated by a Krohn-Heit 4400A ultra-low distortion analogue signal generator, which then passes through the device, and then is amplified using a Signal Recovery model by 5128 current-sensitive pre-amplifier for conductance measurement or Signal Recovery model 5186 differential-voltage pre-amplifier for resistance measurement, in the last stage a Signal Recovery model 7265 digital lock-in amplifier is used to recover the detected signal. Although the lock-in amplifier can generate excitation and inner reference signal, an external signal was used in this study.

DC voltage for gate operation and source-drain bias is provided by an Iotech DAC488/hr eight-channel 16-bit high resolution digital-to-analogue converter (DAC) which has a minimum resolution of 15.3 μV (at 1 V range) and an output voltage range up to $\pm$10 V.

All the equipment are connected to a computer via a GPIB interface and are controlled by CryoMeas, a data-acquisition programme developed by Professor Christopher Ford of University of Cambridge for the National Instruments LabVIEW platform.

Chapter 4

Direct observation of spin polarization in a GaAs quantum wire

4.1 Introduction

Soon after the first observation of quantised conductance in units of $2e^2/h$ in a ballistic one dimensional quantum wire[84, 85], often termed as quantum point contact (QPC) for smaller quantum wire, defined using a pair of split gates[15] on a GaAs/AlGaAs heterostructure, a number of novel interesting observations have been made and the 0.7 structure is one of them[19]. The 0.7 structure is reported to be spin related[19], however, according to the Lieb-Mattis theorem, a spin-polarized ground state in a one-dimensional system is not allowed[25]. To explain such an observation several frameworks have been proposed including spontaneous spin polarization [42, 43], Kondo screening [86, 87] and Wigner crystallisation [88]. Therefore it is of fundamental importance to measure degree of spin polarization to understand the origin of the 0.7 structure. However, it is suggested that the two terminal conductance measurement cannot address spin polarization directly and instead a transverse electron focusing method has been proposed to overcome such a limitation[89].

In a pioneering work by van Houten et al., it was demonstrated that periodic peaks in semiconductor electron gas with a transverse electron focusing setup where injector and detector are defined with QPCs[90], the periodicity follows a quasi-classical picture such that the peaks occur when the separation L between the centre of two QPCs equals to integer multiple of cyclotron diameter. Therefore periodicity in magnetic field is

$$B_{focus} = \frac{2\hbar k_F}{eL} \tag{4.1}$$

where $\hbar$ is the reduced Planck constant, k_F the Fermi wavevector and e the electron charge. The pre-factor 2 depends on the geometry of the focusing device.

The transverse electron focusing method provides direct evidence of intrinsic spin polarisation of the 1D system by virtue of split in the first focusing peak[89, 91]. Based on this fact, a few observations had been made in the past in p-type GaAs[92, 93] and n-type InSb[94]. However, there is hardly any such observations made in n-type GaAs.

In terms of application, the fast developing field of spintronics where the electron spin rather than charge should be used for logic operation leads to a requirement for precise generation, manipulation and detection of electron spin. Among all the candidate materials, n-type GaAs is of particular interest because of the long spin relaxation time. Thus, measuring spin polarization in n-type GaAs quantum devices is one of the key issues to pave the way for spintronics.

Another promising application of such a focusing technique is studying quantum entanglement. If the electrons contributing to split focusing peaks are entangled, then once one of the electrons flips its spin then the other electron will alter the spin orientation accordingly, in this case, the sub focusing peaks shall exchange their intensity, because the position of the sub-peak is decided by the spin orientation of injected electrons while the intensity is directly proportional to the electron population.

Both the theoretical and experimental importance mentioned above motivates us to perform the experiments presented here.

4.2 Device design and characteristic

Devices studied in the present work were fabricated from a high mobility two dimensional electron gas formed at the interface of GaAs/$Al_{0.33}Ga_{0.67}As$ heterostructure. At 1.5K, the measured electron density was $1.80\times10^{11}\text{cm}^{-2}$ and mobility was $2.17\times10^{6}\text{cm}^{2}\text{V}^{-1}\text{s}^{-1}$, therefore both the mean free path l_m and phase coherence length l_ϕ[1] are over 10 μm which is much larger than electron propagation length. The experiments were performed in a cryofree dilution refrigerator with an electron temperature of 70 mK, using standard lockin technique. For conductance (G) measurement an excitation voltage of 10 μV at 77 Hz is applied while

[1] l_ϕ can be calculated from $l_\phi = \sqrt{D\tau_\phi}$, and the diffusion constant D is, $D = \pi h^2 n\mu/m^* e$ where n is the electron density, μ is the electron mobility, m^* is the electron effective mass the dephasing time τ_ϕ is derived from Nyquist equation[95], $\frac{1}{\tau_\phi} = \frac{e^2/h}{g}\frac{k_B T}{\hbar} ln(\frac{g}{2e^2/h})$ where g is the sheet conductance of the wafer (g = 0.3 S, extracted from SdH oscillations), k_B is the Boltzmann constant, T is the temperature, the calculated value suggests l_ϕ = 30 μm. In addition, l_ϕ is estimated to be 15μm from the temperature dependence of quantum inference in figure 5.12.

for focusing measurement a current excitation of 10 nA at 77 Hz is used. Results were reproducible with thermal cycling.

Unlike the conventional transverse focusing measurement layout where the injector and the detector share a common gate and sit along a line[90, 96, 97], the injector and detector in the present work share no gates and are aligned at 90° to each other (see inset of figure 4.1 (a)). This provides flexibility in controlling the two split gates independently and avoids possibility of creation of lateral electric field due to asymmetric gate voltage across the length of the split gates. In addition, a splitter inclined at 45° is patterned between the injector and detector. Lithographic defined separation between injector and detector is 1.5 μm. Since the gap between the edge of injector and detector is smaller (300 nm) than the width of the QPC (500 nm), the focused electrons get reflected by the potential barrier created between them which results in the second and higher focusing peaks as shown by dashed lines in the inset.

In presence of positive transverse magnetic field $B_{\perp}$ the electrons are bent from the injector to the detector under Lorentz force and gives periodic peaks as shown in the main plot of figure 4.1 (a). The calculated periodicity of 0.06 T is in good agreement with experimental result. On the other hand, with negative transverse magnetic field the signal is almost zero. The comparison between negative and positive magnetic field suggests that Quantum Hall effect and Shubnikov-de Haas (SdH) oscillations are negligible in the regime of focusing[90], and all the features are due to transverse electron focusing only. Apart from the well resolved focusing peaks, it is striking to note that the first and the third peak split into two sub-peaks while the second peak remain as a single peak, this behaviour is consistent with observations in p-type GaAs and n-type InSb[92–94], however, the splitting of the first focusing peak (around 6 mT) is much smaller compared to p-type GaAs (around 36 mT) and n-type InSb (around 60 mT).

4.3 Focusing as a function of injector conductance

It is predicted that electron polarization is sensitive to the conductance of the quasi-1D channel[42, 43]. To verify the theoretical prediction we study the transverse electron focusing as a function of the injector conductance. In this study, the injector is slowly opened setting the conductance from the beginning of 0.7 anomaly up to the end of the second conductance plateau (2 G_0) with the detector fixed at the centre of first conductance plateau, so that the measured variation in spin polarization is due to the injector only. It is found that splitting of the first focusing peak is pronounced in the whole range while the second focusing peak does not show similar splitting as shown in figure 4.2.

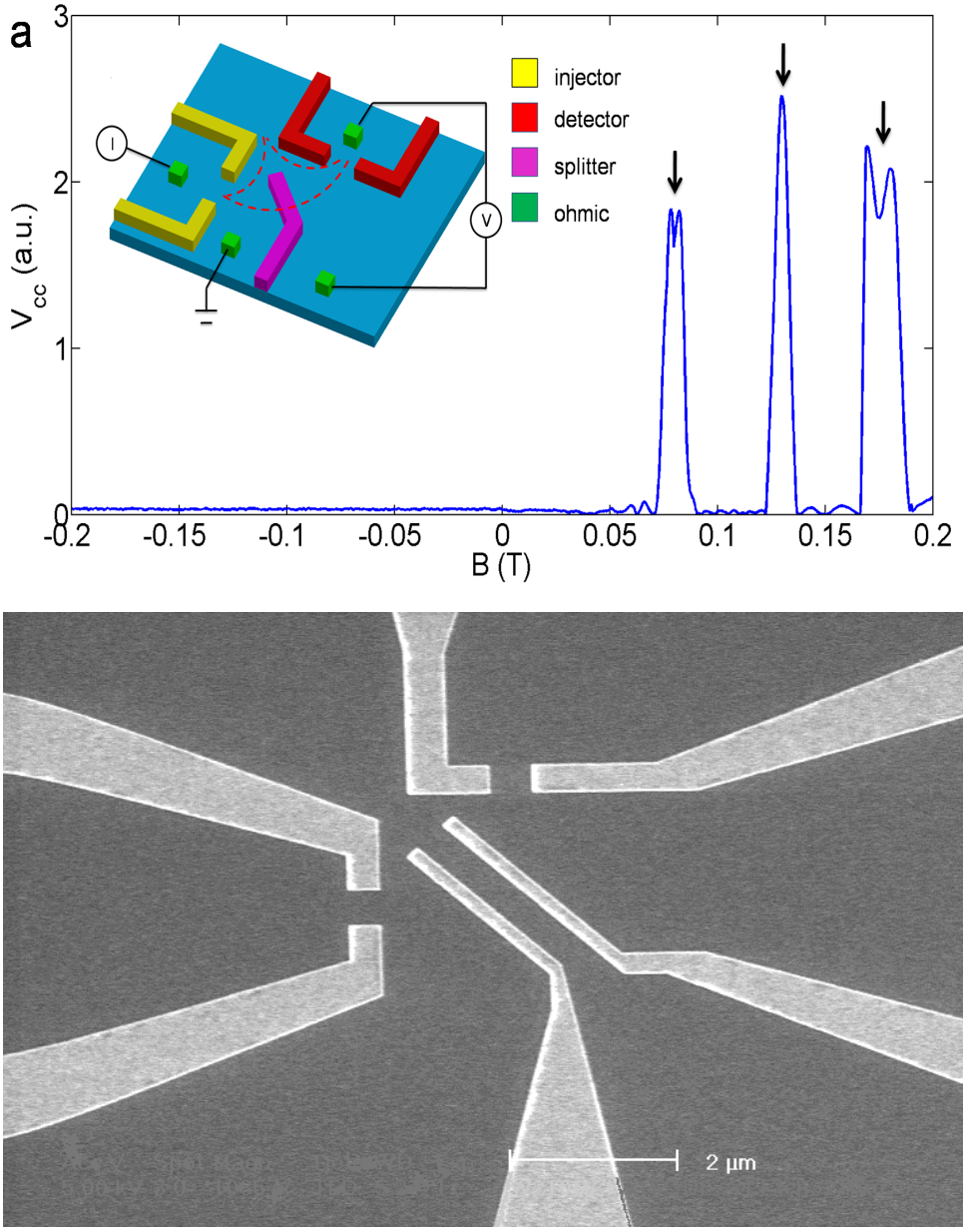

Fig. 4.1 **The experiment setup and device characteristic.** **a**, a representative result of transverse electron focusing. Periodic focusing peaks are well defined and the position is in good agreement with calculation as highlighted by the arrows. First and third focusing peak shows pronounced splitting. Inset shows a schematic of the experiment setup. Injector, detector and splitter are defined with metallic gate. Lithographic defined separation between emitter and detector is 1.5 um. Since the gap between the edge of injector and detector is smaller (300 nm) than the width of the QPC (500 nm), the focused electrons get reflected by the potential barrier created between them which results in the second and higher focusing peaks as shown by dashed lines in the inset. **b**, SEM image of the device, the finger gate on the right hand side is grounded within the experiments.

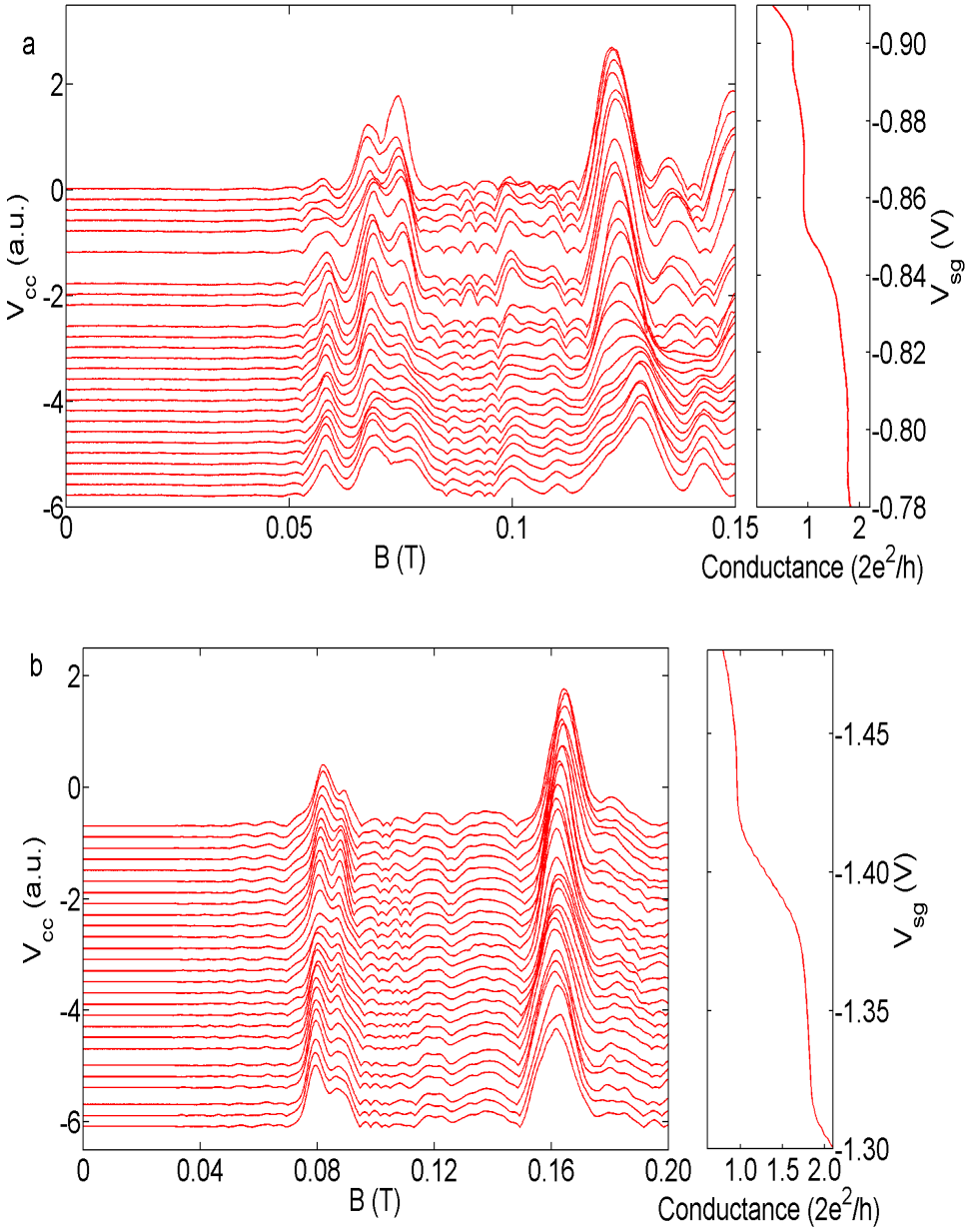

Fig. 4.2 **Focusing as a function of injector conductance a** First and second focusing peak at different injector conductance with detector fixed at centre of first conductance plateau. The top trace corresponds to beginning of 0.7 structure while bottom trace is at end of second conductance plateau. **b** Same as plot (a) but after illumination. The top trace corresponds to beginning of 0.7 structure while bottom trace is at end of second conductance plateau. Data have been offset vertically for clarity.

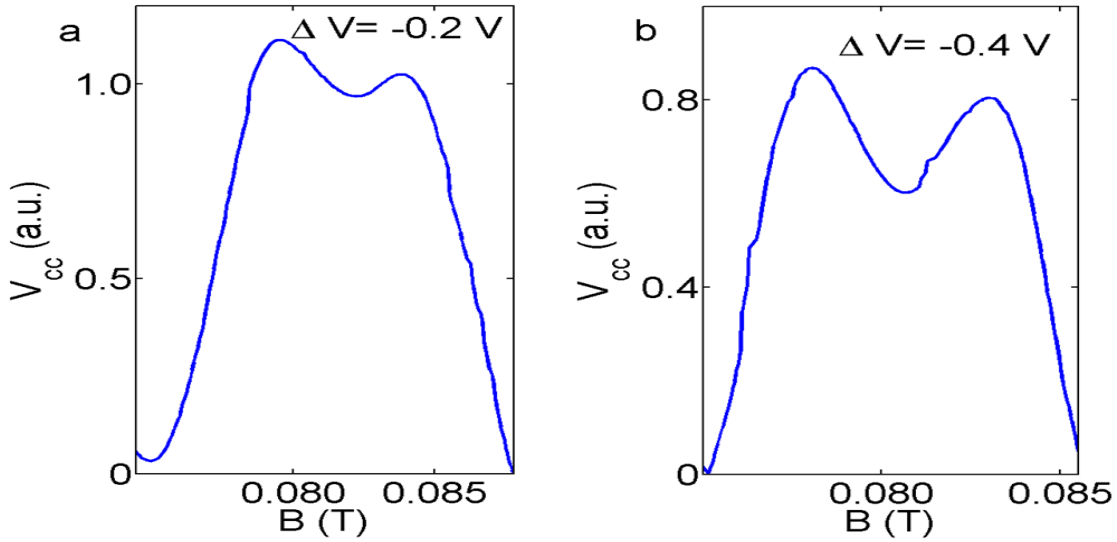

Fig. 4.3 **Transverse electron focusing with lateral shift of the quasi-1D channel.** Injector with given asymmetric gate bias is set to G_0 according to conductance measurement with the same bias. Detector is symmetrically biased and fixed at G_0. Plot a and b show results of asymmetric bias voltage of - 0.2 and - 0.4 V respectively. Splitting of focusing peak is still observable after channel shifting. It is noticed that position of both sub-peaks changes slightly, however, the absolute value of splitting remains unaffected.

Two things to be noticed here. Firstly, it's obvious that the asymmetry of two sub-peaks of first focusing peak oscillates against the injector conductance, these two sub-peaks are almost equivalent in height when the injector conductance is at the centre of conductance plateaux and diverge from each other when the injector is fixed at elsewhere. Secondly, the position of the two sub-peaks and therefore the splitting does not change against the injector conductance which is a sign that the splitting does not arise from an impurity. Scattering with impurity will affect the trajectory of the injected electrons and hence the position of focusing peaks. The impurity effect can be further ruled out by laterally shifting the injector-quasi-1D channel via asymmetric gate biasing. Figure 4.3 shows the transverse electron focusing with the injector asymmetrically biased, and bias voltage set to - 0.2 and - 0.4 V respectively. The injector with a given asymmetric gate bias was set to G_0 while the detector was symmetrically biased and fixed at G_0. It may be noted that the splitting of first focusing peak does not change appreciably. More importantly, although both sub-peaks shift slightly in the same direction which is a direct result of the change of separation between injector and detector, the absolute value of peak splitting is almost the same. This is in agreement with the focusing result reported in a GaAs hole gas[92]. This robustness of peak splitting against channel shift

is evidence that the observation is an impurity-free effect. These observations are in good agreement with previous observation[92, 94].

Apart from the main focusing peaks, an extra small peak appears at around 0.06 T just before the first focusing peak and enhances significantly when injector conductance is larger than G_0, however, it is not present when the role of injector and detector are reversed (data is not shown here) or after illumination[2] (figure 4.2(b)).This additional peak is most likely due to scattering with impurities which is screened after illumination. In addition, it is pointed out that interference between edge state can also lead to additional peaks in focusing spectrum[98].

After illumination, as shown in figure 4.2(b), the periodicity increases from 0.06 T to 0.08 T due to an increase of the 2D Fermi wavevector and each focusing peak shifts to higher magnetic field correspondingly while the splitting of first focusing peak does not change too much, i.e. the absolute splitting is not that sensitive to the 2D electron density. The two sub-peaks become equal at the conductance plateaux and asymmetrical elsewhere. The second peak remains unsplit. Meanwhile, focusing data become cleaner i.e. residual peaks between first and second peaks disappear. This further proves that our observation arises from the physical property of the system studied here.

In the previous study[92–94], the splitting of the first peak and the absence of splitting of the second peak is thought to be evidence such behaviour is spin-related. Because the two spin branches possess different phases $\Delta\phi_1$ in presence of magnetic field, $\Delta\phi_1$ is present for both first and second focusing peak. However, the reflection off the confinement wall will introduce an extra phase change $\Delta\phi_2$, $\Delta\phi_2$ is for second peak only, and under the focusing condition, $\Delta\phi_1$ cancels out with $\Delta\phi_2$ so that the two spin branches get mixed together, as a consequence, the second peak should not split out.

4.4 In-plane field dependence

Although the splitting of focusing peak is in line with previous work where such splitting is proved to be spin related[92, 94], however, this phenomena has not been observed in n-type GaAs previously. In order to confirm our observation of splitting of first focusing peak also arises from spin we applied a tilted magnetic field. This experiment was performed in a He-3 cryogenic fridge with a rotatable sample holder and the base temperature was 300 mK. When

[2]The sample was illuminated with a red LED (the wavelength is 635 nm, corresponding to an energy of 1.95 eV) at base temperature.

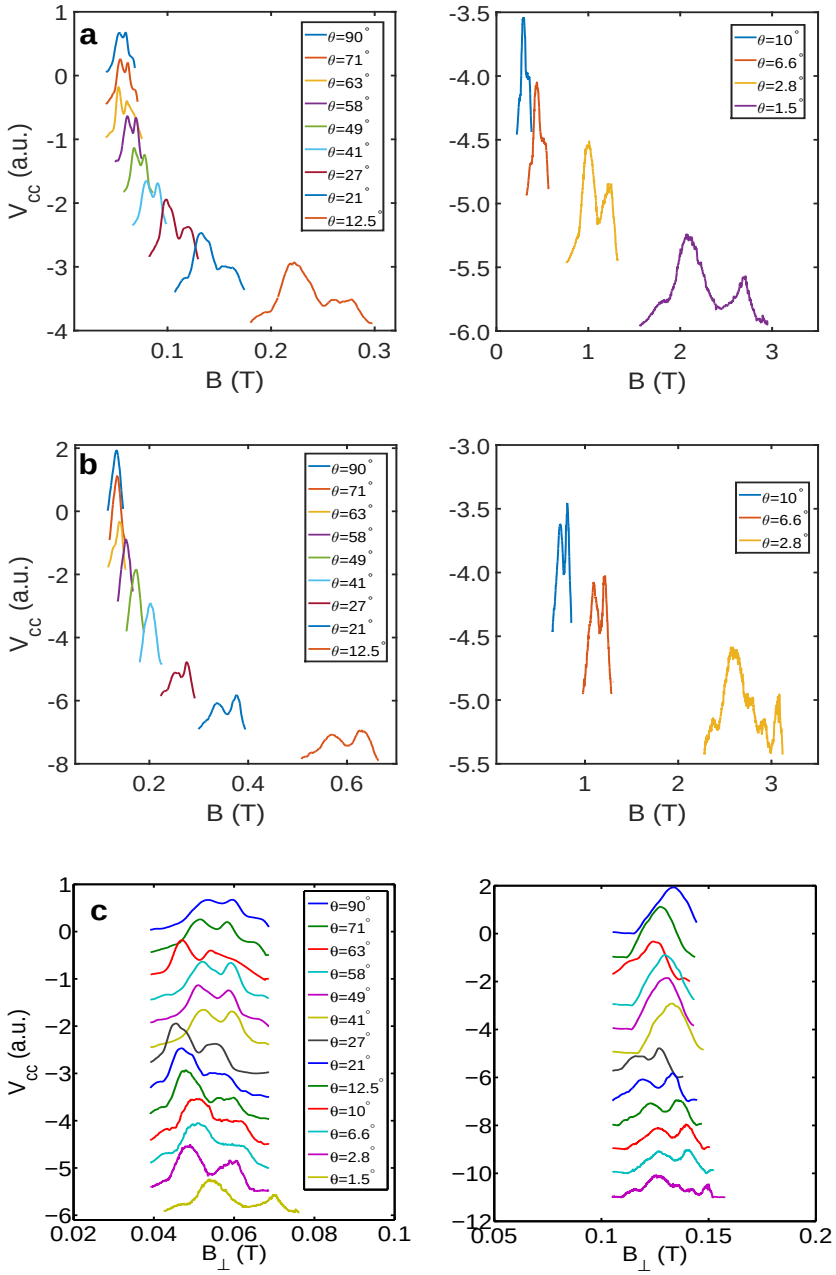

Fig. 4.4 **Field dependence of transverse electron focusing.** **(a)** First focusing peak at different angle Θ. **(b)** Second focusing peak at different Θ. Second focusing peak at 1.5 ° is above the maximum allowed field of the He-3 system and therefore not available. **(c)** Collector voltage against out plane component $B_\perp$ with varying Θ, left subplot is for first focusing peak and right one for second focusing peak. Data have been offset for clarity, result for large Θ is on the top while that for small Θ at bottom.

the angle between 2DEG plane and magnetic field Θ equals to 90°, the field is perpendicular to 2DEG plane and when Θ decreases toward 0 an in-plane field is introduced.

Results shown in figure 4.4 (a) and (b) correspond to the first and second focusing peak at different Θ respectively. The injector conductance was fixed at 0.9 G_0 while detector was set to G_0. The two sub-peaks of the first focusing peak are pronounced in the whole range studied here, both sub-peaks shift toward higher magnetic field and splitting becomes larger when Θ decreases. It is interesting to notice that sub-peak at higher magnetic field side is weakened initially and almost disappears when Θ is around 6.6° and then reappears when Θ deceases further. This reminds us of the observation in p-type GaAs [93] where the authors suggest such behaviour is due to cubic Rashba spin-orbit coupling in a hole gas. However, this is unlikely to be the case with n-type GaAs. It is known that in-plane field leads to half-integer conductance plateau therefore weakening and reappearance of one of the sub-peaks may arise from crossing of the spin-split subbands (e.g $n_\uparrow$ and $n+1_\downarrow$). The second focusing peak splits into two when Θ is below 27° when in-plane field is sufficiently large. It is important to note that the sum of the heights of the two sub-peaks of the seconds focusing peak is almost equal to its unsplit counterpart. This could be explained by the fact that the height of the focusing peak corresponds to the number of electrons detected at the collector and within ballistic limit this number remain constant as demonstrated in two QPCs in series where the total resistance $R = min(R_1, R_2)$ (R_1, R_2 are the resistance of the two QPCs receptively) [99].

To extract more information we plot the focusing signal against out-of-plane component of magnetic field $B_\perp$ as seen in figure 4.4 (c). It is noticed that the position of focusing peak and periodicity do not change significantly with increasing in plane field $B_\parallel$. The irregular shift of focusing peak is mainly due to slight mis-calibration of angle Θ vs field. It is apparent that splitting of first focusing peak is enhanced by an in-plane field in the whole range studied here. Second peak shows a similar behaviour after it splits into two.

Figure 4.5 (a) and (b) present splitting of first and second peak $\Delta B_\perp$ against in plane field $B_\parallel$ respectively. It is noticed that the splitting of first peak experiences a sharp increase from 6.5 mT to around 11.5 mT when in plane field is less than 200 mT and then it rises slowly but linearly to 16.3 mT in large field regime. Splitting of second focusing peak follows a similar trend from 10 mT to 34 mT. It is important to make clear that second focusing peak occurs at higher magnetic field compared to first focusing peak, so the in plane field experienced by second focusing peak is larger than that by first focusing peak for a given Θ. The turning point of increasing rate of splitting of first focusing peak happens to occur when second peak also splits into two.

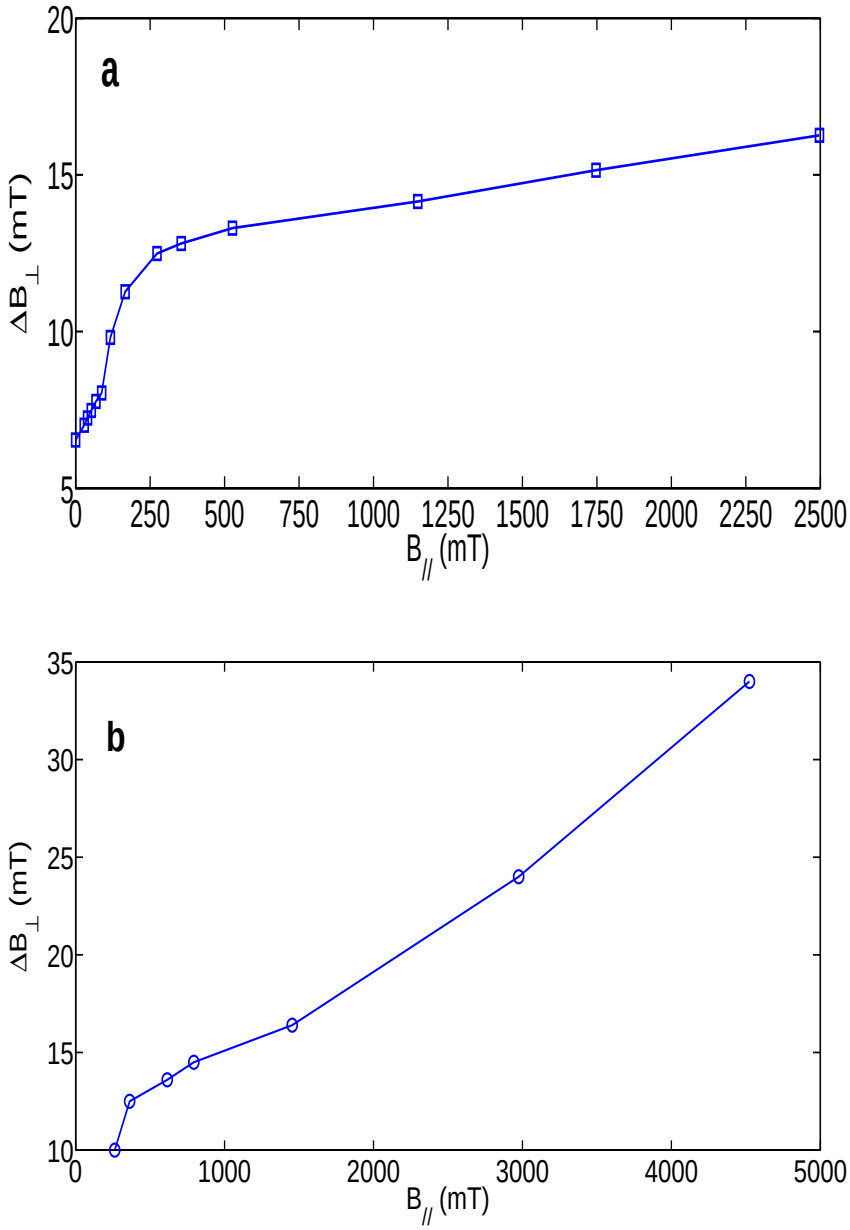

Fig. 4.5 **Splitting of first and second focusing peak against in-plane field.** **(a)** Splitting of first focusing peak against in plane component of total field. The in plane field $B_{||}$ is chosen as $B_{||}=\frac{1}{2}(B_{1H}+B_{1L})\cos\Theta$ where B_{1H} and B_{1L} stand for position for sub-peaks of first focusing peak in terms of total field. **(b)** Splitting of second focusing peak against in plane component of total field. $B_{||}=\frac{1}{2}(B_{2H}+B_{2L})\cos\Theta$ where B_{2H} and B_{2L} stand for position for sub-peaks of second focusing peak in terms of total field.

The in-field dependence supports that our observation is spin-related. In-plane magnetic field mainly introduces Zeeman splitting and thus change in peak splitting allow us to the estimate g factor,

$$\Delta E(B_{\parallel,2}) - \Delta E(B_{\parallel,1}) = g\mu_B(B_{\parallel,2} - B_{\parallel,1}) \tag{4.2}$$

$$\Delta E(B_{\parallel}) = \frac{e\Delta B(B_{\parallel})}{m^*} \tag{4.3}$$

where g is Landé g-factor, μ_B is Bohr magneton, $\Delta B(B_{\parallel})$ is the peak splitting at given in-plane field. g-factor estimated from small field regime is around 1.2 consistent with result reported in GaAs[31, 32, 100]. On the other hand, the slow change in the splitting gives a much smaller g-factor in large field regime and this further splitting may arise from a different origin such as the distortion of Fermi surface in presence of large in-plane field[101, 102]. The splitting of the second focusing peak which was not observed in previous work[92–94] might be attributed to such distortion as well.

In a previous transverse focusing experiment in a GaAs electron gas, a large in-plane field of 7 T was applied but no splitting was observed[97]. Considering the fact that a half integer plateaus start appearing with large in-plane field which indicates spin-up and spin-down have different k_x and k_y component and should be injected to different position of Fermi sphere and leave at different point as well. The Fermi sphere splits into spin-up and spin-down branches (in addition the shape of the Fermi surface may be distorted at large field, e.g. it evolves from a sphere into an ellipse), as a result, the spin-up and spin-down electrons will take different trajectories and contribute to two sub-peaks. The obvious discrepancy between the expectation (peak splitting should present) and experimental result (peak splitting is absent) suggests the way electron is injected into 2D regime is crucial for peak splitting and this would be discussed later.

4.5 Focusing with a beam splitter

Electrons contributing to different sub-peaks have different momentum <k_x, k_y>, and thus can be detected when they pass through a potential barrier as demonstrated in a previous quantum pump experiment[103]. In this section, the finger gate inclined at 45° to both injector and detector will be activated and generate a potential barrier to differentiate the difference in the momentum. Both the injector and detector are fixed at the centre of the first conductance plateau. For the ease of discussion, we will discuss the height and position of the focusing peak separately.

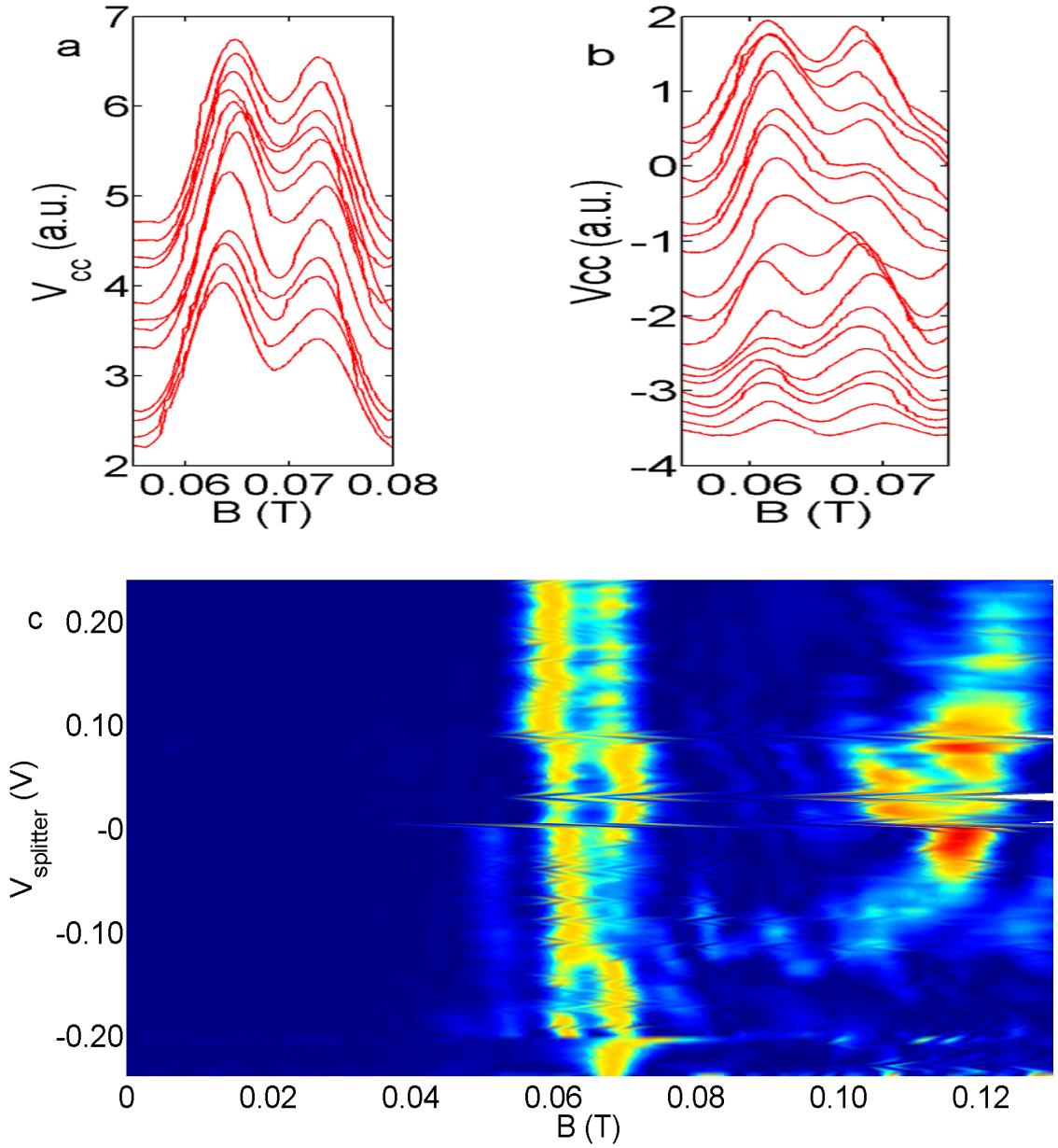

Fig. 4.6 **Beam splitter voltage dependence of focusing.** **a**, first peak with positive beam splitter voltage swept from 250 mV (top) to 5 mV (bottom), both sub-peaks are clearly viable and the amplitude of the peaks almost remain the same. **b**, first peak with negative beam splitter voltage swept from 0 mV (top) to - 250 mV (bottom) amplitude of both peaks reduce when splitter voltage become more negative but the splitting is robust. **c**, normalized colourmap of the focusing against splitter voltage. The bright (yellow) patterns are focusing peaks and dark (blue) regime is background signal. Data in plot a and b have been offset vertically for clarity.

In figure 4.6 (a) splitter voltage changes from 250 mV to 5 mV from top to bottom. Positive splitter voltage modifies the wavevector of electrons passing under the beam splitter. Both sub-peaks of the first focusing peak are pronounced in this regime while heights of the two sub-peaks show an oscillation against splitter voltage. On the other hand, results for focusing with a negative splitter is presented in figure 4.6 (b). Briefly speaking, the focusing peaks are well defined when splitter voltage is close to 0 where the potential barrier is low and all the features disappear when the splitter voltage is sufficiently negative where the potential barrier blocks current flow. If we look deep into the problem, it is found out that height of sub-peaks of first focusing peak follow a complicated trend with negative splitter voltage. Initially, heights of the two sub-peaks oscillate in a way similar to that observed with positive splitter voltage. Then the height of sub-peak at higher magnetic field reduces rapidly with splitter voltage up to $V_{splitter}$= - 120 mV. After this point height of sub-peak at lower magnetic field side drops sharply while that at higher magnetic field side only changes slightly. Eventually, both sub-peaks weaken gradually and both of them almost disappear at beam splitter voltage of - 200 mV.

Figure 4.6 (c) is the colour map for the same experiment and data are normalized against higher sub-peak of first focusing peak for each $V_{splitter}$. It is apparent that position of sub-peaks of first focusing peak remain the same in the range studied here and hence the splitting itself is not affected by beam splitter voltage. Position of second peak shifts monotonically against splitter voltage, it occurs at higher magnetic field with more positive splitter voltage. The reason that such a shift is present for second focusing peak while absent for first peak are twofold: first, the primary orbit (the one give rise to first focusing peak, refer to inset of figure 4.1) is normal to splitter so that trajectory of electrons is not affected by the splitter, on the contrary, the incident angle between secondary orbit (correspond to second peak) and splitter is not 90° so that electrons acquire a lateral shift when they pass the through potential barrier, in analogy with refraction of light; second, the primary orbit is a direct transport between injector and detector without scattering from a boundary while such scattering is necessary to give the second peak, the position where the scattering occurs is sensitive to the change of electron trajectory.

To get a more comprehensive understanding of the observation, the same experiment was repeat with injector set to 0.8 G_0 and 1.2 G_0 and the measured polarization is summarized in figure 4.7. It is necessary to clarify here that the spin polarization obtained in the experiment with beam splitter is the population difference of detected electrons from different spin branches (so, it can be refereed as filtered spin polarization) rather than the real spin polarization within the injector (also injected spin polarization). It is apparent

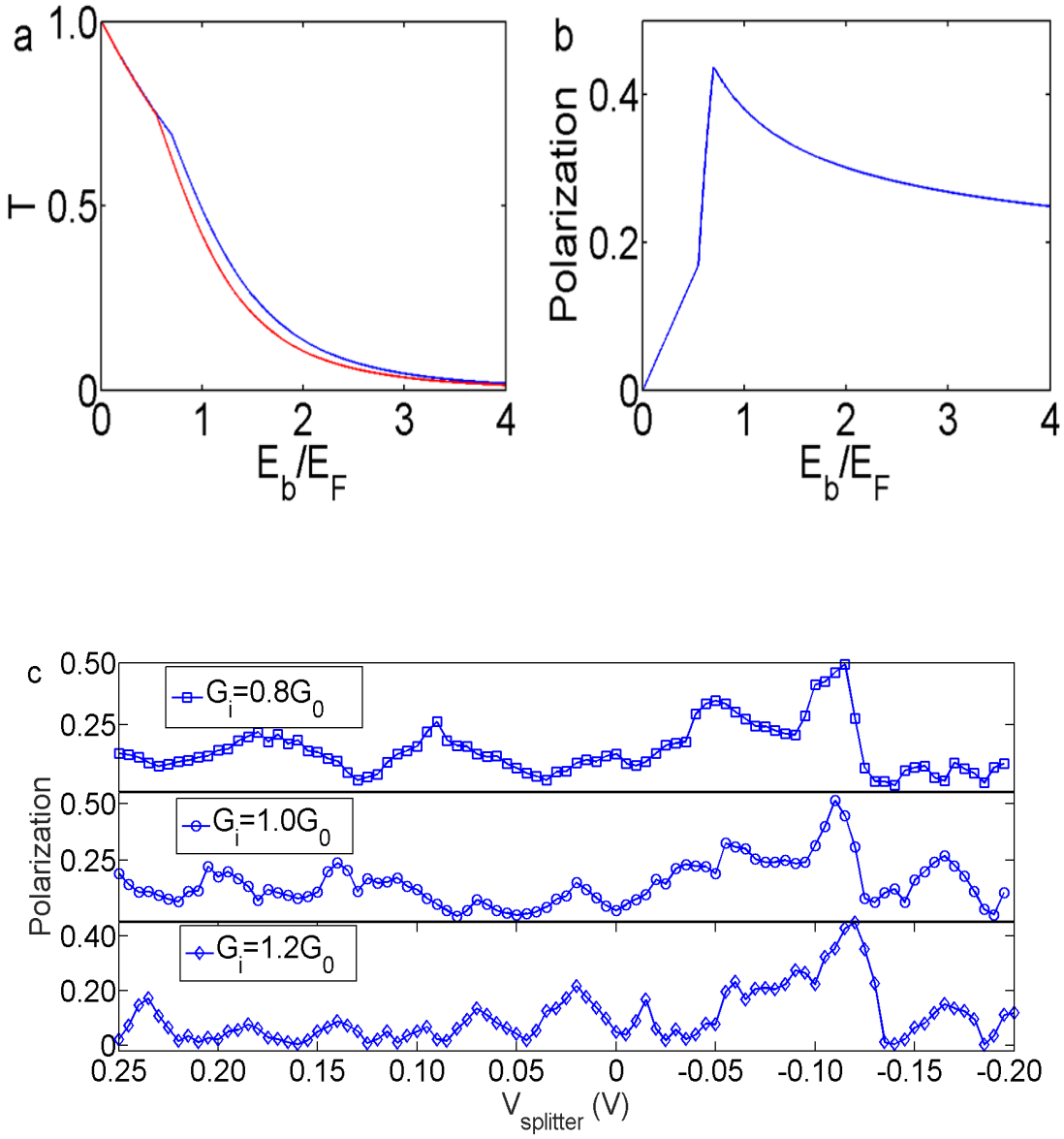

Fig. 4.7 **Polarization as a function of splitter voltage. a**, calculated transmission probability (T) through the splitter for spin-down (red) and spin-up (blue) electron by simplifying the problem as tunnelling through a 1D barrier, E_b is barrier height and E_F is Fermi energy. **b**, calculated polarization from plot a, the polarization resembles an inverse 'V-shape'. **c**, measured polarization as a function of splitter voltage at three different injector conductance with detector fixed at first conductance plateau, the polarization shows a quasi-periodic oscillation in the whole range and an inverse 'V-shape' is observed when splitter voltage is swept between - 0.10 V to - 0.14 V.

that the polarization shows a quasi-periodic oscillation in the whole range and an invert 'V-shape' is observed when splitter voltage is swept between - 0.10 V to - 0.14 V. Below, a phenomenological model is proposed, and the polarization follows such a relation,

$$R = \frac{A_H}{A_L} \propto \Theta(\hbar(k_H - k_L)) \bullet \frac{\tau(E_H - E_b)}{\tau(E_L - E_b)} \tag{4.4}$$

$$P = |\frac{1-R}{1+R}| \tag{4.5}$$

where R denotes the ratio between two sub-peaks, P denotes polarization, Θ describes ratio difference due to phase difference and τ denotes transmission probability for different spin branches, therefore these two functions depend on momentum (k_H and k_L) and energy (E_H and E_L) of two spin branches. E_b is the height of barrier.

For the ease of discussion, the beam splitter voltage is divided into three regime: regime 1, splitter is swept from 250 mV to - 90 mV; regime 2, - 90 mV to - 140 mV; regime 3, - 140 mV to - 200 mV.

In regime 1, there is either no potential barrier or a low potential barrier so that perfect transmission through beam splitter is expected, $\frac{\tau(E_H)}{\tau(E_L)} \approx 1$ and Θ term dominates in this regime, therefore the peak height ratio follows a nice oscillation. This oscillation is likely due to change in wavevector when electrons passing through the splitter similar to that reported in quantum interference experiment[104].

In regime 2, electrons experience a change from perfect transmission to partial transmission via the tunnelling process and therefore the ratio $\frac{\tau(E_H)}{\tau(E_L)}$ changes dramatically in this range as shown in figure 4.7 (a). At the boundary between regime 1 and regime 2, potential barrier is below both spin resolved subband. In splitter voltage range from -0.09V to -0.11V, the rising edge of regime 2, the potential barrier is approaching the lower spin subband (with kinetic energy E_H) and transmission probability for this subband drops, on the other hand, higher spin subband (with kinetic energy E_L) is almost unaffected in this range. Due to conservation of energy, electrons from lower spin subband gets larger kinetic energy and the corresponding focusing peak occurs at higher magnetic side, this is why sub-peak at higher magnetic field weakens first. As a result, $\frac{A_H}{A_L}$ decreases significantly. The lowest point (around -0.11V) indicates the potential barrier just exceeds lower spin subband. When the splitter voltage becomes more negative, i.e. downward edge of regime 2, the potential barrier enters the spin gap, electron from higher spin subband experiences a sudden change from perfect transmission to tunnelling and the corresponding transmission probability changes rapidly while for electrons of lower spin subband as they are already in the tunnelling regime

the transmission reduces relatively slowly. Electrons from higher spin subband give rise to focusing peak at lower magnetic field and therefore we observe a significant reducing in peak height of sub-peak at lower magnetic field side. According to the change in the transmission probability, the calculated polarization in regime 2 resembles a pronounced invert 'V-shape' seen in figure 4.7(b) and this is in good agreement with the experimental result in figure 4.7 (c).

In regime 3, the potential barrier is high so that electron must tunnel through this barrier to be detected, transmission probabilities for both spin branches are low and the ratio $\frac{\tau(E_H)}{\tau(E_L)} \propto \exp(-\frac{E_H - E_L}{E_b})$ and it changes slowly in regime 3. On the other hand, the phase change is still sensitive to splitter voltage and thus the oscillating features dominates again.

It is interesting to note that the result in this section not only prove the two spin branches have different momentum but also suggest such a simple device has the potential to be used as a high efficiency spin filter. As shown in the case when injector is fixed at G_0 conductance plateau, the injected electrons actually has almost zero intrinsic spin polarization but with the splitter set properly (around - 0.12 V) a spin polarization around 50% can be achieved. More importantly, the spin filter here only requires an energy difference between the two spin branches which are not induced by the small external magnetic field, thus in principle this filter can be operated in the absence of magnetic field.

4.6 Source-drain bias dependence

Many theoretical proposals for spin polarization in a quasi-1D channel predict the existence of spin gap[43, 45–47]. To verify the theoretical prediction we present the result of focusing experiment with dc bias in figure 4.8 (a). We use voltage excitation instead of current excitation for this experiment (current excitation shows similar result), considering the fact that the conductance changes when source-drain bias is applied, it is hard to extract accurate an energy gap value from a dc current. The drawback of voltage excitation is that the population of electrons leaving injector changes with applied voltage and so introduces some ambiguity to peak height, however, this does not affect our conclusion significantly. The gate voltage for the injector is set in such a way that the injector and detector are set to the centre of first conductance plateau (in absence of source-drain bias) and fixed at the same gate voltage regardless of the applied source-drain bias. Sub-peaks of first focusing peak and second focusing peak are well defined in the small bias regime which is the central part (in vertical direction) of figure 4.8(a). When it moves to large bias regime at both positive and

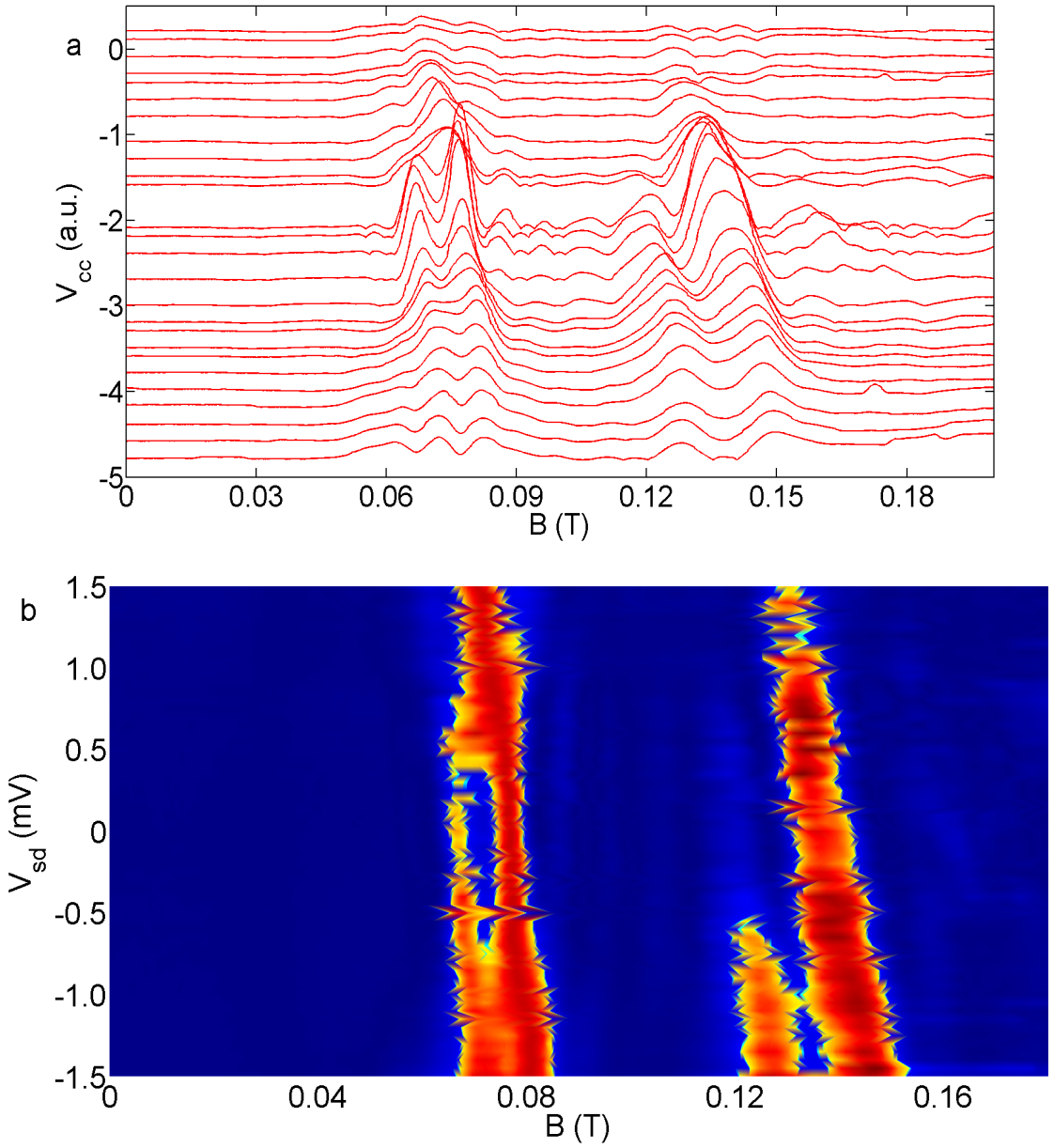

Fig. 4.8 **Source-drain bias dependence of focusing. (a)** Focusing experiment with different dc bias. Both emitter and detector are fixed at centre of first conductance plateau at zero bias. DC bias changes from 2.5 mV (top) to -2.5 mV (bottom). Data are offset for clarity. **(b)** Colourplot of plot a. Data are normalized against higher sub-peak for each bias voltage.

negative end, focusing signal is significantly weakened this is either due to electron heating as reported in hot electron focusing [105] or change in injector conductance.

More information could be obtained from the colour plot in figure 4.8 (b) where the raw data are normalized against higher sub-peak at each bias voltage. There are several things to be noticed here. (1) Both the first focusing peak and second focusing peak follow a linear shift against dc bias voltage, they occurs at lower magnetic field with negative dc source-drain bias and higher magnetic field with positive bias, this is in line with hot electron focusing experiment[105] and arises from the change in chemical potential of source reservoir μ_s. (2) The periodicity of focusing peak remains the same because it is determined by the wavevector in the 2D regime which is the drain reservoir in this case, the drain reservoir is grounded and thus the wavevector remain the same. (3) Both sub-peaks of first focusing peak are observable from most negative bias studied here (- 2.5 mV) up to around 0.5 mV, then sub-peak at higher magnetic field side weakens rapidly. (4) Splitting between sub-peaks is almost unaffected by bias voltage in the range where both of them are observable. (5) Second focusing peak disappears at less positive bias compared to first focusing peak as seen in figure 4.8 (a).

The main observation can be explained by the spin-gap model proposed for the 0.7 anomaly[45–47]. In this experiment the drain of the injector is always grounded, therefore we can assume the chemical potential of the drain μ_d is constant and bias voltage V_{sd} only affects the chemical potential of the source which is $\mu_s{}^*=\mu_s$-eV_{sd} in this case. Negative bias moves $\mu_s{}^*$ upward with respect to 1D subbands and both lower and higher spin-subband are occupied, as a consequence both sub-peaks are observed in focusing experiment. On the contrary, positive bias moves $\mu_s{}^*$ downward, when $\mu_s{}^*$ is lower than a given subband population of injected electrons from this subband reduces dramatically and hence the corresponding focusing peak weakens significantly. Due to the existence of the spin gap, $\mu_s{}^*$ passes the spin-resolved subbands one at a time rather than simultaneously, thus one of the sub-peaks disappears first.

Regarding the additional satellite peak that occurs near the second focusing peak it might be attributed to occupation of higher 2D subband[106] or change in the mean free path due to the large bias[105]. However, the fact that the additional peak is absent in the positive bias end seems to challenge the interpretation based on change in the mean free path which is insensitive to the sign of source-drain[104].

The spin-gap model can be further supported with result in figure 4.9 where the focusing is performed with a horn-shape injector with a source-drain bias current. In figure 4.9 (a), the injector is fixed at 0.5 G_0 and only a single peak is visible because in this case only one spin branch is populated and the chemical potential μ_s is set in the spin-gap. With negative bias

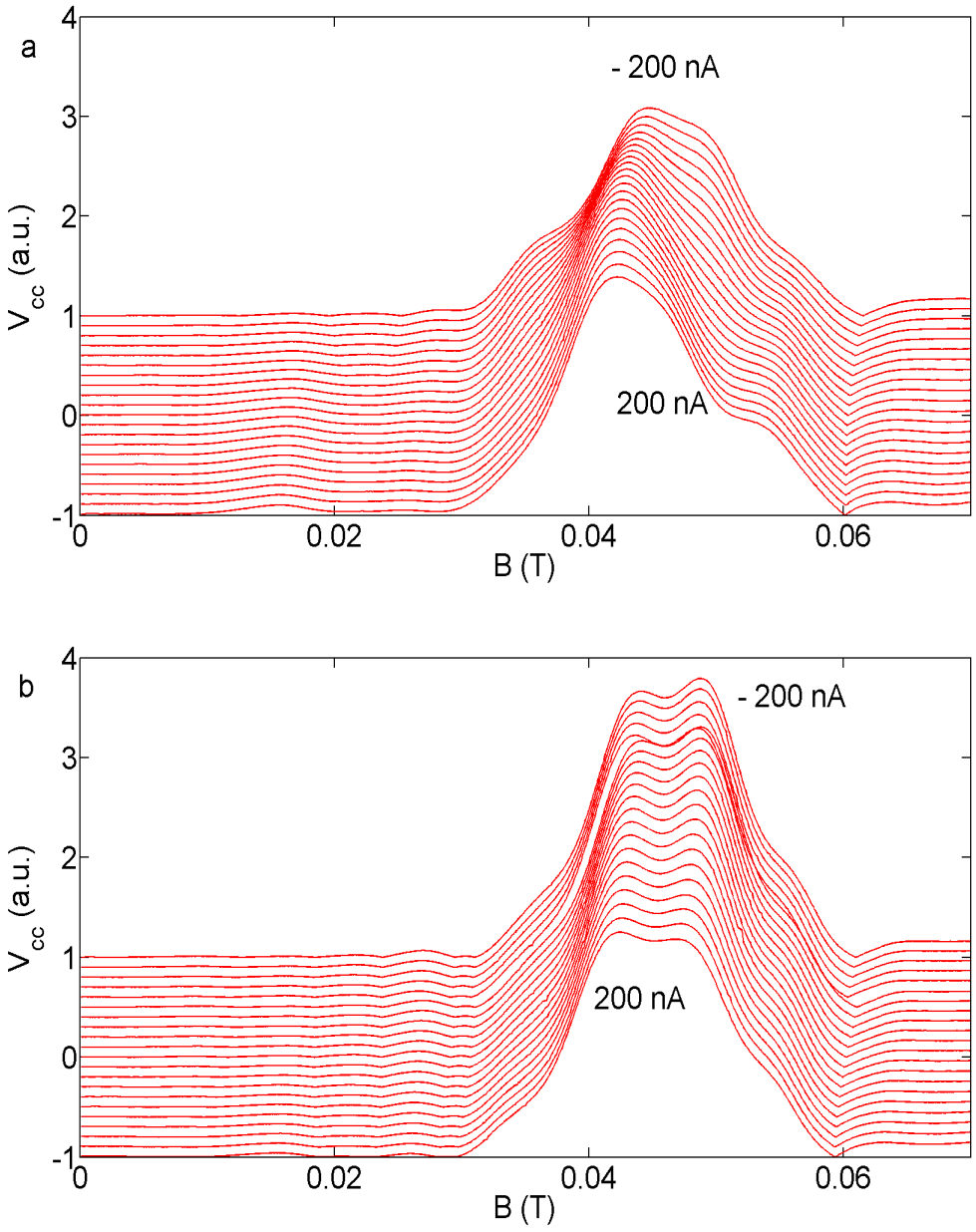

Fig. 4.9 **Source-drain bias dependence of focusing with a horn-shape QPC. (a-b)** Focusing experiment with different dc bias for injector conductance at 0.5 G_0 and G_0 respectively, the shape of peak change dramatically for 0.5 G_0 while it is almost insensitive to source drain bias for G_0. Data have been offset vertically for clarity, the top trace is with - 200 nA DC current while bottom is with 200 nA.

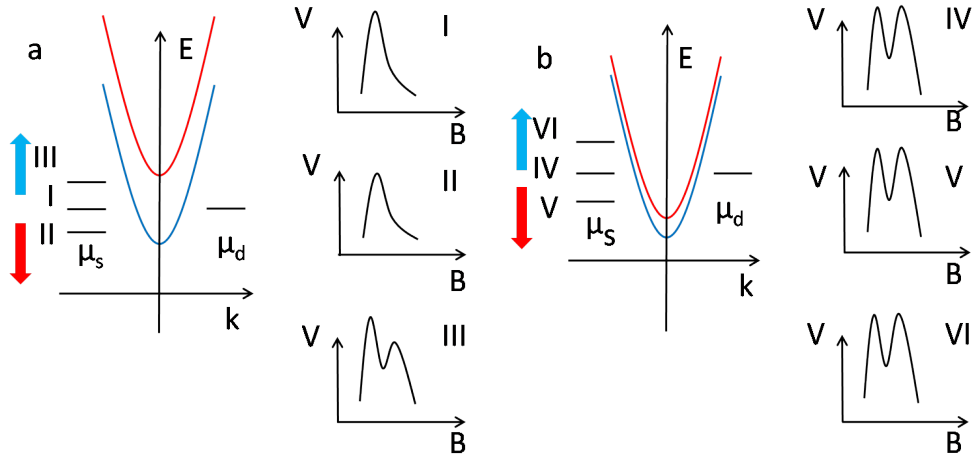

Fig. 4.10 **Spin gap model for TEF.** The spin degeneracy is lifted and gives two spin resolved subbands represented by the blue and red parabola. **a**, injector set to $0.5G_0$, at zero bias current μ_s is at position I and only peak I is present, positive bias current (bold red arrow) pushes μ_s downward to position II still only peak I appears, negative bias current (bold blue arrow) pushed μ_s upward to position III so that peak II starts forming while peak I is pronounced. **b**, injector set to G_0, both peak I and peak II are present and almost have equal intensity in the range of studied bias current (position IV - VI).

current it is seen that the peak at higher magnetic field is lifted up and makes the focusing peak broad while positive bias current does not affect the peak explicitly. The dramatic difference, as shown in figure 4.10, can be understood from the fact negative bias current rises μ_s and therefore if the bias is sufficient large then μ_s moves above higher spin subband and the subband is populated resulting in another sub focusing peak, on the contrary, positive bias current move μ_s downward and makes it more difficult to populate the higher spin subband and thus cannot lead to another sub peak. When the injector is fixed at G_0 (4.9 (b)), both sub-peaks are pronounced and seems to less sensitive to bias current, because in this case both spin-subbands are populated initially and a relatively large (positive) bias is required to move μ_s into the spin-gap (so that one of the sub-peaks will be weakened).

4.7 Temperature dependence

Temperature dependence in mesoscopic system provides a way to estimate the energy scale, e.g. it is noticed from the conductance measurement the well defined conductance plateaux weaken and eventually smear out due to the enhanced transition probability between different

subbands when the thermal energy k_BT becomes comparable with the 1D subband spacing. In this section the temperature dependence of the transverse electron focusing is studied.

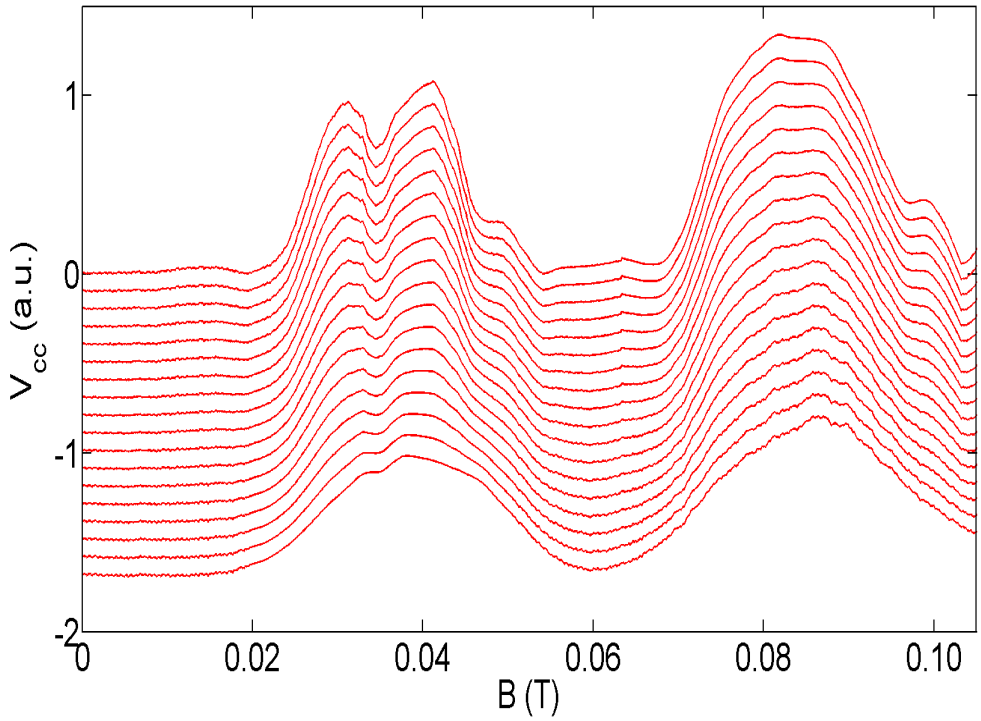

Fig. 4.11 **Temperature dependence of focusing.** Temperature is tuned from 1.5 K (top trace) to 3.3 K (bottom trace), the two sub-peaks merge into a signal peak at high temperature. Both injector and detector are fixed at the centre of first conductance plateau. Data have been offset for clarity.

The experiment is performed in the Teslatron system with a base temperature of 1.5 K where a pronounced splitting of first focusing peak is present and second focusing peak remain unsplit. As temperature goes up, the intensity of both sub-peaks reduces gradually and finally a single peak is left over (see result at 3.3 K), on the other hand, there is no significant change in second focusing peak except the amplitude of this peak drops with increasing temperature. Meanwhile. there is a slight shift of the position of focusing peak against temperature, i.e. it occurs at lower magnetic field when temperature is low and drifts to higher field at higher temperature, which is a result of change of k_F against temperature.

The thermal energy at 3.3 K where the peak disappears is around 0.29 meV and this roughly agrees with the fact one of the sub-peaks of first focusing peak almost disappears at with a source-drain bias of 0.40 mV as shown in figure 4.8 (in terms of energy is 0.4 meV).

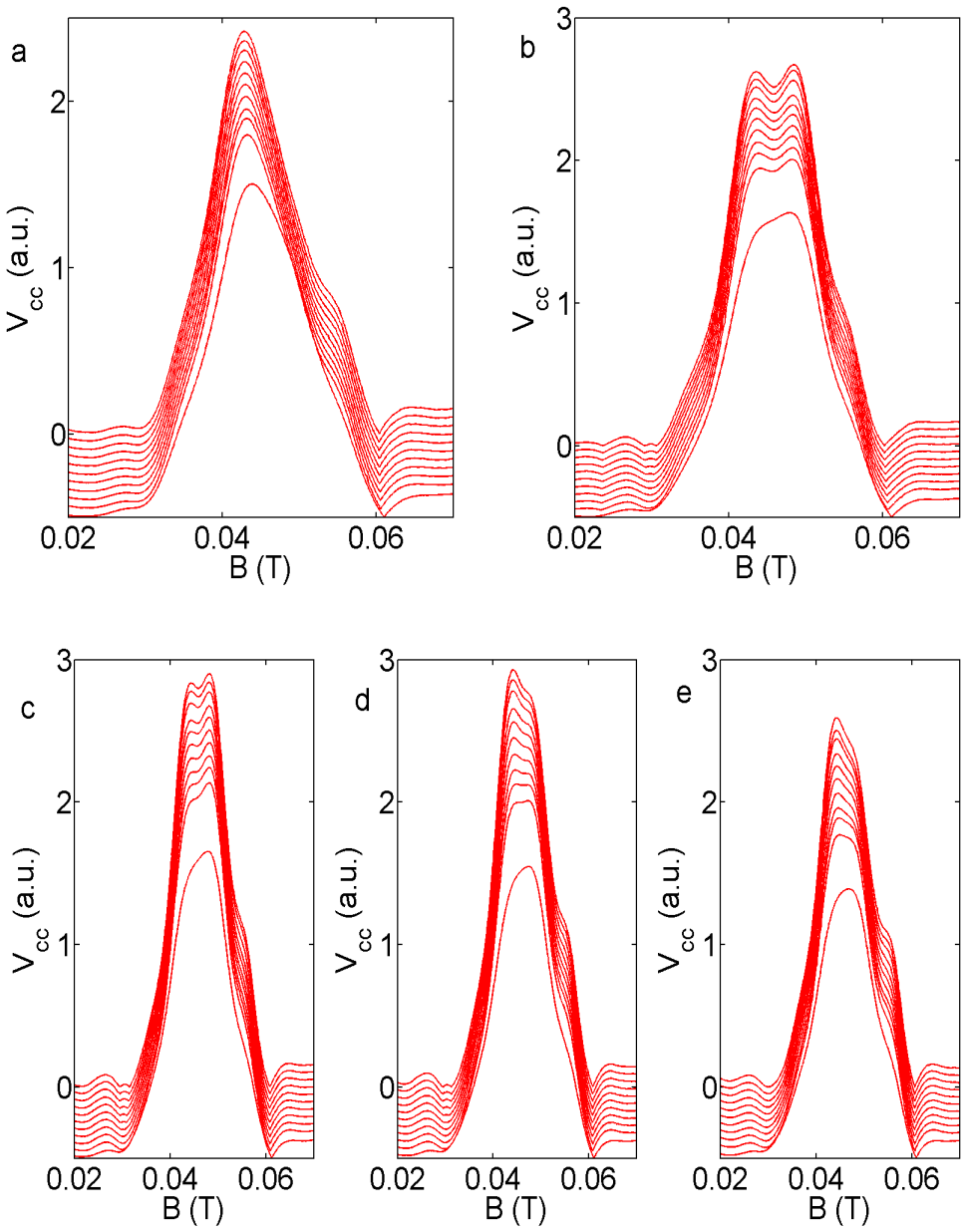

Fig. 4.12 **Temperature dependence of the focusing with a horn shape QPC. (a-e)** Injector is fixed at 0.5 G_0, G_0, 1.5 G_0, 2.0 G_0, 3.0 G_0 respectively. It is clear that sub-peaks merge into one due to thermal broadening. The top trace is the result for 70 mK while the bottom trace is for 2 K, data have been offset for clarity.

A similar result is obtained when the experiment is performed with a horn-shape injector and detector as shown in figure 4.12 for different injector conductance. It is clear that sub-peaks merge into one at high temperature due to thermal broadening. Meanwhile, it is also worthy of noticing the splitting is pronounced up to 1.1 K (second last trace in figure 4.12 (b)) for the lower conductance value while it is already not visible at around 1.0 K (third last trace in figure 4.12 (d) and (e)) for the higher injector conductance. This suggests that the energy difference between the two spin branches reduces when the conductance increases and this agrees with prediction from density-dependent spin gap model[46, 47].

4.8 Varying adiabaticity of the injector

There is one crucial problem remaining: why was similar splitting is not observed previously in n-type GaAs even in presence of strong in-plane magnetic field[97] where spin splitting of 1D subbands and 2D Fermi sphere should result in the focusing peak splitting? It is then noticed that a sharp (angled) QPC was used in previous studies[90, 96, 97], while here a rectangular QPC is used as the injector/detector. It was pointed out in an early work the adabacity of the QPC significantly affects the way 1D electrons enter into 2D regime[107], in the case of an adiabatic QPC 1D electrons enter into 2D regime without reflection at the exit of the 1D channel, on the other end, the contribution from different subbands mixed together when electrons leave the 1D channel if the QPC is non-adiabatic. The adiabaticity of QPC is naturally related to the shape of the QPC[108]. A QPC is adiabatic if the condition below is fulfilled,

$$R(x) \gg d(x) \tag{4.6}$$

where R(x) is the radius of the curvature at a given point of the confinement wall induced by the gate and d(x) is the width of constriction at the same point. In the measured device, because all the other dimension parameters are fixed the same, the R(x) and d(x) mainly depend on the shape/angle of the QPC. The constriction width d(x) is similar when the conductance is same, and therefore only the curvature R(x) matters in this case. R(x) is large when the QPC is more flat (i.e. the angle is large), e.g. without considering the potential get rounded at the corner of the gate then $R(x) \to \infty$ for 90° QPC, so that eq. (4.6) is matched and thus the QPC is adiabatic. On the other end, if QPC is sharp, R(x) is then relatively small and QPC becomes non-adiabatic. To observe the splitting of focusing peak, it requires that the contribution of the two spin-branches can remain separate rather than get mixed,

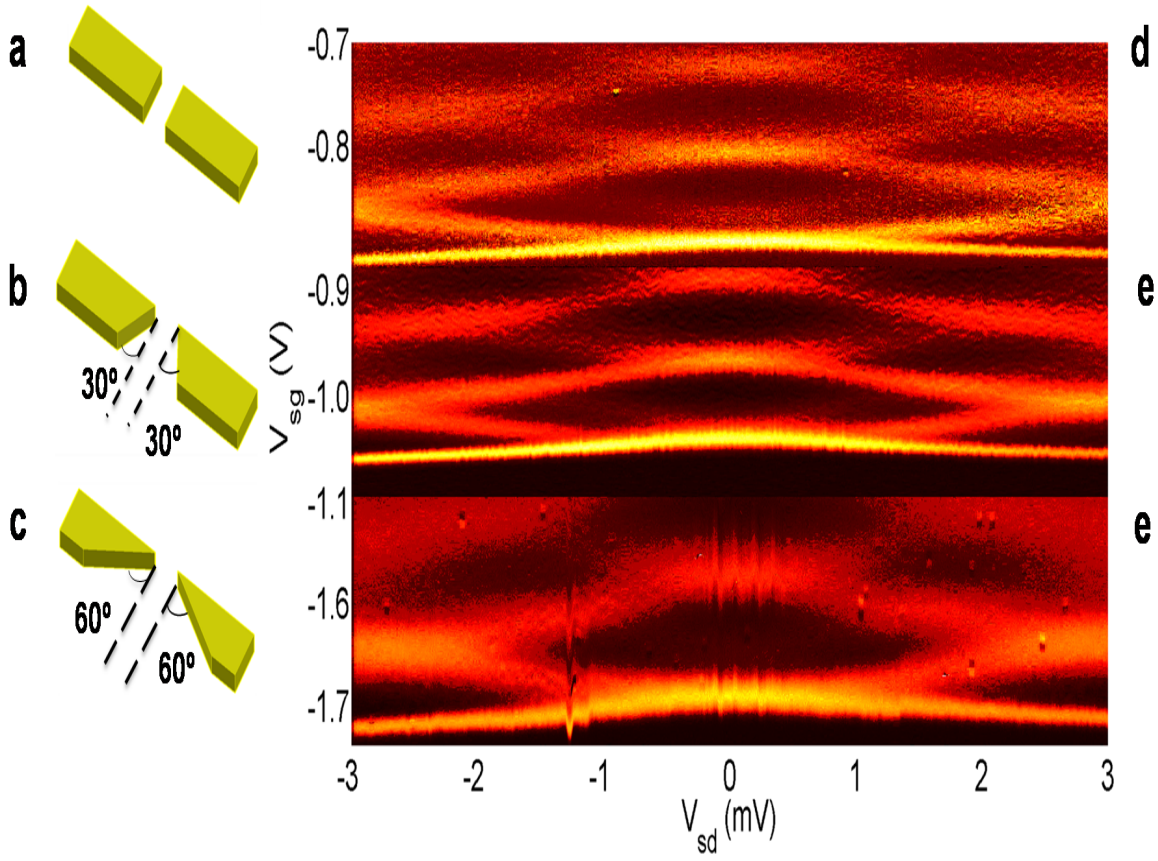

Fig. 4.13 **Different geometries of QPCs studied in the present work. a-c** show 90°, 60° and 30° shaped QPCs respectively to tune the adiabacity of the 1D channel. The width of narrow end of QPCs are kept constant at 500 nm, electrons are injected (detected) from the narrow end of injector (detector). **d-f**, colourplots of source-drain bias of the corresponding QPCs, the bright (dark) area is for high (low) transconductance, subband spacing are 3.0, 2.2 and 1.7 meV respectively.

as a result, it is expected that when the injection varies from adiabatic to non-adiabatic the splitting of the focusing peak should change accordingly (i.e. from splitting to non-splitting).

To investigate the influence of adiabaticity on focusing peak, we studied QPC with different shape (the injector and detector always take the same shape), rectangular QPC (or 90° QPC), two sharp QPCs with different angle of 60° and 30° respectively, while keeping the length of the QPC (separation between exit and entrance of the QPC) and width at the exit end of the QPC the same, so that the result is mainly affected by adiabaticity of QPC only. The schematic of the three QPCs and the corresponding source-drain bias colourplot which tells the characteristic of each QPC are present in figure 4.13. All the QPCs show

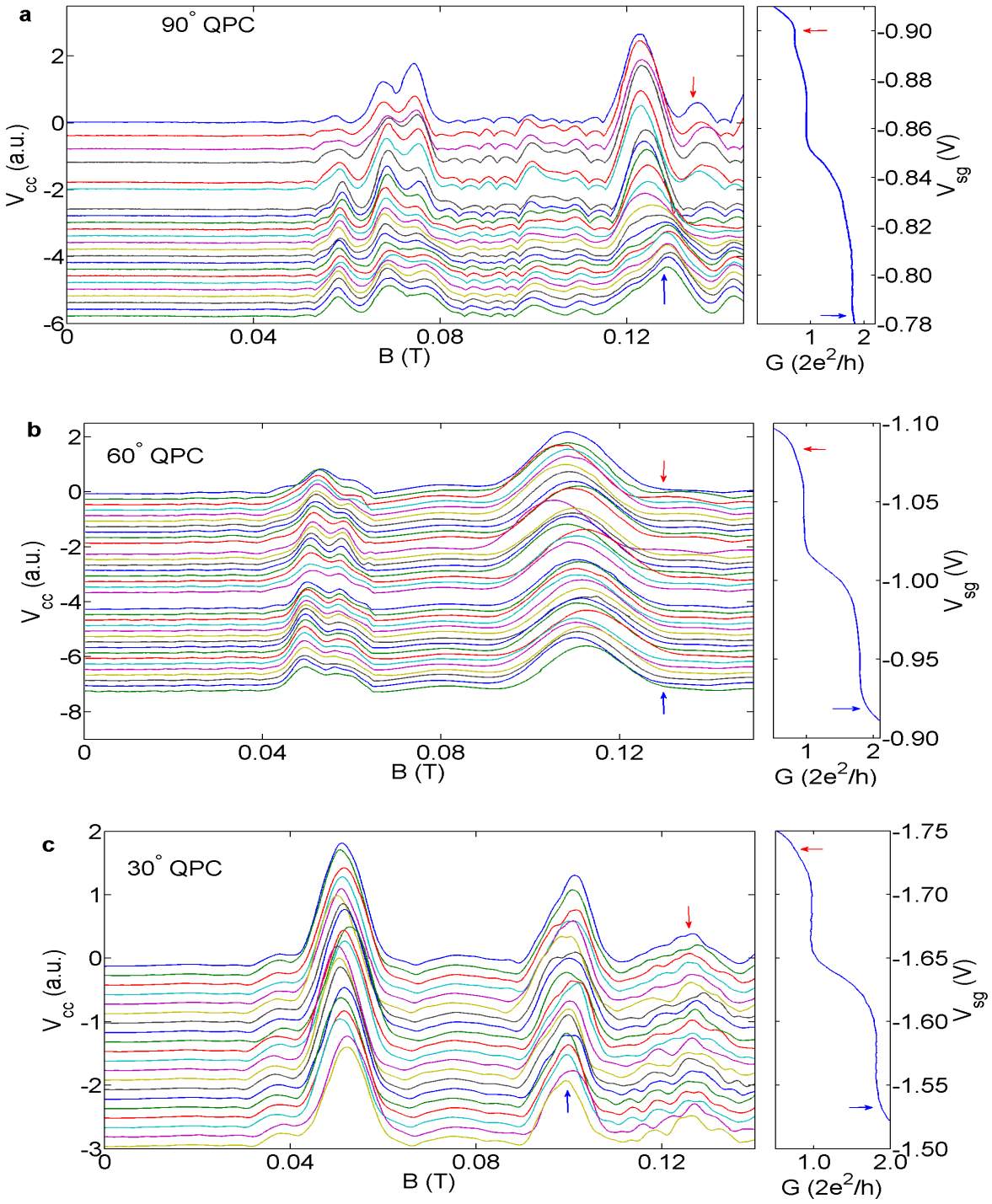

Fig. 4.14 **Transverse electron focusing of different angled QPC. a-c,** focusing result for different angled QPCs (left) and 1D characteristic of injector (right); injector conductance is tuned from 0.7 G0 (top trace, red arrow) to 2.1 G0 (bottom trace), for 90° and 60° QPCs both sub-peaks of first focusing peak are well defined while second focusing peak remains unsplit, for 30° QPC only single focusing peaks are observable. Data have been offset vertically for clarity.

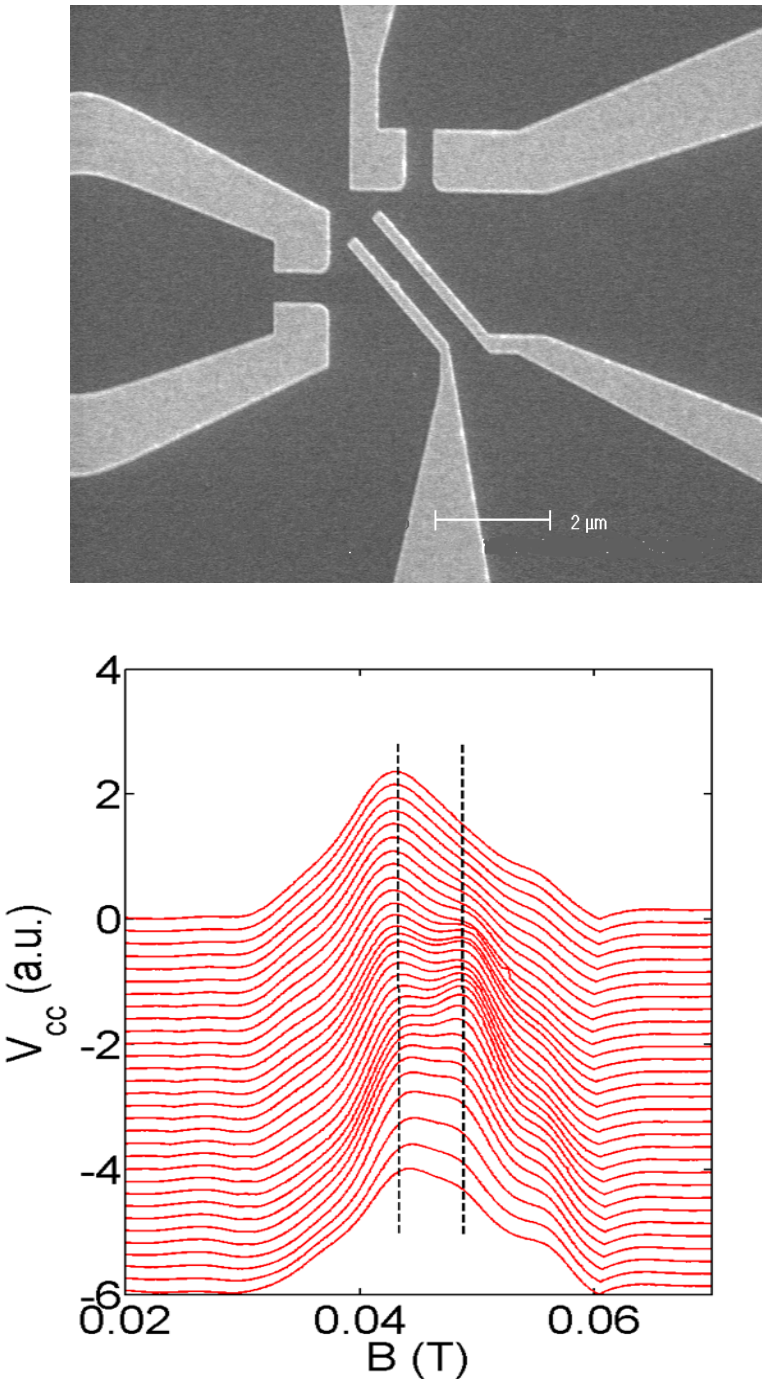

Fig. 4.15 **Transverse electron focusing of horn-shape QPC. a**, SEM image of the focusing device with horn-shape injector and detector, the flat segment of the channel is 800 nm in length and 400 nm in width, the rounded corner has a radius of 300 nm. **b**, first focusing peak at different injector conductance with detector fixed at G_0, the top trace is for injector at 0.4 G_0 where only single peak is observed and with injector slowly open up two sub-peaks are well resolved and finally merge into a broad peak at higher conductance plateau (e.g. the bottom trace is at 3 G_0). Data have been offset vertically for clarity.

well-defined conductance plateaus with a subband spacing of 3.0 (90°), 2.2 (60°) and 1.7 (30°) meV respectively.

The corresponding focusing data is shown in figure 4.14, where the injector conductance is incremented from the 0.7 structure to the end of second conductance plateau while the detector is fixed at the first conductance plateau. It is remarkable that for both 90° and 60° QPC, the first focusing peak shows a pronounced splitting while the second peak remain unsplit. On the contrary, only single peaks are observed for the 30° QPC which is in agreement with result elsewhere[90, 96, 97].

As a conclusion, experiments in this section show that the non-adiabatic injection prevents the observation of peak splitting. It should be mentioned that the angle of QPC is not the only factor that affects adiabaticity, other parameters such as width/length ratio of the QPC are equally important.

To further support the argument , a focusing device with a horn-shape injector and detector is measured and the result is shown in figure 4.15. In this experiment, the injector is swept from 0.4 G_0 to 3 G_0 with detector fixed at the first conductance plateau. It is seen that at low conductance (around 0.5 G_0) only one peak is present, with injector slowly opening up both sub-peaks become pronounced then eventually the two peaks merge into one at high conductance value (above 2 G_0). It is interesting to note that, the single peak at low conductance value aligns with one of the sub-peaks (after the peaks split out) rather than occurring in the centre of the sub-peaks, this again confirms position of sub-peaks is not affected by the injector conductance. The horn shape QPC is a typical adiabtic QPC, thus it is not surprising to see the focusing peak splitting.

4.9 Channel length dependence of focusing

The transverse electron focusing measurement is a sensitive tool to monitor spin polarization, thus it can be used to verify theoretical prediction on quasi-1D system. In this section the length dependence of spin polarization of quasi-1D channel is investigated with transverse electron focusing technique.

It is pointed that by solving the self-consistent Kohn-Sham equation which includes electrostatic confinement, Hartree, and exchange-correlation terms, spin polarization is found to be enhanced with longer channel and thereby the shape of 0.7 anomaly also changes accordingly, the 0.7 anomaly occurs at higher conductance value with shorter channel and shift towards to 0.5 G_0 with longer channel[109].

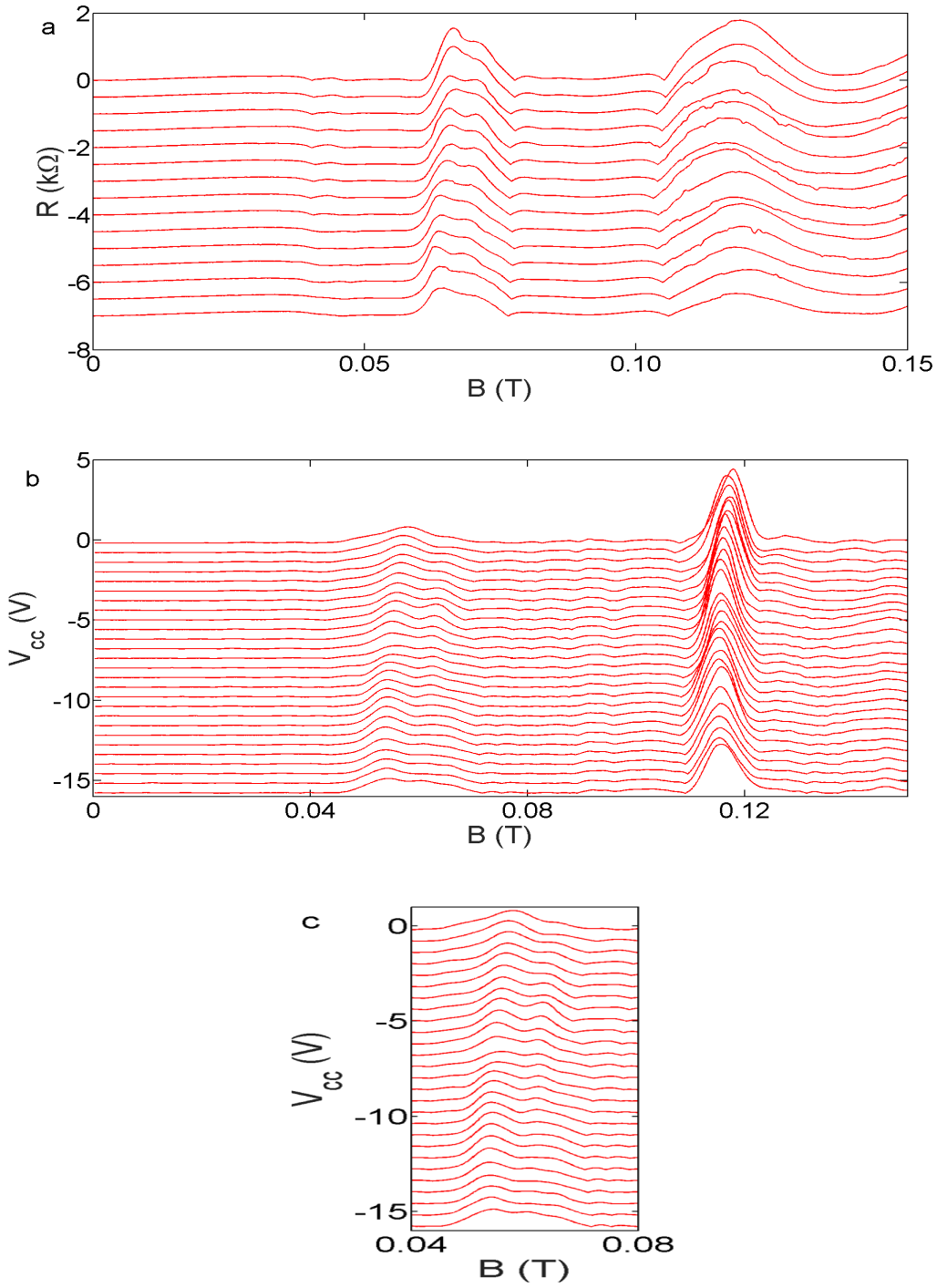

Fig. 4.16 **Channel length dependence of transverse electron focusing.** **a**, channel length is 200 nm, injector is swept from 0.7 G_0 to 2.1 G_0, splitting of first focusing peak is observed, second focusing peak remain as a single peak. **b**, , channel length is 800 nm, injector is swept from 0.6 G_0 to 2.1 G_0, splitting of first focusing peak is present, second focusing peak remain as a single peak, however, the amplitude of second peak is relatively large in this case. **c**, zoom in of first focusing peak of 800 nm QPC. Data have been offset vertically for clarity.

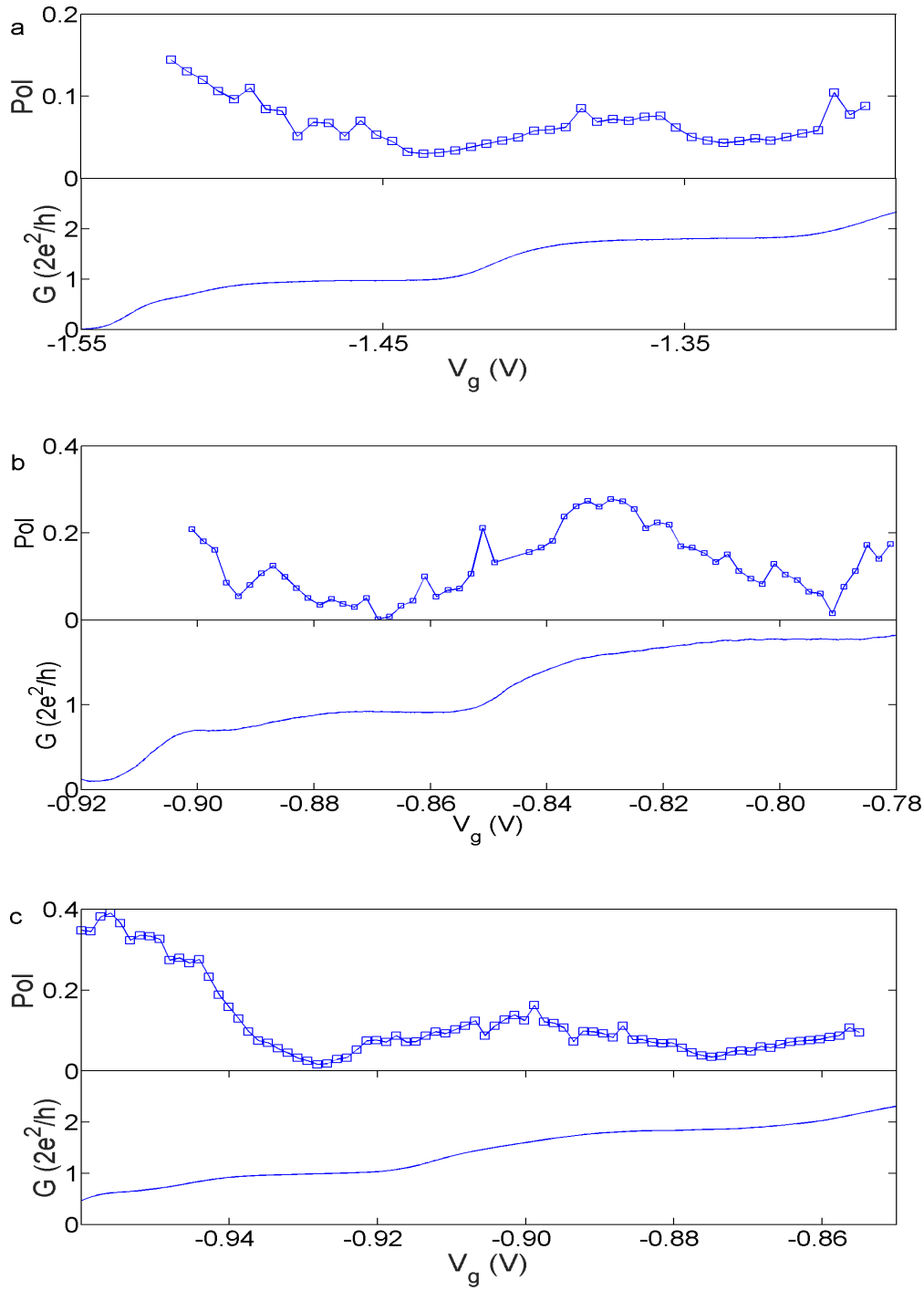

Fig. 4.17 **Channel length dependence of spin polarization.** **a-c**, spin polarization measured at different injector conductance for 200 nm, 400 nm and 800 nm QPC respectively. It is clear polarization almost drop to zero at centre of conductance plateau and become finite at elsewhere. Polarization at 0.7 G_0 is around 15%, 20% and 35 % for the three length.

In this section, QPC with lithographic lengths of 200 nm, 400 nm and 800 nm are studied and the width of the devices is fixed at 400 nm. Injector and detector are with same dimension. It ought to be pointed out that when the quasi-1D channel forms, the effective length is actually different from the lithographic length, but generally speaking with the same lithographic width, the longer the lithographic length the longer the effective length[110]. Focusing result for 200 nm and 800 nm is present in figure 4.16 and that for 400 nm is the same as figure 4.14 (a). In all the three cases, splitting of first focusing peak are observed and the second focusing peak are always remain as a single peak. For the 800 nm QPC, the amplitude of second focusing peak is relatively large and this arises from the enhanced reflection due to the potential barrier defined in the gap between injector and detector, the reflection enhancement is not clear at the moment but we suspect it is closely related to the shape of the potential barrier.

From the asymmetry of the sub-peaks, it is straight forward to extract the spin polarization[97],

$$P = |\frac{A_H - A_L}{A_H + A_L}| \tag{4.7}$$

where A_H and A_L are the amplitude of the sub-peaks. The measured spin polarization is present in figure 4.17 for the three different length. It is clear that the spin polarization drops significantly at the centre of conductance plateau, around 5% for 200 nm QPC and less than 1 % for 400 nm and 800 nm device at first conductance plateau, and become finite elsewhere, this in agreement with theoretical prediction[42, 43, 111] . Meanwhile, the spin polarization at 0.7 G_0 is around 15%, 20% and 35 % for the three length. This is in good agreement with the proposal spin polarization increase with increasing channel length[109]. On the other hand, the shape of the 0.7 anomaly, known from the conductance measurement, changes dramatically, it is more like a shoulder structure when the channel length is 200 nm and become flat at 400 nm and 800 nm, similar to result of a recent experiment where multiple QPCs are measured within single cool down[112].

4.10 Conclusion

According to previous study the splitting of odd peaks (i.e. 1^{st} and 3^{rd}) and absence of splitting of even peaks (2^{nd}) observed in our experiment are a result of spin-orbit interaction[89, 92–94, 91], more interestingly, the energy difference between the two spin branch extracted from cyclotron energy in our device is 0.023 meV while the calculated

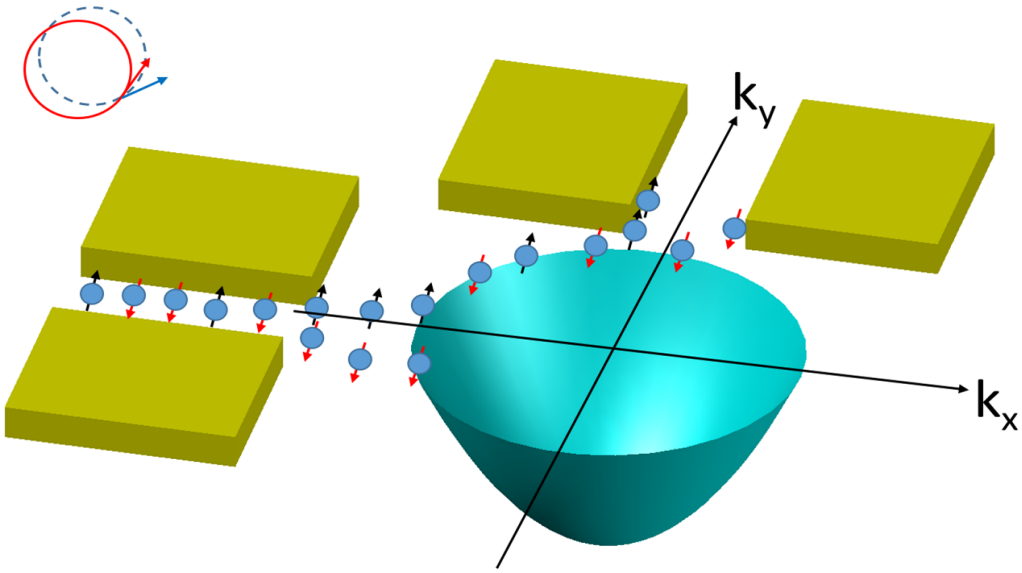

Fig. 4.18 **Schematic of electron focusing in momentum space.** The yellow bars on the left form the injector while those on the top form the detector. The cyan cone represents the Fermi surface. The blue rigid balls are electrons while the black and arrows represent electron spin. Electrons are partially polarized in the 1D channel, spin-up and spin-down electrons which posses different k_x and k_y component are thus injected to different positions of Fermi surface and then enter detector from different positions of Fermi surface accordingly. Inset, spatial separated trajectory of spin-up and spin-down electrons due to difference in k_x and k_y component, the arrows show the direction of momentum at the vicinity of exist of injector.

value from Dresselhaus SOI[113]

$$\Delta E = \beta(-\sigma_x p_x + \sigma_y p_y) \tag{4.8}$$

where σ is the Pauli matrix and p is the momentum, by using spin-orbit parameter $\beta = 1.7 \times 10^{-13}$ eVm extracted from a similar heterojunction[114], is 0.022 meV. It seems that the result presented here can be understood from SOI, however, SOI of 2DEG should not be influenced by the shape of injector.

In an earlier electron-spin resonance work, it was observed that the zero field splitting attributed to SOI depends on spin polarization (more precisely, depends on filling factor of Landau level) with the largest splitting at zero magnetic field 0.033 meV[115, 116]. Therefore, we suggests a similar dependence of SOI on spin polarization leads to the result here. Partial polarized electrons injected from an adiabatic QPC will enter different points of 2D Fermi surface according to the spin orientation, thereby giving two streams of fully

polarized electrons as shown in figure 4.18. It is necessary to emphasize that the total spin polarization is the imbalance between the two streams. A relatively large SOI can be obtained for each stream. Meanwhile, although the total spin polarization itself can be tuned by injector conductance, as long as the two streams are separated they are fully polarized and gives a constant SOI. On the hand, if the injection is non-adiabatic, the two streams emerge into single stream when they enter the 2DEG, the SOI is determined by real spin polarization and thus expected to be small.

The reason why the SOI can be tuned via spin polarization needs more study, we think this may be attributed to the dynamic nuclear spin polarization[117]. Previous experiments indicated that nuclear spin can be polarized via hyperfine interaction and highly sensitive to electron polarization and once it is polarized due to the long relaxation time (over 10 mS)[118] it would almost remain as constant during electron propagating from injector to detector (in the order of 10 pS). In our experiment, if the injection is adiabatic, the fully polarized electron streams lead to larger hyperfine interaction and therefore result in larger nuclear spin polarization. A small nuclear spin polarization is achieved if the injection is non-adiabatic.

Other mechanisms including strain field induced SOI[119] may also contribute to the focusing peak splitting observed here and it needs further investigation.

In conclusion, we present a transverse electron focusing in n-type GaAs heterojunction. In addition to well resolved focusing peaks, the first peak splits into two and this splitting is proved to arise from SOI where strength of SOI is tuned by the adiabatic condition of electron injection. Different aspects of focusing have been studied systemically and found to be consistent with earlier work. With the same setup we also demonstrate a high efficiency spin filter. The main observations are summarized below:

(I) Splitting of odd numbered (1st, 3rd) focusing peaks is observed in n-type GaAs;

(II) The splitting is found to be enhanced by in-plane magnetic field and therefore is proved to be spin related;

(III) The splitting is sensitive to the shape of the injector QPC;

(IV) The spin polarization extracted from the asymmetry of the sub-peaks of first focusing peak depends on the length of the 1D channel, this suggests that exchange interaction is likely the reason of the observed spin polarization;

(V) The spin polarization can be modulated by a beam splitter which acts as a spin filter, a spin polarization of 50% can be achieved;

(VI) The source-drain bias and temperature dependence data support the density-dependent spin-gap model in a 1D constriction.

Chapter 5

Interference effects in a tunable open-cavity-reflector quantum integrated system

5.1 Introduction

Quantum interference, one of the most remarkable effects of quantum mechanics, arising from the wave nature of particles has led to some of the most celebrated results in mescoscopic systems, including weak localization in two dimensional (2D) systems[61–63], Aharonov-Bohm oscillations in ring structures[64–66], sharp peaks in magnetoresistance in a chaotic cavity[67, 68] etc. Among its various applications, quantum interference has been used successfully as a tool to investigate properties of particles such as monitoring correlation and entanglement as demonstrated in the Mach-Zehnder interferometer[69, 70], the Aharonov-Bohm interferometer[71, 72] and the Hanbury Brown-Twiss interferometer[73, 74], and highlighting differences between Fermions and Bosons with the electronic analogue of a Hong-Ou-Mandel device[75, 76]. Among all the striking phenomenon, it is particularly interesting to note that quantum interference is extremely suitable for studying coupling between different quantum systems[77–79] which is crucial for the design of integrated quantum circuits.

A notable quantum mechanical system is a ballistic quantum wire, often called a quantum point contact (QPC), defined using a pair of split gates[84, 85] on a semiconductor heterostructure. Soon after the first observation of quantised conductance in a quasi-one-dimensional (1D) quantum wire[84, 85], a number of novel interesting observations have

been made such as the '0.7 structure'[120], the incipient Wigner lattice[121, 122] and coherent electron focusing[123, 90] etc. However, due to the restrictions of the transmission measurement, it is relatively hard to investigate the 1D property without distorting the system and thus difficult to form a comprehensive understanding of these issues. Therefore it is natural to transfer the 1D property into other information which is easier to measure.

In previous study, coupling between a QPC and a waveguide was investigated demonstrating that each 1D subband of the QPC gives a well-defined peak in the waveguide spectrum[77] via the coupling effect. The importance of such a measurement is that what measured is the waveguide state and thus the quasi-1D states are unaffected by the measurement, and yet the quasi-1D state can still be monitored via the peaks in waveguide spectrum. Later on, the coupling between two QPCs was studied in a similar way, and it was striking to note that when one of the QPCs was swept (the so called swept-QPC) to the near pinch-off regime, an anomalous modulation of conductance of the other QPC was observed and the shape of the modulation resembled a Fano resonance[79]. Such a modulation is only observable when the conductance of the swept-QPC is below the last conductance plateau and thus the authors argued that it supported the existence of bound state in the QPC. In a recent work which was performed with a quantum dot (QD) and a specially designed electronic cavity[78], it has shown that the coupling between the QD and cavity can be used to detect the fine variation in the ground state of the QD, such as the orientation of spin, via the shape change of Coulomb resonance peaks after the switching on of the cavity.

These successes motivate us to utilize the coupling between different quantum systems and to detect and analyse properties of quasi-1D systems via measuring the change in coupling arising from the reconfiguration of electron states, alternatively speaking the change of density of states (DOS).

5.2 Device design and characteristics

Fano resonances which arise from the quantum interference between discrete (bound) states of one medium to the continuum states of a neighbouring medium resulting in asymmetry in resonance structures[124], is one of the definite tools to monitor quantum interference particularly in systems with smaller length scales and tunable electron path. Hence it is suitable to realize the idea mentioned in the previous section. Here we present one such system using an integrated quantum circuit having three components: a coherent source of electrons (emitted by a QPC); a continuum state (an electronic cavity of 2D electrons); and a reflector (a potential barrier to reflect collimated electrons). Such an ensemble would allow

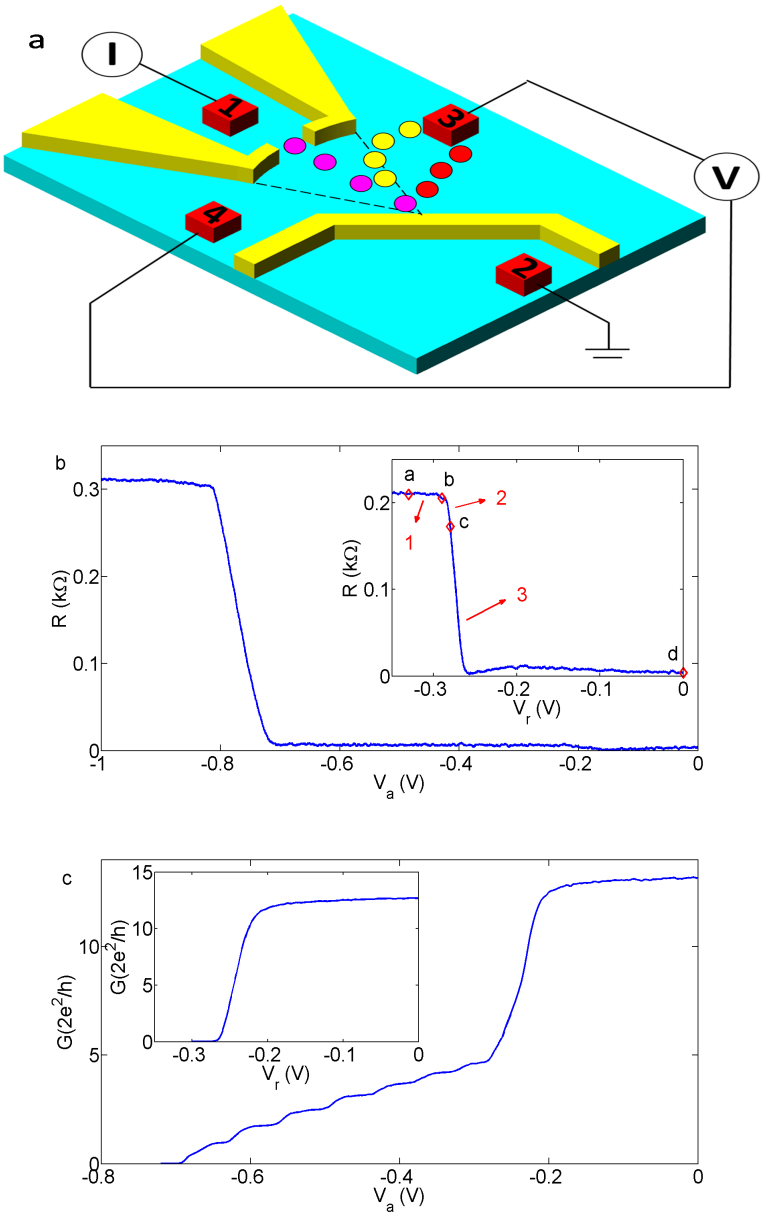

Fig. 5.1 **Device characteristic and experiment setup. a**, schematic of the device, the yellow blocks are metallic gates and red squares are Ohmics; excitation current is fed to Ohmic 1 while 2 is grounded, Ohmics 3 and 4 are voltage probes. The opening angle of the arch is 45° and the radius (also the distance between arch-gate and reflector) is 1.5 μm, both the length and width of the QPC embedded in the arch is 200 nm, the length of inclined surface of the reflector is 3.0 μm and the width is 300 nm. **b**, $R_{12,34}$ of the arch-shaped QPC (blue trace) and the reflector (red trace). Four regimes are identified from the reflector voltage characteristic and labelled as regime 1 (a-b), regime 2 (b-c), regime 3 (c-d) and regime 4 (d-e). **c**, Differential conductance measurement of the QPC (blue trace) and reflector (red trace). It may be noticed from these curves that 1D and 2D electrons behave differently.

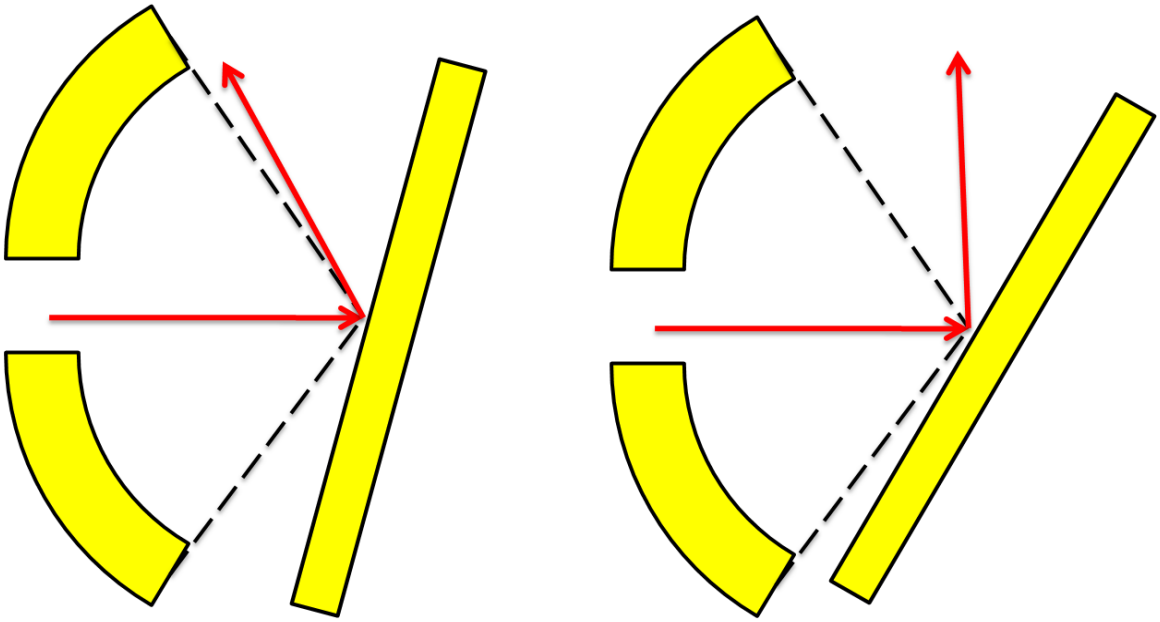

Fig. 5.2 **Schematic highlights the influence of the inclined angle of the reflector.** The red arrow shows the semi-classical trajectory of the injected electron beams. For the 75° inclined reflector (left panel), the major branch of the reflected electrons is close to the edge of the cavity (marked by the dashed black line), thus get a high probability of entering the cavity. For the 45° inclined reflector (right panel), the reflected electrons are far away from the edge of the cavity and hence it is unlikely for them to populate the cavity state.

a beam of 1D electron to interference constructively and destructively with the continuum states of the cavity after being reflected by the potential barrier, resulting in the observation of a Fano resonance.

The samples studied in the present work consisting of a pair of arch-shaped gates, with a QPC forming in the centre of the arch, and a reflector inclined at 75° against the current flow direction such that centre of the QPC and the reflector are aligned as shown in figure 5.1 (a). The opening angle of the cavity is 45°. These quantum discrete devices were fabricated on a high mobility two-dimensional electron gas formed at the interface of GaAs/$Al_{0.33}Ga_{0.67}As$ heterostructure. The measured electron density was $1.80\times10^{11}cm^{-2}$ and mobility was $2.1\times10^{6}cm^{2}V^{-1}s^{-1}$ therefore both mean free path l and phase coherence length l_{ϕ} were over 10 μm which is much larger than the distance between the QPC and reflector (1.5 μm), thus it guarantees electrons still have a high probability of remaining coherent even after multiple reflection in the cavity. All the measurements were performed with standard lock-in technique in a cryofree dilution refrigerator with an electron temperature of 70 mK unless specified. For four terminal resistance measurement a 10 nA at 77 Hz ac current is applied while 10 μV at 77 Hz voltage is used for two terminal conductance measurement.

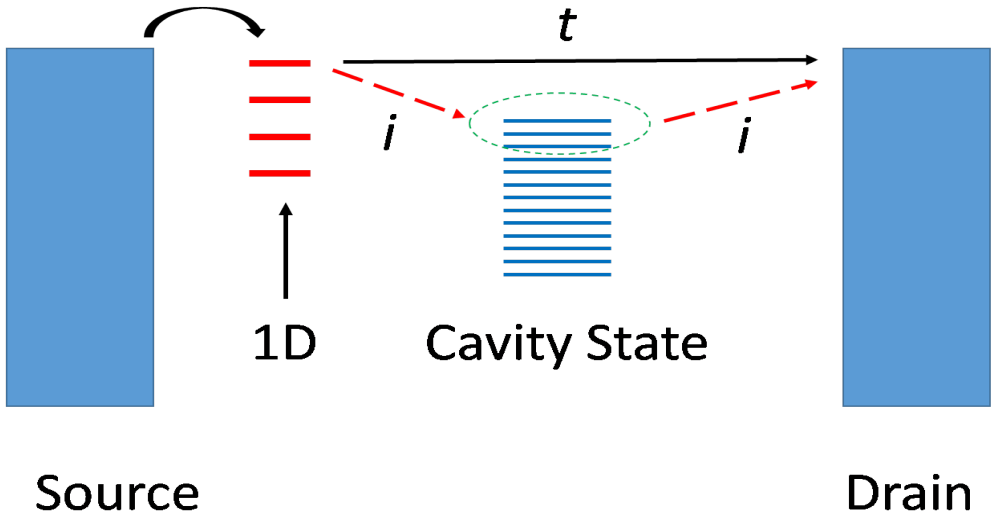

Fig. 5.3 **Schematic for two route interference.** energy diagram of the transport through the cavity-reflector system, electrons from source (Ohmic 1) occupy 1D states in the injector QPC and then get injected to drain (Ohmic 3) either through the route *t* (black solid arrow) without being modulated by cavity states or route *i* (red dashed arrow) with modulation. 1D state, e.g. the upper most one, selectively couples to energy matched cavity states (the bundles highlighted by dashed ellipse).

When operated separately the arch-QPC and reflector show trivial behaviour. Figure 5.1 (b) and (c) show the four terminal resistance $R_{12,34} = V_{34}/I_{12}$ (denoted as R in the rest part of the thesis) and the corresponding two-terminal conductance of the arch-QPC and reflector against gate voltage V_g, respectively. The measured resistance is almost 0 before the 2DEG under the gates is fully depleted ($V_a >$ - 0.70 V for arch-gate and $V_r >$ - 0.25 V for reflector) because electrons have equal probability to accumulate at Ohmics 3 and 4, followed by a sharp rising and then a saturation in the pinch-off regime. It is helpful to emphasize here that the longitudinal resistance $R_{12,12} = V_{12}/I_{12}$ shows the trivial resistance quantization and it shoots up to infinity (data is not shown here) in the pinch-off regime. Four regimes identified from the characteristic of the reflector are labelled as regime 1-4 as shown in figure 5.1 (a) and the behaviour of the system in these four regimes will be discussed in detail in next section. Conductance characteristic of the QPC shows well defined conductance plateaus from which the 1D modes can be identified (e.g. the first conductance plateau $\frac{2e^2}{h}$ is referred as mode 1), on the other hand the conductance of the reflector drops around - 0.2 V which indicates a sharp change in the transmission probability.

Before moving to the main result of the experiment, it is necessary to discuss the importance of the inclined angle of the reflector. Injected electrons from the QPC, treated

as electron beams in the semi-classical picture, get reflected by the reflector if the applied reflector voltage is sufficiently negative. The inclined angle of the reflector determines the probability of electrons entering the cavity after the reflection as shown in figure 5.2. In the first case, the inclined angle is suitably large (e.g. 75° in our design), the major branch of the reflected electrons is outside the cavity but close to the edge of cavity, considering the usual ±20° angular distribution of electrons from QPC[125], some of these electrons will propagate to Ohmic 3 directly (refer to figure 5.1 (a)) while the others enter the cavity and populate cavity states. This will lead to the two-route interference as shown in figure 5.3. However, it is also necessary to avoid making the inclined angle too large (take 90° as an example), otherwise the majority of electrons would be reflected into the QPC and thus perturbs electron configuration in the QPC. On the other hand, if the inclined angle is small, the major branch of the reflected electrons would be far away from the edge of cavity and then get mirror chance of being trapped in the cavity as shown in right panel of figure 5.2, in this case it might be difficult to get the two-route interference.

5.3 Modulation of resistance $R_{12,34}$ due to electronic cavity

When the arch-QPC and reflector are operated together, collimated ballistic electrons[125] injected from the QPC are reflected by the potential barrier created by the reflector and lead to a voltage drop V_{34} between Ohmics 3 and 4 because the inclined reflector prefers the electrons accumulate at Ohmic 3, such that

$$V_{34} \propto n \times r \tag{5.1}$$

where n is the number of injected electron and r is the reflection probability. Meanwhile, V_{34} and hence $R_{12,34}$ is further modulated due to the formation of the electronic cavity, and such modulation is the main result of this chapter. In this section, results at both 1.5 K and 70 mK will be presented and analysed.

5.3.1 Result at 1.5 K

The results shown in figure 5.4 (a)-(d) are taken from four regimes of the reflector voltage (see figure 5.1 (b)) respectively measured at 1.5 K. It is apparent the result changes dramatically from regime 1 to regime 4.

In regime 1 where the reflector voltage V_r is swept from - 0.33 V (top trace) to - 0.31 V (bottom trace), a pronounced asymmetric resonance structure is observed, which shows a

peak at more negative arch-QPC voltage V_a and valley at less negative end, this structure centres around V_a= - 0.2 V which is also the centre of 1D to 2D transition regime of the arch-QPC. When the arch-QPC is tuned into quasi-1D regime (- 0.7 V $\leq V_a \leq$ - 0.2 V), some weak oscillations are present.

When reflector is set to regime 2, V_r is from - 0.31 to - 0.29 V (top to bottom), the asymmetric resonance structure gradually alters into a broad shoulder structure, meanwhile the oscillations smear out, and a dip slowly forms around the pinch-off regime of the QPC. Unlike in regime 1 where the background signal in quasi-1D regime remains flat regardless of V_r, it is seen that the background increases against reducing V_a at less negative V_r (bottom trace). The reason for the change of background ground signal will be explained in the next subsection.

In regime 3 (- 0.29 V $\leq V_a \leq$ - 0.27 V), the intensity of both the shoulder structure and the dip around pinch-off decrease with less negative reflector voltage, meanwhile the up-going background signal in the quasi-1D regime gradually flattens out with increasing reflector voltage (top to bottom) . All the features smear out in regime 4.

5.3.2 Result at 70 mK

The results shown in figure 5.5 (a)-(d) are taken for the four regimes of the reflector voltage respectively measured at 70 mK. The four regimes show some common behaviour, when arch-gate voltage V_a is swept between 0 to - 0.2 V which is the 2D regime (refer to figure 5.1(c)) the measured resistance is almost zero due to the diffusive nature of the 2D electrons, such that electrons have equal probability to accumulate at Ohmic 3 and 4, when V_a is more negative than - 0.7 V, i.e. in the pinch-off regime of the QPC, the resistance shoots up and then saturates. When the arch-QPC is operated in quasi-1D regime (- 0.7 V $\leq V_a \leq$ - 0.2 V), we observe interesting interference pattern in various regimes of V_r which we will discuss in detail.

In the quasi-1D regime of the arch-QPC, when reflector voltage V_r is incremented from - 0.33 V (bottom trace) to - 0.31 V (top trace) i.e. regime 1, we first see a pronounced double peak structure when V_a is tuned from - 0.2 V to around - 0.3 V, the peak at - 0.24 V (denoted as peak I) has larger intensity than the neighbouring peak at - 0.21 V (peak II). Interestingly the position of the double-peak structure coincides with the 1D-2D transition regime of the QPC. When the quasi-1D channel forms in the QPC (for - 0.7 V $\leq V_a \leq$ - 0.3 V), the resistance reduces monotonically when V_a becomes more negative. This reduction in resistance can be explained by the fact the potential barrier in this regime is sufficiently high

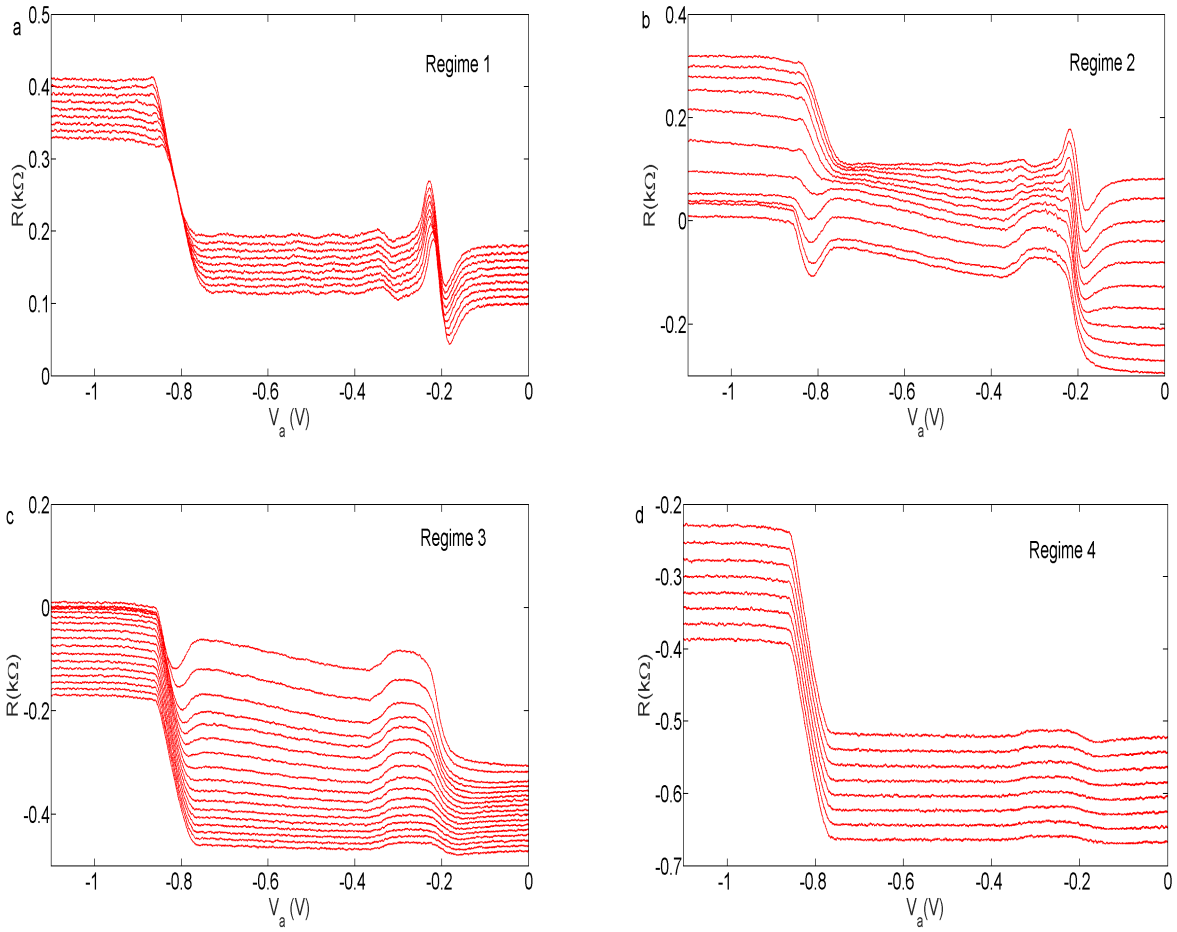

Fig. 5.4 ***R* as a function of arch-QPC voltage for various V_r at 1.5 K. a**, result in regime 1, a strong asymmetry resonance structure, a peak at more negative V_a and valley at less negative end, is observed around - 0.2 V which is the definition point of arch-QPC, while weak oscillation pattern is visible in the quasi-1D regime of QPC. **b**, result in regime 2, the asymmetry resonance structure alters into a broad shoulder structure while the oscillation smear out, a dip gradually forms around the pinch-off regime. **c**, result in regime 3, intensity of both the shoulder structure and dip around pinch-off decreases with less negative reflector voltage. **d**, result in regime 4, all the structures smear out. Data in plot a-d have been offset vertically for clarity and top trace in each plot (a-d) is for the most negative reflector voltage.

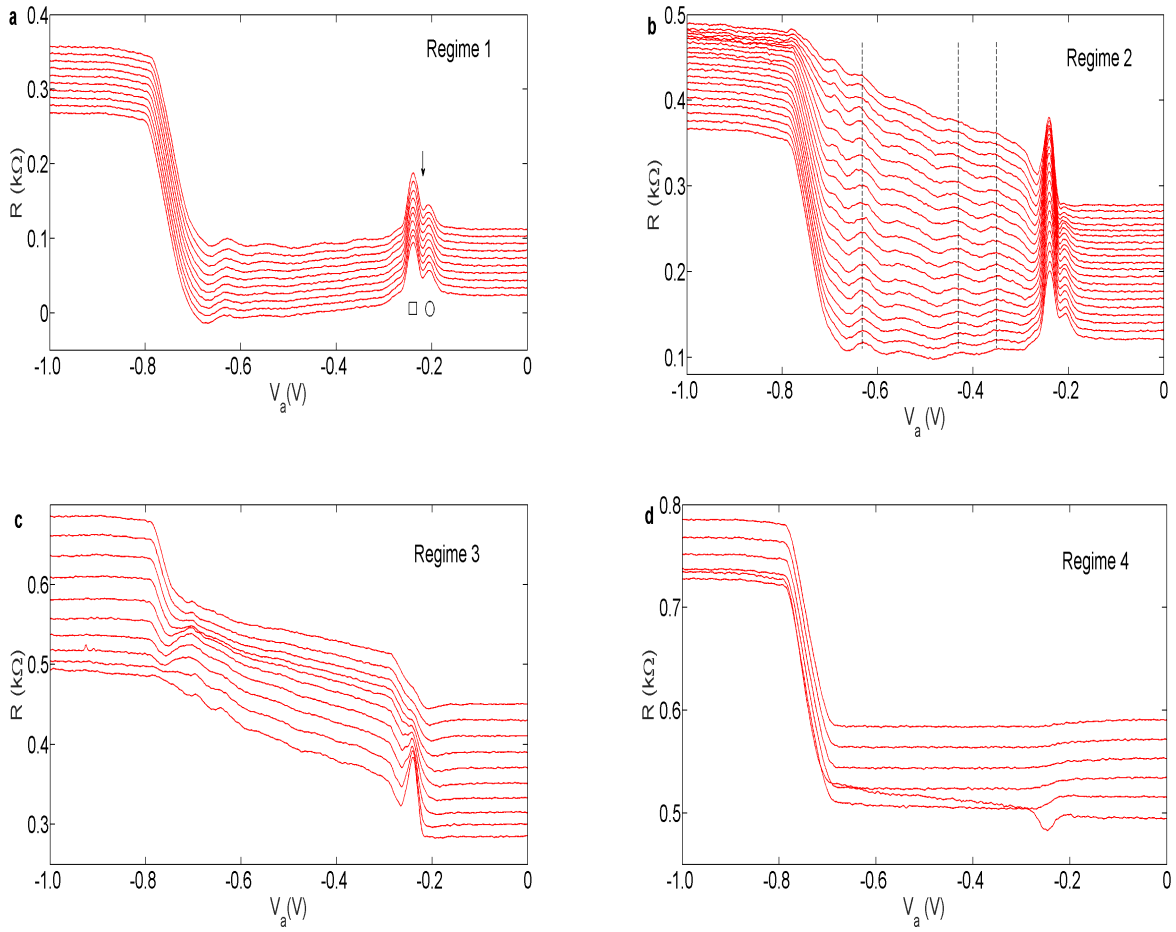

Fig. 5.5 ***R* as a function of arch-QPC voltage for various V_r at 70 mK. a**, result in regime 1, a pronounced double-peak structure is observed as indicated by an arrow when arch-gate voltage V_a is around -0.2 V, peak at - 0.24 V is referred as Peak I (denoted by square) and peak at - 0.21 V is peak II (denoted by circle). **b**, result in regime 2, in addition to the double peak structure, fine oscillations, highlighted by the vertical dash line, occur when arch-QPC forms a quasi-1D channel. **c**, result in regime 3, both the double-peak structure and fine oscillations weaken in this regime. **d**, result in regime 4, all the structures smear out. Data in plot a-d have been offset vertically for clarity and bottom trace in each plot (a-d) is for the most negative reflector voltage.

so that the reflection probability is unity and V_{34} only depends on n (electron population), n decreases against more negative V_a as less 1D subbands are available with decreasing gate voltage.

In regime 2, V_r is swept from - 0.31 to - 0.29 V (bottom to top) , the double-peak structure is still clearly visible, however, peak II weakens gradually when V_r become less negative while peak I is fairly robust in this regime. It is necessary to emphasize the position of double peak structure is insensitive to V_r in both regime 1 and 2. Apart from the double peak structure, some signatures of fine oscillations strengthen and become observable in the quasi-1D regime of the QPC indicated by the dotted lines in figure 5.5(b). Meanwhile, an evolution of background in 1D regime is also noticed, the resistance reduces against V_a at most negative reflector voltage (bottom trace in 5.5(b)) while other way round at less negative reflector voltage (top trace in same plot), this evolution is a direct result of competition between n and r, large V_a reduces n meanwhile it enhances reflection probability r by reducing averaged momentum $< k_x >$ (x is the direction of current flow, y is the direction of confinement in the QPC), by simplifying the problem as tunnelling through a 1D barrier, the smaller $< k_x >$ results in less transmission probability through the reflector and thus increases r.

In regime 3 (V_r is tuned from - 0.29 to - 0.27 V) where the transmission probability changes dramatically from small value to unity (as seen in figure 5.1 (a)) , peak II of double peak structure finally vanishes and the intensity of peak I also decreases rapidly. Similarly the fine oscillations gradually become invisible when V_r become less negative. In this regime the background signal follow the same trend, i.e. it increases against decreasing V_a, and this suggests the dependence of reflection probability of r on $< k_x >$ is the dominated mechanism on deciding imbalance between chemical potential μ_3 and μ_4. All the features finally smear out in regime in regime 1 and the result is self-consistent with that obtained when arch-QPC is measured individually.

To understand the origin of the double-peak structure and fine oscillations we start with regime 2 where both the features are present. Position of fine oscillations in regime 2 is almost fixed regardless of reflector voltage V_r and this is more apparent in the colourplot in figure 5.6 (a) where the regions of red/yellow are of large resistance (peak) and regions which are blue are of low resistance (valley).

The fine oscillation is only observable in the quasi-1D regime of arch-QPC, thus it is natural to compare a typical result in regime 2, for which the reflector voltage V_r is fixed at -0.3 V, with the conductance plot of QPC as shown in figure 5.6 (b) to find out the relation between the oscillation and 1D mode. It is interesting to note that the fine oscillations almost

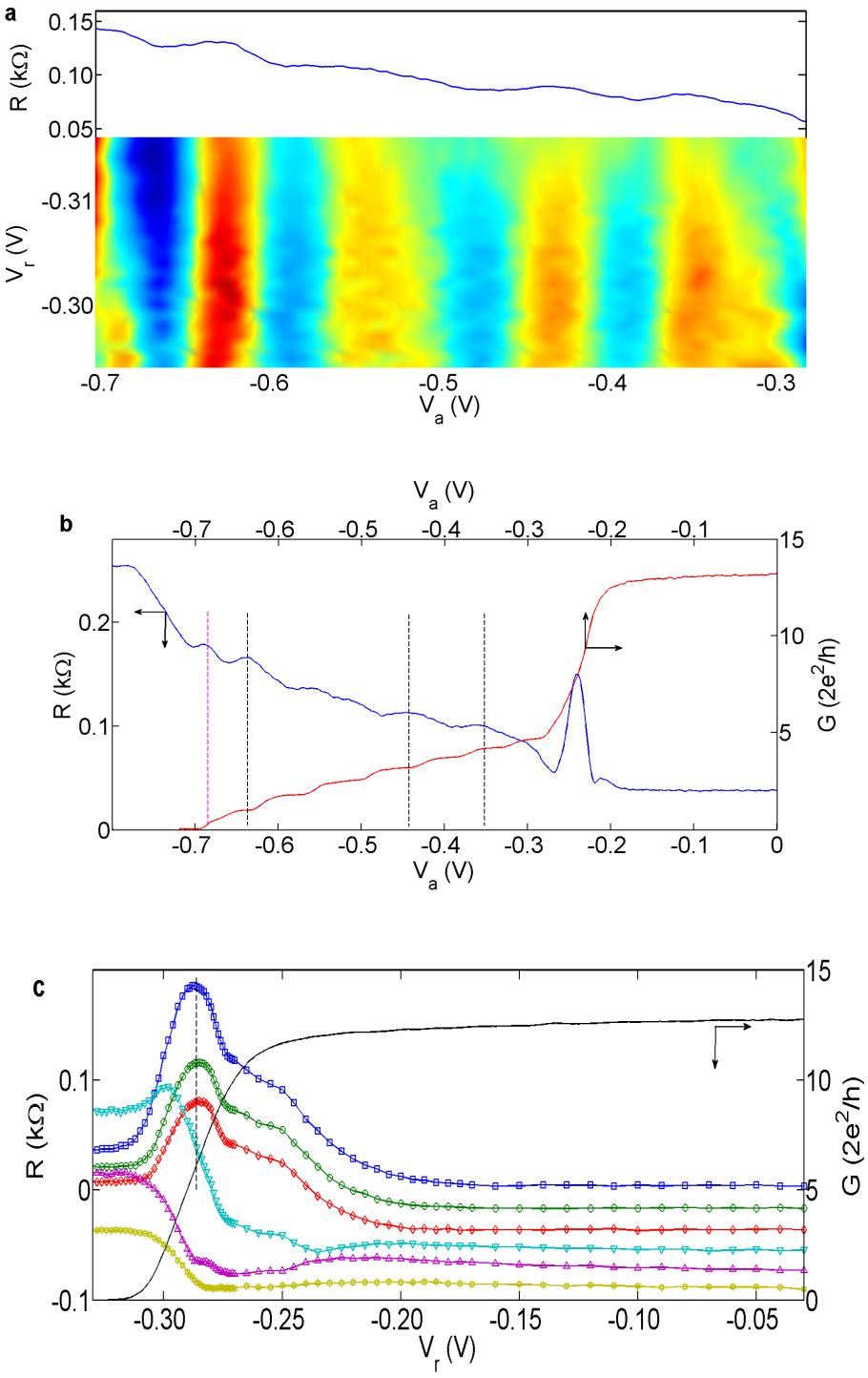

Fig. 5.6 **Correlation between *R* and conductance of arch-QPC**. **a**, colour plot of fine structures in regime 2, here the regions of red/yellow are of large resistance (peak) and regions which are blue are of low resistance (valley). A typical trace in regime 2 (V_r = - 0.3 V) is chosen as a guide to eye. **b**, a representative non-local resistance in regime 2 (blue trace, same as that in (a)) and conductance trace of QPC (red trace), the fine oscillations almost align with conductance plateaus while the structure around - 0.7 V associates with 0.7 anomaly as highlighted by a magenta dotted line. The other dotted lines are guide to the eye for correlation. **c**, the arch gate voltage is fixed at -0.63 (□), - 0.43 (◯), - 0.36 (♢), - 0.24 (▽), - 0.21 (△) and 0 V (⋆) while sweeping reflector voltage, data have been offset vertically for clarity.

align with conductance plateaus similar to that reported in the tunnelling spectroscopy of waveguide[77, 126], meanwhile the 0.7 structure also gives a pronounced peak. However, unlike the results in the waveguide experiment[77, 126] where each subband contributes to a rather sharp peak, the oscillation pattern in our experiment is quite broad, in addition there are no well resolved peaks for conductance plateaus at - 0.6 V (2^{nd} mode) and - 0.5 V (3^{rd} mode). Besides, the double-peak structure in the 1D-2D transition regime has no analogue in the waveguide structure[126–128]. Another issue, which may be more important, is simple that the model baed on the correlation between fine oscillations and 1D-density of states (DOS) cannot explain the strong sensitivity of the additional structures on reflector voltage because in our device the reflected electrons do not interfere with injected electrons directly because they are spatially separated.

In our system, considering the relatively large distance between arch-gate and reflector it is unlikely to get a waveguide, however, we could visualise our system as an electronic cavity[78], having its states filled up to chemical potential, which is defined with arch-gate and reflector. Due to the arch-shape, the distance between any point on the arch and the focal point of the cavity is the same and thereby the energy level, alternatively speaking the cavity state, has a uniform distribution in the cavity. When the electrons under the gates are depleted and thus the cavity is switched on, the 1D states can couple to cavity states and give rise to the observed non-trivial features.

The framework above can be verified by changing coupling between 1D and cavity states. A strong coupling will result in appearance of fine oscillations while at weak coupling they will smear out.

The coupling can be tuned by both arch-QPC voltage V_a and reflector voltage V_r, however, it is worthy of noticing that V_a affects both the 1D and cavity state thus makes the problem complicated while V_r only influences the cavity state, hence we fix the arch-QPC voltage at -0.63, - 0.43, - 0.36 (these three voltages are the centre of fine oscillations, as indicated by the vertical lines in figure 5.5 (b)), - 0.24 (Peak I), - 0.21 (Peak II) and 0 V and sweep the reflector voltage for the ease of discussion.

The result shown in figure 5.6 (c) is a direct measurement of strength and visibility of the coupling effect. When arch-gate voltage is fixed the number of injected electrons n in eq. (5.1) is constant, so the measured resistance depends on reflection probability r only; r increases monotonically when V_r becomes more negative, therefore resistance R should follow a similar monotonic change. The bottom two traces in figure 5.6 (c) are for arch-QPC voltages V_a, 0 and - 0.21 V respectively (cavity is off). The results match well with the semi-classical picture. The resistance is initially almost constant when reflector

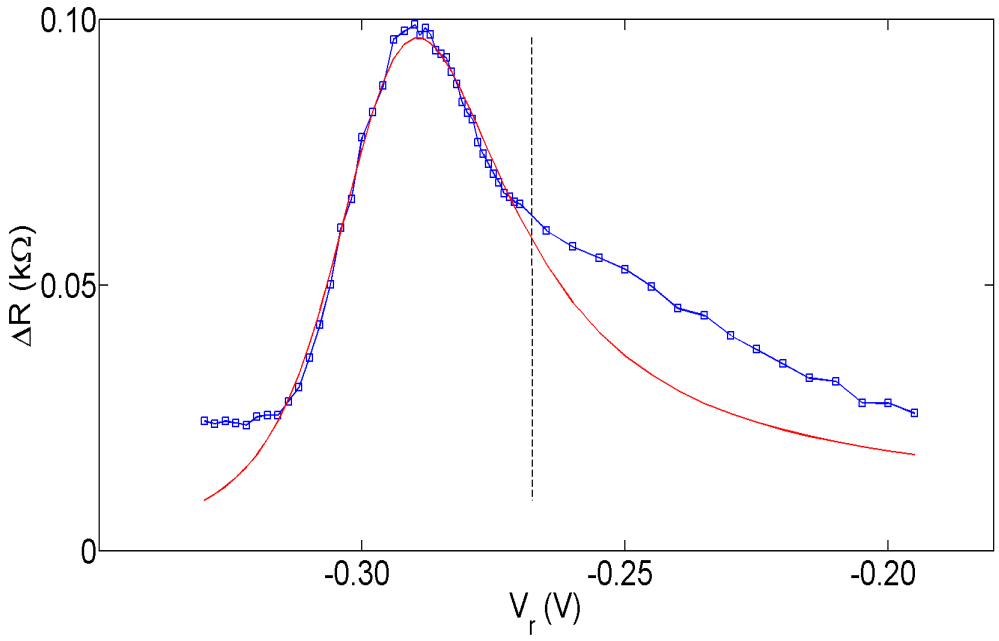

Fig. 5.7 **Fano resonance against reflector voltage.** Theoretical fitting of $\Delta R(V_r,V_a)$ = $R(V_r,V_a)$ - $R(V_r,0)$, where V_r = -0.63 V is taken as an example, after switching on the cavity (indicated by the vertical dotted line) ΔR follows a well defined Fano line shape. The Fano factor q is 1.57.

voltage $V_r > -0.25$ V, then a sharp rise in resistance occurs simultaneously when reflector conductance drops where reflection probability r increases rapidly, and then saturates when r becomes unity. When we make arch-QPC more negative (top four traces, cavity turns on), the resistance initially keeps on increasing and then drops down until it saturates, and thereby results in a pronounced peak in the plot. It is necessary to emphasize the voltage range (from - 0.28 to - 0.31 V) where the peak in resistance occurs corresponds to regime 2 where the fine oscillations are most pronounced. The dramatic change between different traces is a clear indication of the effect of the cavity. Once the cavity is on, i.e. both V_a and V_r are sufficiently negative, its size and therefore the energy spacing of cavity states can be adjusted by sweeping reflector voltage. When the cavity states and 1D states get aligned, the strong coupling between 1D and cavity leads to a peak in the measurement. Peak in figure 5.6 (c) means the corresponding feature in figure 5.5 is more visible, hence it supports the argument that strong coupling results in pronounced features.

An analysis of the line shape of peak in 5.6 (c) clearly indicate after the cavity is switched on, the dynamic $\Delta R(V_r,V_a) = R(V_a,V_a) - R(V_r,0)$ follows the well known Fano resonance arising from the interference between a discrete state and continuum[124] as shown in figure

5.7, formulated as

$$\sigma = \frac{(\varepsilon + q)^2}{\varepsilon^2 + 1} \tag{5.2}$$

where ε denotes the energy scale for a given problem and q is the asymmetry parameter which describes transition probabilities to the mixed state and to the continuum. In our device the 1D states are naturally discrete while the cavity can be treated as a continuum due to the small energy spacing between different cavity states, thus Fano resonance provide a direct evidence on the coupling/interference between 1D and cavity states.

The energy spacing between different cavity states is small (of the order of 100 μeV, from Ref. [78]) due to the large size of cavity which results in each 1D-state may couple to several cavity states and thus results in the relatively broad fine oscillations rather than sharp peaks observed in waveguide experiment[77] , on the other hand, the single pattern arise from 2^{nd} (V_a = -0.6 V) and 3^{rd} mode (V_a = - 0.5 V) of the QPC (see figure 5.6 (b)) can be explained by different modes of QPC couple to same cavity states and get hybridized. Moreover, it is also reported that intersubband transition probability can be enhanced[129] in these devices and thus results in mixed states.

Equipped with the cavity state, it is straightforward to understand the reason why the fine oscillations appear in regime 1 at 1.5 K while they occur in regime 2 at 70 mK. In the considered problem here, the thermal energy k_BT is more crucial to the energy spacing in the cavity rather than the quasi-1D channel, thus to make the cavity state resolvable at higher temperature, it thus require larger energy spacing and thereby smaller size of cavity, which in turn means more negative reflector voltage. The detail temperature dependence will be discussed later.

5.4 Effect of transverse magnetic field

An applied transverse magnetic field will modify the trajectory of injected electrons and affects *R* dramatically. First, the probability of electrons entering the cavity is magnetic field dependent. Second, the cavity states, which represent the quantization of standing waves in the cavity, are highly dependent on the trajectory of electrons, with large magnetic field, the electrons in the cavity become more localized and therefore coupling between 1D and cavity state are weakened. Third, perpendicular magnetic field also leads to a reduction of phase coherence length and thereby weakens the interference effect[63]. As a consequence, the fine oscillations arising from coupling between cavity and 1D states should also be field sensitive[77].

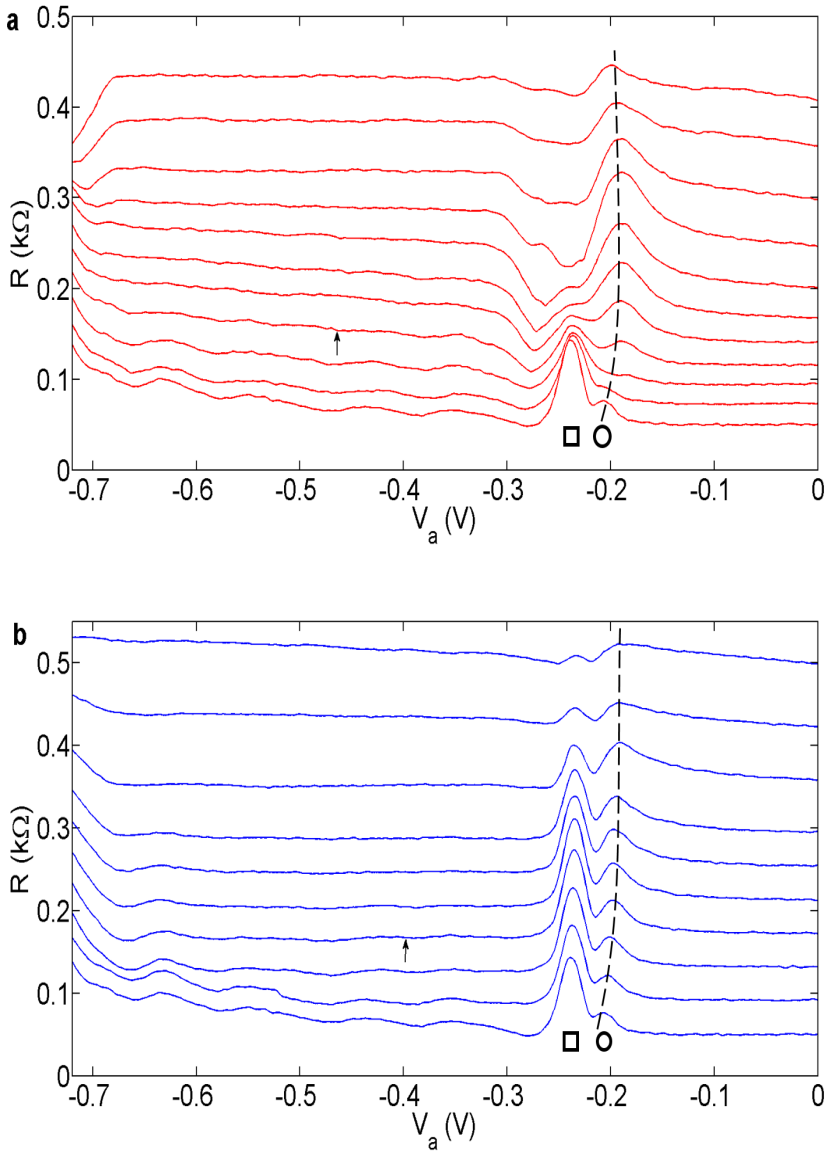

Fig. 5.8 **Effect of perpendicular magnetic field.** **a**, the evolution of R against negative magnetic field. The field is increased from 0 (bottom trace) to - 200 mT (top trace) by - 20 mT. It is clear that the fine oscillations disappear around - 60 mT (marked by an arrow), peak I of the double-peak structure (marked by the square) weakens with increasing field while peak II (marked by the circle) is enhanced by magnetic field and shifts towards less negative V_a as indicated by a dashed black curve. **b**, the evolution against positive magnetic field, fine oscillations show a similar behaviour (disappear at 60 mT) as in (a); the double-peak follow the same trend as its negative field counterpart, however, the rate at which the peak intensity is reducing is slower than the data shown in (a).

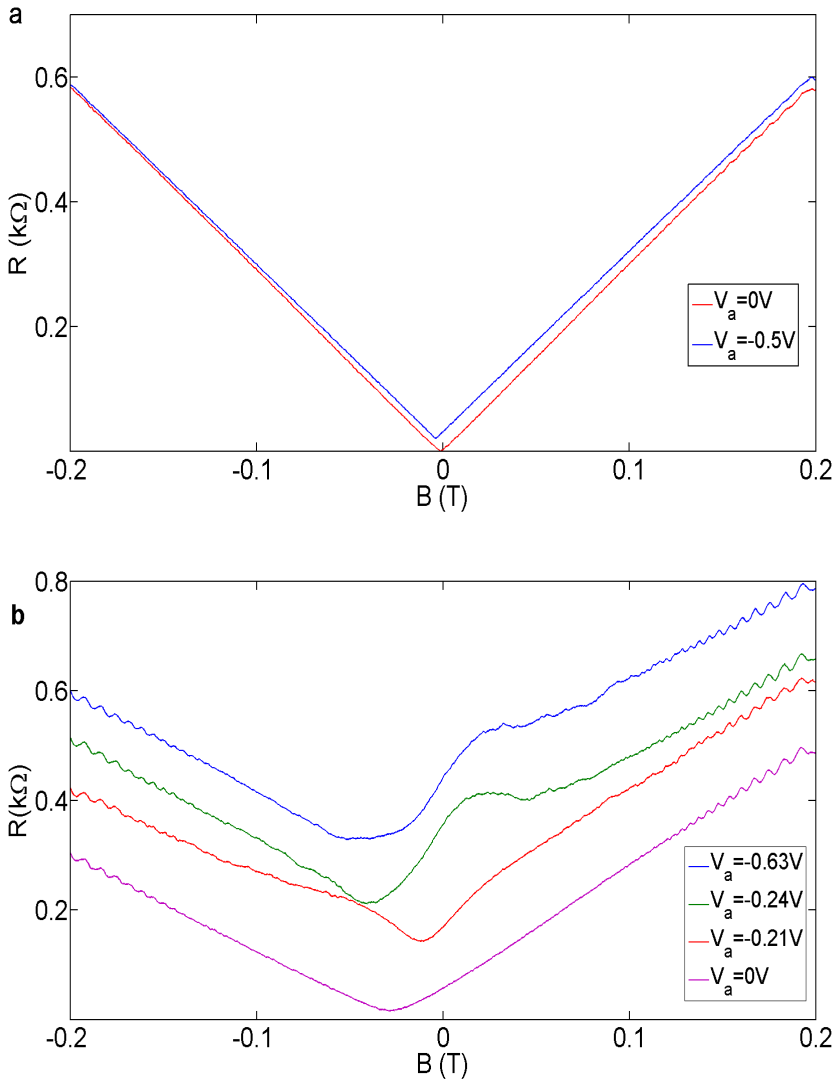

Fig. 5.9 **Magneto resistance of the arch-QPC with reflector assembly.** **a**, the reflector is grounded; the results show a typical Hall voltage development as the magnetic field is swept for different QPC voltage. **b**, reflector is set to - 0.3 V, QPC voltage V_a is set at - 0.63 (fine oscillation), - 0.24 (peak I), - 0.20 (peak II) and 0 V respectively, magnetoresistance becomes quite asymmetric which highlights the role of the reflector. Data have been offset vertically for clarity.

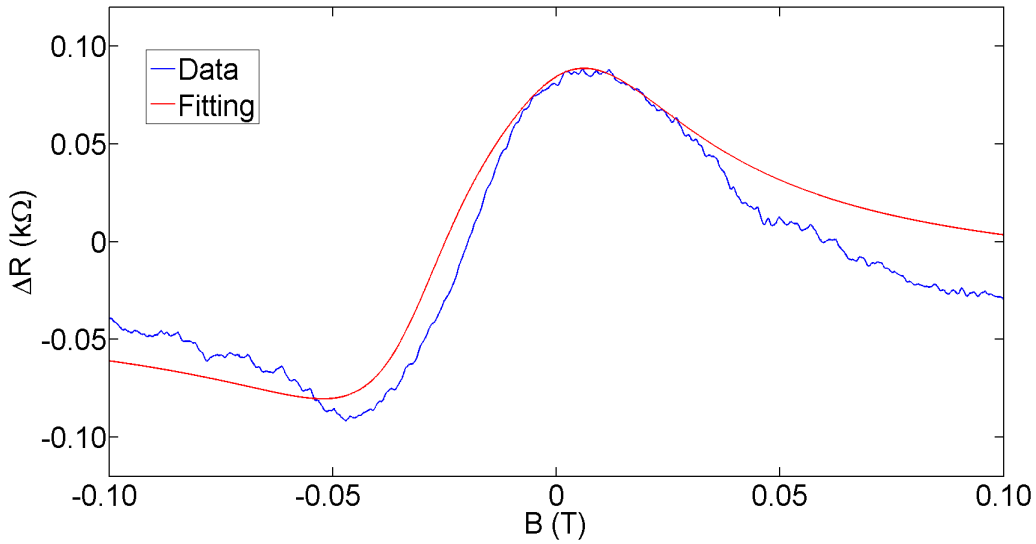

Fig. 5.10 **Fano line shape against magnetic field .** Theoretical fitting of $\Delta R(V_a,B)$ = $R(V_a,B)$ - R(0,B) where V_a = -0.24 V, the dynamic resembles a clear Fano line shape. Fano factor q is 1.17.

In figure 5.8 (a) and (b), we show both negative and positive perpendicular magnetic field dependence of data in figure 5.6 (b) . Is clear that the fine oscillations smear out at a weak field of $\pm$ 60 mT, it is necessary to mention the conductance of the arch-QPC is almost unaffected by the small field, thus it ensures the smearing out is a consequence related to the cavity state solely. The double-peak structure (in 1D-2D transition regime) follows a more complicated trend, the intensity of peak I (marked by a square) is reduced by increasing field but it survives at much higher field compared to the fine structures (- 120 mT at negative field end and 200 mT at positive end), on the contrary, peak II (marked by a circle) is enhanced by magnetic field. It can be noticed that there is a difference in the rate at which intensity of peaks slows down from negative field to positive field, this can be attributed to the fact the inclined reflector prefers electrons going to Ohmic 3, and negative field also favors Ohmic 3 therefore the influence of reflector and magnetic field adds together while positive field makes electron accumulate at Ohmic 4 hence reflector and field compete with each other. In addition, peak II shift towards to less negative V_a while peak I always occurs at same V_a regardless of magnetic field.

Although the reason for the shift of peak I needs more study, it clearly indicates the distinction between 1D and 2D electrons. Here we propose a possible explanation for the shift. Considering peak I actually occurs at the beginning of 1D-2D transition regime, it may have the contribution from electrons which tunnel underneath the gate (because the

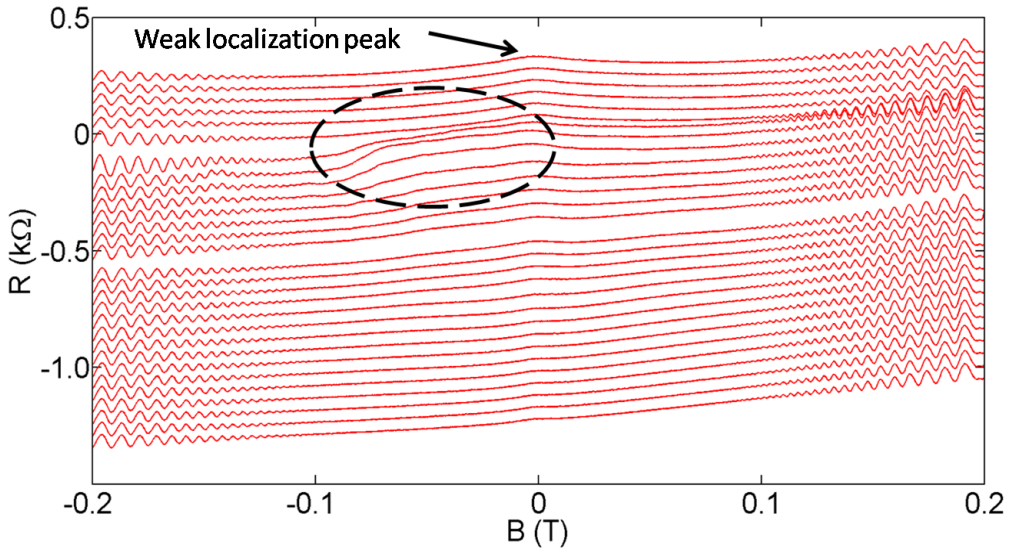

Fig. 5.11 **Magnetoresistance as a function of relfector voltage near pinch-off regime .** The data have been offset vertically for clarity, the top is most negative reflector voltage and the bottom is the zero reflector voltage. At both large and small reflector voltage, the result resembles typical weak localization behaviour. In the medium reflector voltage a broad shoulder structure is present in the negative field regime.

electron under the gate is only partially depleted) in addition to those through the channel, and this effectively broad the distribution angle of injected electrons. The applied magnetic field applies additional confinement, i.e. it tries to squeeze the wavefunction and hence the electron-electron interaction should be enhanced with electrons become more concentrated, however, electrons tend to keep the same distribution to reduce electron-electron interaction, thus requiring to release the electronic confinement (which in turn means less negative V_a). As a result, peak I shift to less negative V_a where the electronic confinement is weaker. On the other hand, tunnelling probability underneath the gate is reduced considerably at the gate voltage corresponding to peak II, the angular distribution of injected electron is mainly decided by the width of conducting channel and insensitive to the applied small magnetic field, thus peak I always occurs at same position.

A detail magnetoresistance study is presented in figure 5.9. When the reflector is grounded, a typical Hall voltage development is seen for both V_a = 0 V where QPC is in 2D regime and V_a = - 0.5 V when quasi-1D channel forms in the QPC as seen in figure 5.9 (a). This is line width the fact the experiment setup is typically used to measure Hall voltage. In figure 5.9 (b), a voltage of - 0.3 V is applied to reflector, when arch-gate voltage is 0 V and - 0.20 V (cavity is not formed) the result is almost similar to that in figure 5.9

(a), however, SdH oscillations are seen in the large field regime which come from the contribution of the reflected electrons. The slight shift of the minimum of the magnetoresistance can be attributed to the competition between the magnetic field and reflector mentioned previously. When cavity is switched on (V_a = - 0.24 V or - 0.63 V), additional structures highly asymmetry against magnetic field are observed in the small field regime up to $\pm$ 70 mT, i.e. same field value where fine oscillations quenched in figure 5.8. A pronounced peak forms at the positive field end while a dip is observed in the negative field end. In the large field regime a superposition of Hall voltage and SdH oscillations is visible. It is interesting to note in the large field regime the background Hall voltage measured at all the four arch-QPC voltage is almost parallel to each other, this also suggest the typical 2D behaviour instead of cavity related mechanism become dominant in this regime.

The dynamics in resistance with cavity switched on, e.g. green trace in figure 5.9(b), defined as $\Delta R(V_a,B) = R(V_a, B) - R(0, B)$, also resembles a well defined Fano resonance. Figure 5.10 shows a consistent theoretical fitting of $\Delta R(-0.24\ V, B)$ (corresponding to green trace in figure 5.9 (b)) with Fano resonance. The experimental result diverges from the fitting curve around $\pm$ 60 mT, this is in good agreement with fact 'fine oscillation' smears out at the same field value which suggests the coupling between 1D and cavity states are significantly reduced. The self-consistency between reflector (figure 5.7) and magnetic field (figure 5.10) induced Fano resonance proves that we can tune the coupling both electrically and magnetically.

Another noticeable result, although not directly related to the coupling between 1D and cavity state, is the magnetoresistance performed in the pinch-off regime of the arch-QPC as shown in figure 5.11. It is seen that when reflector voltage is either quite negative or close to zero, the result shows typical weak localization (WL) behaviour, the WL peak is more pronounced at larger reflector voltage end (e.g. the top trace). In the medium reflector voltage, a broad shoulder structure become observable only at negative field side, the reason for such behaviour need further investigation.

5.5 Temperature dependence

Temperature dependence is also a useful tool to investigate quantum effect such as the origin of the fine oscillations and double-peak structure. As mentioned previously, the energy spacing for cavity states is an order of magnitude smaller than the 1D subband spacing in the QPC, a slightly higher temperature makes the cavity states become a continuum while 1D subbands are still well resolved. The thermal smearing of the cavity states in turn leads to

smear out of the fine oscillations. In this section we will show the temperature dependence data in both low temperature regime and high temperature regime respectively because the mechanism involved in may change quite dramatically.

5.5.1 Low temperature regime

Figure 5.12 shows the evolution of the fine oscillations in the range of 70 mK to 1.8 K, it is clear that the fine oscillations smear out at 1.8 K where conductance plateaus of QPC still persists. Interestingly, a change of gradient of the background signal in quasi-1D regime is also observed, i.e. although the trend is the same, the increasing rate of R against arch-QPC voltage is much smaller at higher temperature, this can be attributed to the thermal broadening of $< k_X >$.

The double-peak structure is a consequence of interference effect according to the previous discussion. Unlike the fine oscillations, the double-peak structure is present even at 1.8 K, however, its intensity decreases against rising temperature. Meanwhile, it is noticeable that peak I is more temperature sensitive than peak II, this again suggests the two two peaks have different microscopic origin. Nevertheless, the intensity of peak I can be expressed by[130]

$$R \propto exp(-l/l_\phi) \tag{5.3}$$

, where l is electron propagation length and l_ϕ is the phase coherence length, and the temperature dependence of phase coherence length l_ϕ is ,

$$l_\phi \propto \sqrt{T^{-p}} \tag{5.4}$$

where $p = 1$ for 2D system[131] and $p = \frac{2}{3}$ for 1D system[132]. In our device $p = 1$ gives the best fitting as shown in figure 5.12 (b). To avoid confusion, it ought to be mentioned that the fitting here is performed against $\Delta R(T) = R(V_a, T) - R(0, T)$ to minimise the contribution of background signal which may be also temperature dependent.

The fact p=1 gives the best fitting agrees well with the premise that the interference mainly occurs in the 2D cavity. Meanwhile, the phase coherence length (15 μm at base temperature) extracted from the fitting is much larger than the device size, and this in turn ensures the validity of eq.(5.3).

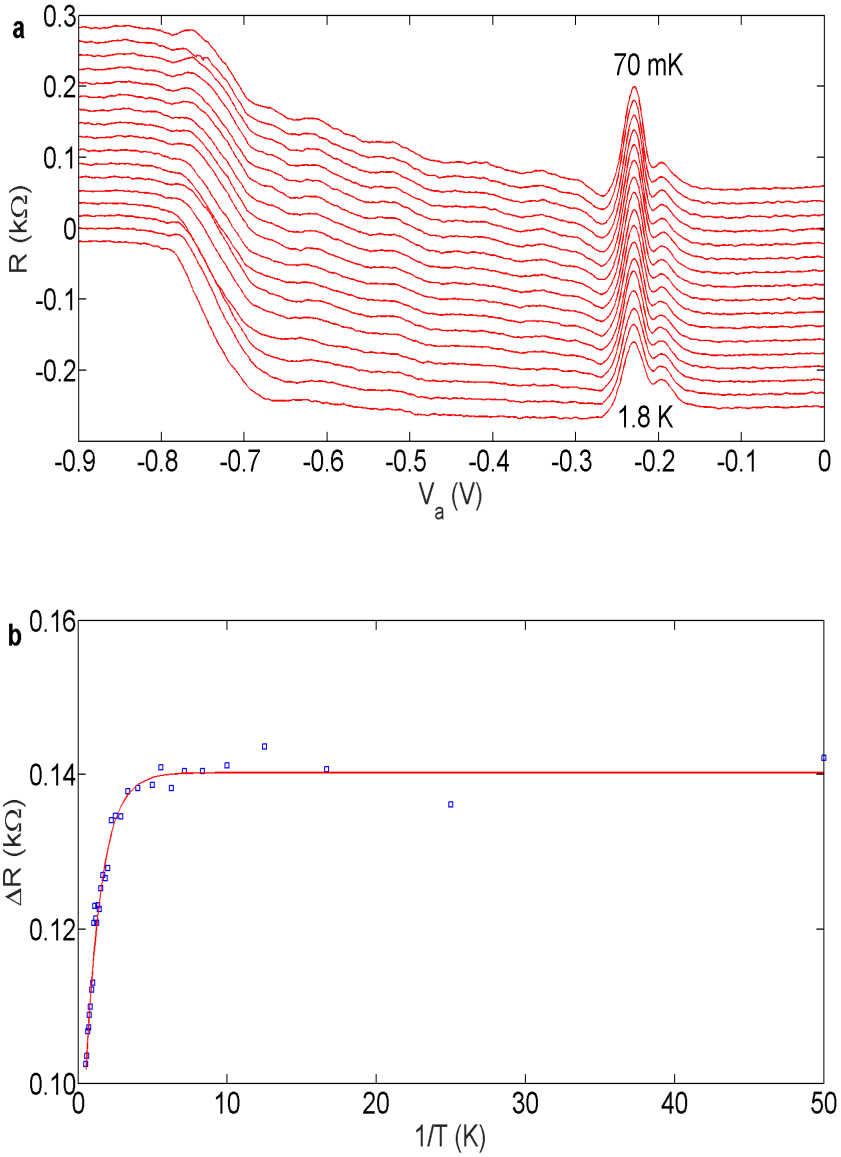

Fig. 5.12 **Temperature dependence of the fine oscillations. a**, the evolution of non-local resistance at V_r= - 0.3 V against temperature; the temperature increases from 70 mK (top trace) to 1.8 K (bottom trace), it is clear that the fine oscillations smear out with increasing temperature, data have been offset vertically for clarity. **b**, theoretical fitting of the height of the peak I of double-peak structure, p = 1. At the base temperature, the extracted phase coherence length is 15 μm.

5.5.2 High temperature regime

Increasing the temperature even further, it is then expected that at some point the phase coherence length becomes smaller than the electron propagation length (especially after several reflections), considering this, the temperature dependence may diverge from its low temperature counterpart.

In figure 5.13 we show the results of temperature dependence in from 1. 5 K to 20 K in both regime 1 and 2 performed in a teslatron system with a base temperature of 1.5 K. The reflector voltage dependence data is shown in figure 5.4. Generally speaking, the results follow the same trend as was observed in the low temperature regime, i.e. the features weaken against rising temperature. However, there is some noticeable difference as well.

In regime 1, intensity of the peak of the resonance structure reduces when temperature goes up but it survives even at the highest temperature (20 K), on the other end the dip is lifted up with increasing temperature and gradually emerge with the background signal. At the higher temperature, the background signal in the left and right side of the peak almost have same strength. In regime 2, the behaviour is slightly different. Both the peak and dip of the resonance structure smears at a lower temperature compared to regime 1. This is in line with the fact energy spacing between different cavity states is larger in regime 1 compared to regime 2 because of the smaller cavity size.

An analytic investigation on the temperature dependence in the high temperature regime indicates it follows Mott's law[133],

$$R = R_1 exp^{\frac{T_0}{T}^{\frac{1}{2}}} + R_2 exp^{\frac{T_0}{T}^{\frac{1}{3}}} \tag{5.5}$$

where R_1, R_2 are fitting parameters while T_0 defined as

$$T_0 \propto \frac{1}{k_B N(E_F) \varepsilon^3} \tag{5.6}$$

where k_B is Boltzmann constant, $N(E_F)$ is the density of state in the absence of electron-electron interaction and ε is the localization length[134] . It ought to emphasize that no suitable fitting is possible with eq.(5.3) and this suggests the result here is not mainly due to the change of phase coherence length l_ϕ. The $\frac{1}{2}$ and $\frac{1}{3}$ term arise from the contribution of 1D and 2D respectively, this agrees with both the fact quasi-1D states (QPC state) and quasi-2D states (cavity state) are present in the system.

It is interesting to notice that both eq.(5.3) and (5.5) can describe the temperature dependence in the range of 1 K to 2 K, it seems to suggest this is the transition regime of the two

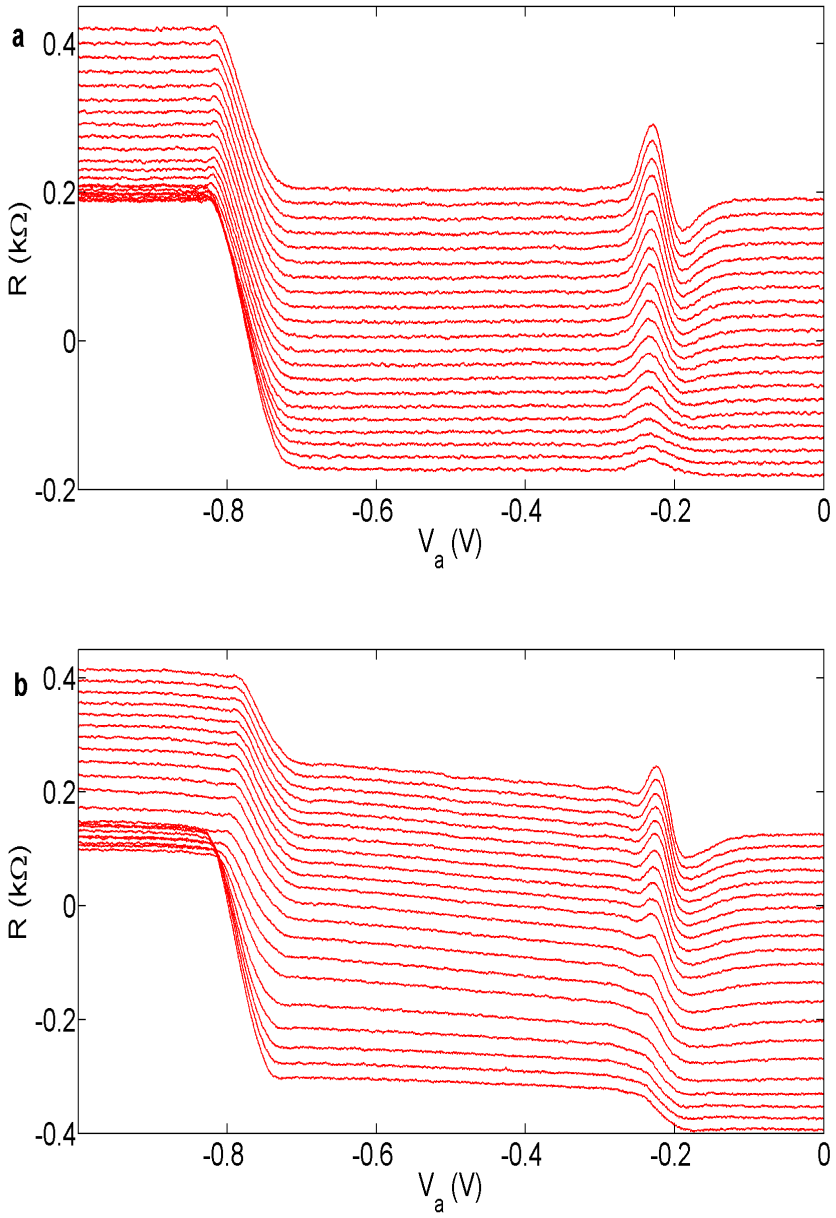

Fig. 5.13 **temperature dependence in high temperature regime.** The temperature is increased from 1.5 K (top trace) to 20 K (bottom), panel a and b show temperature dependence of typical trace in regime 1 and regime 2 in this temperature range respectively, it is seen that the intensity of the resonance structure reduces significantly. Data have been offset vertically for clarity.

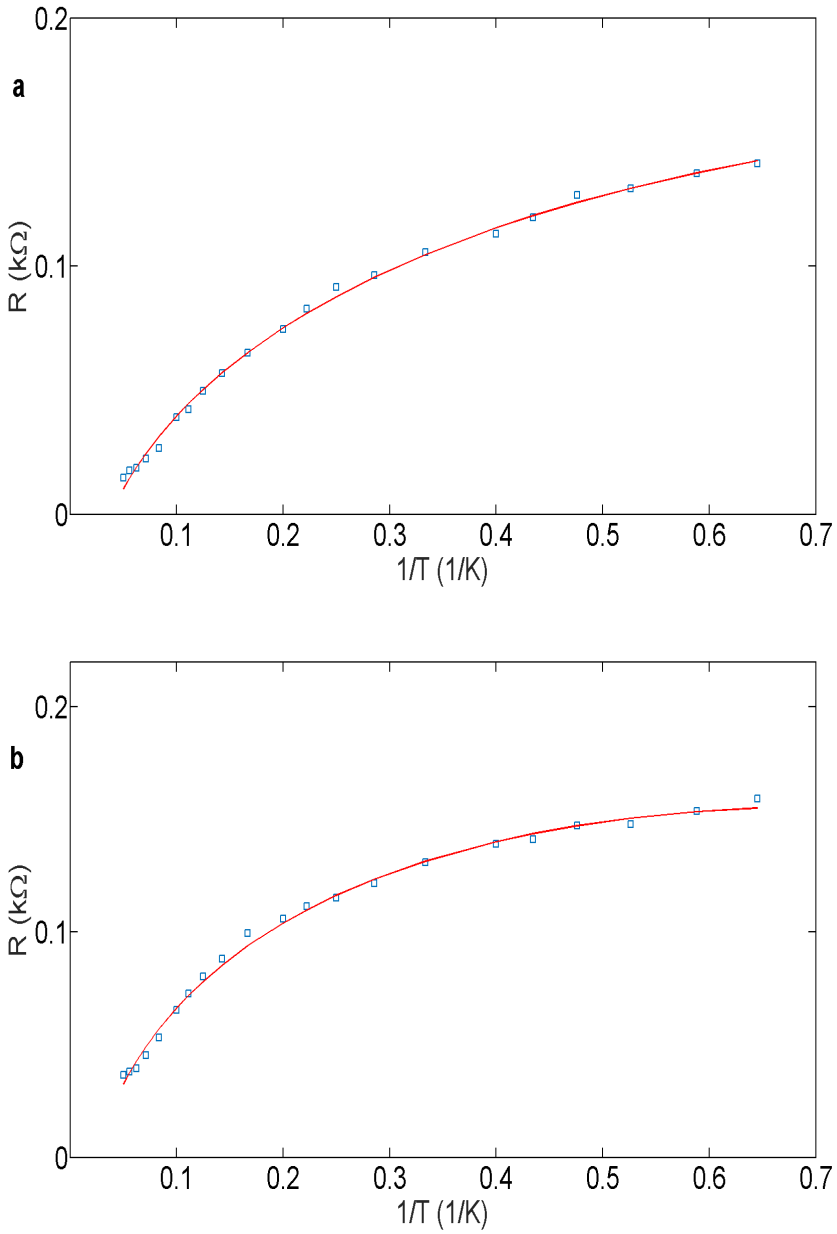

Fig. 5.14 **theoretical fitting of temperature dependence in high temperature.** It is seen that the temperature dependence of peak height of resonance structure in both regime 1 (panel a) and regime 2 (panel b) agrees well with Mott's power law. For the fitting in plot **a**, R_1 = -0.2656, R_2 = 0.4238, T_0 = 1.2; for the fitting in plot **b**, R_1 = -0.4482, R_2 = 0.6068, T_0 = 1.2.

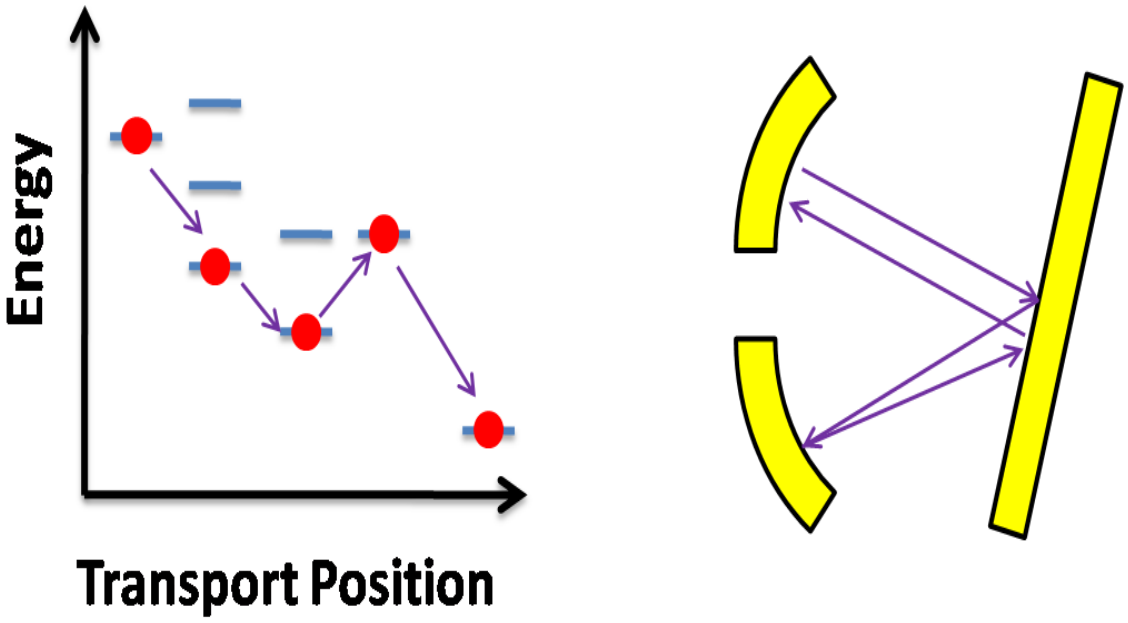

Fig. 5.15 **Comparison between variable-range hopping and transport in cavity .** Left panel shows a schematic of variable-range hopping, where electrons (red ball) transport between different spatially separated energy states, the right panel shows the multiple reflection in the cavity.

mechanisms. The fact characteristic temperature T_0 in eq. (5.5) is 1.2 K further supports the argument.

Mott's law was initially proposed for a problem where electrons transport through localized state around spatially separated impurities, indicating the most probable path is the one compromise distance between two states and energy separation between them. This is actually a direct result of the least action principle. In terms of real experiment this can be applied for electron transport between localized state around impurity centres in any dimensional system with a relatively large size. Contributions from different electrons are averaged out within the hopping process and thus gives a uniform behaviour. However, the hopping mechanism in Mott's original work is unlikely to be case in our experiment because firstly the number of impurity centres is negligible considering the high quality of the wafer and secondly the size of the device is even smaller than the typical length scale of a transport problem.

To understand the why the temperature dependence still follows Mott's law, alternatively speaking the analogy between transport in our device and hopping process, it is necessary to consider the multiple reflection in the cavity as shown in figure 5.15. Firstly, with the

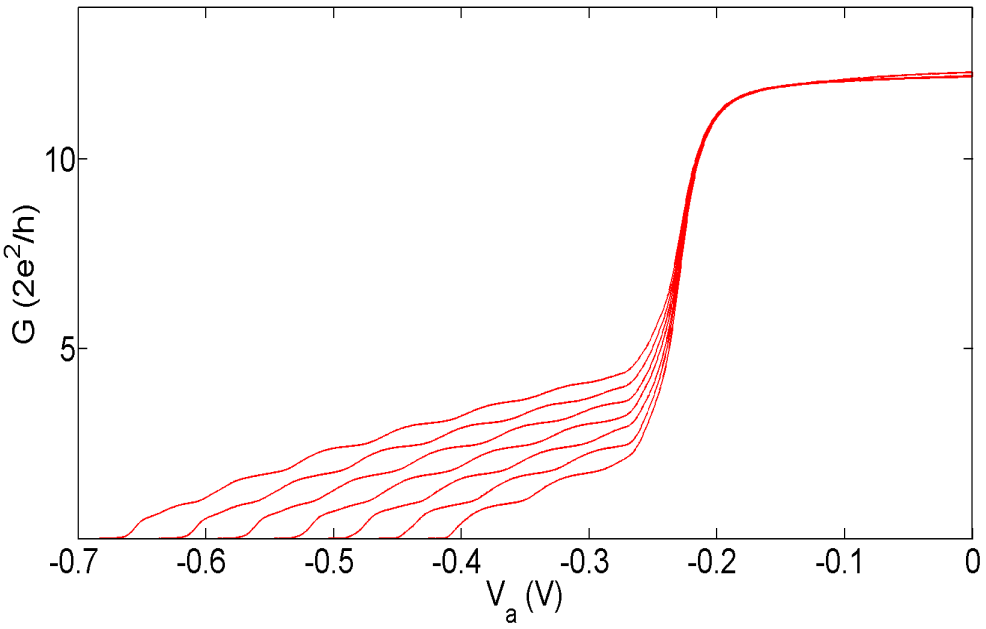

Fig. 5.16 **Conductance of arch-QPC with channel lateral shifted .** The left most trace is for zero shift and the right trace is for larger channel shift (the asymmetry between two gates is - 0.6 V). Well defined conductance plateaus are observed for all the traces.

multiple reflection in cavity the total propagation length of electrons in the cavity may exceed phase coherence length at relatively high temperature, however, due to the large coherence length at low temperature this is unlikely to be the case in low temperature regime, this then leads to different temperature dependence in low temperature and high temperature regime. Secondly, energy loss or gain process, e.g. the non-specular reflection, in the cavity is likely to change the electron propagation direction and thus the confinement length, thereby, when electron in the cavity takes different trajectory it will naturally occupy a new cavity state which is energetically different from the previous state. As a result, the multiple reflection process is then a mimic of variable-range hopping, therefore, the temperature dependence in our device follows Mott's law in the high temperature regime.

5.6 Lateral shift of the quasi-1D channel

In previous sections, it is seen that the result is sensitive to change of cavity state, in this section we focus on the lateral shift of the quasi-1D channel. Although the experiment is performed at 1.5 K, variation in the results with different asymmetric gate bias is quite remarkable.

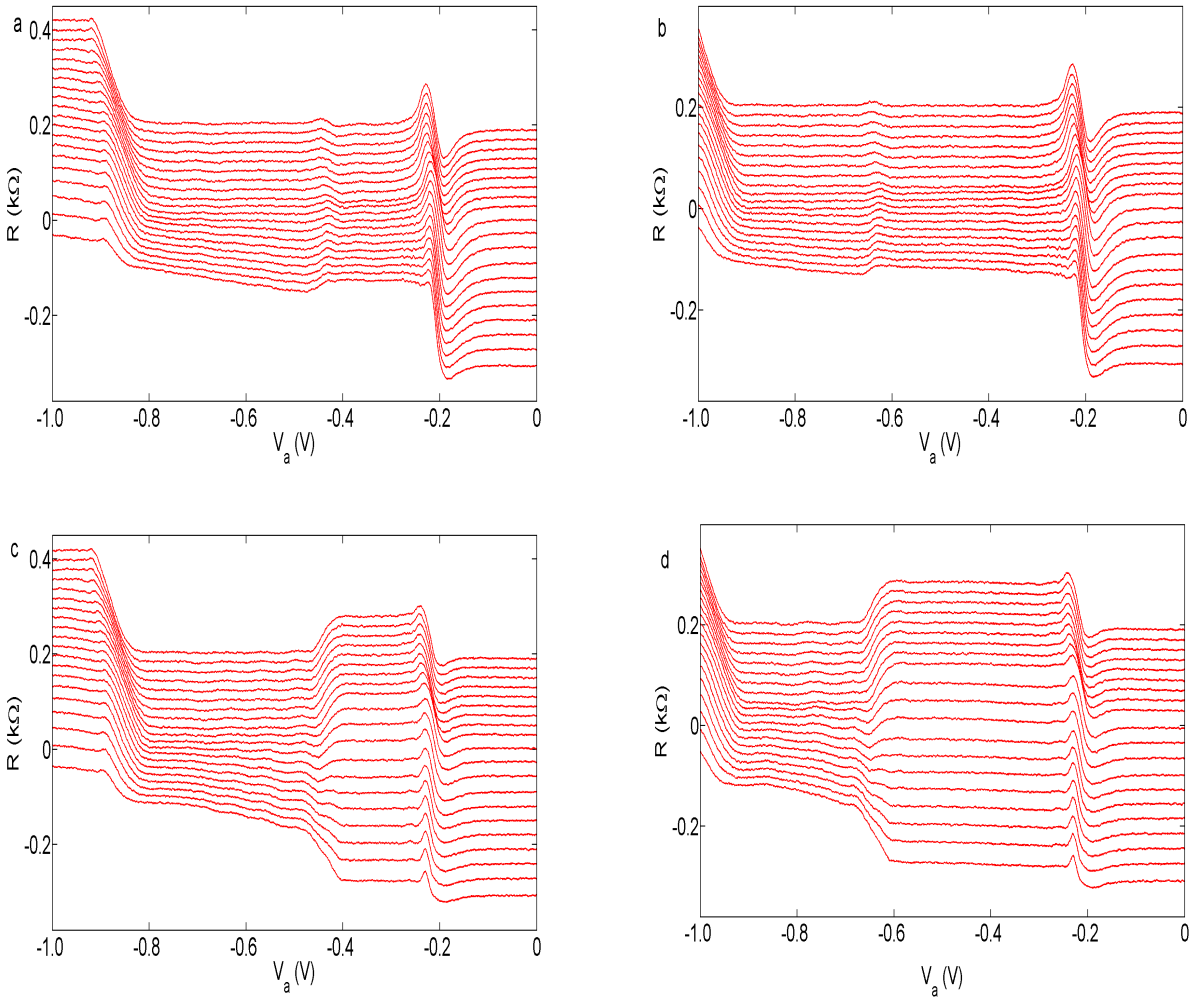

Fig. 5.17 **Effect of channel shift on cavity state in regime 1 and regime 2.** Plot **a** and **b** are for negative asymmetry voltage - 0.2 and - 0.4 V respectively where the quasi-1D channel is shift towards Ohmic 3, an additional small peak occurs around - 0.4 and - 0.6 V respectively compared to figure 5.4. Plot **c** and **d** are for positive asymmetry voltage + 0.2 and + 0.4 V respectively where the quasi-1D channel is shift towards Ohmic 4, a dip of asymmetry resonance structure is weakened significantly and meanwhile a broad shoulder structure is observable. The data have been offset vertically for clarity.

Figure 5.16 shows the typical characteristic of arch-QPC with asymmetric gate bias and this is used as voltage reference in the cavity experiment. Figure 5.17 highlights the effect of channel shift in regime 1 and regime 2 when different asymmetric voltages are applied between two arms of arch-QPC. Plot (a) and (b) are for negative asymmetry voltage - 0.2 and - 0.4 V respectively where the quasi-1D channel is shift towards Ohmic 3. In this case both the peak and dip of the asymmetric resonance structure are quite robust. An additional small peak occurs around - 0.4 and - 0.6 V respectively compared to figure 5.4, the shape of the additional peak is found to be reflector voltage dependent, meanwhile the weak fine oscillation smears out. When the QPC shift towards to Ohmic 3, the distance between centre of QPC and reflector increases and thereby energy spacing between cavity states reduces and this then leads to deforming of fine oscillations. On the other end, plot (c) and (d) are for positive asymmetry voltage + 0.2 and + 0.4 V respectively where the quasi-1D channel is shift towards Ohmic 4. Several dramatic changes are observed. First, the intensity of dip of asymmetric resonance structure is weakened compared to plot (a) and (b) or figure 5.4; second, the fine oscillations appear in regime 2; third, a broad and pronounced shoulder structure forms in the left hand side of the peak of asymmetry structure and the shape of the shoulder structure evolves contentiously against reflector voltage. When the quasi-1D channel shift towards to Ohmic 4 the energy spacing of cavity states increases if the reflector voltage is the same as that in figure 5.4 due to the smaller size, thus to get the same energy spacing it needs smaller reflector voltage, as a result fine oscillations in this case appears in regime 2 while they occur in regime 1 when the channel is not shift. Meanwhile, the shift of quasi-1D channel also affect angular distribution of the injected electron, this together with the change of cavity size may give rise to the broad shoulder structure and also affects the intensity of the dip of asymmetric resonance structure, however this requires more investigation.

A detail study for channel shifting is present in figure 5.18 and figure 5.19 for negative and positive asymmetric bias respectively.

For negative asymmetric bias, the result is quite similar to that without channel shifting as shown in figure 5.4, however, the weak fine oscillations is not observable regardless of the reflector voltage, meanwhile the shoulder structure present in regime 2 - 4 is broader than that obtained with symmetrical bias.

On the other hand, the result with positive asymmetry bias shows significant change. In regime 1, the pronounced shoulder structure is already observable and interestingly its strength goes down with less and less negative reflector voltage in this regime. In regime 2 -

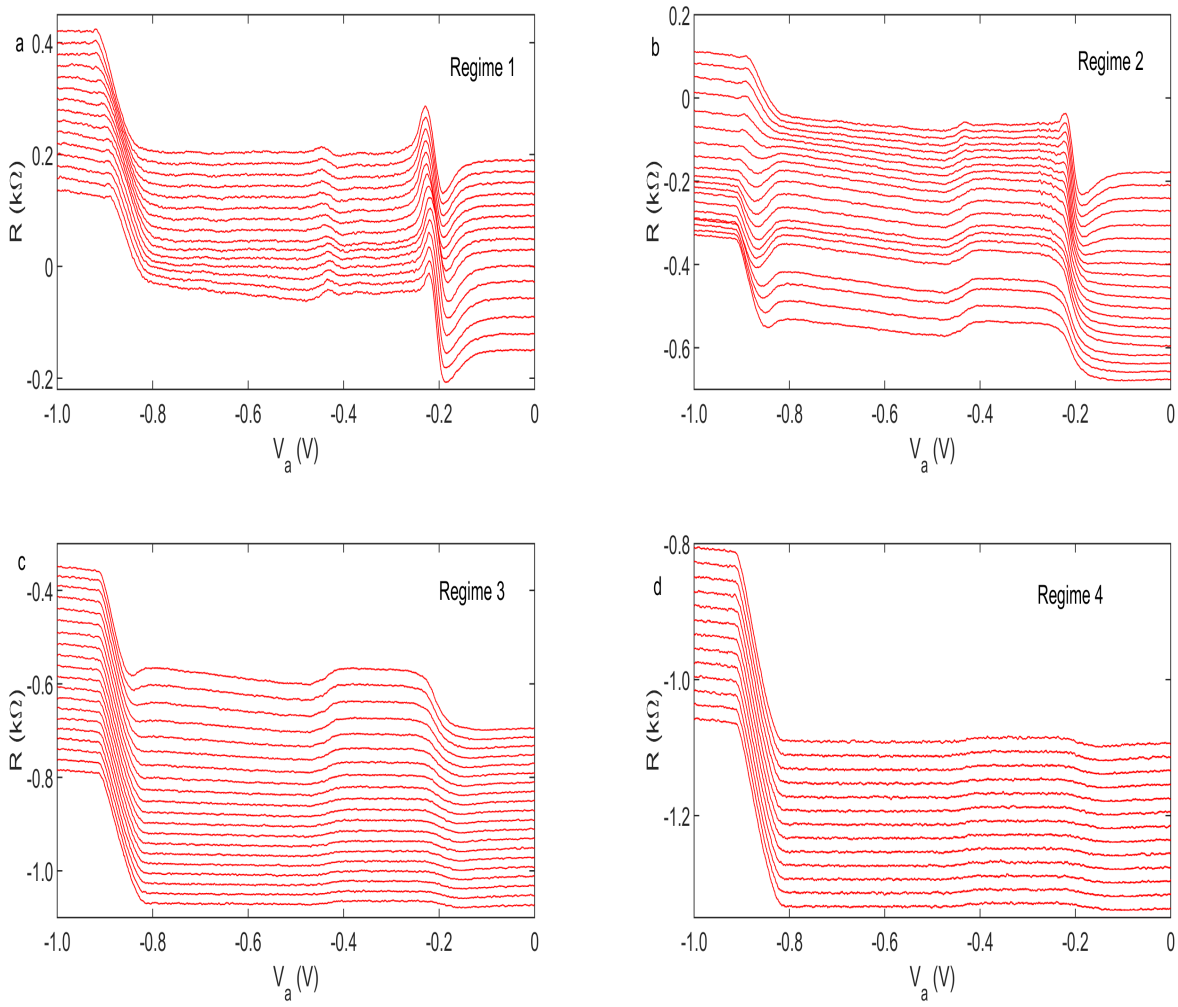

Fig. 5.18 **Detail study of $R_{12,34}$ with negative asymmetry bias of - 0.2 V. a**, result in regime 1, the result is similar to that without channel shifting as shown in figure 5.4, in addition a small peak occurs around - 0.4 V. **b** - **d**, result in regime 2 - 4 , there is no significant change compared to the zero channel shift version except the shoulder structure become broader. Data have been offset vertically for clarity and the top trace in each plot corresponds to the most negative reflector voltage in the regime.

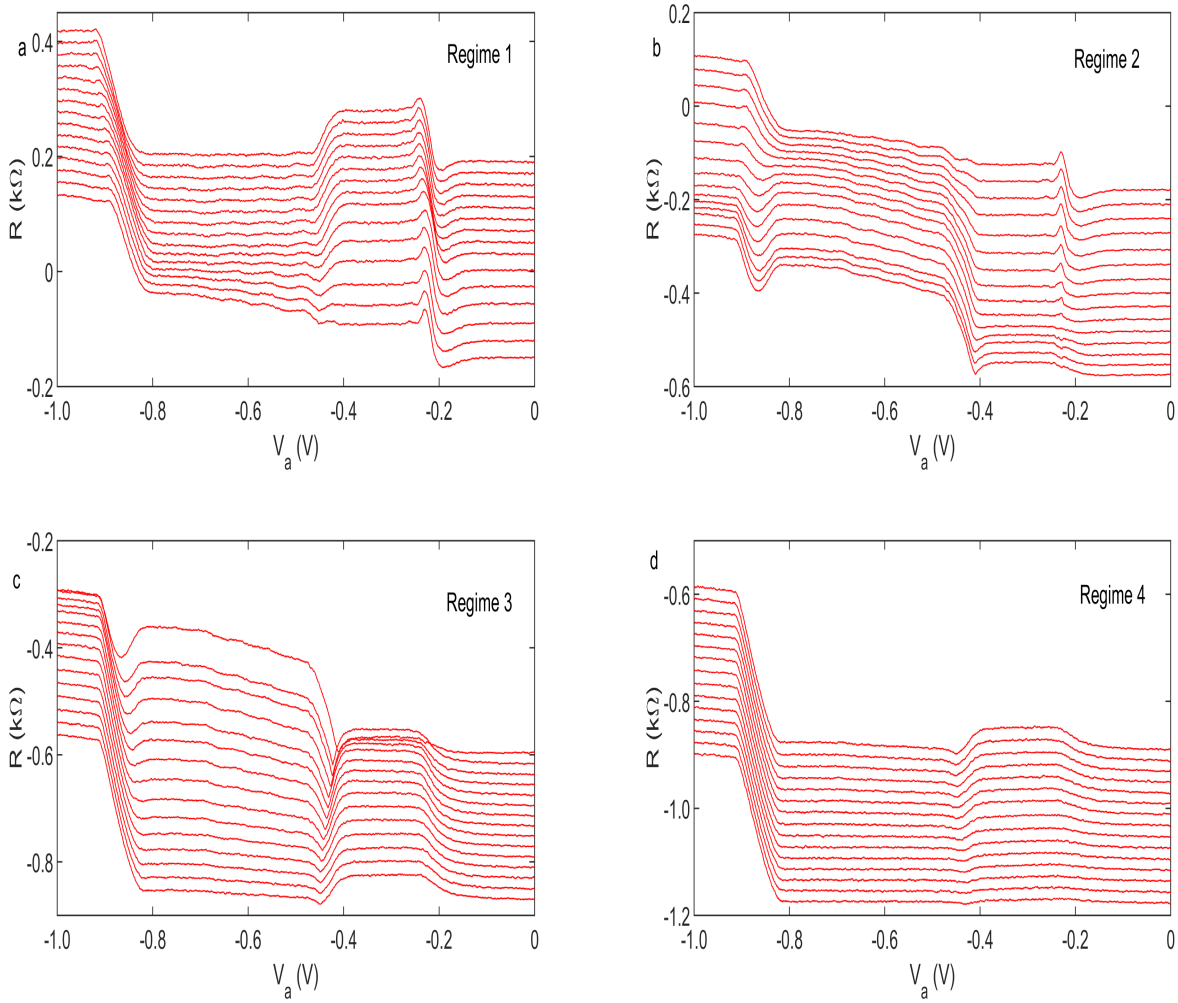

Fig. 5.19 **Detail study of $R_{12,34}$ with positive asymmetry bias of 0.2 V.a**, the dip of asymmetry resonance structure is weakened, the shoulder structure on the left side of the peak is observable in this regime, however the strength of the shoulder structure goes down with reflector voltage become less negative. **b** - **c**, result in regime 2 and 3, the shoulder structure disappears and reappear with increasing reflector voltage, faint 'fine oscillations' are present in regime 2. **d**, all the additional features smear out in this regime. Data have been offset vertically for clarity and the top trace in each plot corresponds to the most negative reflector voltage in the regime.

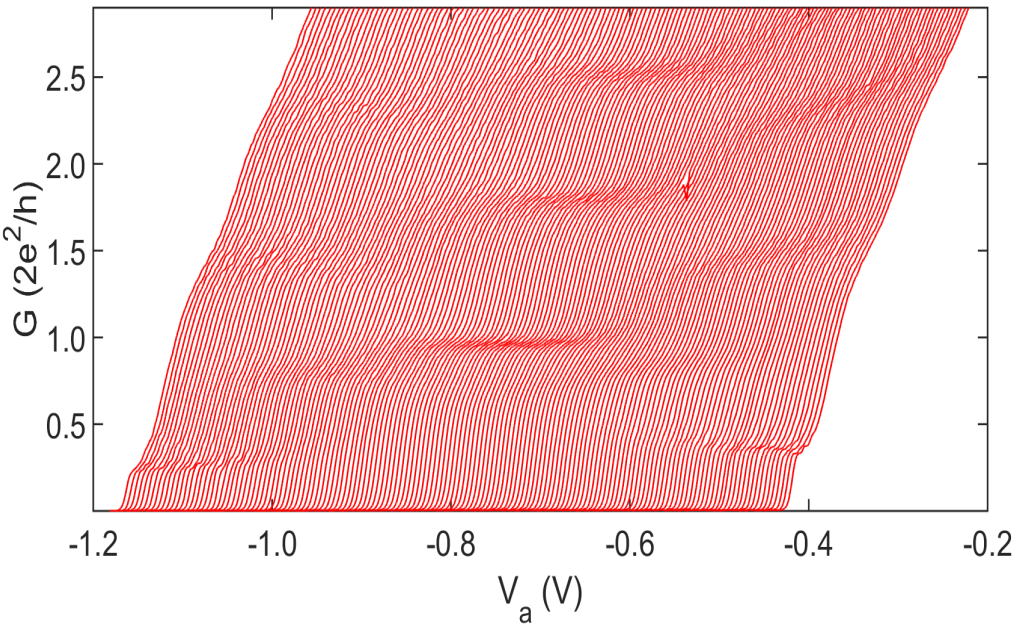

Fig. 5.20 **Conductance of the arch-QPC with source-drain bias at 1.5 K.** The source drain bias is swept from -3 mV to 3 mV, 0.25 structure appears with large bias voltage. The data have been offset horizontally for clarity.

3, the shoulder structure initially vanishes and then gradually forms again. This anomalous evolution needs more study which is beyond the scope of this work.

5.7 Source-drain bias dependence

Applying the source-drain bias allows to the quasi-1D states in QPC to be modulated and thus results in change in $R_{12,34}$ correspondingly. The conductance of arch-QPC with source-drain bias measured at 1.5 K shows typical behaviour[55]. The 0.25 structure forms with large bias voltage.

Measurement of $R_{12,34}$ with large bias current is present in figure 5.21 for both negative and positive bias. The reflector voltage is set to regime 2 so that both double-peak structure and fine oscillation are present without bias current. With negative bias current, fine oscillations are observable in the whole range, however, the double peak structures disappears with increasing bias current. On the other hand, the double peak structure shows quite different behaviour with positive bias current. It is noticed that peak I gets weakened with bias current while peak II is enhanced, meanwhile peak II shifts towards less negative V_a. The evolution of double-peak structure with positive bias is similar to that with transverse magnetic field as

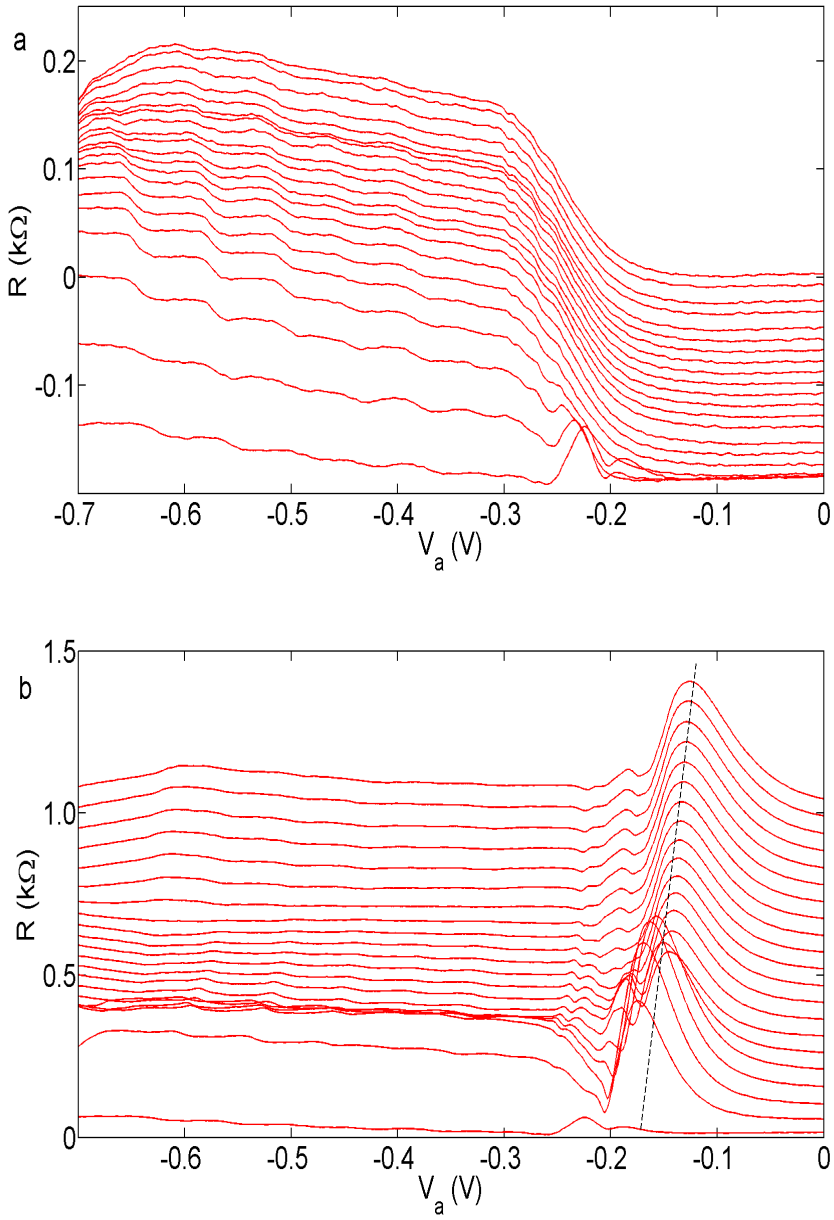

Fig. 5.21 **$R_{12,34}$ as a function of large bias current.** Reflector voltage is set in regime 2. **a**, negative bias current incremented from 0 (bottom trace) to - 200 nA (top trace), 'fine oscillations' are observable in the whole range, however, the double peak structures disappears with increasing bias current. **b**, positive bias current incremented from 0 (bottom trace) to 200 nA (top trace), 'fine oscillations' is also robust (not that apparent due to relatively large offset) as the negative bias current counterpart, peak I gets weakened by bias current while peak II is enhanced, meanwhile peak II shifts towards less negative V_a.

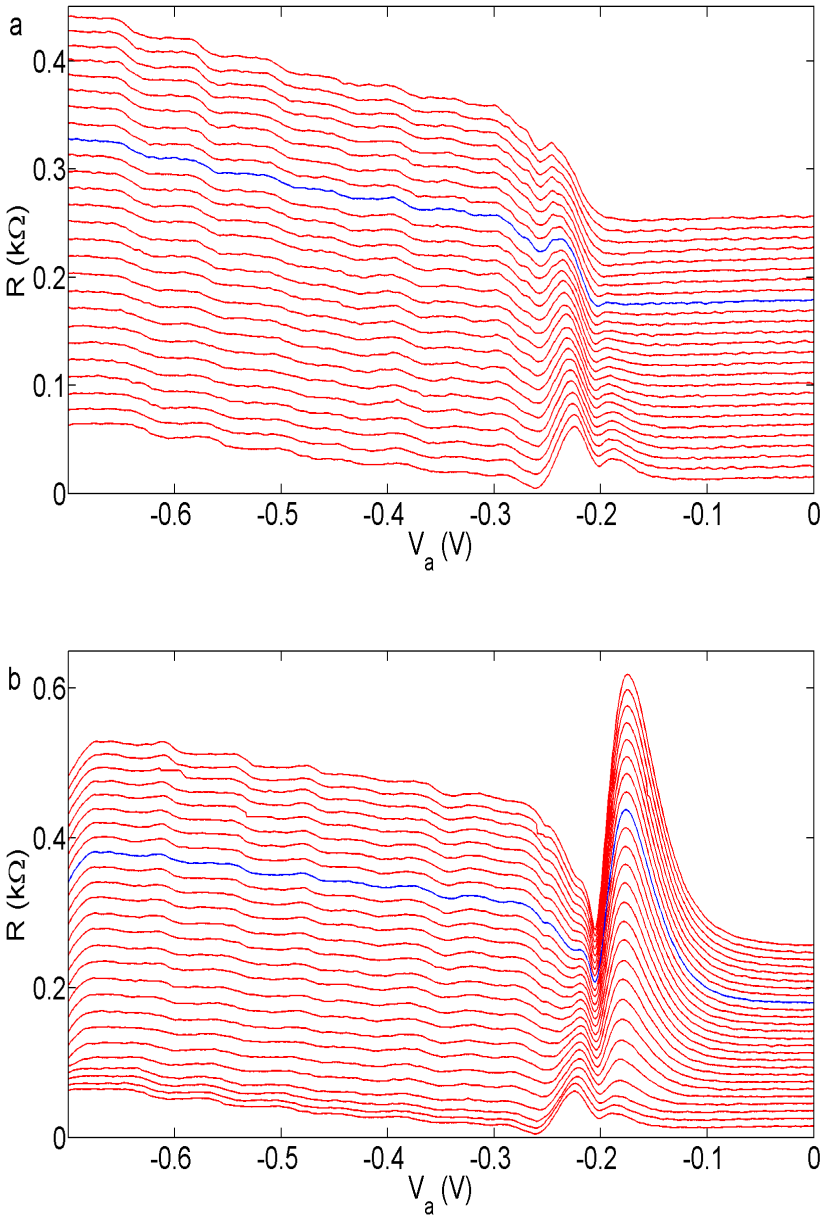

Fig. 5.22 **$R_{12,34}$ as a function of small bias current.** Reflector voltage is set in regime 2. **a**, negative bias current incremented from 0 (bottom trace) to - 10 nA (top trace), the 'fine oscillation' is present in the whole range, the double peak structure weakens gradually, the blue trace highlights where peak I disappears (around - 7 nA). **b**, positive bias current incremented from 0 (bottom trace) to 10 nA (top trace), robust 'fine oscillation' are observed, intensity of peak II reduces with increasing bias current and smear out at around 7 nA marked by blue trace while peak I gets enhanced. Data have been offset vertically for clarity.

shown in figure 5.8, however, the magnetic field dependence is relatively symmetry in both direction while bias current dependence is highly asymmetric.

To understand of the mechanism involved, the same experiment is performed in a small bias current regime to avoid significant change of property of arch-QPC as shown in figure 5.22. With bias current up to $\pm$ 10 nA, the fine oscillations are pronounced. Both peak I and peak II weaken against increasing negative bias current and peak I disappears with a bias current of - 7 nA. On the positive end, intensity of peak II reduces with increasing bias current and smear out at around 7 nA while peak I gets enhanced monotonically. The reason for the dramatic difference between positive and negative bias current requires further investigation.

A more quantitative study of peak I with positive bias current is presented in figure 5.23. It is clearly that the intensity of peak I increases linearly with bias current when bias current is larger than 2 nA, while no apparent change is observed with smaller bias. The linear dependence seems to be a result of increasing of electron density in the cavity, because

$$n_{2D} \propto \mu^* = \mu + eV_{sd} \tag{5.7}$$

, with more cavity states available the coupling effect might be enhanced .

The position of peak I follows an exponential change as shown in 5.23(b). Similar shift of anomalous interference induced peak, occurs in the near pinch-off regime of QPC, was observed in presence of source-drain bias in a two-QPCs Fano experiment[135] and the authors attributed such shift to reconfiguration of 1D state in the QPC due to source-drain bias, similarly, reconfiguration of 2D and 1D states in the 1D-2D transition regime may result in the observed shift of peak I.

5.8 Conclusion

In conclusion, we have shown the operation of an integrated quantum device consisting of an arch-shaped QPC coupled to an electronic cavity, whose states could be tuned using a reflector gate. We have shown that it is possible to couple and decouple the 1D states with the cavity states, using either the reflector barrier or transverse magnetic field, resulting in direct observation of Fano resonance arising from interference between these states .

Detailed study of four-terminal resistance $R_{12,34}$ as a function of reflector voltage, transverse magnetic field, temperature, channel shifting and source-drain bias is presented. The

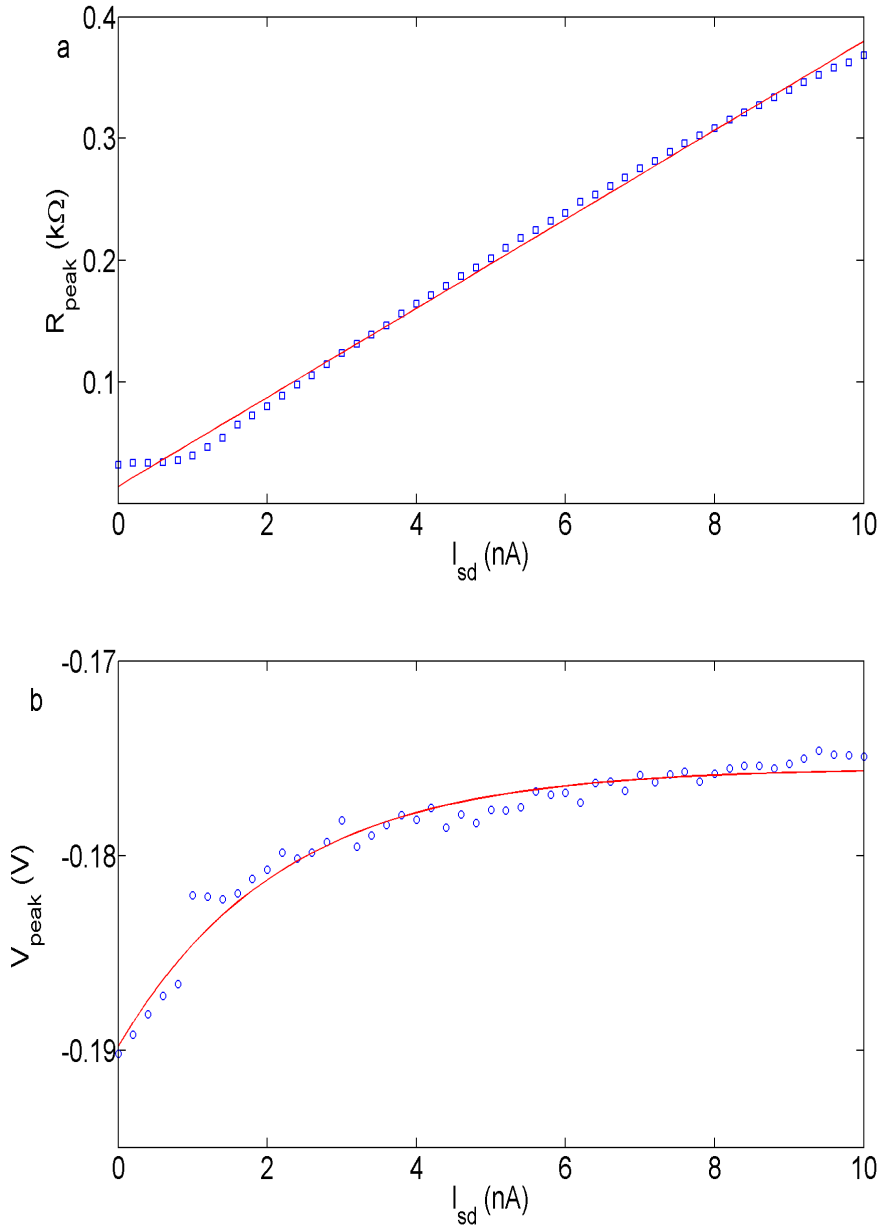

Fig. 5.23 **Fitting of peak I with small positive bias current . a**, the intensity of peak I increases linearly with bias current. **b**, the position of peak I follows a exponential change against bias current.

results are self-consistent and proves that coupling between cavity state and 1D state are ultra sensitive to external perturbation. The main observations are summarized below:

(I) Anomalous features arising from the coupling between the QPC and the cavity is observed in the 1D-2D transition and 1D regime of the QPC when the reflector voltage is sufficiently negative;

(II) A Fano resonance is observed by adjusting the coupling both electrically and magnetically, however, why Fano resonance can arise interference between QPC and cavity state (because both of them are continuous state) requires further study;

(III) The temperature dependence of the data is dominated by the change of phase coherence length in low temperature regime, while it follows Mott's law in high temperature regime.

Chapter 6

Magnetoresistance in a double cavity system

6.1 Introduction

One of the key parameters in a quantum system is the phase coherence length l_ϕ where the charge carriers remain coherent and the phase of wavefunction can be predicted. Within the phase coherence length the quantum interference effect is strong while on the other hand if the particle propagation length exceeds l_ϕ, quantum interference just manifests as a minor correction to the wavefunction. The phase coherence length is extractable using a quantum interference experiment, such as a quantum interferometer[69–74]. Among them weak localization[61–63] is a simple tool to monitor l_ϕ. Weak localization (WL), manifests itself as a resistance peak around zero transverse magnetic field, which is observed in disordered two-dimensional arising from the fact electron trajectory returns to its origin site via a series of coherent back-scattering events with impurities[136]. In the absence of magnetic field, the time reversal symmetry is preserved and the phase coherent length is thereby sufficiently long compared to the propagation length, the increase of the backscattering probability is apparent, hence the resistance is large. In contrast, time reversal system is broken with the application of magnetic field, thus l_ϕ is reduced significantly and leads to a drop in resistance. WL is straightforward and easily accessible in different materials, however, in a clean system (i.e. the amount of impurity is negligible) which is fundamental to the quantum device, the amplitude of WL is small due to the large propagation length of electrons.

To overcome such a problem, it is important to create back-scattering events artificially such as that demonstrated in a chaotic quantum dot also referred to as a chaotic quantum cavity [68, 80]. A typical chaotic quantum dot defined with metallic gates usually has a

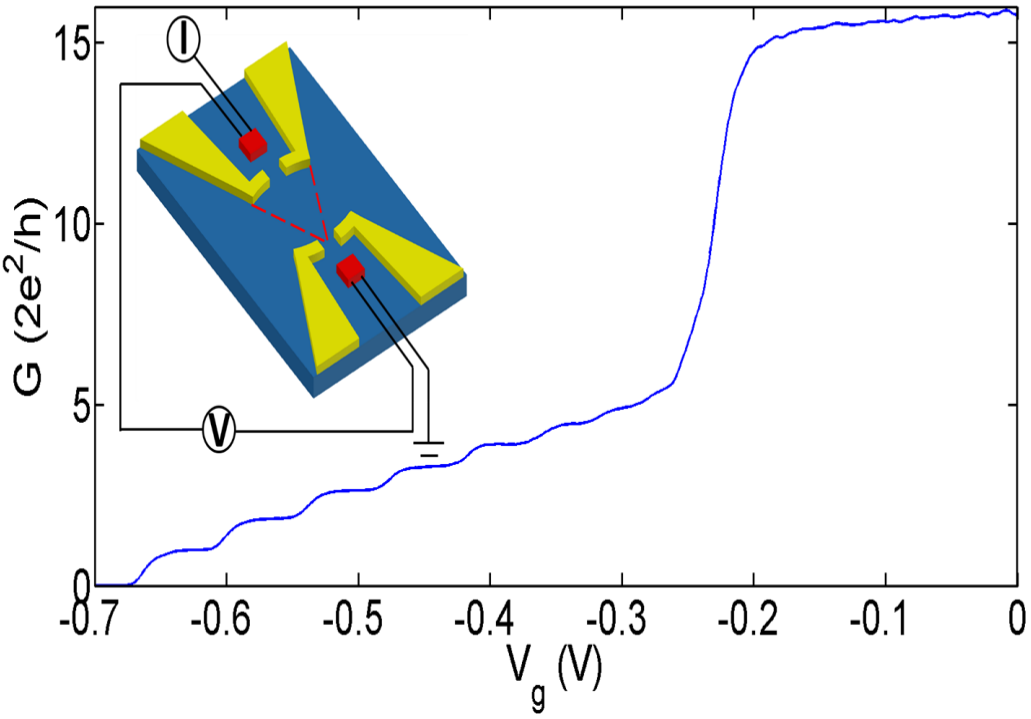

Fig. 6.1 **Schematic and characteristic of the double cavity device.** Differential conductance measurement of QPC shows well defined conductance plateaus. Inset shows schematic of the device, the yellow blocks are metallic gates and red squares are Ohmics. The opening angle of the arch, more precisely the electronic concave mirror, is 45° and radius is 2 um, both the length and width of the QPC embedded in the arch is 200 nm. The two arches are assembled in such a way that focal point of one arch aligns with the QPC in other arch as illustrated by the red dash lines.

stadium shape and the entrance and exit (can be treated as two QPCs) are orthogonal to each other[80], with this setup the probability of direct transport where electrons transport from entrance to exit without scattering with the confinement wall is significantly reduced, most of the electrons experience multiple bounces before they leave the dot. As a result, the probability of back-scattering is enhanced dramatically. Magnetoresistance of a chaotic dot produces a peak around zero magnetic field which is analogue to weak localization while the 2D weak localization is rather faint in these devices. Unlike the conventional 2D weak localization where the line shape of the magnetoresistance can be described with a digamma function[137], the line shape of the magnetoresistance of a chaotic dot can either be linear if the scattering is regular or Lorentzian if the scattering is chaotic[68, 138]. In brief, it is determined by the trajectory of electrons.

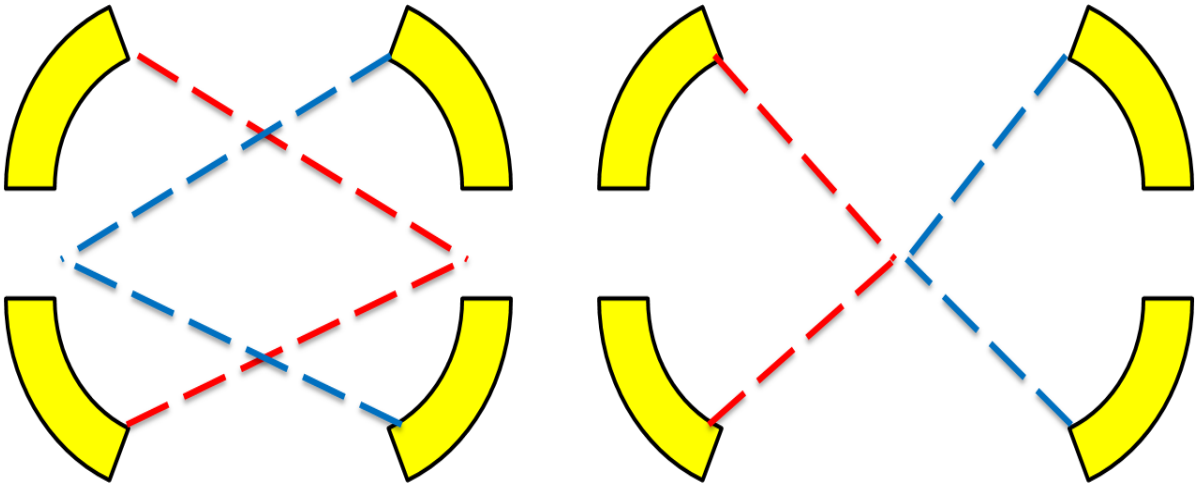

Fig. 6.2 **Comparison between a double cavity and a ring structure.** In the double cavity studied here the focal point of arch one one side is aligned with the potential barrier of the QPC on the other side so that the focal point is physically defined. In the ring structure the focal point of the two arch overlap together and focal point is virtually defined because there is no potential barrier formed at the focal point.

Meanwhile, a similar magnetoresistance peak was also reported in an experiment where two QPCs are connected in series and aligned to each other, an additional stripe gate was patterned in between[67]. The peak changes dramatically when the stripe gate voltage is varied. However, such effect is not observed in a similar device where the QPCs are misaligned intentionally[139]. The discrepancy between these two works suggests the interesting line shape may arise from some other origin rather than the trajectory of the electrons.

To get more clues on the parameter that affects the line shape of magnetoresistance in these cavity devices and make it more understandable tool for further application, we investigate magnetoresistance in a double cavity.

6.2 Device design and characteristic

Devices studied in the present work were fabricated from high mobility two dimensional electron gas formed at the interface of GaAs/$Al_{0.33}Ga_{0.67}As$ heterostructure. At 1.5 K, the measured electron density was $1.80\times10^{11}cm^{-2}$ and mobility was $2.17\times10^{6}cm^{2}V^{-1}s^{-1}$, therefore both the free path l_m and phase coherence length l_ϕ are over 10 μm which is much larger than electron propagation length. The experiments were performed in a cryofree dilution refrigerator with an electron temperature of 70 mK, unless specified, using standard

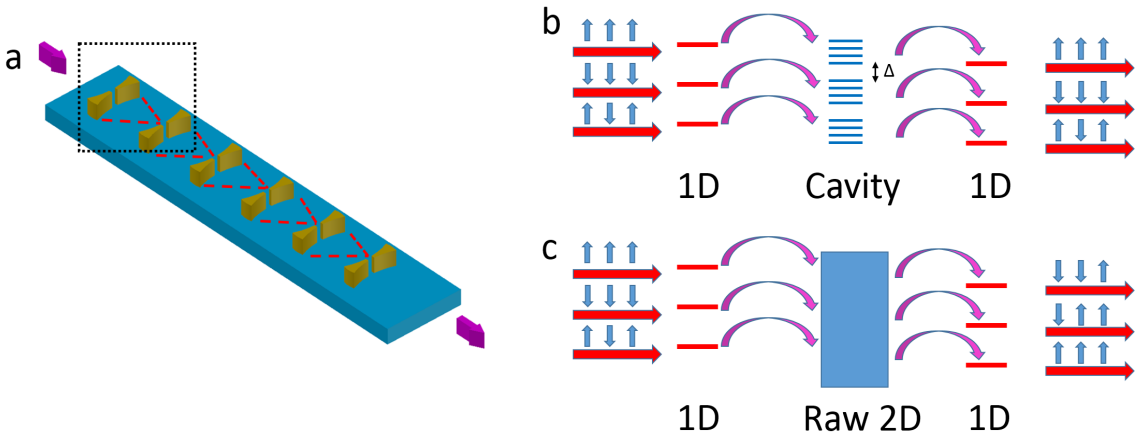

Fig. 6.3 **Schematic and principle of the proposed quantum bus. a**, quantum bus consists of a series of quantum point contact (QPC) - cavity hybridized device, the gold blocks are metallic gates where the blue pattern is the 2DEG. **b**, working principle of the proposed quantum bus, quantum information is assigned to 1D subbands in the QPC of initial stage, then coupled to energy matched cavity states bundles (the bundles are operated by charging energy Δ), and eventually fed to QPC of next stage. Information is preserved after transmission. Then 1D subbands in the two QPCs are intentionally miss-matched to highlight the quantum bus is error-tolerable. **c**, a comparison to plot **b** if there is no cavity states, quantum information get mixed in the 2DEG connecting two QPCs, output is arbitrary information.

lockin technique. For two terminal conductance measurement a voltage excitation of 10 μV at 77 Hz are applied while for resistance measurement a current excitation of 10 nA at 77 Hz are utilized to avoid electron heating. Results were reproducible with thermal cycling.

As shown in figure 6.1 the device consists two pairs of EBL defined arch-shaped gates, more precisely speaking the gates are in a concave shape rather than a segment of circle (the reciprocal of the curvature is larger than the radius of the circle at the tip of the arch, similar to the design of the optical lens, in order to avoid the deformation of the tip), with a QPC formed in the centre. The opening angle of the arch is 45° and radius is 2 um, both the length and width of the QPC embedded in the arch is 200 nm. The two arch-QPCs are assembled in such a way that the focal point of the concave at the injector end overlaps on the detector QPC and vice versa.

It is necessary to discuss the difference between the double cavity structure and the conventional ring structure. In the double cavity studied here, the focal point of the arch on one side is aligned with the potential barrier of the QPC on the other side, thus the focal point is physically defined. In the ring structure, the focal point of the two arch overlaps together and the focal point is virtually defined because there is no potential barrier formed there.

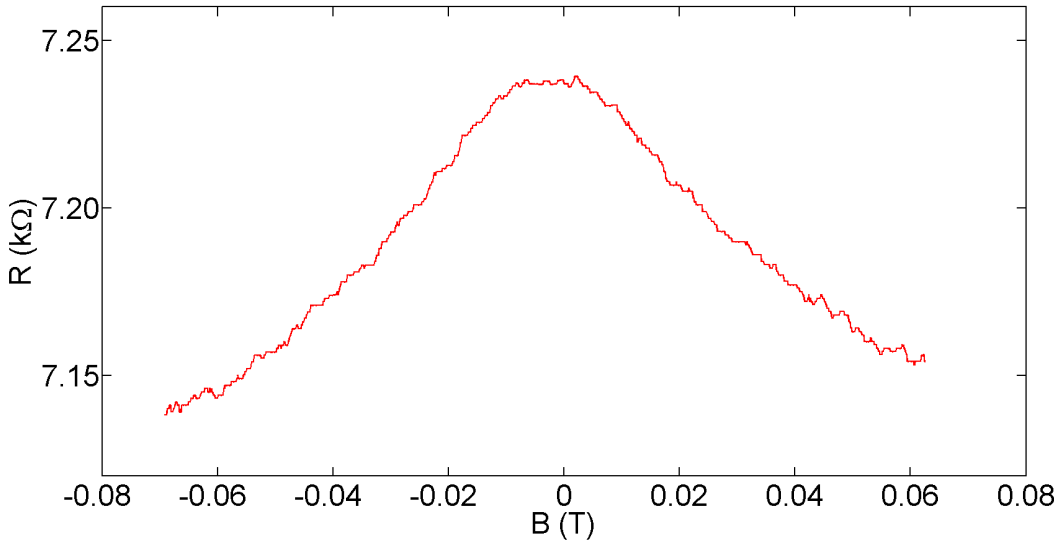

Fig. 6.4 **Representative trace of magnetoresistance of the injector.** The injector is set on the second conductance plateau (2 G_0) and detector is grounded. The magnetoresistance resembles a broad peak centred around 0 T and the amplitude goes down towards higher magnetic field. The change in resistance is less than 100 Ω.

When measured separately both the injector and detector QPC show well defined conductance plateau quantized at integer multiples of $2e^2/h$, this indicates the 1D density of states are well resolved in these devices.

It is interesting to note that the double-cavity devices is suitable to be used as robust and meanwhile scalable quantum bus (channel for qauntum information) consisting of arrays of quantum point contact (QPC) - cavity hybridized device as shown in figure 6.3(a). The principle of this novel quantum bus is demonstrated in figure 6.3(b), quantum information (such as spin configuration) is assigned to distinguishable channels (1D subbands) in the QPC of initial stage, all these channels are strongly coupled to the energy matched cavity state bundles (the bundles are separated by charging energy Δ), and then fed to the QPC of next stage. Both the cavity state spacing and charging energy ($\sim$ 100 μV[78]) is roughly an order smaller than typical 1D subband spacing ($\sim$ 1 meV). The coupling between the 1D subbands and cavity states ensures the information will not mix together over long distance. Meanwhile, even the 1D subbands in the two QPCs are slightly miss-aligned considering the fabrication divergence, as long as they are coupled to same bundles of cavity states information is still allowed to transmitted correctly, in other word, the quantum bus is error tolerable. On the contrary, if the two QPCs are connected via raw 2DEG (this is case especially for long quantum bus), the information from different channels of initial stage QPC gets mixed in the

2DEG, then the output is simply arbitrary information. In the present work we focus on the property of the fundamental building block, double-cavity device, highlighted by the dashed box in figure 6.1(a).

6.3 Magnetoresistance as a function of injector conductance

The intrinsic weak localization effect of the studied device is weak reflecting the high quality of the wafer. When measured separately the magnetoresistance of both the injector and detector show a typical broad peak[140, 141] as presented by a typical trace in figure 6.4 where injector is set on the second conductance plateau (2 G_0) and the detector is grounded.

Interesting magnetoresistance features are observed when both injector and detector are activated as shown in figure 6.5. In this experiment, the voltage applied to the injector is incremented slowly from - 0.65 V (beginning of first conductance plateau) to zero gate voltage while the detector is fixed at first conductance plateau. For the ease of discussion, the magnetoresistance is investigated in four different regimes according to the injector conductance (denoted as G_i).

In general, the total resistance, which is the summation of the resistance of injector and detector with quantum correction, reduces with increasing injector conductance. The magnetoresistance resembles a camel back shape with additional peaks superimposed on the central dip in all four regimes.

In regime 1, the injector is tuned from G_0 to 2 G_0. Three pronounced peaks (denoted as a tri-peak structure in the rest of the chapter) are observed around 0 T with several satellite peaks on each side of the tri-peak structure. The magnetoresistance is almost symmetric against magnetic field, however, the central peak of the tri-peak structure which in principle should occur at 0 T shift slightly to the negative field end. The shift is likely due to the hysteresis of the superconducting magnet because the shift is symmetric against 0 T when the magnetic field is swept forward and backward (see figure A.1 and the discussion in the appendix). Position of the tri-peak structure and satellite peaks does not change with increasing injector conductance. Amplitude of these features, on the other hand, shows a rather complicated trend, it is noticeable that the central peak of tri-peak structure is more insensitive to injector conductance, while the left and right peaks of tri-peak structure are depressed when the injector becomes more open, the satellite peaks also experience a similar reduction in amplitude. Meanwhile, it is important to point out that the additional peaks observed here are not periodic against magnetic field B nor 1/B and this indicates they are unlikely to arise from Aharonov-Bohm effect (AB effect) or SdH oscillations.

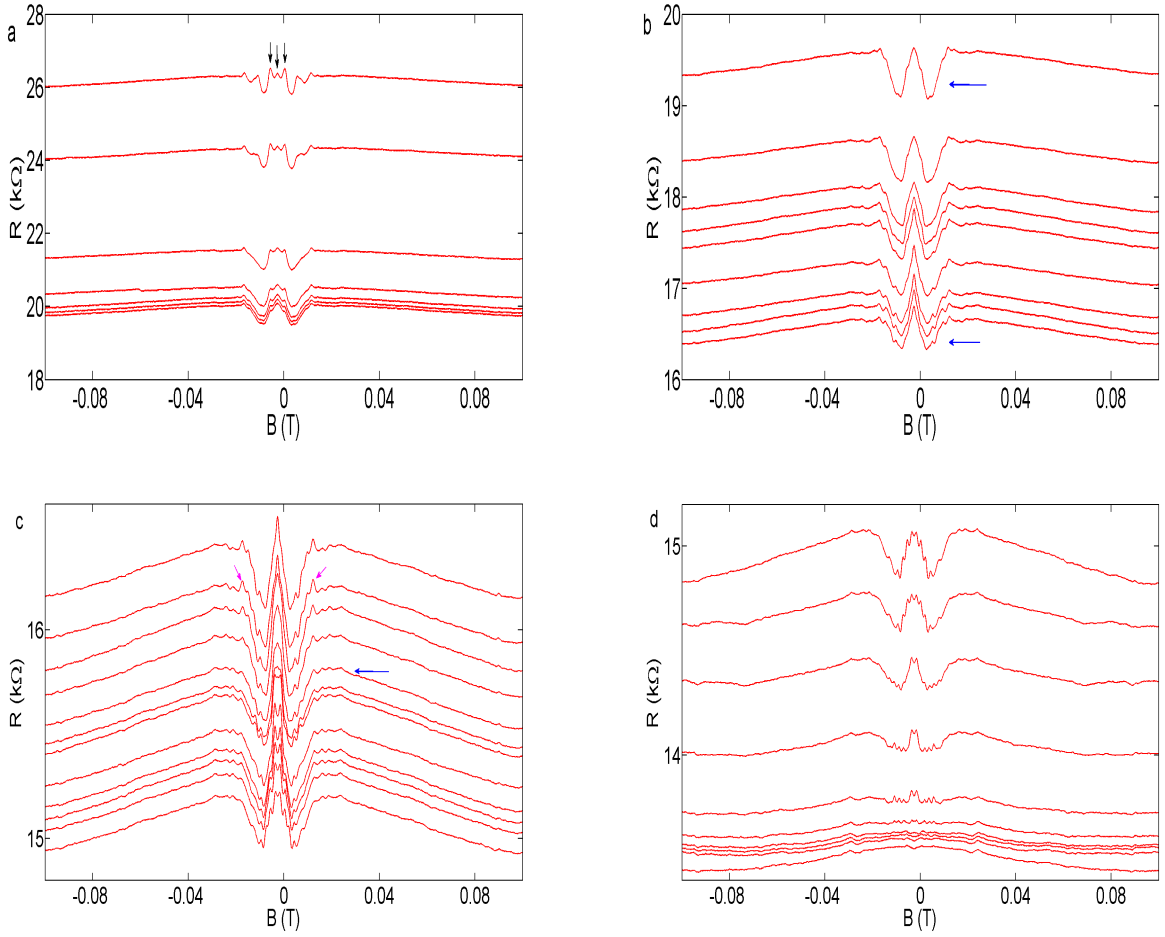

Fig. 6.5 **Magnetoresistance of the double cavity system as a function of injector conductance. a**, result in regime 1 (G_0 to 2 G_0), three pronounced peaks marked by black arrows are seen around 0 T, the intensity of the peaks on the left and right hand side decrease when gate voltage of injector V_i becomes less negative. **b**, result in regime 2 (2 G_0 to 3 G_0), the central structure gradually merges into a single rounded peak and then a sharp peak with decreasing V_i. **c**, result in regime 3 (3 G_0 to 5 G_0), the single sharp peak broadens up and splits into multiple peaks. **d**, result in regime 4 (5 G_0 to fully open), the amplitude of the central structures drops sharply and magnetoresistance shows a smooth and broad peak when injector is fully open ($V_i = 0$). Data is without offset.

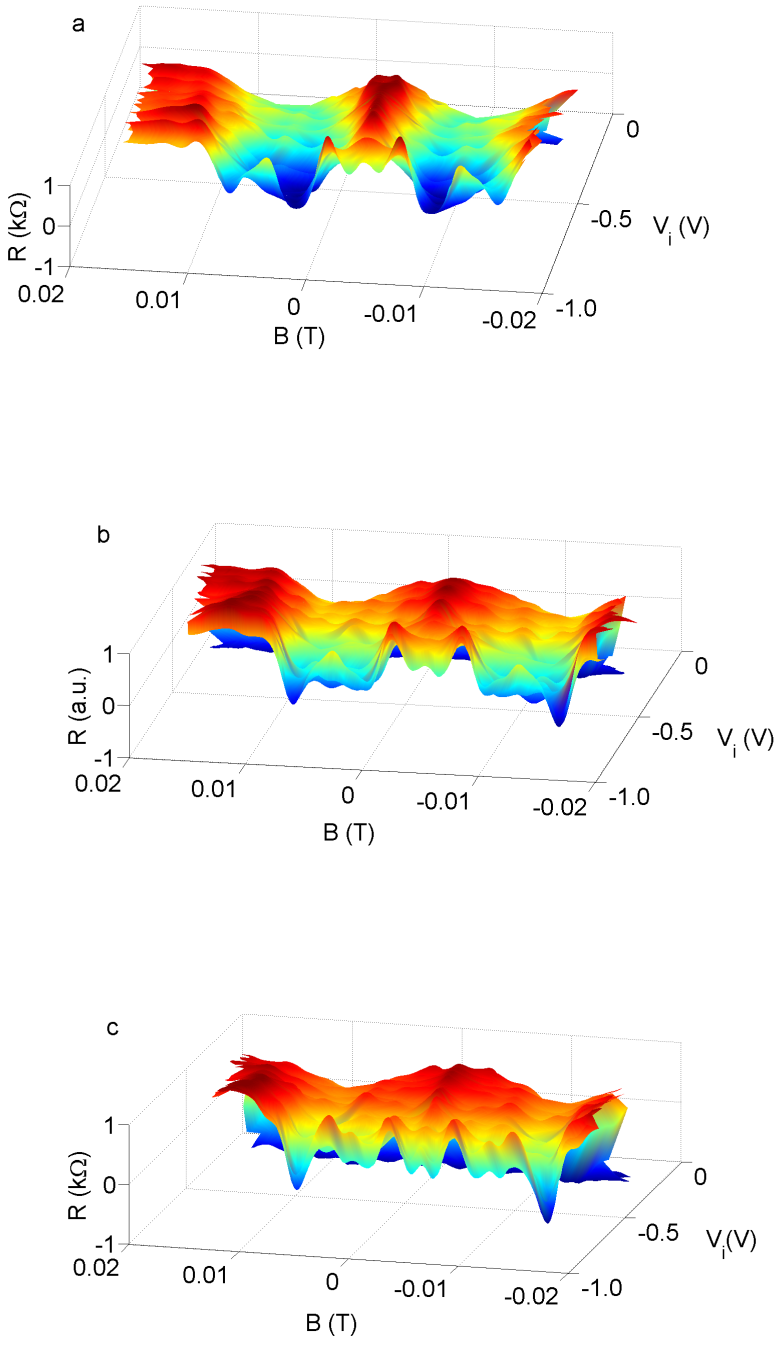

Fig. 6.6 **Colour-plot of magnetoresistance as a function of injector voltage at different detector. a-c**, the detector is set to G_0, 2 G_0 and 3 G_0 respectively, the similar evolution of the central structure is observed in all the cases, however, more peaks are observed with larger detector conductance. The data is normalized against the amplitude of the central structure for each trace.

In regime 2, the injector is set between 2 G_0 and 3 G_0, the tri-peak structure merges into a single peak. The single peak is initially a rounded one as marked by the upper blue arrow in figure 6.5 (b) (G_i = 2 G_0) and eventually develops into a sharp one (e.g. the trace marked by the lower blue arrow where G_i is around 3 G_0).

In regime 3 (3 $G_0 \leq G_i \leq$ 5 G_0), the sharp central peak slowly broadens up and then splits into two peaks at a conductance slightly larger than 4 G_0 (the trace marked by blue arrow in figure 6.5 (c) is with a conductance of 4 G_0), by opening the injector even further more peaks are observed around 0 T and these peaks are also aperiodic against magnetic field. In addition the amplitude of satellite peaks (marked by magenta arrow) reduces significantly in this regime.

In regime 4 (5 G_0 to fully open), the amplitude of the central structures drops sharply and magnetoresistance shows a smooth and broad peak when injector is fully open (V_i = 0).

Similar evolution of the central peak is observed with detector set to G_0, 2 G_0 and 3 G_0 as shown in figure 6.6. Moreover, more peaks are observed with detector open up.

6.3.1 Shape of the central peak

The line shape of the magnetoresistance can give detailed information on electron motion in the system[138], thus here we give a quantitative analysis of the line shape.

Figure 6.7 shows fitting of the central peak with injector tuned to 2 G_0, 3 G_0 and 4 G_0 respectively (corresponding to traces marked by blue arrows in figure 6.5) where the central structure is basically a single peak. When the injector is fixed at 2 G_0, the central peak has a well defined Lorentzian shape[138],

$$R(B) = R_0 + \Delta/[1 + (\frac{2B}{\alpha\phi_0})^2] \tag{6.1}$$

where R(B) is the resistance at given magnetic field B, R_0 characterises the resistance of the system without the quantum correction, Δ = R(0) - R_0, ϕ_0 is h/e and α is a fitting parameter which describes the distribution of the electron trajectory in the system. When the injector is open further, at 3 G_0, the shape of the peak changes significantly, it follows a linear shape and no Lorentzian fitting is possible. Somehow, at even larger injector conductance 4 G_0, the peak become Lorentzian again.

The Lorentzian line shape is a sign of chaotic motion and arises from the exponential distribution of the electron trajectory[138]. On the other hand, the linear line shape is a result of regular motion where electron trajectory has a power-law-like distribution[81].

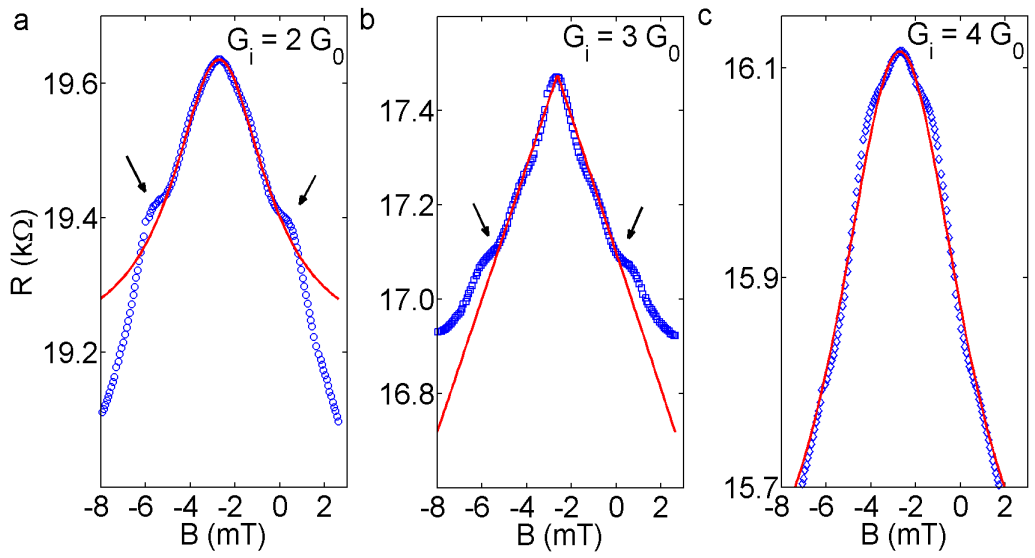

Fig. 6.7 **Line shape of magnetoresistance at different injector conductance. a**, injector is set to 2 G_0, the peak is with Lorentzian shape. **b**, injector is set to 3 G_0, the peak agrees well with a linear fitting while no Lorentzian fitting is possible. **c**, injector is set to 4 G_0, the peak resembles Lorentzian shape again.

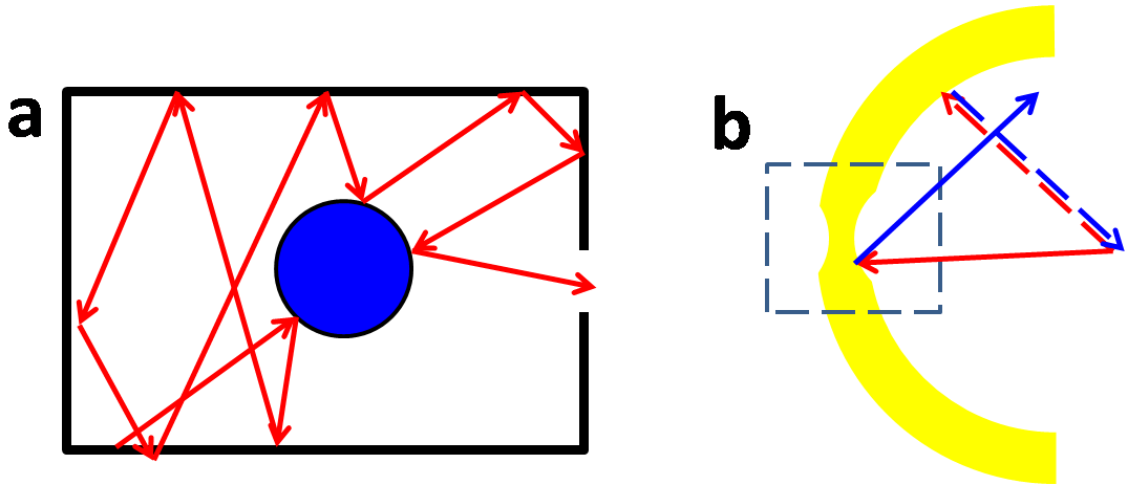

Fig. 6.8 **Model for chaotic scattering in the double cavity system. a**, model for interacting cavity system where the red arrows represents a typical trajectory of particle. **b**, the shape of confinement wall on one side of the double cavity system, the deformation highlighted with dashed box is due to the opening of the quasi-1D channel, the red (blue) dashed arrow is for the incident (reflected) trajectory against the confinement wall far from the 1D channel, the incident and reflected trajectory should overlap together but in the plot they have been offset for clarity, the red (blue) solid arrow is for the incident (reflected) trajectory against the potential barrier in the vicinity of the 1D channel.

In the conventional chaotic dot device[68, 80], the curvature of the confinement wall varies spatially and thus electron distribution become irregular after colliding with the boundary of the dot. On the other hand, the Lorentzian shape magnetoresistance observed in the two series QPCs arranged in parallel to each other[67, 125] is probably due to the frequent change of the confinement length at different incident angle. In contrast, in the double cavity device presented here, electrons always follow the radial direction of either left or right cavity where both the confinement length and curvature of the potential wall remain the same, therefore the reflection is likely to be regular, so the shape of peak is expected to be linear. It is important to figure out what leads to the chaotic motion in the double-cavity.

In a previous study, it was suggested that the lead of the chaotic dot can affect the distribution of the electron trajectory[68]. The authors reported a linear shape peak at the total resistance around 18.5 kΩ and a Lorentzian peak when the resistance is around 13.5 kΩ, once the Lorentzian shaped peak forms it preserves when the lead opens further. In contrast, the results here show the peak follows a Lorentzian → linear → Lorentzian change.

In an early theoretical work[81], a cavity system is modelled as a box with a small window in one of the walls, the interaction between particles is characterised by a circular scattering centre embedded in the centre as shown in figure 6.8(a). The elastic scattering with the walls can be characterised as below,

$$\begin{bmatrix} p_1(i+1) \\ p_2(i+1) \end{bmatrix} = \begin{bmatrix} \mp 1 & 0 \\ 0 & \pm 1 \end{bmatrix} \times \begin{bmatrix} p_1(i) \\ p_2(i) \end{bmatrix} \tag{6.2}$$

where ($p_1(0)$, $p_2(0)$) is the initial momentum for a given particle. It is straightforward to find out that the particle will only occupy four states namely ($p_1(0)$, $p_2(0)$), ($-p_1(0)$, $p_2(0)$), ($p_1(0)$, $-p_2(0)$) and ($-p_1(0)$, $-p_2(0)$). However, with the introduction of the circular scattering centre, the reflection become much more complicated,

$$\begin{bmatrix} p_1(i+1) \\ p_2(i+1) \end{bmatrix} = \frac{1}{R^2} \begin{bmatrix} q_2(i)^2 - q_1(i)^2 & -2q_1(i)q_2(i) \\ -2q_1(i)q_2(i) & q_1(i)^2 - q_2(i)^2 \end{bmatrix} \times \begin{bmatrix} p_1(i) \\ p_2(i) \end{bmatrix} \tag{6.3}$$

where R is the radius of the scattering centre and ($q_1(i)$, $q_2(i)$) is the coordinate of the starting point of trajectory for i^{th} scattering event. Thereby, it will expand the available momentum states into a circle in the momentum space. More importantly, the trajectory of the particle will become ergodic i.e. it will scan the entire coordinate space within the box[81].

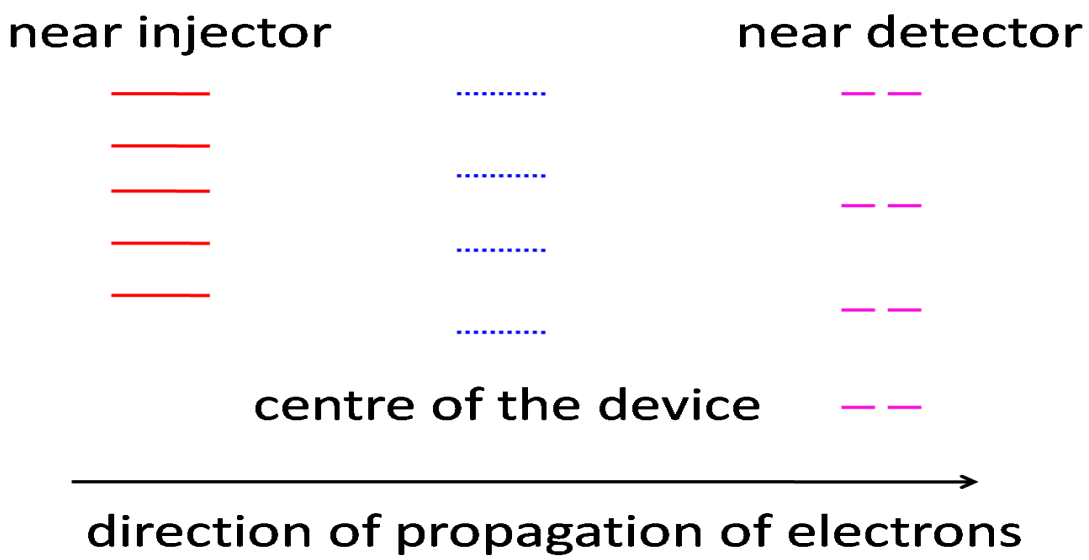

Fig. 6.9 **Spatial distribution of cavity state.** The energy spacing between cavity states is smaller near the injector because the gate voltage on injector is less negative and size of cavity defined with arc-shaped potential at injector end is larger, while the spacing is larger near the detector because the gate voltage on detector is more negative and size of cavity is smaller, in the centre of the device, the left and right cavity states hybridized and thus the energy spacing roughly takes the average value.

In an ordered system, the authors of Ref.[81] assume that there is either no central scattering centre or a negligible one (the scattering centre here is the one in the model which characterises interaction between particles not the disorder in the device), so that electrons can only occupy the four states allowed by Eq.(6.2). In the chaotic system, the motion of electrons is governed by Eq.(6.3).

Although the authors of Ref[81] only considers the case where the interaction between particle plays the role of a scattering centre and leads to the spread out of momentum, same expanding of momentum can be realized via other mechanisms, e.g. in the chaotic cavity work[68, 80] this is achieved by varying curvature of the confinement wall.

In an ideal double cavity system, due to the arch-shape of the confinement wall, scattering with the boundary will simply reverse the direction of electrons, thereby for a particle with initial momentum ($p_1(0)$, $p_2(0)$) the only available states is then ($p_1(0)$, $p_2(0)$) and ($-p_1(0)$, $-p_2(0)$). However, this conclusion is only valid for a uniform arch-shaped confinement wall. In the device studied here the QPC embedded in the arch-shaped gate will lead to the deformation of shape of the confinement wall especially in the vicinity of the quasi-1D channel as shown in figure 6.8(b), and therefore the scattering near the channel spreads out the momentum of electrons, thus results in a chaotic motion.

In addition to the distribution of trajectory of electrons, the cavity states may also influence the momentum of electrons via coupling effect as demonstrated in last chapter. In the double cavity device the left and right cavity states overlaps in the centre of the system and become hybridized while the overlap is minimised in the vicinity of injector and detector, thus it lead to a coordinate dependence in the coupling.

Equipped with the discussion above, the Lorentzian $\rightarrow$ linear $\rightarrow$ Lorentzian can be understood as below.

In the small injector conductance regime (corresponds to figure 6.7(a)), the size of the left cavity is similar to the that of right cavity (large gate voltage is applied to the detector), thus the electrons experience a nearly uniform coupling in the entire double cavity. The uniform coupling does not change the electron trajectory significantly. However, the deformation in the shape of the confinement wall becomes more noticeable with large gate voltage, the irregular reflection in the vicinity of QPC results in the divergence of electron trajectory. Thus ergodic motion and the Lorentzian line shape in the small conductance regime is dominated by the deformation of the potential wall.

On the contrary, if the gate voltage is small (corresponds to figure 6.7(c)), the influence of deformation of confinement wall is negligible because electrons prefer passing through the quasi-1D channel rather than get reflected (because the potential is lowered down). However, the size of the left cavity is considerably different from that of the right cavity in this regime (the voltage applied to the left arch is much smaller than gate voltage applied to right arch), the energy spacing of cavity states as well as the coupling between cavity electrons and injected electrons are inhomogeneous as shown in figure 6.9. The cavity states spacing is smaller in the vicinity of injector and larger near detector. Such non-uniform coupling modulates trajectory of electrons and is the key to Lorentzian peak shape.

In the medium gate voltage regime (corresponds to figure 6.7(b)), neither the deformation of the shape of confinement wall nor spatial variation of cavity states is sufficiently strong, thus the system behaves more like an ordered system, thereby a linear line shape is observed.

The mechanisms is likely to be the explanation for the other observations of the magnetoresistance.

6.3.2 Width of the tri-peak structure

In addition to the shape of the magnetoresistance peak, the width of the tri-peak structure is also directly related to the distribution of the injected electrons.

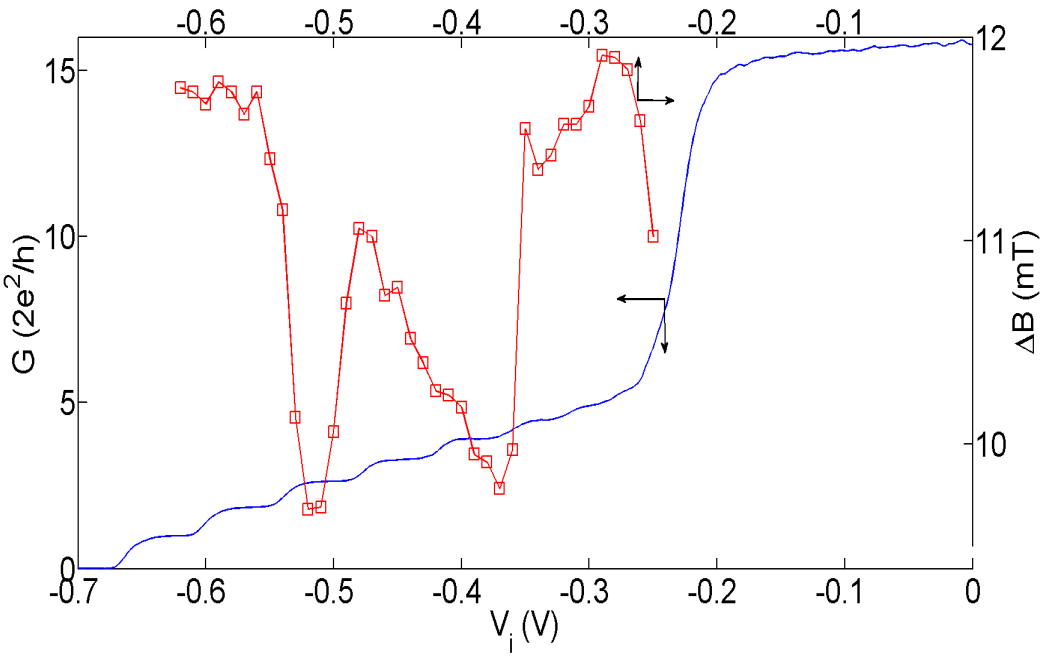

Fig. 6.10 **Width of the tri-peak structure as a function of injector conductance.** The width is defined as the distance between the left and right minimum next to the tri-peak structure, it narrows down at odd conductance plateaus and opens up at even conductance plateaus, while no significance change is observed at first conductance plateau.

The width of the tri-peak structure is defined as the separation between the left and right minimum next to the tri-peak structure (refers to figure 6.5 (a)) and the correlation between the peak width and injector conductance is shown in figure 6.10. It is interesting to notice that there is a fluctuation of 2 mT in the peak width through the quasi-1D regime of the injector. The tri-peak structure narrows down at odd conductance plateaus and opens up at even conductance plateaus, this trend is strictly followed from 2^{nd} to 6^{th} conductance plateaus while it is not that apparent at higher conductance plateaus, however, there is no significant change in the width of tri-peak structure at first conductance plateau.

It is natural to relate fluctuation in width of tri-peak structure either to width of quasi-1D channel or wavefunction which determines the angular distribution of the injected electrons. However, the width of the channel increases monotonically with increasing conductance thus cannot not lead to the fluctuation here. Similarly, the wavefunction become more spread out at higher conductance value and thereby is unlikely the direct reason for the fluctuation.

Interpretation based on channel width only considers the intrinsic angular distribution of injected electrons while the width of the tri-peak structure depends on the effective angular

distribution of electrons after multiple reflection. The reflection process causes the difference between the angular distribution of injected and detected electrons.

The opening of the quasi-1D channel of course increases the intrinsic angular distribution of the injected electrons, however, it minimizes the effect of deformation of the arch-shaped confinement wall (discussed in last section) and thus reduces contribution of reflection. These two effect compete with each other and thus give the beating pattern. Another problem to address is why the maximum and minimum are associated with particular conductance plateau, this area needs further study.

6.3.3 Height of the tri-peak structure

Compared to the shape and width of the central structure, the height of the tri-peak structure is easier to understand. Figure 6.11 shows the relative height of central peak (the one around 0 T) as a function of voltage applied to injector at fixed detector conductance of G_0, 2 G_0 and 3 G_0 respectively. The visibility $\Delta R(0)$ is defined as difference between the central peak and the minimum next to tri-peak structure (to remove the contribution of background signal mainly due to the resistance of the two QPCs).

Quasi-periodic peaks in ΔR (0) are observed when the injector is swept through the conductance plateaus in the case of all the three detector conductances. This is a natural consequence of the coupling between the 1D states in the injector QPC and the cavity states similar to that reported in the cavity-waveguide experiment[77] and the result shown in last chapter. When the injector is swept to the 2D regimes ΔR (0) drops significantly which arises from the fact electronic cavity is not well defined in this case thus the coupling effect weakens noticeably. The oscillation observed here is a sign that the information from a given channel is transported correctly from the injector through the cavity to the detector, if the electrons carry the information are missed in the 2DEG there will not be an oscillation (when detector is fixed a particular conductance), because the information carriers (the injected electrons) are then indistinguishable from other 2D electrons .

6.3.4 Temperature dependence of the magnetoresistance

Temperature dependence of weak localization or magnetoresistance in chaotic quantum dot is well understood due to the quantum interference nature of these observations. Thus a similar experiment was performed to give more clues on the property of the double cavity system.

Before operating on both gates, the temperature dependence of magnetoresistance with either injector or detector activated was studied. Result for injector magnetoresistance as a

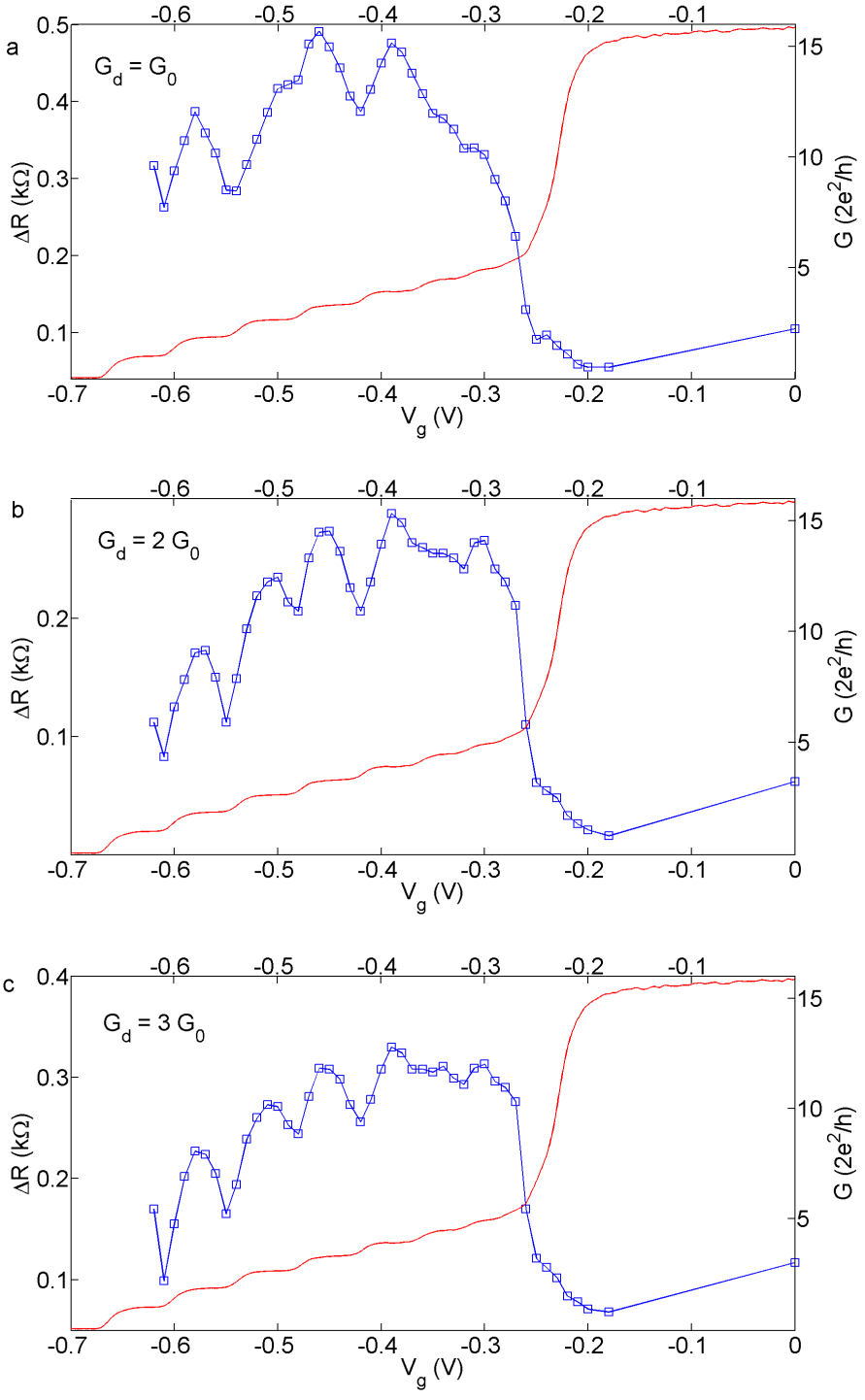

Fig. 6.11 **Visibility of the central peak as a function of injector conductance.** The visibility ΔR(0) is defined as difference between the central peak and minimum next to tri-peak structure. In plot **a - c**, the detector is fixed at G_0, 2 G_0 and 3 G_0 respectively, it is apparent that the periodicity of fluctuation of ΔR is associated with conductance plateaus in the case of all the three detector conductance. ΔR reduces significantly when the injector is tuned into 2D regime.

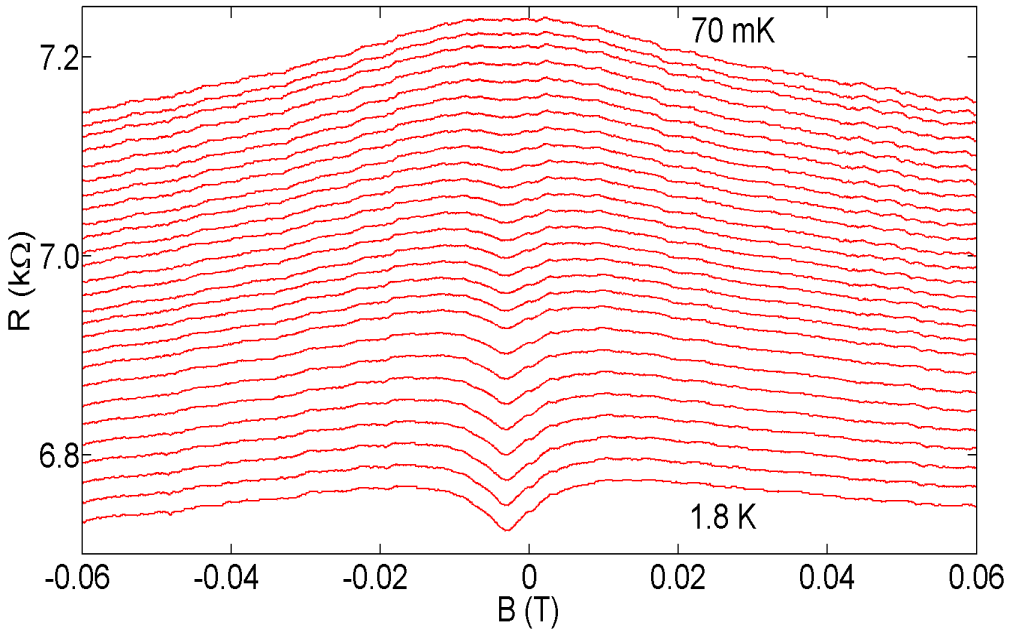

Fig. 6.12 **Temperature dependence of magnetoresistance of injector.** Injector is set at G_0 and detector is grounded. The top trace is at base temperature while the bottom one is at 1.8 K. Data have been offset for clarity.

function of temperature T is shown in figure 6.12 while detector shows a similar behaviour. It is quite striking to note that at base temperature (top trace) the magnetoresistance shows a broad peak while at higher temperature (bottom trace, 1.8 K) a pronounced dip forms around 0 T which is similar to weak anti-localization observed in system with relatively strong spin-orbit interaction. However, to observe weak anti-localization it requires that

$$L_{SO} \ll L_{\phi} \tag{6.4}$$

where L_{SO} is the spin orbit scattering length and L_{ϕ} is phase coherence length, in a typical GaAs device L_{SO} is relatively insensitive to the temperature in the low temperature regime [114] while L_{ϕ} is phase coherence length shows a power law of temperature[131, 132], thereby eq.(6.4) is generally fulfilled at a relatively low temperature where L_{ϕ} is sufficiently large. Thus the observation here is not weak antilocalization. Similarly Kondo effect can be excluded because it leads an enhancement in conductance (thus a dip in resistance) at lower temperature. Although the reason for such an observation is not clear at the moment, the change in background signal does not affect the temperature dependence of magnetoresistance significantly.

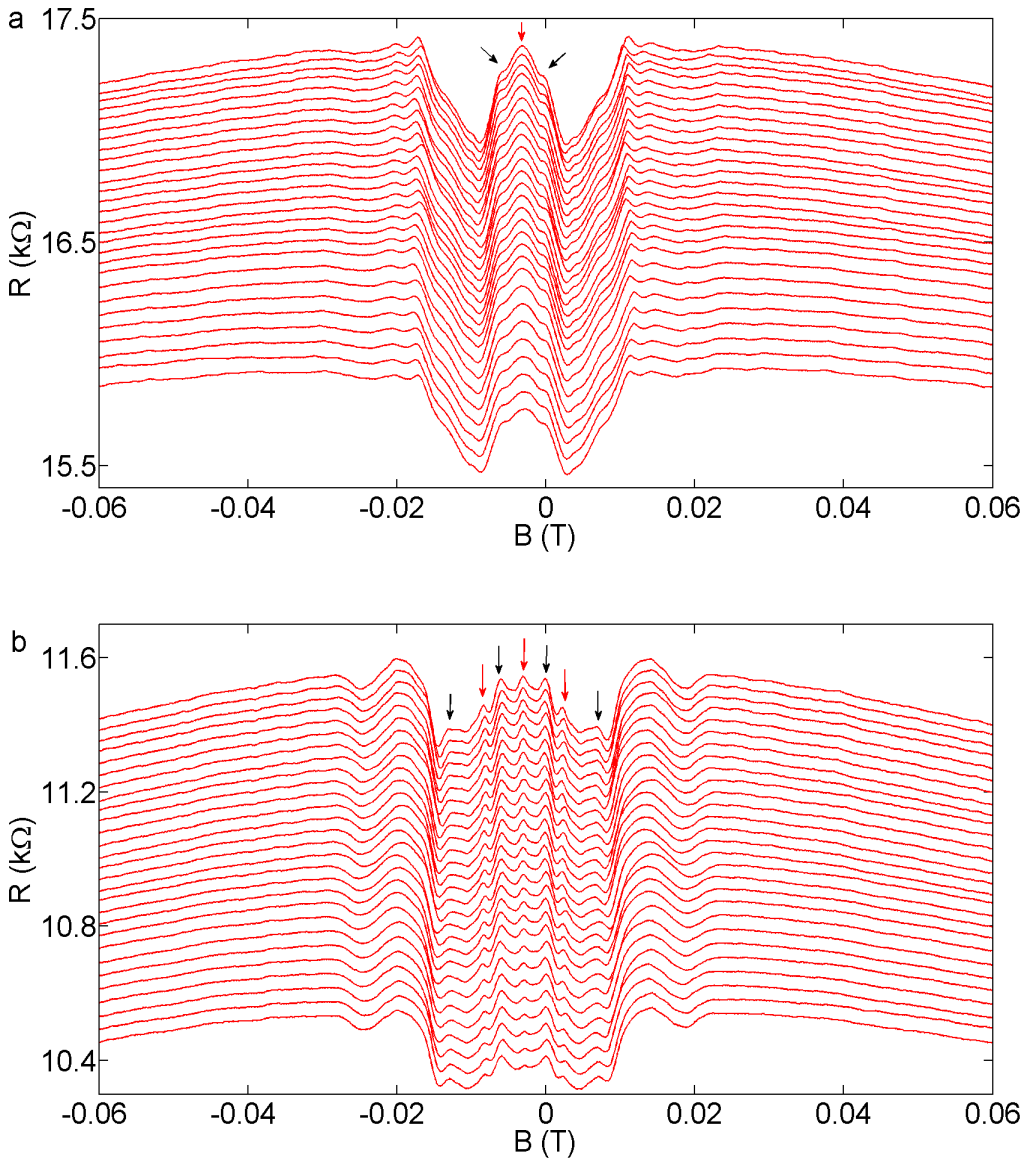

Fig. 6.13 **Temperature dependence of magnetoresistance of double cavity system. a and b** is for injector set to 2 G_0 while detector fixed at G_0 and 2 G_0 respectively. The top trace is at base temperature while the bottom one is at 1.8 K. Structures marked by red arrows are more temperature sensitive compared to structures marked by black arrows. Data have been offset for clarity.

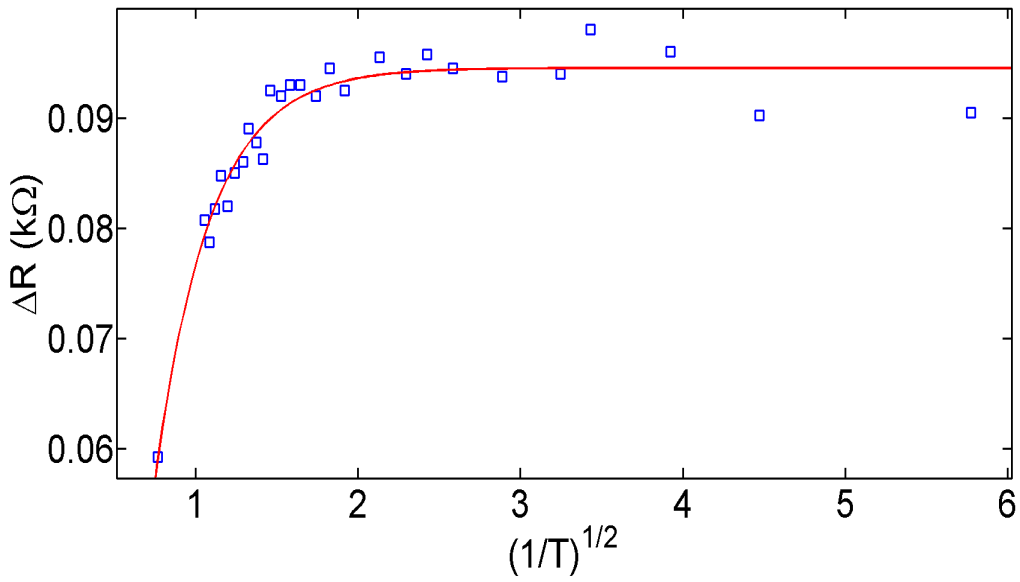

Fig. 6.14 **Fitting of relative height of central peak as a function of temperature.** Injector is set to 2 G_0 while detector is tuned to G_0 (corresponding to figure 6.13(a)). The relative height is defined as the difference between the central peak (red arrow) and shoulder structures next to it (black arrow). The red solid line is a fitting based on eq.(5.3) and (5.4), for this firring p = 1.

To make the results easier to discuss for the temperature dependence study, the injector is fixed at 2 G_0 where the central trip-peak structure has such form that central peak is stronger while peak at left and right have smaller intensity. The detector is set to G_0 and 2 G_0 for comparison. The result is shown in figure 6.13. Apparently, more structures are revealed when detector is fixed to 2 G_0, however, temperature dependence of magnetoresistance of these two cases show a similar behaviour. Firstly, the resistance in larger field regime (e.g. at $\pm$ 100 mT) does not change appreciably against temperature. Secondly, the central structures show well defined odd-even effect (central peak marked by red arrow is denoted as 1^{st} peak and peaks next to it on both left and right hand side are referred as 2^{nd} peak), the odd peaks marked by red arrows are more sensitive to temperature and smears out at much faster. At 1.8 K (bottom trace in both plot) the intensity of odd peaks is reduced significantly. On the other hand, even peaks marked with black arrows are less sensitive to rising temperature, they are pronounced even at 1.8 K.

In a previous chaotic dot experiment[80], all the features follow an universal trend when temperature increases. Thus, the odd-even effect observed here is quite unique. However, at this moment there is no theoretical interpretation for this observation. Parameters that affect

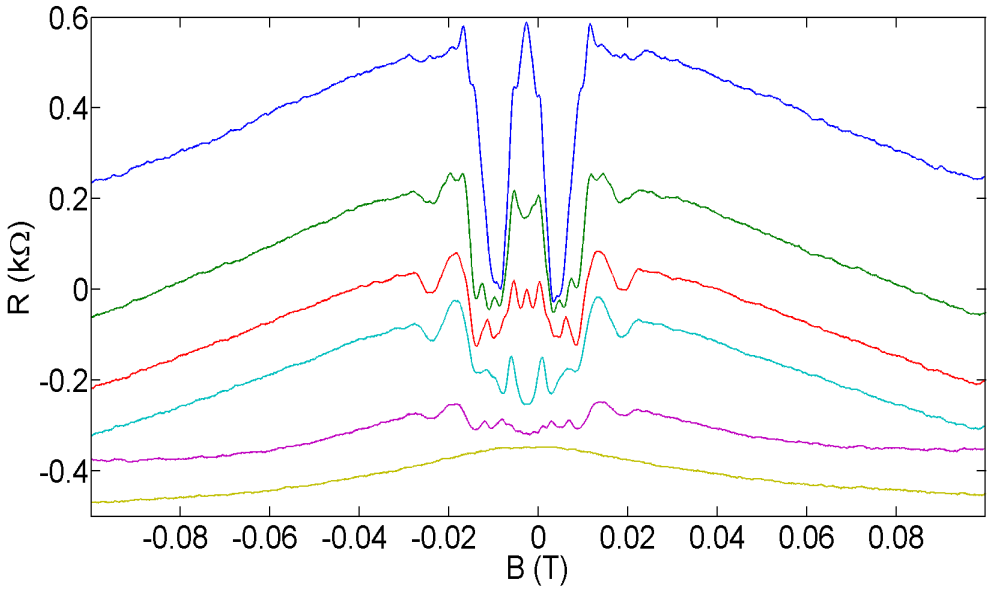

Fig. 6.15 **Representative magnetoresistance with varying detector conductance.** Injector is set to 2 G_0 while detector is tuned to different conductance value, from top to bottom, the detector is set to G_0, 1.5 G_0, 2 G_0, 3 G_0, 4 G_0 and fully open. At lower detector conductance the central structure is a broad peak while more peaks forms with detector opening up. Data have been offset vertically for clarity.

the height of the peaks such as phase coherence length or magnetic flux enclosed by electron trajectory do not follow the odd-even trend.

Nevertheless, an analysis of the relative height of central peak is shown in figure 6.14 which corresponds to raw data in 6.13(a). To avoid ambiguity introduced by the change of the background signal shown in figure 6.12, the relative height which is defined as the difference between the central peak (red arrow) and shoulder structures next to it (black arrow). However, it is necessary to emphasize the result remains in the same form with absolute height of central peak. It is clear that the height of peak follows the typical exponential-decay behaviour of quantum interference effect which is described by eq. (5.3) and (5.4). The best fitting is given by p=1 (p is defined in eq.(5.4))which suggests the interference arises from a 2D system[131] and this is consistent with the fact the interference mainly occurs in the 2D double-cavity.

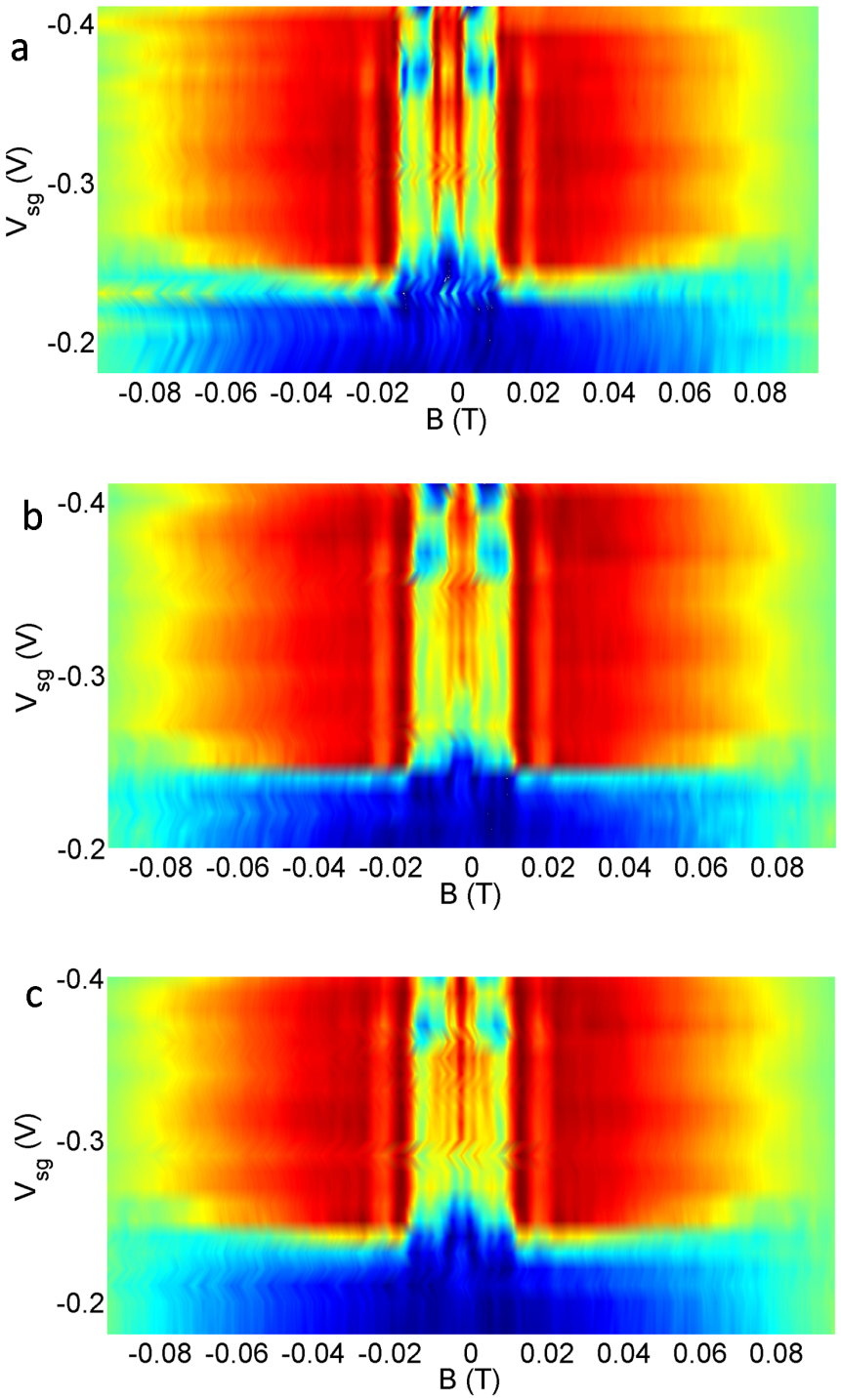

Fig. 6.16 **Colour-plot of magnetoresistance as a function of detector gate voltage.** Regions of red/orange are of large resistance and regions which are blue/green are of low resistance. In **a - c** injector is fixed at G_0, 2 G_0 and 3 G_0 respectively. It is clear that more peaks are resolved when the detector opens up. Comparison between **a - c** shows that intensity of the peaks at higher magnetic field are enhanced (become more red) at larger injector conductance.

6.4 Magnetoresistance as a function of detector conductance

In previous sections, the detector is fixed at given conductance and thus the observation is mainly due to the property of injector and cavity, in this section, a complementary experiment is performed where the injector is fixed and detector is varied. In this experiment the current is still fed from injector to detector, therefore the measurement is different from the one exchanges the role of injector and detector. Although tuning the detector influences the angular distribution of electrons via adjusting right cavity, however, compared to changing injector which affects both direct transport and reflection, the modulation of angular distribution by the detector is less significant. Instead, detector affects the result via diffraction of electrons, in other words, experiment in this section is a close analogy to Young's slit experiment.

Figure 6.15 shows representative magnetoresistance at different detector conductances to give a quick look on the evolution of the result against detector conductance. A more detailed study on the electronic split experiment is present in figure 6.16 where detector is slowly open and injector is set to G_0, 2 G_0 an 3 G_0 for plot (a) - (c) respectively. When the injector is set to G_0 (plot (a)), initially a broad central peak is observed when the detector conductance is small and then the central peak split into two main peaks (the red strips around 0 T) at higher detector conductance. Meanwhile the intensity of satellite peaks (the yellow strip) also get enhanced with increasing detector conductance. When for injector set at 2 G_0 and 3 G_0 (plot (b) and (c)), the story is slightly different, the broad peak structure at large detector voltage develops into 5 peaks with increasing detector conductance, the separation between peaks slowly enlarges with increasing detector conductance. Also, it is interesting to notice the 5 peaks are better resolved when injector is set to 3 G_0 compared to 2 G_0. When detector is swept to 2D regimes, the intensity of all the features reduced significantly in the case of all the three injector conductance.

The difference between the three plots is apparently due to angular distribution of injected electrons, while the change of magnetoresistance for a given injector conductance arises from different mechanism.

One of the possible explanations for the observation is based on diffraction of electron through a single slit. In an optical slit, the separation Δd between different diffraction patterns have a general form,

$$\Delta d = \frac{D}{a_0} \tag{6.5}$$

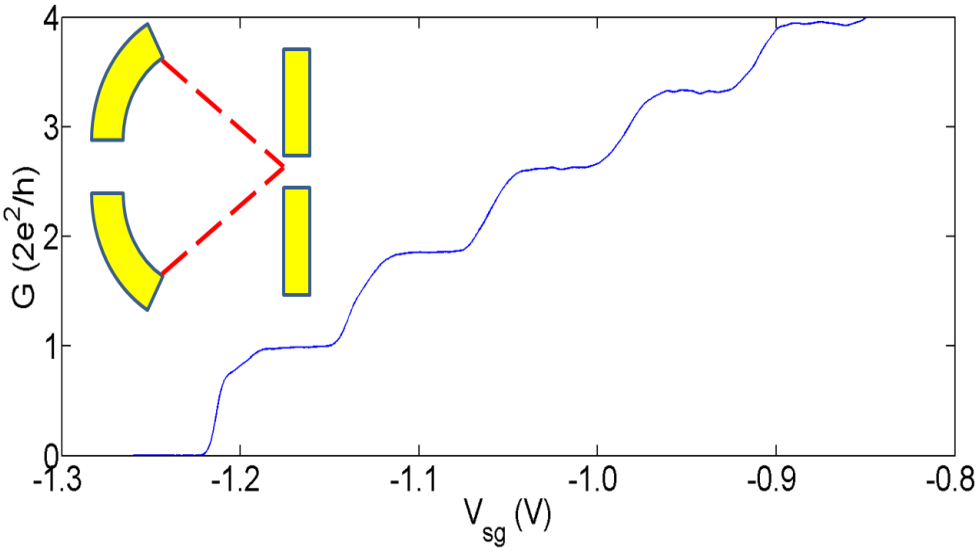

Fig. 6.17 **Schematic and characteristic of cavity-split gate device.** The flat split gate shows typical behaviour where quantized conductance plateaus are well resolved. Inset: the arc-shaped QPC is identical to the one used in double cavity device, with its focal point aligned with the entrance barrier of the flat QPC.

where D is distance between the 'slit' and 'screen' while a_0 is the width of the 'slit'. In the conventional slit experiment the apparatus is moveable to detect the spatial distribution of particles, in the magnetoresistance measurement present here, the apparatus (detector QPC) is spatially fixed but the distribution of electrons is modified by magnetic field, so the role of Δd is replaced by ΔB via such a way,

$$\Delta B \propto \frac{1}{\Delta d} \tag{6.6}$$

because magnetic field squeezes the distribution of electrons. Thereby, it is straight forward to find out that ΔB is small when the slit (detector QPC) is narrow and thus all the diffraction patten concentrates at centre and gives a broad structure, ΔB increases when the slit slowly opens up and thereby the diffraction patten spreads apart and becomes resolved, opening the detector even further (i.e. detector is swept to 1D-2D transition regime) leads to the relaxation of diffraction condition that wavelength should be comparable with slit size resulting in the disappearance of diffraction pattern.

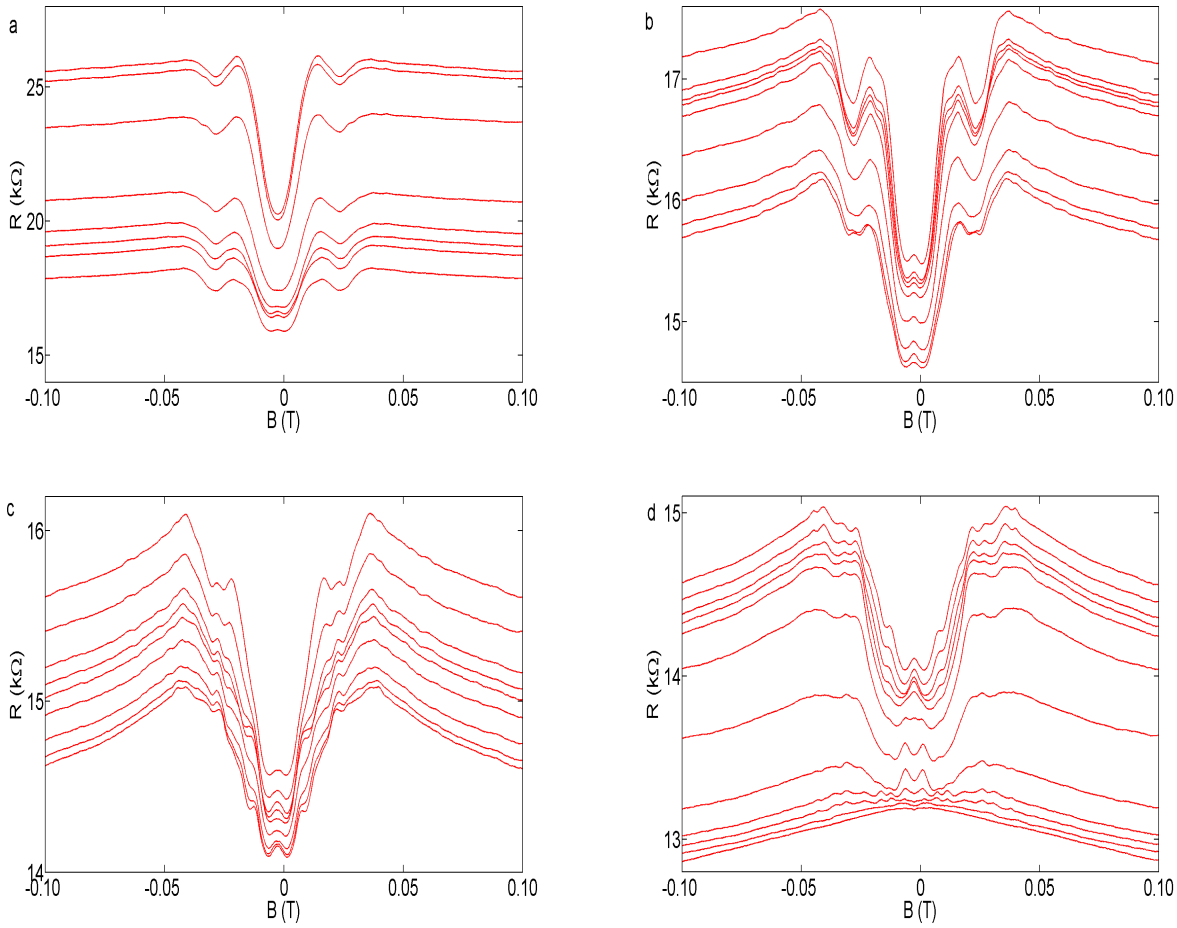

Fig. 6.18 **Magnetoresistance of the cavity-split gate system as a function of injector conductance.** Detector conductance is fixed at G_0. **a**, result in regime 1 (G_0 to 2 G_0), a pronounced dip occurs around 0 T with its depth decreases when gate voltage of injector V_i become less negative. **b**, result in regime 2 (2 G_0 to 3 G_0), a peak superposes on the central dip, the strength of the small peak fluctuates against injector conductance V_i.**c**, result in regime 3 (3 G_0 to 4 G_0), behaviour is similar to regime 2, however, the residual peaks become more complicated. **d**, result in regime 4 (4 G_0 to fully open), central peak gradually splits into more sub-peaks and eventually all the features smear out with injector fully open.

6.5 Magnetoresistance in a cavity-split gate device

To confirm result of double cavity device does arise from the specially designed configuration, we present magnetoresistance from a cavity-split gate device as shown in figure 6.17. In this device, the arch-shaped gate at the detector end of the double cavity device is replaced with a conventional flat split gate device, the focal point of the arc-shaped gate at the injector end aligns with the entrance potential barrier of flat split gate. Thereby in this case only one cavity is defined.

For the magnetoresistance measurement the arc-shaped QPC is used as injector and normal split gate is used as detector. Figure 6.18 presents detail of magnetoresistance as a function injector conductance while detector is fixed at G_0. The result is quite different from that of double-cavity device.

In regime 1, the injector is tuned from G_0 to 2 G_0, a pronounced dip is observed around 0 T while in the double cavity device a tri-peak structure forms in the same regime. The dip become shallow with injector opening up. This dip is similar to dip arises from weak anti-localization, however, spin-orbit coupling is weak in GaAs thus the condition for weak anti-localization (eq.(6.4)) is hard to fulfil. On the other hand, strong residual peaks occur at $\pm$ 30 mT and these residual peaks are similar to those observed in the double cavity regime.

Regime 2 (2 $G_0 \leq G_i \leq$ 3 G_0) and regime 3 (3 $G_0 \leq G_i \leq$ 4 G_0) shows similar behaviour. A small peak almost occurs at 0T superposes on the dip. More interestingly, the strength of this peak fluctuates against injector conductance. Meanwhile, the shape of the peak always remain as Lorentzian shape which is likely due to the irregular reflection introduced by the flat split gate.

In regime 4 (4 G_0 to fully open), the central peak gradually splits into more sub-peaks and eventually all the features smear out with injector fully open. This behaviour is similar to that observed in double cavity device.

The fluctuation of the central peak provides more information on the difference between the double-cavity device and cavity-split gate device. Figure 6.19 shows the relatively height of the central structure as a function of injector conductance with detector fixed at G_0, 2 G_0 and 3 G_0 respectively, it is noted that ΔR roughly follows an odd-even trend, weakens at odd numbered conductance plateaus and enhanced at even numbered plateaus, and finally reduces significantly when the injector is tuned into 2D regime. On the other hand, as shown in figure 6.11, ΔR get enhanced at all the conductance plateaus in the double-cavity setup. This may be because in the double cavity devices electrons are modulated by the two cavity simultaneously while in cavity-split gate device it is only tuned by one cavity, thus the phase

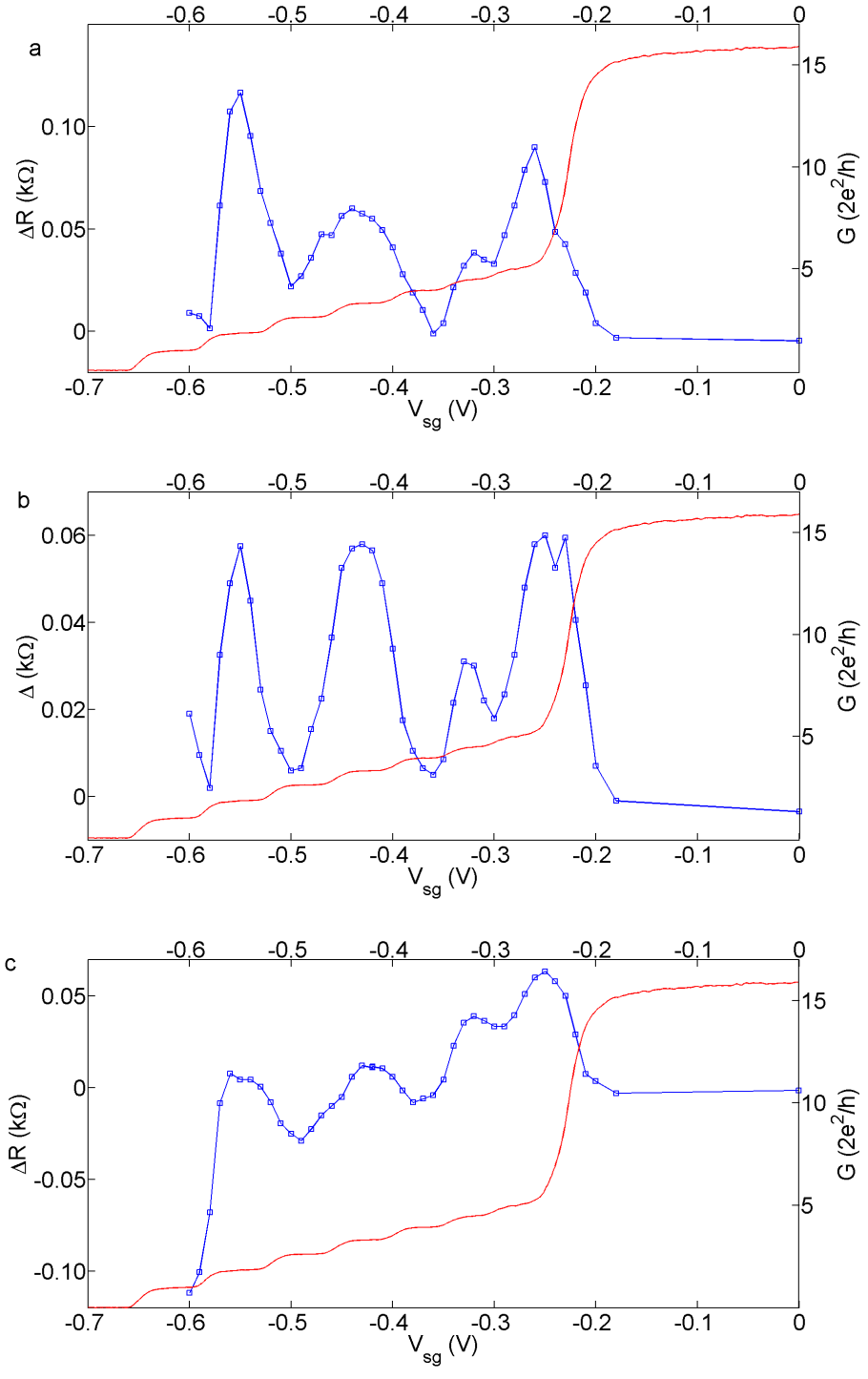

Fig. 6.19 **Height of the central peak as a function of injector conductance for the cavity-split gate device.** The height is defined as the ΔR (0) = R (0) - R(1 mT). In plot **a - c**, the detector is fixed at G_0, 2 G_0 and 3 G_0 respectively, it can be noted that the periodicity of fluctuation of ΔR roughly follows an odd-even trend (weakens at odd conductance plateaus and enhanced at even plateaus) at all the three detector conductance. ΔR reduces significantly when the injector is tuned into 2D regime.

change with the same propagation length is doubled in double cavity system compared to device here. Nevertheless, the comparison between figure 6.11 and figure 6.19 stresses that the presence of the peaks of ΔR is not due to the 1D subbands only but also depends on the coupling effect.

In brief the dramatical difference between the double cavity system and cavity-split gate device emphasis the importance role of presence of both cavity.

6.6 Conclusion

In conclusion we have shown anomalous magnetoresistance measured in a specially designed double-cavity device. The evolution of the line shape of magnetoresistance indicates the system takes a transition from ergodic and chaotic regime where the line shape is Lorentzian to non-ergodic and regular regime where the line shape is linear and then eventually altered into ergodic and chaotic motion, such change in line shape is most likely due to the reflection induced by the deformation of the arc-shaped potential barrier in the vicinity of injector and detector QPC as well as the modulation on the electron momentum due to the inhomogeneous cavity states. The mechanism is further confirmed by a reference experiment performed with a cavity-split gate device where the magnetoresistance always takes a Lorentzian line shape.

The device demonstrated here is a promising prototype of a quantum bus which is the main building block in the quantum computer, this quantum bus has two channels one is a chaotic channel and one is a regular channel and the control/switch of the two channel is highly sensitive to gate voltage.

The main observations are summarized as below:

(I) A novel prototype of quantum bus is proposed where the reliability of quantum information transport is enhanced by the use of quantum cavities;

(II) Anomalous magnetoresistance feature is observed in a double-cavity device;

(III) The line shape of the central magnetoresistance feature is found to follow a Lorentzian (chaotic motion) $\rightarrow$ linear (linear motion) $\rightarrow$ Lorentzian (chaotic motion) evolution, the indicates the quantum bus have two function mode;

(IV) The height of the central magnetoresistance feature shows an oscillation against injector conductance, such an oscillation is a sign that the information from a given channel is transported correctly from the injector through the cavity to the detector, if the electrons carry the information are missed in the 2DEG there will not be an oscillation (when detector is fixed a particular conductance), because the information carriers (the injected electrons) are then indistinguishable from other 2D electrons;

(V) The temperature dependence shows an anomalous odd-even effect which needs further investigation.

Chapter 7

Conclusion and future work

7.1 Summary

In this thesis, integrated quantum devices defined using a split gate technique are studied experimentally. These integrated devices provide a novel platform to investigate the properties of a quantum system, such as the spin polarization. Information extracted from these integrated devices leads to a comprehensive understanding of puzzling phenomenon such as 0.7 anomaly. Meanwhile, these devices are suitable for studying quantum entanglement because perturbation due to measurement is minimized in the non-local setup. Devices demonstrated here are also promising to be used as building block such as a quantum injector/detector or a quantum bus for a more complicated quantum system.

In chapter 4, a transverse electron focusing in n-type GaAs heterojunction is presented where a pronounced splitting of the odd focusing numbered peak are observed. From the asymmetry of sub-peaks of the first focusing, the spin polarization is extracted directly, this provides direct evidence for intrinsic spin polarization in a quasi-one-dimensional system. Parameters which may affect transverse electron focusing are studied systemically. Changing the shape of the injector, thus tuning the adiabaticity of the injection process, can influence the presence of peak splitting or not, with the shape and non-adiabatic injector the peak splitting is absent while peak splitting is observed with the flat and adiabatic injector. Adjusting the length of injector affects the spin polarization, the longer the channel the higher the spin polarization can be achieved, this highlights the role of exchange interaction in the quasi-1D channel. Applying dc source-drain bias leads to such a result, peak splitting is preserved with negative bias while it is smeared out with positive bias when the bias is above a particular value (0.5 mV in the experiment), this proves the existence of a spin-gap.

In chapter 5, the coupling between different quantum devices are investigated by using an integrated quantum device consisting of a QPC and an electronic cavity, where the cavity is defined with an arc-shaped gate and an inclined reflector. Unique structure such as the double-peak structure occurs in the 1D-2D transition regime of the arc-shaped QPC and fine oscillations associated with conductance plateaus and 0.7 anomaly are observed when the reflector voltage is sufficient negative and these features smear out when the reflector voltage is less negative. The double-peak structure or fine oscillations are proved to arise from the coupling between the discrete states in the QPC and continuum cavity state by the manifestation of Fano resonance via tuning reflector voltage or small transverse magnetic field.

In chapter 6, quantum interference in a double-cavity system is studied by magneo-resistance measurement. An unique evolution of the line shape of the magnetoresistance is observed, the magnetoresistance has a Lorentzian shape, corresponding to ergodic and chaotic motion, when the injector conductance is sufficient small and then alter into linear line shape arises from non-ergodic and regular motion when the injector opens further and finally a Lorentzian shape when the injector opens widely. Apart from the line shape, the strength of the magnetoresistance is found to fluctuate with injector conductance. It get enhanced at conductance plateaus and weakens elsewhere. Such behaviours are likely to arise from both deformation of the arch-shaped potential barrier at the vicinity of injector and detector QPC as well as the non-uniform spatial distribution of the cavity state.

7.2 Future work

Experiments presented above can be further extended by integrating these device together. Among all the novel experiments, those directly related to quantum entanglement are of particular interest, and thus below several possible experiments that can be used to monitor entanglement are discussed.

Detecting entanglement with transverse electron focusing

The basic principle of the entanglement is that if two electrons are entangled together when one of the electrons is perturbed and changes its state, the other electron will change its state accordingly and simultaneously. In order to confirm the existing of entanglement it is crucial to decide what state/parameter to monitor. The transverse focusing experiment can be used to monitor electron spin, at least the imbalance of spin-up and spin-down, via the focusing

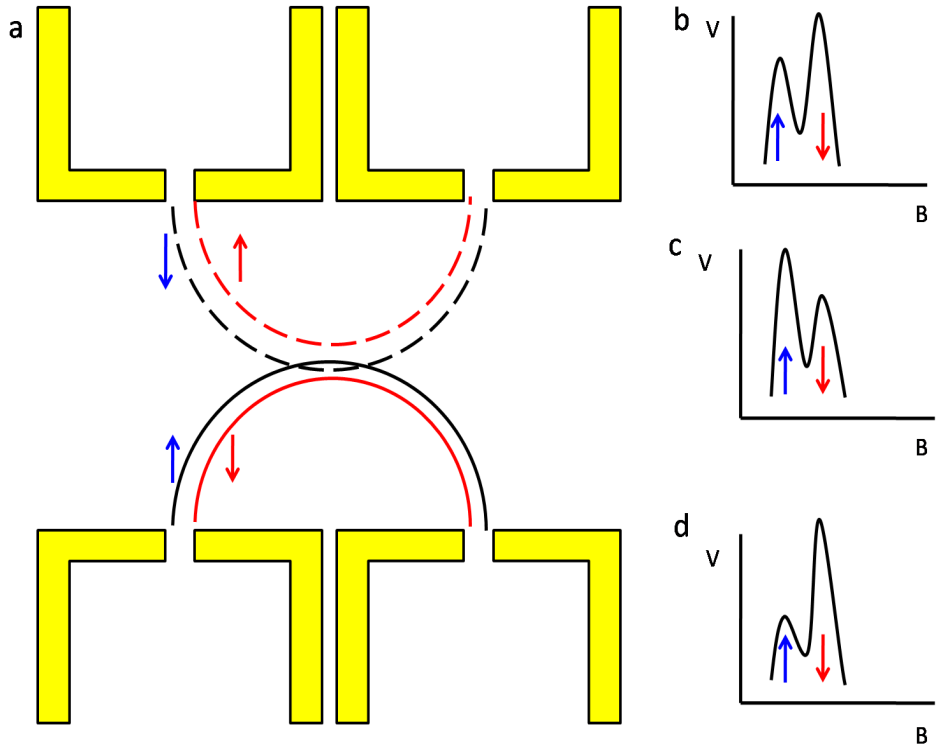

Fig. 7.1 **Detecting entanglement with transverse electron focusing technique.** **a**, schematic of the device, two pairs of transverse electron focusing devices are used (the upper pair is referred as pair-A, the lower pair is pair-B), the separation between pair-A and pair-B is carefully designed so that only the outer branch of pair-A can scatter with outer branch of pair-B. **b**, first focusing peak of pair-B measured individually, the gate voltage of the injector of pair-B is tuned that the spin-down branch has larger electron population compared to the spin-down branch (the injector of pair-A is tuned in the same way). **c**, first focusing peak of pair-A after the scattering shown in **a** if the injected electrons are entangled, the peak intensity will swap compared to **b**. **d**, first focusing peak of pair-A after the scattering if the injected electrons are not entangled, the intensity of sub-peak corresponding to spin-up electrons reduces compared to result in **b** while the peak corresponding to spin-up electrons is enhanced.

peak splitting, thus it is expected that if one of the entangled electrons alters its spin and the other one flip the spin accordingly, then the in terms of focusing spectrum the intensity of the two sub-peaks should exchange.

However, similar results can occur if the two electrons are actually not entangled but the spin of them are affected simultaneously by the perturbation, e.g. if two electrons with opposite spin pass through an asymmetrically biased 1D channel spin of the electrons would precess in opposite direction due to the lateral electric field even the two electrons are not entangled.

Thus it is necessary to find a way to selectively control the spin orientation of the target electrons without affecting other electrons directly, this can be possibly achieved by integrating two transverse electron focusing pairs (each pair consisting an injector and a detector, and the two pairs are denoted as pair-A and pair-B) as shown in figure 7.1, the separation of the focusing pairs is designed properly so that only the outer branch of pair-A can scatter with outer branch of pair-B. Assuming the spin configuration of the injected electrons from pair-A and pair-B is as illustrated in the figure, after the scattering the electrons of outer branches from pair-A and pair-B will exchange their spin, due to the spin-flip the electrons initially follow the outer branch emerge into the inner branch (this is because the spin-orbit interaction induced correction to the momentum depends on the spin-orientation).

Assuming the gate voltage of the injector of pair-B is set at a value such that the spin-down branch (inner branch) has larger electron population compared to the spin-down branch (outer branch), after the scattering, the outer branch electrons will flip their spin, i.e. from spin-up to spin-down, so that they have to jump to inner branch due to spin-orbit interaction, however, depends on whether or not the injected electrons from pair-B are entangled, there would be two scenarios: (I), if the injected electrons are entangled, the inner branch electrons will flip their spin accordingly, thereby they jump to outer branch, as a result, the intensity of the sub-peaks swap compared to the result before scatter; (II), if the injected electrons are not entangled, the inner branch electrons will not flip spin and thus still follow the inner trajectory, however, some electrons which initially take the outer branch have to jump into the inner trajectory due to the spin-flip scattering, so that electron population of inner branch increases, as a result, the intensity of the sub-peak corresponding to inner branch is enhanced compared to result before scattering.

References

[1] K. v. Klitzing, G. Dorda, and M. Pepper. New method for high-accuracy determination of the fine-structure constant based on quantized Hall resistance. *Phys. Rev. Lett.*, 45:494–497, Aug 1980.

[2] D. C. Tsui, H. L. Stormer, and A. C. Gossard. Two-dimensional magnetotransport in the extreme quantum limit. *Phys. Rev. Lett.*, 48:1559–1562, May 1982.

[3] D. A. Wharam, T. J. Thornton, R. Newbury, M. Pepper, H. Ahmed, J. E. F. Frost, D. G. Hasko, D. C. Peacock, D A. Ritchie, and G. A. C Jones. One-dimensional transport and the quantisation of the ballistic resistance. *Journal of Physics C: Solid State Physics*, 21(8):L209, 1988.

[4] B. J. van Wees, H. van Houten, C. W. J. Beenakker, J. G. Williamson, L. P. Kouwenhoven, D. van der Marel, and C. T. Foxon. Quantized conductance of point contacts in a two-dimensional electron gas. *Phys. Rev. Lett.*, 60:848–850, Feb 1988.

[5] U. Meirav, M. A. Kastner, and S. J. Wind. Single-electron charging and periodic conductance resonances in GaAs nanostructures. *Phys. Rev. Lett.*, 65:771–774, Aug 1990.

[6] Ian M Mills, Peter J Mohr, Terry J Quinn, Barry N Taylor, and Edwin R Williams. Redefinition of the kilogram, Ampere, kelvin and mole: a proposed approach to implementing CIPM recommendation 1 (CI-2005). *Metrologia*, 43(3):227, 2006.

[7] R. Landauer. Spatial variation of currents and fields due to localized scatterers in metallic conduction. *IBM Journal of Research and Development*, 1(3):223–231, July 1957.

[8] R. Landauer. Electrical resistance of disordered one-dimensional lattices. *Philosophical Magazine*, 21(172):863–867, 1970.

[9] M. Büttiker, Y. Imry, R. Landauer, and S. Pinhas. Generalized many-channel conductance formula with application to small rings. *Phys. Rev. B*, 31:6207–6215, May 1985.

[10] *1D hetero-structure tool for atomistic simulation of nano-devices*, volume 0, 09 2008.

[11] H.L. Störmer, R. Dingle, A.C. Gossard, W. Wiegmann, and M.D. Sturge. Two-dimensional electron gas at a semiconductor-semiconductor interface. *Solid State Communications*, 29(10):705 – 709, 1979.

[12] Christoph Siegert, Arindam Ghosh, Michael Pepper, Ian Farrer, and David A Ritchie. The possibility of an intrinsic spin lattice in high-mobility semiconductor heterostructures. *Nature Physics*, 3(5):315–318, 2007.

[13] B. E. Kane, L. N. Pfeiffer, K. W. West, and C. K. Harnett. Variable density high mobility two-dimensional electron and hole gases in a gated GaAs/$Al_xGa_{1-x}As$ heterostructure. *Applied Physics Letters*, 63(15):2132–2134, 1993.

[14] K. S. Pyshkin, C. J. B. Ford, R. H. Harrell, M. Pepper, E. H. Linfield, and D. A. Ritchie. Spin splitting of one-dimensional subbands in high quality quantum wires at zero magnetic field. *Phys. Rev. B*, 62:15842–15850, Dec 2000.

[15] T. J. Thornton, M. Pepper, H. Ahmed, D. Andrews, and G. J. Davies. One-dimensional conduction in the 2D electron gas of a GaAs-AlGaAs heterojunction. *Phys. Rev. Lett.*, 56:1198–1201, Mar 1986.

[16] M. Büttiker. Quantized transmission of a saddle-point constriction. *Phys. Rev. B*, 41:7906–7909, Apr 1990.

[17] John H. Davies, Ivan A. Larkin, and E. V. Sukhorukov. Modeling the patterned two−dimensional electron gas: Electrostatics. *Journal of Applied Physics*, 77(9):4504–4512, 1995.

[18] L Martin-Moreno, J T Nicholls, N K Patel, and M Pepper. Non-linear conductance of a saddle-point constriction. *Journal of Physics: Condensed Matter*, 4(5):1323, 1992.

[19] K. J. Thomas, J. T. Nicholls, M. Y. Simmons, M. Pepper, D. R. Mace, and D. A. Ritchie. Possible spin polarization in a one-dimensional electron gas. *Phys. Rev. Lett.*, 77:135–138, Jul 1996.

[20] R. de Picciotto, L. N. Pfeiffer, K. W. Baldwin, and K. W. West. Nonlinear response of a clean one-dimensional wire. *Phys. Rev. Lett.*, 92:036805, Jan 2004.

[21] Y. Hirayama, T. Saku, and Y. Horikoshi. Electronic transport through very short and narrow channels constricted in gaas by highly resistive Ga-implanted regions. *Phys. Rev. B*, 39:5535–5537, Mar 1989.

[22] Takashi Honda, Seigo Tarucha, Tadashi Saku, and Yasuhiro Tokura. Quantized conductance observed in quantum wires 2 to 10 μm long. *Japanese Journal of Applied Physics*, 34(1A):L72, 1995.

[23] A. Yacoby, H. L. Stormer, Ned S. Wingreen, L. N. Pfeiffer, K. W. Baldwin, and K. W. West. Nonuniversal conductance quantization in quantum wires. *Phys. Rev. Lett.*, 77:4612–4615, Nov 1996.

[24] NJ Curson, R Nemutudi, NJ Appleyard, M Pepper, DA Ritchie, and GAC Jones. Ballistic transport in a $GaAs/Al_xGa_{1-x}As$ one-dimensional channel fabricated using an atomic force microscope. *Applied Physics Letters*, 78:3466, 2001.

[25] Elliott Lieb and Daniel Mattis. Theory of ferromagnetism and the ordering of electronic energy levels. *Phys. Rev.*, 125:164–172, Jan 1962.

[26] K. J. Thomas, J. T. Nicholls, M. Y. Simmons, M. Pepper, D. R. Mace, and D. A. Ritchie. Possible spin polarization in a one-dimensional electron gas. *Phys. Rev. Lett.*, 77:135–138, Jul 1996.

[27] K. J. Thomas, J. T. Nicholls, N. J. Appleyard, M. Y. Simmons, M. Pepper, D. R. Mace, W. R. Tribe, and D. A. Ritchie. Interaction effects in a one-dimensional constriction. *Phys. Rev. B*, 58:4846–4852, Aug 1998.

[28] K. F. Berggren, T. J. Thornton, D. J. Newson, and M. Pepper. Magnetic depopulation of 1d subbands in a narrow 2D electron gas in a GaAs:AlGaAs heterojunction. *Phys. Rev. Lett.*, 57:1769–1772, Oct 1986.

[29] G. Salis, T. Heinzel, K. Ensslin, O. J. Homan, W. Bächtold, K. Maranowski, and A. C. Gossard. Mode spectroscopy and level coupling in ballistic electron waveguides. *Phys. Rev. B*, 60:7756–7759, Sep 1999.

[30] E. Tutuc, S. Melinte, and M. Shayegan. Spin polarization and g factor of a dilute GaAs two-dimensional electron system. *Phys. Rev. Lett.*, 88:036805, Jan 2002.

[31] T.-M. Chen, A. C. Graham, M. Pepper, I. Farrer, and D. A. Ritchie. Non-Kondo zero-bias anomaly in quantum wires. *Phys. Rev. B*, 79:153303, Apr 2009.

[32] T.-M. Chen, A. C. Graham, M. Pepper, F. Sfigakis, I. Farrer, and D. A. Ritchie. Odd-even spin effects and variation of g factor in a quasi-one-dimensional subband. *Phys. Rev. B*, 79:081301, Feb 2009.

[33] R. C. Liu, B. Odom, Y. Yamamoto, and S. Tarucha. Quantum interference in electron collision. *Nature*, 391:263–265, Jan 1998.

[34] M. Reznikov, M. Heiblum, Hadas Shtrikman, and D. Mahalu. Temporal correlation of electrons: Suppression of shot noise in a ballistic quantum point contact. *Phys. Rev. Lett.*, 75:3340–3343, Oct 1995.

[35] P. Roche, J. Ségala, D. C. Glattli, J. T. Nicholls, M. Pepper, A. C. Graham, K. J. Thomas, M. Y. Simmons, and D. A. Ritchie. Fano factor reduction on the 0.7 conductance structure of a ballistic one-dimensional wire. *Phys. Rev. Lett.*, 93:116602, Sep 2004.

[36] N. J. Appleyard, J. T. Nicholls, M. Pepper, W. R. Tribe, M. Y. Simmons, and D. A. Ritchie. Direction-resolved transport and possible many-body effects in one-dimensional thermopower. *Phys. Rev. B*, 62:R16275–R16278, Dec 2000.

[37] Toshiyuki Kobayashi, Shoei Tsuruta, Satoshi Sasaki, Hiroyuki Tamura, and Tatsushi Akazaki. Transmission-phase measurement of the 0.7 anomaly in a quantum point contact. *arXiv preprint arXiv:1306.6689*, 2013.

[38] N. J. Appleyard, J. T. Nicholls, M. Y. Simmons, W. R. Tribe, and M. Pepper. Thermometer for the 2D electron gas using 1D thermopower. *Phys. Rev. Lett.*, 81:3491–3494, Oct 1998.

[39] Nevill Francis Mott and Harry Jones. *The theory of the properties of metals and alloys*. Courier Corporation, 1958.

[40] Minoru Kawamura, Keiji Ono, Peter Stano, Kimitoshi Kono, and Tomosuke Aono. Electronic magnetization of a quantum point contact measured by nuclear magnetic resonance. *Phys. Rev. Lett.*, 115:036601, Jul 2015.

[41] CP Slichter. *Principles of Nuclear Magnetism*. Oxford University, 1961.

[42] Chuan-Kui Wang and K.-F. Berggren. Spin splitting of subbands in quasi-one-dimensional electron quantum channels. *Phys. Rev. B*, 54:R14257–R14260, Nov 1996.

[43] Chuan-Kui Wang and K.-F. Berggren. Local spin polarization in ballistic quantum point contacts. *Phys. Rev. B*, 57:4552–4556, Feb 1998.

[44] K. F. Berggren and I. I. Yakimenko. Effects of exchange and electron correlation on conductance and nanomagnetism in ballistic semiconductor quantum point contacts. *Phys. Rev. B*, 66:085323, Aug 2002.

[45] Henrik Bruus, Vadim V Cheianov, and Karsten Flensberg. The anomalous 0.5 and 0.7 conductance plateaus in quantum point contacts. *Physica E: Low-dimensional Systems and Nanostructures*, 10(1–3):97 – 102, 2001. Proceedings of the First International Conference on the Physics and Applications of Spin-Related Phenomena in Semiconductors.

[46] D. J. Reilly, T. M. Buehler, J. L. O'Brien, A. R. Hamilton, A. S. Dzurak, R. G. Clark, B. E. Kane, L. N. Pfeiffer, and K. W. West. Density-dependent spin polarization in ultra-low-disorder quantum wires. *Phys. Rev. Lett.*, 89:246801, Nov 2002.

[47] D. J. Reilly. Phenomenological model for the 0.7 conductance feature in quantum wires. *Phys. Rev. B*, 72:033309, Jul 2005.

[48] D. J. Reilly, G. R. Facer, A. S. Dzurak, B. E. Kane, R. G. Clark, P. J. Stiles, R. G. Clark, A. R. Hamilton, J. L. O'Brien, N. E. Lumpkin, L. N. Pfeiffer, and K. W. West. Many-body spin-related phenomena in ultra low-disorder quantum wires. *Phys. Rev. B*, 63:121311, Mar 2001.

[49] David Goldhaber-Gordon, Hadas Shtrikman, D Mahalu, David Abusch-Magder, U Meirav, and MA Kastner. Kondo effect in a single-electron transistor. *Nature*, 391(6663):156–159, 1998.

[50] Sara M Cronenwett, Tjerk H Oosterkamp, and Leo P Kouwenhoven. A tunable Kondo effect in quantum dots. *Science*, 281(5376):540–544, 1998.

[51] S. M. Cronenwett, H. J. Lynch, D. Goldhaber-Gordon, L. P. Kouwenhoven, C. M. Marcus, K. Hirose, N. S. Wingreen, and V. Umansky. Low-temperature fate of the 0.7 structure in a point contact: A Kondo-like correlated state in an open system. *Phys. Rev. Lett.*, 88:226805, May 2002.

[52] PE Lindelof. Effect on conductance of an isomer state in a quantum point contact. In *Advanced Optical Materials and Devices*, pages 77–85. International Society for Optics and Photonics, 2001.

[53] L. I. Glazman and A. V. Khaetskii. Nonlinear quantum conductance of a lateral microconstraint in a heterostructure. *EPL (Europhysics Letters)*, 9(3):263, 1989.

[54] A. Kristensen, H. Bruus, A. E. Hansen, J. B. Jensen, P. E. Lindelof, C. J. Marckmann, J. Nygård, C. B. Sørensen, F. Beuscher, A. Forchel, and M. Michel. Bias and temperature dependence of the 0.7 conductance anomaly in quantum point contacts. *Phys. Rev. B*, 62:10950–10957, Oct 2000.

[55] T.-M. Chen, A. C. Graham, M. Pepper, I. Farrer, and D. A. Ritchie. Bias-controlled spin polarization in quantum wires. *Applied Physics Letters*, 93(3), 2008.

[56] H. van Houten, C. W. J. Beenakker, J. G. Williamson, M. E. I. Broekaart, P. H. M. van Loosdrecht, B. J. van Wees, J. E. Mooij, C. T. Foxon, and J. J. Harris. Coherent electron focusing with quantum point contacts in a two-dimensional electron gas. *Phys. Rev. B*, 39:8556–8575, Apr 1989.

[57] L. P. Rokhinson, L. N. Pfeiffer, and K. W. West. Spontaneous spin polarization in quantum point contacts. *Phys. Rev. Lett.*, 96:156602, Apr 2006.

[58] A.R. Dedigama, D. Deen, S.Q. Murphy, N. Goel, J.C. Keay, M.B. Santos, K. Suzuki, S. Miyashita, and Y. Hirayama. Current focusing in InSb heterostructures. *Physica E: Low-dimensional Systems and Nanostructures*, 34(1–2):647 – 650, 2006. Proceedings of the 16th International Conference on Electronic Properties of Two-Dimensional Systems (EP2DS-16).

[59] Stefano Chesi, Gabriele F. Giuliani, L. P. Rokhinson, L. N. Pfeiffer, and K. W. West. Anomalous spin-resolved point-contact transmission of holes due to cubic Rashba spin-orbit coupling. *Phys. Rev. Lett.*, 106:236601, Jun 2011.

[60] Gonzalo Usaj and C. A. Balseiro. Transverse electron focusing in systems with spin-orbit coupling. *Phys. Rev. B*, 70:041301, Jul 2004.

[61] M J Uren, R A Davies, M Kaveh, and M Pepper. Magnetic delocalisation of a two-dimensional electron gas and the quantum law of electron-electron scattering. *Journal of Physics C: Solid State Physics*, 14(13):L395, 1981.

[62] R A Davies, M J Uren, and M Pepper. Magnetic separation of localisation and interaction effects in a two-dimensional electron gas at low temperatures. *Journal of Physics C: Solid State Physics*, 14(19):L531, 1981.

[63] M Kaveh, M J Uren, R A Davies, and M Pepper. Localisation in disordered two-dimensional systems and the universal dependence on diffusion length. *Journal of Physics C: Solid State Physics*, 14(14):L413, 1981.

[64] C.J.B. Ford, T.J. Thornton, R. Newbury, M. Pepper, H. Ahmed, G.J. Davies, and D. Andrews. Transport in GaAs heterojunction ring structures. *Superlattices and Microstructures*, 4(4):541 – 544, 1988.

[65] Adrian Bachtold, Christoph Strunk, Jean-Paul Salvetat, Jean-Marc Bonard, Laszló Forró, Thomas Nussbaumer, and Christian Schönenberger. Aharonov–Bohm oscillations in carbon nanotubes. *Nature*, 397(6721):673–675, 1999.

[66] Dong-In Chang, Gyong Luck Khym, Kicheon Kang, Yunchul Chung, Hu-Jong Lee, Minky Seo, Moty Heiblum, Diana Mahalu, and Vladimir Umansky. Quantum mechanical complementarity probed in a closed-loop Aharonov–Bohm interferometer. *Nature Physics*, 4(3):205–209, 2008.

[67] R. P. Taylor, R. Newbury, R. B. Dunford, P. T. Coleridge, A. S. Sachrajda, and J. A. Adams. Classical and weak localization processes in a tunable ballistic-electron cavity. *Phys. Rev. B*, 51:9801–9805, Apr 1995.

[68] J. P. Bird, D. M. Olatona, R. Newbury, R. P. Taylor, K. Ishibashi, M. Stopa, Y. Aoyagi, T. Sugano, and Y. Ochiai. Lead-induced transition to chaos in ballistic mesoscopic billiards. *Phys. Rev. B*, 52:R14336–R14339, Nov 1995.

[69] Yang Ji, Yunchul Chung, D Sprinzak, M Heiblum, D Mahalu, and Hadas Shtrikman. An electronic Mach–Zehnder interferometer. *Nature*, 422(6930):415–418, 2003.

[70] Sergey I Bozhevolnyi, Valentyn S Volkov, Eloise Devaux, Jean-Yves Laluet, and Thomas W Ebbesen. Channel plasmon subwavelength waveguide components including interferometers and ring resonators. *Nature*, 440(7083):508–511, 2006.

[71] Izhar Neder, Nissim Ofek, Y Chung, M Heiblum, D Mahalu, and V Umansky. Interference between two indistinguishable electrons from independent sources. *Nature*, 448(7151):333–337, 2007.

[72] A. W. Holleitner, C. R. Decker, H. Qin, K. Eberl, and R. H. Blick. Coherent coupling of two quantum dots embedded in an Aharonov-Bohm interferometer. *Phys. Rev. Lett.*, 87:256802, Nov 2001.

[73] Tom Jeltes, John M McNamara, Wim Hogervorst, Wim Vassen, Valentina Krachmalnicoff, Martijn Schellekens, Aurélien Perrin, Hong Chang, Denis Boiron, Alain Aspect, et al. Comparison of the Hanbury Brown–Twiss effect for bosons and fermions. *Nature*, 445(7126):402–405, 2007.

[74] Harald Kiesel, Andreas Renz, and Franz Hasselbach. Observation of Hanbury Brown–Twiss anticorrelations for free electrons. *Nature*, 418(6896):392–394, 2002.

[75] RC Liu, B Odom, Y Yamamoto, and S Tarucha. Quantum interference in electron collision. *Nature*, 391(6664):263–265, 1998.

[76] E. Bocquillon, V. Freulon, J.-M Berroir, P. Degiovanni, B. Plaçais, A. Cavanna, Y. Jin, and G. Fève. Coherence and indistinguishability of single electrons emitted by independent sources. *Science*, 339(6123):1054–1057, 2013.

[77] M. Saito, T. Usuki, M. Okada, T. Futatsugi, R. A. Kiehl, and N. Yokoyama. Coupling between one-dimensional states in a quantum point contact and an electron waveguide. *Applied Physics Letters*, 65(24), 1994.

[78] C. Rössler, D. Oehri, O. Zilberberg, G. Blatter, M. Karalic, J. Pijnenburg, A. Hofmann, T. Ihn, K. Ensslin, C. Reichl, and W. Wegscheider. Transport spectroscopy of a spin-coherent dot-cavity system. *Phys. Rev. Lett.*, 115:166603, Oct 2015.

[79] J. Fransson, M.-G. Kang, Y. Yoon, S. Xiao, Y. Ochiai, J. L. Reno, N. Aoki, and J. P. Bird. Tuning the fano resonance with an intruder continuum. *Nano Letters*, 14(2):788–793, 2014.

[80] MJ Berry, JA Katine, CM Marcus, RM Westervelt, and AC Gossard. Weak localization and conductance fluctuations in a chaotic quantum dot. *Surface science*, 305(1):495–500, 1994.

[81] W. Bauer and G. F. Bertsch. Decay of ordered and chaotic systems. *Phys. Rev. Lett.*, 65:2213–2216, Oct 1990.

[82] Friso Jacobus Jedema, AT Filip, and BJ Van Wees. Electrical spin injection and accumulation at room temperature in an all-metal mesoscopic spin valve. *Nature*, 410(6826):345–348, 2001.

[83] Nikolaos Tombros, Csaba Jozsa, Mihaita Popinciuc, Harry T Jonkman, and Bart J Van Wees. Electronic spin transport and spin precession in single graphene layers at room temperature. *Nature*, 448(7153):571–574, 2007.

[84] D A Wharam, T J Thornton, R Newbury, M Pepper, H Ahmed, J E F Frost, D G Hasko, D C Peacock, D A Ritchie, and G A C Jones. One-dimensional transport and the quantisation of the ballistic resistance. *Journal of Physics C: Solid State Physics*, 21(8):L209, 1988.

[85] B. J. van Wees, H. van Houten, C. W. J. Beenakker, J. G. Williamson, L. P. Kouwenhoven, D. van der Marel, and C. T. Foxon. Quantized conductance of point contacts in a two-dimensional electron gas. *Phys. Rev. Lett.*, 60:848–850, Feb 1988.

[86] S. M. Cronenwett, H. J. Lynch, D. Goldhaber-Gordon, L. P. Kouwenhoven, C. M. Marcus, K. Hirose, N. S. Wingreen, and V. Umansky. Low-temperature fate of the 0.7 structure in a point contact: A Kondo-like correlated state in an open system. *Phys. Rev. Lett.*, 88:226805, May 2002.

[87] Tomaž Rejec and Yigal Meir. Magnetic impurity formation in quantum point contacts. *Nature*, 442(7105):900–903, 2006.

[88] K. A. Matveev. Conductance of a quantum wire in the Wigner-crystal regime. *Phys. Rev. Lett.*, 92:106801, Mar 2004.

[89] A. Reynoso, Gonzalo Usaj, and C. A. Balseiro. Detection of spin polarized currents in quantum point contacts via transverse electron focusing. *Phys. Rev. B*, 75:085321, Feb 2007.

[90] H. van Houten, C. W. J. Beenakker, J. G. Williamson, M. E. I. Broekaart, P. H. M. van Loosdrecht, B. J. van Wees, J. E. Mooij, C. T. Foxon, and J. J. Harris. Coherent electron focusing with quantum point contacts in a two-dimensional electron gas. *Phys. Rev. B*, 39:8556–8575, Apr 1989.

[91] Gonzalo Usaj and C. A. Balseiro. Transverse electron focusing in systems with spin-orbit coupling. *Phys. Rev. B*, 70:041301, Jul 2004.

[92] L. P. Rokhinson, L. N. Pfeiffer, and K. W. West. Spontaneous spin polarization in quantum point contacts. *Phys. Rev. Lett.*, 96:156602, Apr 2006.

[93] Stefano Chesi, Gabriele F. Giuliani, L. P. Rokhinson, L. N. Pfeiffer, and K. W. West. Anomalous spin-resolved point-contact transmission of holes due to cubic Rashba spin-orbit coupling. *Phys. Rev. Lett.*, 106:236601, Jun 2011.

[94] A.R. Dedigama, D. Deen, S.Q. Murphy, N. Goel, J.C. Keay, M.B. Santos, K. Suzuki, S. Miyashita, and Y. Hirayama. Current focusing in InSb heterostructures. *Physica E: Low-dimensional Systems and Nanostructures*, 34(1–2):647 – 650, 2006.

[95] Boris L Altshuler, AG Aronov, and DE Khmelnitsky. Effects of electron-electron collisions with small energy transfers on quantum localisation. *Journal of Physics C: Solid State Physics*, 15(36):7367, 1982.

[96] T.-M. Chen, M. Pepper, I. Farrer, G. A. C. Jones, and D. A. Ritchie. All-electrical injection and detection of a spin-polarized current using 1d conductors. *Phys. Rev. Lett.*, 109:177202, Oct 2012.

[97] R. M. Potok, J. A. Folk, C. M. Marcus, and V. Umansky. Detecting spin-polarized currents in ballistic nanostructures. *Phys. Rev. Lett.*, 89:266602, Dec 2002.

[98] Andor Kormányos. Semiclassical study of edge states and transverse electron focusing for strong spin-orbit coupling. *Phys. Rev. B*, 82:155316, Oct 2010.

[99] D A Wharam, M Pepper, H Ahmed, J E F Frost, D G Hasko, D C Peacock, D A Ritchie, and G A C Jones. Addition of the one-dimensional quantised ballistic resistance. *Journal of Physics C: Solid State Physics*, 21(24):L887, 1988.

[100] A. J. Daneshvar, C. J. B. Ford, A. R. Hamilton, M. Y. Simmons, M. Pepper, and D. A. Ritchie. Enhanced g factors of a one-dimensional hole gas with quantized conductance. *Phys. Rev. B*, 55:R13409–R13412, May 1997.

[101] K Ohtsuka, S Takaoka, K Oto, K Murase, and K Gamo. Distortion of Fermi surface induced by parallel magnetic field in a two-dimensional electron gas. *Physica B: Condensed Matter*, 249–251:780 – 783, 1998.

[102] D. Kamburov, M. A. Mueed, M. Shayegan, L. N. Pfeiffer, K. W. West, K. W. Baldwin, J. J. D. Lee, and R. Winkler. Anisotropic Fermi contour of (001) GaAs electrons in parallel magnetic fields. *Phys. Rev. B*, 88:125435, Sep 2013.

[103] J. D. Fletcher, P. See, H. Howe, M. Pepper, S. P. Giblin, J. P. Griffiths, G. A. C. Jones, I. Farrer, D. A. Ritchie, T. J. B. M. Janssen, and M. Kataoka. Clock-controlled emission of single-electron wave packets in a solid-state circuit. *Phys. Rev. Lett.*, 111:216807, Nov 2013.

[104] A. Yacoby, U. Sivan, C. P. Umbach, and J. M. Hong. Interference and dephasing by electron-electron interaction on length scales shorter than the elastic mean free path. *Phys. Rev. Lett.*, 66:1938–1941, Apr 1991.

[105] R. I. Hornsey, J. R. A. Cleaver, and H. Ahmed. Transverse hot-electron focusing. *Phys. Rev. B*, 48:14679–14682, Nov 1993.

[106] B. Laikhtman, U. Sivan, A. Yacoby, C. P. Umbach, M. Heiblum, J. A. Kash, and H. Shtrikman. Long mean free path of hot electrons selectively injected to higher subbands. *Phys. Rev. Lett.*, 65:2181–2184, Oct 1990.

[107] L. I. Glazman and M. Jonson. Global adiabatic regime in quantum ballistic transport. *Phys. Rev. B*, 41:10686–10699, May 1990.

[108] LI Glazman, GB Lesovik, DE Khmel'Nitskii, and RI Shekhter. Reflectionless quantum transport and fundamental ballistic-resistance steps in microscopic constrictions. *Soviet Journal of Experimental and Theoretical Physics Letters*, 48:238, 1988.

[109] Peter Jaksch, Irina Yakimenko, and Karl-Fredrik Berggren. From quantum point contacts to quantum wires: Density-functional calculations with exchange and correlation effects. *Phys. Rev. B*, 74:235320, Dec 2006.

[110] D A Wharam, M Pepper, R Newbury, H Ahmed, D G Hasko, D C Peacock, J E F Frost, D A Ritchie, and G A C Jones. Observation of Aharonov-Bohm oscillations in a narrow two-dimensional electron gas. *Journal of Physics: Condensed Matter*, 1(21):3369, 1989.

[111] Olga Goulko, Florian Bauer, Jan Heyder, and Jan von Delft. Effect of spin-orbit interactions on the 0.7 anomaly in quantum point contacts. *Phys. Rev. Lett.*, 113:266402, Dec 2014.

[112] L. W. Smith, H. Al-Taie, A. A. J. Lesage, F. Sfigakis, P. See, J. P. Griffiths, H. E. Beere, G. A. C. Jones, D. A. Ritchie, A. R. Hamilton, M. J. Kelly, and C. G. Smith. Dependence of the 0.7 anomaly on the curvature of the potential barrier in quantum wires. *Phys. Rev. B*, 91:235402, Jun 2015.

[113] G. Dresselhaus. Spin-orbit coupling effects in zinc blende structures. *Phys. Rev.*, 100:580–586, Oct 1955.

[114] M. Studer, M. P. Walser, S. Baer, H. Rusterholz, S. Schön, D. Schuh, W. Wegscheider, K. Ensslin, and G. Salis. Role of linear and cubic terms for drift-induced Dresselhaus spin-orbit splitting in a two-dimensional electron gas. *Phys. Rev. B*, 82:235320, Dec 2010.

[115] D. Stein, K. v. Klitzing, and G. Weimann. Electron spin resonance on GaAs – $Al_xGa_{1-x}As$ heterostructures. *Phys. Rev. Lett.*, 51:130–133, Jul 1983.

[116] M. Dobers, K. v. Klitzing, J. Schneider, G. Weimann, and K. Ploog. Electrical detection of nuclear magnetic resonance in GaAs – $Al_xGa_{1-x}As$ heterostructures. *Phys. Rev. Lett.*, 61:1650–1653, Oct 1988.

[117] Minoru Kawamura, Keiji Ono, Peter Stano, Kimitoshi Kono, and Tomosuke Aono. Electronic magnetization of a quantum point contact measured by nuclear magnetic resonance. *Phys. Rev. Lett.*, 115:036601, Jul 2015.

[118] A. Berg, M. Dobers, R. R. Gerhardts, and K. v. Klitzing. Magnetoquantum oscillations of the nuclear-spin-lattice relaxation near a two-dimensional electron gas. *Phys. Rev. Lett.*, 64:2563–2566, May 1990.

[119] S. A. Crooker and D. L. Smith. Imaging spin flows in semiconductors subject to electric, magnetic, and strain fields. *Phys. Rev. Lett.*, 94:236601, Jun 2005.

[120] K. J. Thomas, J. T. Nicholls, M. Y. Simmons, M. Pepper, D. R. Mace, and D. A. Ritchie. Possible spin polarization in a one-dimensional electron gas. *Phys. Rev. Lett.*, 77:135–138, Jul 1996.

[121] Sanjeev Kumar, Kalarikad J. Thomas, Luke W. Smith, Michael Pepper, Graham L. Creeth, Ian Farrer, David Ritchie, Geraint Jones, and Jonathan Griffiths. Many-body effects in a quasi-one-dimensional electron gas. *Phys. Rev. B*, 90:201304, Nov 2014.

[122] W. K. Hew, K. J. Thomas, M. Pepper, I. Farrer, D. Anderson, G. A. C. Jones, and D. A. Ritchie. Incipient formation of an electron lattice in a weakly confined quantum wire. *Phys. Rev. Lett.*, 102:056804, Feb 2009.

[123] C. W. J. Beenakker, H. van Houten, and B. J. van Wees. Mode interference effect in coherent electron focusing. *EPL (Europhysics Letters)*, 7(4):359, 1988.

[124] U. Fano. Effects of configuration interaction on intensities and phase shifts. *Phys. Rev.*, 124:1866–1878, Dec 1961.

[125] L. W. Molenkamp, A. A. M. Staring, C. W. J. Beenakker, R. Eppenga, C. E. Timmering, J. G. Williamson, C. J. P. M. Harmans, and C. T. Foxon. Electron-beam collimation with a quantum point contact. *Phys. Rev. B*, 41:1274–1277, Jan 1990.

[126] Cristopher C. Eugster and Jesús A. del Alamo. Tunnelling spectroscopy of an electron waveguide. *Phys. Rev. Lett.*, 67:3586–3589, Dec 1991.

[127] Y. Takagaki and D. K. Ferry. Tunnelling spectroscopy of quantum point contacts. *Phys. Rev. B*, 45:12152–12155, May 1992.

[128] Y. Takagaki and D. K. Ferry. Tunnelling spectroscopy of a quantum resonator. *J. Appl. Phys.*, 72(10), 1992.

[129] Y. Oowaki, J. E. F. Frost, L. Martin-Moreno, M. Pepper, D. A. Ritchie, and G. A. C. Jones. Enhancement of intersubband transition probability in a one-dimensional constriction. *Phys. Rev. B*, 47:4088–4091, Feb 1993.

[130] A. Yacoby, U. Sivan, C. P. Umbach, and J. M. Hong. Interference and dephasing by electron-electron interaction on length scales shorter than the elastic mean free path. *Phys. Rev. Lett.*, 66:1938–1941, Apr 1991.

[131] R.C. Dynes. 16th international conference on low temperature physics localization and correlation effects in metals and semiconductors — experiment. *Physica B+C*, 109:1857 – 1865, 1982.

[132] K. K. Choi, D. C. Tsui, and K. Alavi. Dephasing time and one-dimensional localization of two-dimensional electrons in GaAs/$Al_xGa_{1-x}As$ heterostructures. *Phys. Rev. B*, 36:7751–7754, Nov 1987.

[133] NF Mott. Conduction in non-crystalline materials: III. localized states in a pseudogap and near extremities of conduction and valence bands. *Philosophical Magazine*, 19(160):835–852, 1969.

[134] NF Mott and EA Davis. Electronic processes in non-crystalline materials, 2nd edn. clarendon, 1979.

[135] S. Xiao, Y. Yoon, Y.-H. Lee, J. P. Bird, Y. Ochiai, N. Aoki, J. L. Reno, and J. Fransson. Detecting weak coupling in mesoscopic systems with a nonequilibrium Fano resonance. *Phys. Rev. B*, 93:165435, Apr 2016.

[136] Gerd Bergmann. Weak localization in thin films: a time-of-flight experiment with conduction electrons. *Physics Reports*, 107(1):1–58, 1984.

[137] Sudip Chakravarty and Albert Schmid. Weak localization: The quasiclassical theory of electrons in a random potential. *Physics Reports*, 140(4):193–236, 1986.

[138] Harold U. Baranger, Rodolfo A. Jalabert, and A. Douglas Stone. Weak localization and integrability in ballistic cavities. *Phys. Rev. Lett.*, 70:3876–3879, Jun 1993.

[139] RP Taylor, AS Sachrajda, JA Adams, P Zawadzki, PT Coleridge, and P Marshall. Collimation effects in quantum point contacts. *Physica B: Condensed Matter*, 175(1-3):243–246, 1991.

[140] Ç. Kurdak, A. M. Chang, A. Chin, and T. Y. Chang. Quantum interference effects and spin-orbit interaction in quasi-one-dimensional wires and rings. *Phys. Rev. B*, 46:6846–6856, Sep 1992.

[141] B. Reulet, H. Bouchiat, and D. Mailly. Magnetoconductance, weak localization and electron-electron interactions in semi-ballistic quantum wires. *EPL (Europhysics Letters)*, 31(5-6):305, 1995.

Appendix A

Magnetic hysteresis in the double cavity measurement

In the double cavity experiment, a shift in central peak which in principle should occur exactly at 0 T is observed, to rule out this shift arises from the property of the device, we swept the magnetic field from negative to positive (forward sweep) and from positive to negative (backward sweep) many times. In such experiments, the injector is set to 2 G_0 and 3 G_0 respectively, while the detector is fixed at G_0 because the central structure appears as a single broad peak with these combinations. This makes the shift easier to observe and differentiate. The result is shown in figure A.1, it is seen that the central peak occurs at positive magnetic field rather than 0 T if the field is swept from negative to positive, while it occurs at negative field if the field is swept in the reversed direction, almost all the peaks and dips are symmetric against magnetic field. Zooming in around 0 T as seen in figure A.1 (b), it is found that the central peak occurs at 3 mT with forward sweep and it locates exactly at - 3 mT with backward sweep. This suggests such this shift is likely arises from magnetic hysteresis of the superconducting magnet. In addition, due to the strict symmetry observed here this shift is unlikely to affect our observation and discussion.

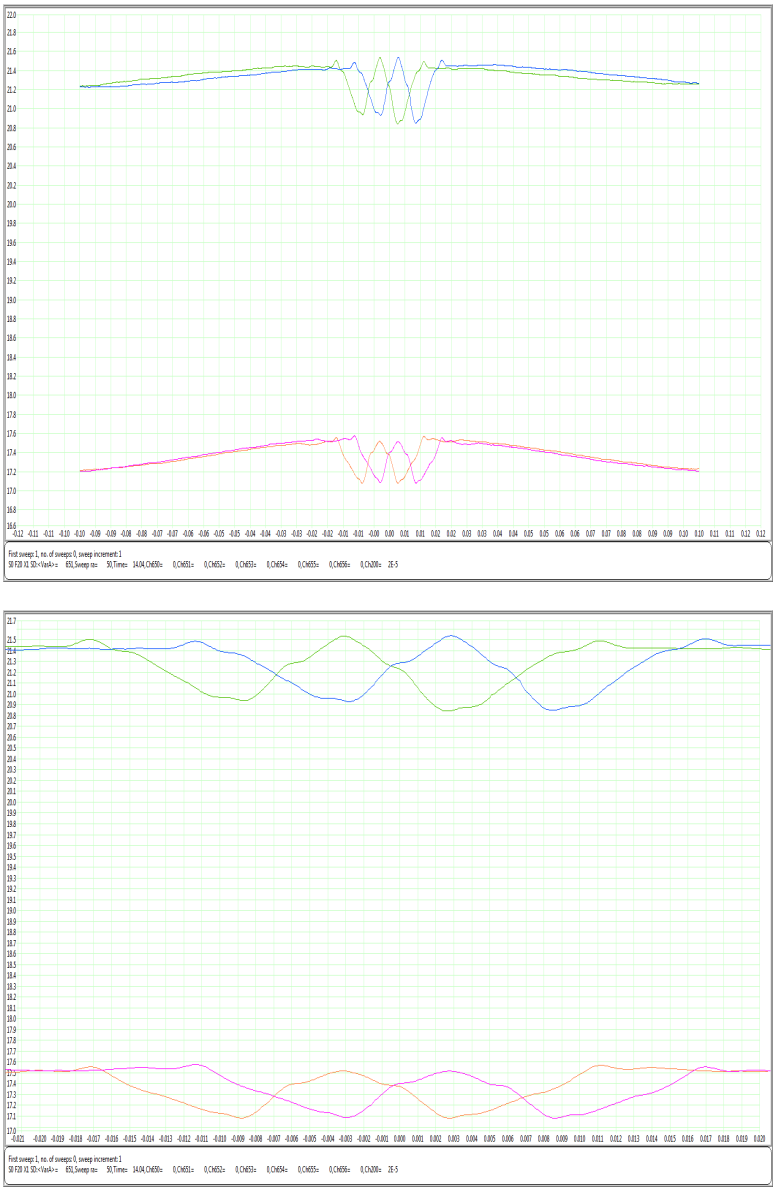

Fig. A.1 **Magnetic hysteresis in the double cavity measurement. a**, typical traces shows hysteresis, top traces injector is tuned to 2 G_0 while detector is set to G_0, bottom traces injector is adjusted to 3 G_0 while detector is set to G_0, it is seen that in both combinations the central peak occurs at positive magnetic field rather than 0 T is the field is swept from negative to positive, while it occurs at negative field if the field is swept in the reversed direction. **b**, zoom in of plot **a** in the vicinity of 0 T, the shift of central peak is quite symmetric against magnetic field.

Appendix B

Matlab code for conductance simulation

This section describes the Matlab code used to generate the potential profile and conductance of a split gate device, the corresponding result is shown in figure 1.3, figure 1.4, figure 2.1, figure 2.15, figure 2.18.

```
%simulated conductance in real device                                    *
%Author: Chengyu Yan                                                     *
%Institution:UCL                                                         *
%*************************************************************************



%I. normalized potential for spit gate
for i=1:1:row
    for j=1:1:col
        for k=1:1:lay
             nor_con(i,j,k)=(1/pi*(atan2((w+x(j)),dep)+atan2((w-x(j)),dep))...
            -1/(2*pi)*atan2((d+y(i))*(w+x(j)),dep*sqrt((d+y(i))^2+(w+x(j))^2+dep^2))...
            -1/(2*pi)*atan2((d-y(i))*(w+x(j)),dep*sqrt((d-y(i))^2+(w+x(j))^2+dep^2))...
            -1/(2*pi)*atan2((d+y(i))*(w-x(j)),dep*sqrt((d+y(i))^2+(w-x(j))^2+dep^2))...
            -1/(2*pi)*atan2((d-y(i))*(w-x(j)),dep*sqrt((d-y(i))^2+(w-x(j))^2+dep^2)));
        end
    end
end



%II. Mapping gate voltage to real potential (including screening effect)
E_g=E_def+(V_g-V_def).^2/(V_pin-V_def)^2*(E_pin-E_def);
```

To get the conductance of a split gate device, it is necessary to know the potential profile at each gate voltage, one of such model is proposed in Ref.[17] which assumes the metallic gate and the 2DEG are the upper and lower plate of a parallel plate capacitor, thus the problem is altered into calculate the electric field distribution in such an effective capacitor. The

```
% III. Extract omega_x and omega_y
f_saddle=fittype('a *x^2','dependent',{'y'},'independent',{'x'},'coefficients',{'a'});
coef_y(k)=coeffvalues(fit(y_fit(:,k),poty_fit(:,k)-pot_con(y0,x0,k),f_saddle));
coef_x(k)=coeffvalues(fit(x_fit(:,k),potx_fit(:,k)-pot_con(y0,x0,k),f_saddle));
```

```
% IV. Number of avaliable subbands
E_diff(k)=Ef-U0(k);  %energy difference between Fermi energy and the top of saddle point
n(k)=ceil(E_diff(k)/hwy(k)); %number of subbands for each gate voltage
```

electric field generated by a pair of split gate is equivalent to the field generated by the infinite long strip (the width of the strip equals to that of split gate) substrates the contribution of a rectangle whose dimension is the same of the 1D channel, this corresponds **step I** of the code. In this model, to simplify the calculation, it assumes the dielectric constant of the effective capacitor is uniform. the Assumption is valid for a AlGaAs/GaAs heretrojunction, however, for other material systems the difference in dielectric constant of different layers should be considered.

It is noticed that the model only considers the influence of the dimension (i.e. the length and width of the split gate and depth of the 2DEG) of the split gate, while other parameters such as the concentration of dopant is ignored. To make the simulation more realistic, I decide to rescale the the obtained potential from **step I** with the help of definition voltage V_{def} (voltage corresponds to the end of the 1D-2D transition of the QPC) and pinch-off voltage V_{pin} (voltage corresponds to conductance of the QPC drops to zero), considering the fact that the potential barrier underneath the gate equals to Fermi level (so that electrons under the gate are depleted and 1D channel forms) when definition voltage is applied, while the potential barrirer in the centre of the 1D channel should exceed Fermi level (so that 1D channel is pinched off) at pinch-off voltage, this is **step II**.

It is found in figure 1.3 the potential has a parabolic shape along both x-direction (current flow direction) and y-direction (confinement direction) within the 1D channel and this agrees with saddle point model[16],

$$V(x,y) = V_0 - \frac{1}{2}m\omega_x^2 x^2 + \frac{1}{2}m\omega_y^2 y^2$$

important parameters V_0, ω_x and ω_y can be determined from the simulated potential profile, this is **step III**.

```
% V. Calculate conductance
E_gap=g*u*B; %Energy difference between spinup and spin down branches, take Zeeman energy as an example

g_u(1,k,j)=1/2*exp((Efn(1,k,j)+0.5*E_gap(1))/E1(k))/(1+exp((Efn(1,k,j)+0.5*E_gap(1))/E1(k)))...
          +1/2*exp((Efn(1,k,j)-V_sd(1)+0.5*E_gap(1))/E1(k))/(1+exp((Efn(1,k,j)-V_sd(1)+0.5*E_gap(1))/E1(k)));

g_d(1,k,j)=1/2*exp((Efn(1,k,j)-0.5*E_gap(1))/E1(k))/(1+exp((Efn(1,k,j)-0.5*E_gap(1))/E1(k)))...
          +1/2*exp((Efn(1,k,j)-V_sd(1)-0.5*E_gap(1))/E1(k))/(1+exp((Efn(1,k,j)-V_sd(1)-0.5*E_gap(1))/E1(k)));

G(1,k)=sum(g(1,k,:))
```

The total conductance is the sum of the contribution of all the available 1D subbands, this it necessary to extract the number of available subbands N, $N = \frac{\Delta}{\hbar\omega_y}$, where Δ is the difference between Fermi level and the (top of) saddle point (for source-drain bias dependence, this is replaced by $\mu_s - \mu_d$) and $\hbar\omega_y$ is 1D subband spacing, this is **step IV**.

The last step, **step V**, is quite straightforward, the conductance of each 1D subbands ,consists of contribution from both spin up and spin down electrons, is determined by Landauer-Büttiker formula. For magnetic field dependence, a energy gap due Zeeman energy is added and thus spin up and spin down contribute different.